frontiers | Research Topics

Image processing methods in animal MRI and their application to evaluate brain function

Edited by
Shengxiang Liang, Georgios A. Keliris, Baoci Shan and Jie Wang

Published in
Frontiers in Neuroscience

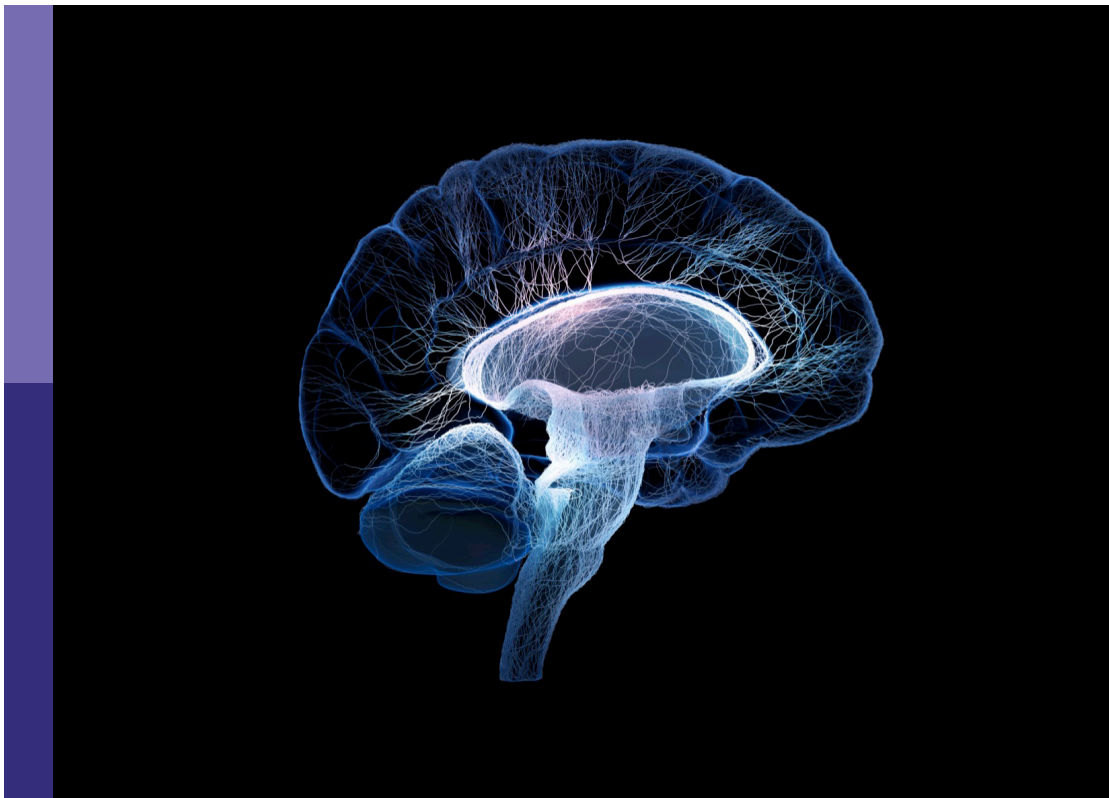

ISSN 1664-8714
ISBN 978-2-83251-713-0
DOI 10.3389/978-2-83251-713-0

About Frontiers

Frontiers is more than just an open access publisher of scholarly articles: it is a pioneering approach to the world of academia, radically improving the way scholarly research is managed. The grand vision of Frontiers is a world where all people have an equal opportunity to seek, share and generate knowledge. Frontiers provides immediate and permanent online open access to all its publications, but this alone is not enough to realize our grand goals.

Frontiers journal series

The Frontiers journal series is a multi-tier and interdisciplinary set of open-access, online journals, promising a paradigm shift from the current review, selection and dissemination processes in academic publishing. All Frontiers journals are driven by researchers for researchers; therefore, they constitute a service to the scholarly community. At the same time, the *Frontiers journal series* operates on a revolutionary invention, the tiered publishing system, initially addressing specific communities of scholars, and gradually climbing up to broader public understanding, thus serving the interests of the lay society, too.

Dedication to quality

Each Frontiers article is a landmark of the highest quality, thanks to genuinely collaborative interactions between authors and review editors, who include some of the world's best academicians. Research must be certified by peers before entering a stream of knowledge that may eventually reach the public - and shape society; therefore, Frontiers only applies the most rigorous and unbiased reviews. Frontiers revolutionizes research publishing by freely delivering the most outstanding research, evaluated with no bias from both the academic and social point of view. By applying the most advanced information technologies, Frontiers is catapulting scholarly publishing into a new generation.

What are Frontiers Research Topics?

Frontiers Research Topics are very popular trademarks of the *Frontiers journals series*: they are collections of at least ten articles, all centered on a particular subject. With their unique mix of varied contributions from Original Research to Review Articles, Frontiers Research Topics unify the most influential researchers, the latest key findings and historical advances in a hot research area.

Find out more on how to host your own Frontiers Research Topic or contribute to one as an author by contacting the Frontiers editorial office: frontiersin.org/about/contact

Image processing methods in animal MRI and their application to evaluate brain function

Topic editors

Shengxiang Liang — Fujian University of Traditional Chinese Medicine, China

Georgios A. Keliris — University of Antwerp, Belgium

Baoci Shan — Institute of High Energy Physics, Chinese Academy of Sciences (CAS), China

Jie Wang — Wuhan Institute of Physics and Mathematics, Chinese Academy of Sciences (CAS), China

Topic coordinator

Hui Xu — McMaster University, Canada

Citation

Liang, S., Keliris, G. A., Shan, B., Wang, J., eds. (2023). *Image processing methods in animal MRI and their application to evaluate brain function*.

Lausanne: Frontiers Media SA. doi: 10.3389/978-2-83251-713-0

Table of contents

frontiers | Frontiers in Neuroscience

TYPE Editorial
PUBLISHED 06 February 2023
DOI 10.3389/fnins.2023.1147057

OPEN ACCESS

EDITED AND REVIEWED BY
Vince D. Calhoun,
Georgia State University, United States

*CORRESPONDENCE
Shengxiang Liang
✉ sxliang@fjtcm.edu.cn
Georgios A. Keliris
✉ georgios.keliris@uantwerpen.be
Jie Wang
✉ jie.wang@apm.ac.cn
Baoci Shan
✉ shanbc@ihep.ac.cn

SPECIALTY SECTION
This article was submitted to Brain Imaging Methods, a section of the journal Frontiers in Neuroscience

RECEIVED 18 January 2023
ACCEPTED 26 January 2023
PUBLISHED 06 February 2023

CITATION
Liang S, Keliris GA, Wang J and Shan B (2023) Editorial: Image processing methods in animal MRI and their application to evaluate brain function. *Front. Neurosci.* 17:1147057. doi: 10.3389/fnins.2023.1147057

Editorial: Image processing methods in animal MRI and their application to evaluate brain function

Shengxiang Liang[1,2,3]*, Georgios A. Keliris[4,5]*, Jie Wang[6,7,8,9]* and Baoci Shan[9,10]*

[1]National-Local Joint Engineering Research Center of Rehabilitation Medicine Technology, Fujian University of Traditional Chinese Medicine, Fuzhou, China, [2]Rehabilitation Industry Institute, Fujian University of Traditional Chinese Medicine, Fuzhou, China, [3]Traditional Chinese Medicine Rehabilitation Research Center of State Administration of Traditional Chinese Medicine, Fujian University of Traditional Chinese Medicine, Fuzhou, China, [4]Bio-Imaging Lab, Department of Biomedical Sciences, University of Antwerp, Antwerp, Belgium, [5]Foundation for Research and Technology – Hellas, Heraklion, Greece, [6]Institute of Neuroscience and Brain Diseases, Xiangyang Central Hospital, Affiliated Hospital of Hubei University of Arts and Science, Xiangyang, Hubei, China, [7]Academy of Integrative Medicine, College of Integrative Medicine, Fujian University of Traditional Chinese Medicine, Fuzhou, China, [8]Key Laboratory of Magnetic Resonance in Biological Systems, State Key Laboratory of Magnetic Resonance and Atomic and Molecular Physics, National Center for Magnetic Resonance in Wuhan, Wuhan Institute of Physics and Mathematics, Innovation Academy for Precision Measurement Science and Technology, Chinese Academy of Sciences, Wuhan National Laboratory for Optoelectronics, Wuhan, China, [9]University of Chinese Academy of Sciences, Beijing, China, [10]Beijing Engineering Research Center of Radiographic Techniques and Equipment, Institute of High Energy Physics, Chinese Academy of Sciences, Beijing, China

KEYWORDS

magnetic resonance imaging, analysis method, neurological diseases, brain function, functional evaluation, animal

Editorial on the Research Topic
Image processing methods in animal MRI and their application to evaluate brain function

As a non-invasive and non-radiative technique, magnetic resonance imaging (MRI) has been widely used in brain research (Ni, 2021). Recently, more and more findings about brain activation mode in specific state were reported *via* animal models and MRI (Benveniste and Blackband, 2002). The purpose of this special topic is to provide knowledge and information on the state-of-the-art methods currently used for image acquisition, (pre)processing, and evaluation of brain function in small animals.

It is difficult to expound brain function at cellular, systematic and functional levels. Multimodal neuroimaging approaches are able to combine techniques such as calcium imaging, optogenetics, electrophysiology, chemogenetics with functional magnetic resonance imaging (fMRI) and help scientists uncover the relationship between neuronal activity and vascular network dynamics, which would promote our knowledge of the brain from the level of single cells or circuits to the whole brain (Kosten et al.). Huang et al. reviewed fMRI papers of small animals under the state of stimulation categorized into electrical, visual, olfactory, auditory and other ways, and analyzed the similarities and differences, advantages and disadvantages of the stimulation sites, electrodes, and stimulation methods. The study provided invaluable comparative information on brain fMRI of small animals combined with stimulation (Huang et al.).

Lopez-Castro et al. proposed a method for operation of long-term implantable monopolar carbon electrodes in rats. Prelimbic cortex (PRL) implantable monopolar carbon electrodes were used to treat alcohol use disorder. This method of implantation generates smaller MRI artifact

and serves clinical and basic research (Lopez-Castro et al.). In terms of data processing, Bao et al. constructed an automatic method for individual parcellation of rat brain MEMRI images, which further benefited case-control statistical analysis and improved the accuracy of ROI-based imaging analysis.

Alzheimer's disease (AD) is the most common cause of dementia. Many clinical and basic studies have aimed at improving effective identification strategies for AD (Valenzuela et al., 2020). Some AD imaging articles are included in this edition. High resolution diffusion tensor imaging (DTI) scanning displayed that the fractional anisotropy (FA) of 5xFAD mice showed differences at 4 months, indicating that the FA index of DTI can be used as a sensitive biomarker to detect amyloid deposition in 5xFAD mice, and can be used for preclinical research and detection of the efficiency of AD drugs (Maharjan et al.). At the same time, resting state fMRI of AD mice after electroacupuncture(EA) at Baihui and Shenting indicated that the ReHo value of local neuronal integration in hippocampus, entorhinal cortex and other brain regions increased, as well as the number of functional connectivity and neural fiber connections between entorhinal cortex and hippocampus increased, suggesting that EA intervention may be an effective strategy to treat memory defects in AD recognition (Lin et al.).

Hippocampus is closely associated with cognition and emotion. Sepsis associated encephalopathy (SAE) has been identified as a common complication of sepsis. SAE-induced pathological changes in the hippocampus may lay the foundation for the development of cognitive dysfunction and affective disorders. Yao et al. found significant changes of hippocampal-related brain networks i-n SAE rats, and the functional connectivity between the hippocampus and thalamus was positively correlated with affective deficits. Li et al. found that increased ALFF value, Glx/Cr ratio and mI/Cr ratio in hippocampus of SAE rats were positively correlated with cognitive impairment. Thus, changes in hippocampal network, ALFF, and metabolites may be potential neuroimaging biomarkers of cognitive impairment in SAE patients, which might provide the basis for the diagnosis of clinical sepsis (Li et al.).

Pan et al. used ^{18}F-FDG PET/CT to identify the subregions of the posterior splenic cortex, the role of RSCDS and RSCGS in the coding process of rat contextual fear conditioning model, and the underlying brain network mechanism. The results showed that the role of rat RSCS in the formation of scene fear memory mainly depends on the RSCDS rather than the RSCGS.

In segmental sampling of rat's sciatic nerve imaging in DTI, RS-5 EPI sequence-derived FA and RD may be highly sensitive quantitative biomarkers for detecting histopathological changes of sciatic nerve in rats. These findings provide some reference value for the optimization of DTI sequence in the future peripheral nerve MRI research (Chen et al.).

We hope that the aforementioned studies which were included in this special topic can inspire new studies and novel future applications of small animal MRI in the fields of data acquisition, analysis methods, pre-clinical applications, biomarker detection and can contribute in more accurate prediction of disease progression and bring us a step close to clinical applications.

Author contributions

All authors listed have made a substantial, direct, and intellectual contribution to the work and approved it for publication.

Funding

This study was supported by the grants from the National Natural Science Foundation of China (82004440), the Natural Science Foundation of Fujian Province (2021J01961), the Youth Science Foundation of Fujian Provincial Health Commission (2019-1-65), and the Scientific Research Foundation for the High-level Talents funded by Fujian University of Traditional Chinese Medicine (X2019002-talents).

Acknowledgments

We would like to thank the authors for their contributions to the topic and the reviewers for their rigorous review. We also thank the editors for their support for the publications of the topic.

Conflict of interest

The authors declare that the research was conducted in the absence of any commercial or financial relationships that could be construed as a potential conflict of interest.

Publisher's note

References

Benveniste, H., and Blackband, S. (2002). MR microscopy and high resolution small animal MRI: applications in neuroscience research. *Prog. Neurobiol.* 67, 393–420. doi: 10.1016/s0301-0082(02)00020-5

Ni, R. (2021). Magnetic resonance imaging in animal models of Alzheimer's disease amyloidosis. *Int. J. Mol. Sci.* 22, 12768. doi: 10.3390/ijms222312768

Valenzuela, P. L., Castillo-Garcia, A., Morales, J. S., de la Villa, P., Hampel, H., Emanuele, E., et al. (2020). Exercise benefits on Alzheimer's disease: state-of-the-science. *Ageing Res. Rev.* 62, 101108. doi: 10.1016/j.arr.2020.101108

frontiers | Frontiers in Neuroscience

ORIGINAL RESEARCH
published: 03 May 2022
doi: 10.3389/fnins.2022.886858

Retrosplenial Cortex Effects Contextual Fear Formation Relying on Dysgranular Constituent in Rats

Ting-Ting Pan[1,2,3†], Chao Liu[3,4†], De-Min Li[1†], Tian-Hao Zhang[2,5], Wei Zhang[2,5], Shi-Lun Zhao[2,5], Qi-Xin Zhou[3,4], Bin-Bin Nie[2,5], Gao-Hong Zhu[6]*, Lin Xu[3,4,7]* and Hua Liu[2,5]**

[1] School of Physics and Microelectronics, Zhengzhou University, Zhengzhou, China, [2] Beijing Engineering Research Center of Radiographic Techniques and Equipment, Institute of High Energy Physics, Chinese Academy of Sciences, Beijing, China, [3] CAS Key Laboratory of Animal Models and Human Disease Mechanisms, and KIZ-SU Joint Laboratory of Animal Model and Drug Development, and Laboratory of Learning and Memory, Kunming Institute of Zoology, Chinese Academy of Sciences, Kunming, China, [4] Kunming College of Life Science, University of Chinese Academy of Sciences, Kunming, China, [5] School of Nuclear Science and Technology, University of Chinese Academy of Sciences, Beijing, China, [6] Department of Nuclear Medicine, The First Affiliated Hospital of Kunming Medical University, Kunming, China, [7] CAS Centre for Excellence in Brain Science and Intelligent Technology, Shanghai, China

Animal contextual fear conditioning (CFC) models are the most-studied forms used to explore the neural substances of posttraumatic stress disorder (PTSD). In addition to the well-recognized hippocampal–amygdalar system, the retrosplenial cortex (RSC) is getting more and more attention due to substantial involvement in CFC, but with a poor understanding of the specific roles of its two major constituents—dysgranular (RSCd) and granular (RSCg). The current study sought to identify their roles and underlying brain network mechanisms during the encoding processing of the rat CFC model. Rats with pharmacologically inactivated RSCd, RSCg, and corresponding controls underwent contextual fear conditioning. [^{18}F]-fluorodeoxyglucose positron emission tomography/computed tomography (^{18}F-FDG PET/CT) scanning was performed for each animal. The 5-h and 24-h retrieval were followed to test the formation of contextual memory. Graph theoretic tools were used to identify the brain metabolic network involved in encoding phase, and changes of nodal (brain region) properties linked, respectively, to disturbed RSCd and RSCg were analyzed. Impaired retrieval occurred in disturbed RSCd animals, not in RSCg ones. The RSC, hippocampus (Hip), amygdala (Amy), piriform cortex (Pir), and visual cortex (VC) are hub nodes of the brain-wide network for contextual fear memory encoding in rats. Nodal degree and efficiency of hippocampus and its connectivity with amygdala, Pir, and VC were decreased in rats with disturbed RSCd, while not in those with suppressed RSCg. The RSC plays its role in contextual fear memory encoding mainly relying on its RSCd part, whose condition would influence the activity of the hippocampal–amygdalar system.

Keywords: contextual fear formation, retrosplenial cortex, brain metabolic network, graph theory, hippocampal-amygdalar system

OPEN ACCESS

Edited by:
Jie Wang,
Wuhan Institute of Physics and Mathematics (CAS), China

Reviewed by:
Tianbin Song,
Xuanwu Hospital, China
Zhiqun Wang,
Aerospace Center Hospital, China

****Correspondence:***
Bin-Bin Nie
niebb@ihep.ac.cn
Gao-Hong Zhu
1026909611@qq.com
Lin Xu
lxu@vip.163.com
Hua Liu
liuhua@ihep.ac.cn

† These authors have contributed equally to this work and share first authorship

Specialty section:
This article was submitted to Brain Imaging Methods, a section of the journal Frontiers in Neuroscience

Received: *01 March 2022*
Accepted: *22 March 2022*
Published: *03 May 2022*

Citation:
Pan T-T, Liu C, Li D-M, Zhang T-H, Zhang W, Zhao S-L, Zhou Q-X, Nie B-B, Zhu G-H, Xu L and Liu H (2022) Retrosplenial Cortex Effects Contextual Fear Formation Relying on Dysgranular Constituent in Rats. Front. Neurosci. 16:886858. doi: 10.3389/fnins.2022.886858

INTRODUCTION

The posttraumatic stress disorder (PTSD) is a kind of anxiety disorder usually occurring after undergoing a traumatic event, of which the neural mechanism remains unclear (Brunello et al., 2001; Keane et al., 2006). Animal contextual fear conditioning (CFC) models are the most-studied forms for understanding PTSD and other stress-related disorders (Izquierdo et al., 2016). Defining the key neural correlates and circuitries involved in CFC is fundamental for understanding its underlying mechanism. Although the hippocampus (Hip), amygdala (Amy) nuclei, and the forebrain cortex are popularly recognized (Izquierdo et al., 2016; Alexandra Kredlow et al., 2022), a comprehensive understanding of the key brain regions and their interactions linked to CFC is still in the face of many challenges. Recently, the retrosplenial cortex (RSC) has received more and more attention because of its general activation in episodic memory (Vann et al., 2009; Corcoran et al., 2018).

Early evidence came from RSC lesion studies in animals showing the RSC was necessary in associative learning situations such as eyeblink conditioning and discrimination reversal learning (Gabriel et al., 1983; Berger et al., 1986). Later, in addition to spatial processing and navigation (Cooper and Mizumori, 2001; Vann and Aggleton, 2002), RSC was also found substantially involved in instrumental and associative learning of aversive stimuli (Lukoyanov and Lukoyanova, 2006; Keene and Bucci, 2008). Recent works exploring interactions between the hippocampus and other cortices in contextual fear memory demonstrated that the RSC was always engaged in, ranging from the encoding and retrieval phases to extinction (Cowansage et al., 2014; Jovasevic et al., 2015; Leaderbrand et al., 2016). Human imaging studies showed increased activity of RSC during contextual memory retrieval and autobiographical memory in healthy and PTSD subjects (Liberzon et al., 1999; Schacter and Addis, 2007). Furthermore, some neurodegenerative disorders with amnesia, typically Alzheimer's disease, often accompany RSC pathological changes (Leech and Sharp, 2014; Weiner et al., 2017). Although numerous studies have suggested in principle the involvement of RSC in fear memory, the issue of its structural heterogeneity should be considered. Cytoarchitecturally, the RSC is composed of two major parts, granular area (RSCg) and dysgranular area (RSCd) (Vann et al., 2009). These two subregions are different in structural connections with other regions (Vogt and Miller, 1983; Vogt et al., 2005), which implies that they likely play distinct roles functionally. A few pilot studies exhibited RSCg and RSCd played different roles in spatial cognitive tasks (Pothuizen et al., 2009), supporting the view of functional heterogeneity of RSC. In contextual fear memory, however, the individual roles of RSCg and RSCd still remain unknown.

The brain is a complex system with glucose as the main energy source (Mergenthaler et al., 2013), and ^{18}F-FDG PET imaging is widely used to study neural activities based on glucose metabolism. Relative to simple tests for regional metabolic patterns due to physiologic and pathologic activity, FDG metabolic brain networks would evaluate the property changes of the system globally as well as the relationships among local brain regions at the whole brain level, which is a significant advantage of this method to reveal the mechanisms of complex systems (Yakushev et al., 2017). Nowadays, metabolic brain networks based on FDG-PET images have been emerging as a useful tool in basic and clinical neuroscience (Zhang et al., 2019; Huang et al., 2020). In this study, to determine the roles of RSCg and RSCd during CFC of rat model, combining pharmacological approaches with [^{18}F]-fluorodeoxyglucose positron emission tomography/computed tomography (^{18}F-FDG PET/CT) imaging and brain network methods, we investigated their effects and the underlying network mechanisms.

MATERIALS AND METHODS

Animals

Nine-week-old male Sprague-Dawley rats obtained from Vital River Laboratory Animal Technology Company (Beijing, China) were used in this study. The metabolic brain networks were generally constructed by Pearson's correlations in an intersubject manner. Based on considerations of statistical power, a large sample size was always employed. In this study, four independent groups and a total of 113 rats were involved. Rats were initially housed in groups (five rats per cage) and then housed individually after surgery. Rats had free access to food and water under a 12-h light/12-h dark cycle in a temperature-regulated environment maintained at 25 ± 2°C at the Kunming Institute of Zoology (CAS, Kunming, China). All protocols were approved by the Institutional Animal Care and Use Committee of Kunming Institute of Zoology, Chinese Academy of Sciences (ID: SMKX-20190820-195).

Surgery and Infusions

Rats had surgery to intracranial implantation stainless steel guide cannula (RWD Life Sciences, Shenzhen, China), using the techniques described previously (Zhou et al., 2017). The stereotaxic coordinates of RSCd (-3 mm posterior, ± 0.6 mm lateral, 1 mm ventral to bregma) and RSCg (-5.20 mm posterior, ± 0.4 mm lateral, 2 mm ventral to bregma) were determined according to the Paxinos and Watson brain atlas (**Supplementary Figure 1**; Paxinos and Watson, 2005). Rats were allowed 7 days to recover from surgery before the behavioral procedures.

Tetrodotoxin (TTX, 20 μM, T111387-1 mg, Aladdin, Shanghai, China), the sodium channel blocker, was used as an inhibitor to inactivate the target regions in this study (Zhou et al., 2017); saline was used as vehicle. The inhibitor was infused at a volume of 1 μl per side into the target brain regions through the implanted guide cannulas by using the injection needles connecting to a syringe pump (LSP02-2B, Longer Precision Pump Co., Ltd., Baoding, China), and infused at a speed of 0.1 μl/min. All inhibitor and vehicle infusions were made 30 min before placing the rat in the conditioning chamber for training.

Contextual Fear Conditioning and Test

The procedures for CFC and retrieval were shown schematically in **Figure 1A** (Zhou et al., 2017). One day before CFC, rats were placed in the training box (MED-VFC-SCT-R, MED Associates

Inc., Fairfax, VT, United States) to acclimate to the box by exploring for 12 min. On the day of training, the rats were placed in the training box and received 5 footshocks (0.8 mA, 2 s duration) with 2 min intertrial interval, and then returned to the homecage 2 min after final footshock. Retrieval tests were performed by placing the rats in the training box for 5 min without footshocks for independent groups at 5 or 24 h after conditioning. Freezing levels were recorded for scoring fear memory through the computer system (MED-VFC-SCT-R, MED Associates Inc., Fairfax, VA, United States).

^{18}F-FDG PET/CT Imaging Protocols and Image Preprocessing

Thirty minutes after the inhibitor (or vehicle) injection into the target brain area, rats were injected intraperitoneally with ^{18}F-FDG (18.5 MBq/100 g of body weight). Then each rat was immediately subjected to fear training; 40 min after FDG injection, rats were anesthetized with isoflurane (5% for induction and 1.5–2% for maintenance) and fixed in a prone position on the scanning bed of an E-plus 166 micro-PET/CT scanner (Institute of High Energy Physics, CAS, Beijing, China). The scanning was performed for 20 min. After acquisition, the PET images were reconstructed by the two-dimensional ordered subset expectation maximization algorithm with corrections for decay, normalization, dead time, photon attenuation, scatter, and random coincidences, and the reconstructed image matrix size was 256 × 256 × 63 with voxel size of 0.5 mm × 0.5 mm × 1 mm (Nie et al., 2014).

All the images were preprocessed using an improved toolbox for voxel-wise analysis of rat brain images based on SPM8 (Wellcome Department of Cognitive Neurology, London, United Kingdom) (Nie et al., 2014). The images preprocessing steps were as follows: (1) the individual images of rat were spatially normalized into Paxinos and Watson space; (2) the normalized images were smoothened with 2 mm × 2 mm × 4 mm Gaussian kernel; and (3) then the intensity of images was globally normalized in each image.

Construction of Brain-Wide Metabolic Network During Contextual Fear Conditioning in Rats

The metabolic networks were constructed as a collection of 39 nodes representing brain regions connected by edges corresponding to the links between them; 39 anatomical brain regions (**Supplementary Figure 2** and **Supplementary Table 1**) were predefined by a three-dimensional digital map based on the Paxinos and Watson atlas (Nie et al., 2013). The correlation coefficient between each pair of nodes was calculated with Pearson's correlation in an intersubject manner, and the absolute value of correlation coefficient was used to define the weight of the edge (Zhang et al., 2019).

Hub Nodes and Nodal Properties

Graph theoretic measurements were used to analyze the node properties. In this study, we mainly focused on the nodal degree and nodal efficiency, which characterized the node's connectivity and efficiency of parallel information transfer in the network, respectively (Choi et al., 2014; Zhang et al., 2019).

The nodal degree is the sum weight that links a node to the rest of the network in a weighted network. We quantitatively determined the hubs by the nodal Z-score. Z_i-score is defined to measure how well-connected node i is to nodes in a network (Zhang et al., 2019), which makes the nodal degree comparable between networks. The Z_i-score is defined as

$$\mathrm{Z_i} = \frac{k_i - \bar{k}}{\sigma_k},$$

where $k_i = \sum_{j \neq i} A_{ij}\delta(i,j)$ is the sum of the weight between node i and other nodes in a weighted network. $\bar{k}$ is the average of k over all the nodes, and σ_k is the standard deviation of k in a weighted network. Node i is defined as a hub when Z_i-score > 1 (Zhang et al., 2019).

Nodal efficiency (E_{nodal}) characterizes the efficiency of this node's parallel information transfer in the network. The E_{nodal} for node i is defined as

$$\mathrm{E_{nodal}}(i) = \frac{1}{N-1}\sum_{i \neq j}\frac{1}{L_{i,j}},$$

where L_{ij} is the minimum path length between nodes i, j, and N is the number of nodes in a graph (Choi et al., 2014).

Core Brain Regions Associated With RSCd/g Metabolism During Contextual Fear Conditioning

Based on the brain-wide metabolic network of vehicle group, RSCd and RSCg were, respectively, selected as seed regions to search for brain regions highly metabolically relevant to them to construct their core network during CFC. Pearson's correlation coefficients were calculated of the mean image intensity between the 39 nodes and the seed region. A strong Pearson's correlation coefficient of 0.7 was used as a threshold to screen the brain regions that were strongly correlated with the seed region, and the supra-threshold brain regions were considered to form the core metabolic network related to RSCd/RSCg during CFC.

Statistical Analysis

Two-way ANOVA followed by Bonferroni's posttests for multiple comparisons was used to analyze parameters of behavior performance. The value of $p < 0.05$ was considered statistically significant. Data were given as mean ± SEM. The permutation tests were used to evaluate statistical differences in node properties. First, the node properties of the metabolic networks were calculated separately for the inhibitor group and the corresponding vehicle group. Then the FDG images of the rat brain were randomly reallocated in two groups, and the correlation matrices for each randomized group were computed. The differences in the node properties between the two randomized networks were then calculated. The permutation tests were also used to evaluate the statistical differences in connection strengths between pairs of nodes in different networks. Permutations were repeated 10,000

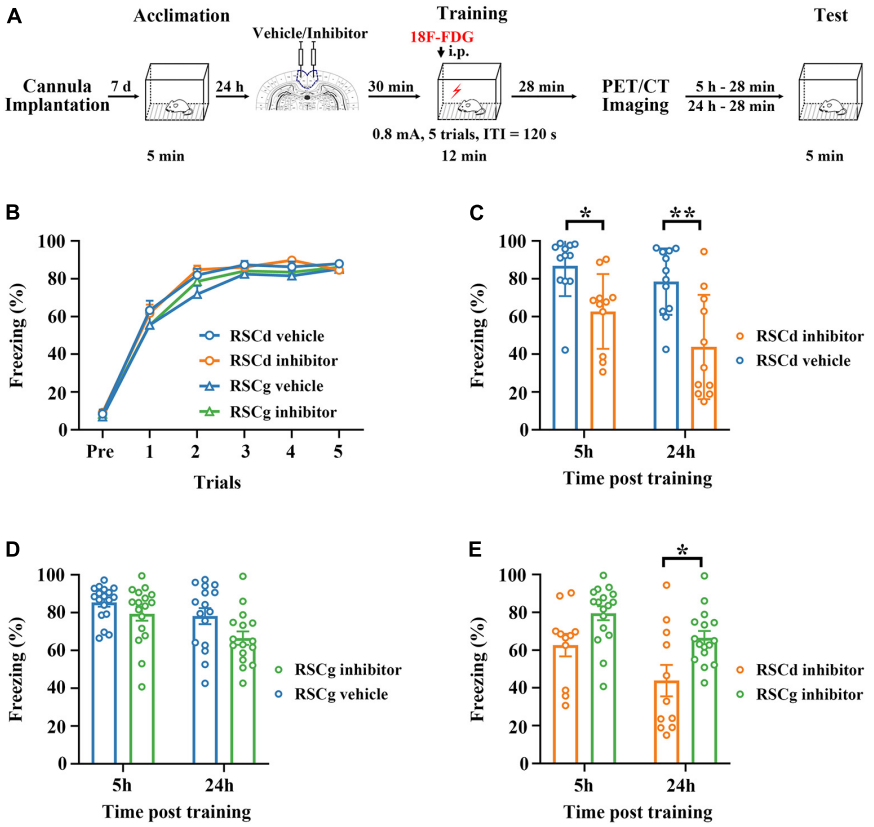

FIGURE 1 | Effects of suppressed RSCd/g on contextual fear memory formation. **(A)** Diagram for experimental procedures. **(B)** The learning curves of four group rats (RSCd vehicle/inhibitor group and RSCg vehicle/inhibitor group) show no significant difference; RSCd vehicle group $n = 24$, inhibitor group $n = 22$; RSCg vehicle group $n = 35$, inhibitor group $n = 32$. **(C)** Memory retrieval during the 5-h and 24-h post-learning tests are significantly impaired in the RSCd inhibitor independent groups compared to the RSCd vehicle independent groups; 5 h, RSCd vehicle group $n = 12$, inhibitor group $n = 11$; 24 h, RSCd vehicle group $n = 12$, inhibitor group $n = 11$. **(D)** There is no significant difference in memory retrieval between the RSCg inhibitor independent groups during the 5-h and 24-h post-learning tests compared to the RSCg vehicle independent groups; 5 h, RSCg vehicle group $n = 18$, inhibitor group $n = 16$; 24 h, RSCg vehicle group $n = 17$, inhibitor group $n = 16$. **(E)** Memory retrieval during the 5-h and 24-h post-learning is significantly impaired in the RSCd inhibitor groups compared to the RSCg inhibitor groups; 5 h, RSCd inhibitor group $n = 11$, RSCg inhibitor group $n = 16$; 24 h, RSCd inhibitor group $n = 11$, RSCg inhibitor group $n = 16$. ITI, intertrial interval; i.p., intraperitoneal injection. $^{*}p < 0.05$, $^{**}p < 0.01$, two-way ANOVA followed by Bonferroni's posttests.

times, and the results were used to estimate 95% confidence interval differences.

RESULTS

Suppressing RSCd During Fear Conditioning Impaired Memory Formation but Not While Suppressing RSCg

We examined the formation of fear memory under different treatments for independent groups, which were RSCd vehicle group, RSCd inhibitor group, RSCg vehicle group, and RSCg inhibitior group. As shown in **Figure 1B**, the freezing of rats was gradually formed as the number of training trials increased, and different vehicle/inhibitor treatment did not cause intergroup differences [**Figure 1B**: RSCd vehicle $n = 24$, inhibitor $n = 22$; RSCg vehicle $n = 35$, inhibitor $n = 32$; trials, $F_{(5,545)} = 561.0$, $p < 0.001$; group, $F_{(3,545)} = 1.300$, $p = 0.278$; trials × group, $F_{(15,545)} = 0.806$, $p = 0.671$; two-way ANOVA with repeated measures followed by Bonferroni's posttests]. Memory retrieval at 5 or 24 h after learning for the independent groups of RSCd inhibitor was impaired to be more severe compared to RSCd vehicle groups [**Figure 1C**, 5 h: RSCd vehicle $n = 12$, inhibitor $n = 11$; 24 h: RSCd vehicle $n = 12$, inhibitor $n = 11$; time, $F_{(1,42)} = 5.003$, $p < 0.05$; group, $F_{(1,42)} = 23.410$, $p < 0.001$; time × group, $F_{(1,42)} = 0.739$, $p = 0.3949$; *post hoc*: 5 h: vehicle vs. inhibitor, $^{*}p < 0.05$; 24 h: vehicle vs. inhibitor, $^{**}p < 0.001$; two-way ANOVA followed by Bonferroni's posttests]. Similarly, for RSCg independent groups, both time and inhibitor treatment provoked significant impairment in memory retrieval. But for the same time point, inhibitor treatment did not induce significant impairment of memory [**Figure 1D**, 5 h: RSCg vehicle $n = 18$, inhibitor $n = 17$; 24 h: RSCg vehicle $n = 16$, inhibitor $n = 16$; time, $F_{(1,63)} = 8.377$, $p < 0.01$; group, $F_{(1,63)} = 6.424$, $p < 0.05$; time × group, $F_{(1,63)} = 0.709$,

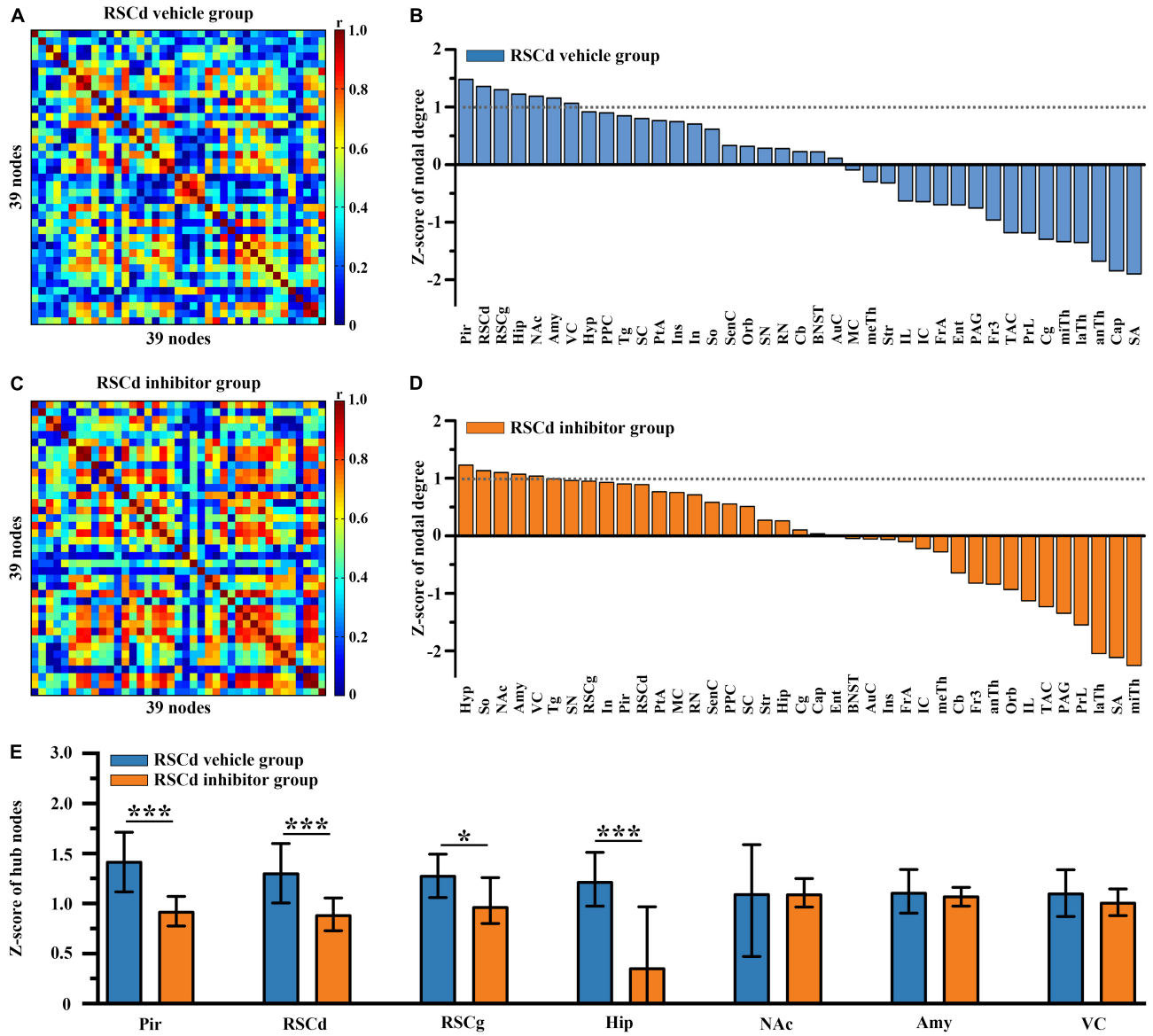

FIGURE 2 | Effects of suppressed RSCd on hub nodes of the brain-wide metabolic network during CFC. Brain-wide metabolic network of **(A)** RSCd vehicle group and **(C)** inhibitor group during CFC. Distribution of nodal degree Z-scores in network of **(B)** RSCd vehicle group and **(D)** inhibitor group. **(E)** Decrease in nodal degree of Pir, RSCd, RSCg, and hippocampus in rats with suppressed RSCd. The error bar indicates the 95% confidence intervals obtained from 1,000-iteration bootstrapping procedures. RSCd vehicle group $n = 24$, RSCd inhibitor group $n = 22$. $^{*}p < 0.05$, $^{***}p < 0.001$, permutation test.

$p = 0.403$; *post hoc*: 5 h: vehicle vs. inhibitor, $p = 0.784$; 24 h: vehicle vs. inhibitor, $p = 0.129$; two-way ANOVA followed by Bonferroni's posttests]. In addition, we contrasted the effects of inhibiting the two subregions; memory retrieval at 5 and 24 h after learning for RSCd inhibitor groups were impaired to be more severe over time compared to RSCg inhibitor groups [**Figure 1E**, time, $F_{(1,51)} = 9.220$, $p < 0.01$; region, $F_{(1,51)} = 14.330$, $p < 0.001$; time × region, $F_{(1,51)} = 0.317$, $p = 0.576$; *post hoc*: 5 h: RSCd vs. RSCg, $p = 0.147$; 24 h: RSCd vs. RSCg, $^{*}p < 0.05$; two-way ANOVA followed by Bonferroni's posttests]. This seems to indicate that, respectively, suppressing the two subregions of the RSC before encoding does not interfere with the formation of the contextual fear memory, but suppressing RSCd would produce a profound disruption in the memory retrieval, whereas suppressing RSCg has no such effect.

Effects on Hub Nodes of the Brain-Wide Metabolic Brain Network of Suppressed RSCd/g During Contextual Fear Conditioning

In order to examine the differences in hub nodes of brain networks between independent groups under different

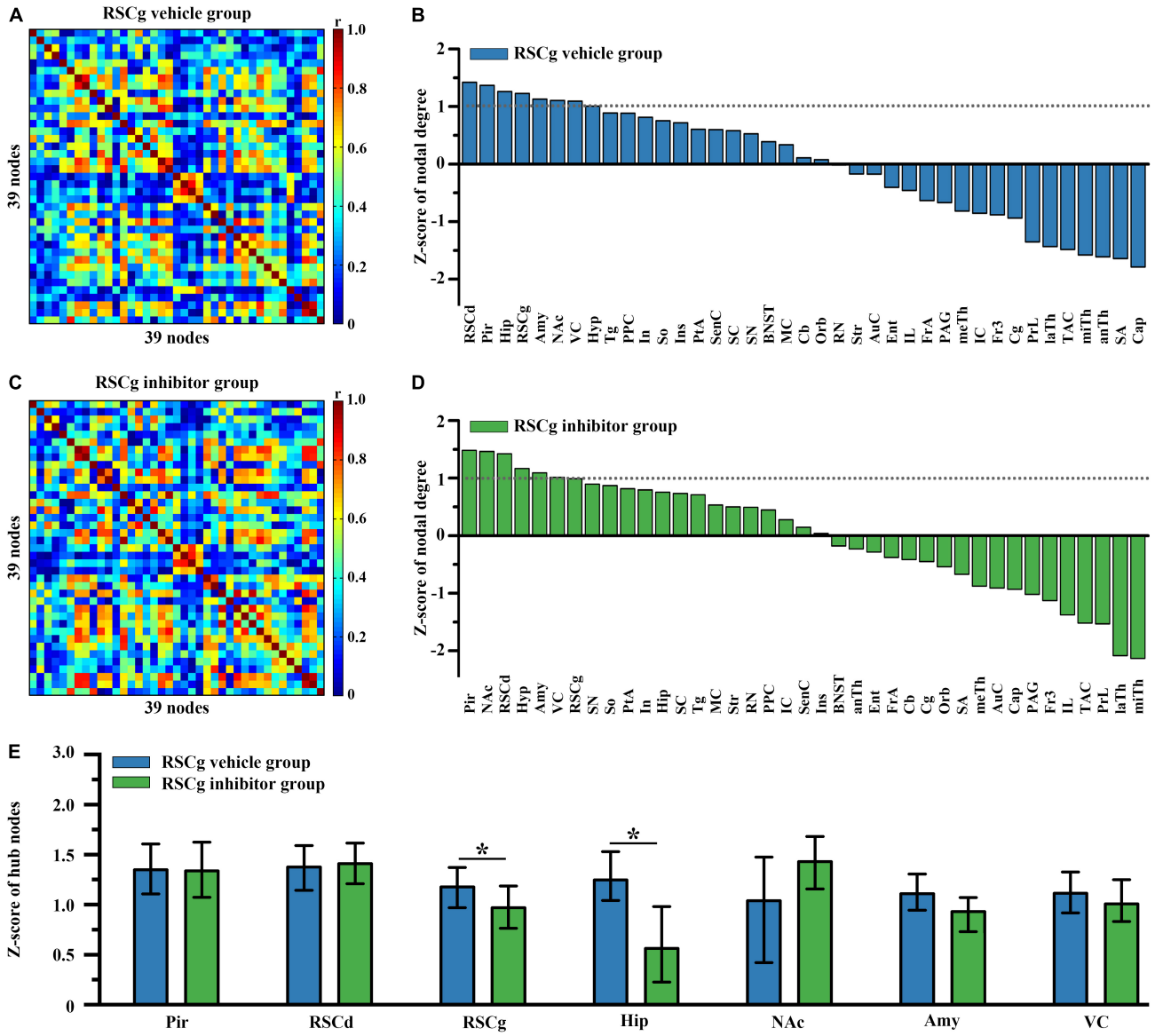

FIGURE 3 | Effects of suppressed RSCg on hub nodes of the brain-wide metabolic network during CFC. Brain-wide metabolic network of **(A)** RSCg vehicle group and **(C)** inhibitor group during CFC. Distribution of nodal degree *Z*-scores in network of **(B)** RSCg vehicle and **(D)** inhibitor group. **(E)** Decrease in nodal degree of RSCg and hippocampus in rats with suppressed RSCg. The error bar indicates the 95% confidence intervals obtained from 1,000-iteration bootstrapping procedures. RSCg vehicle group $n = 35$, RSCg inhibitor group $n = 32$. $^{*}p < 0.05$, permutation test.

treatments, we, respectively, constructed the brain-wide metabolic network during CFC for RSCd vehicle/inhibitor group (**Figures 2A,C**) and RSCg vehicle/inhibitor group (**Figures 3A,C**). The analysis of network nodal degree revealed that the hub nodes of brain-wide metabolic network during CFC included RSCd, piriform cortex (Pir), hippocampus, RSCg, amygdala, nucleus accumbens (NAc), and visual cortex (VC) (**Figures 2B**, **3B** and **Supplementary Table 2**). In the RSCd group, *Z*-score of the nodal degree of hippocampus, Pir, RSCg, RSCd, and amygdala significantly decreased in the inhibitor group ($^{*}p < 0.05$, $^{***}p < 0.001$, permutation test; **Figures 2D,E**). In the RSCg group, Z-score of the nodal degree of hippocampus and RSCg significantly decreased ($^{*}p < 0.05$, permutation test; **Figures 3D,E**).

Effects on Nodal Properties of the Core Network of Suppressed RSCd/g During Contextual Fear Conditioning

Then, we examined the differences in properties of core networks among independent groups under different treatments. The RSCd and RSCg, respectively, served as seed regions to screen nodes that were highly metabolically relevant to them (**Supplementary Table 3**). The members of RSCd core network

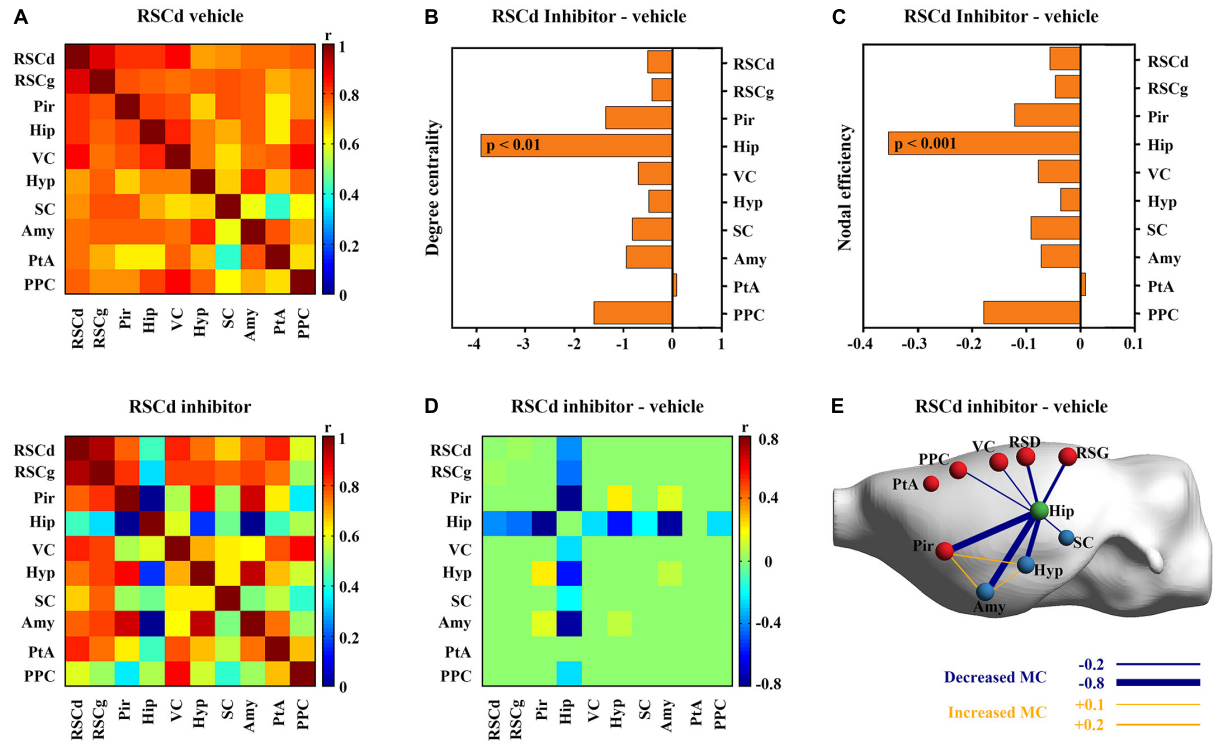

FIGURE 4 | Effects of suppressed RSCd on its core metabolic networks during CFC. **(A)** Core metabolic network of RSCd vehicle group and inhibitor groups during CFC. **(B)** Degree centrality and **(C)** nodal efficiency of the hippocampus significantly decrease in rats with suppressed RSCd. **(D)** 10,000 permutation tests reveal a significant decrease in metabolic correlations between the hippocampus and multiple nodes in rats with suppressed RSCd. **(E)** The links that changed significantly in metabolic connectivity between nodes of rat brain with suppressed RSCd. MC, metabolic connectivity. RSCd vehicle group $n = 24$, RSCd inhibitor group $n = 22$. $p < 0.05$ was considered statistically significant.

during CFC include RSCd, RSCg, Pir, Hip, VC, hypothalamus (Hyp), superior colliculus (SC), Amy, parietal association cortex (PtA), and posterior parietal cortex (PPC) (**Figure 4A**), while the nodes of RSCg core network were RSCg, RSCd, Pir, Hip, VC, Hyp, Amy, PtA, and supraoptic region (So) (**Figure 5A**).

Nodal graph theoretic measures showed a significant reduction in hippocampal degree centrality (permutation test; **Figure 4B**) and nodal efficiency (permutation test; **Figure 4C**) with suppressed RSCd during CFC, whereas the above decrease was not observed upon suppressed RSCg (permutation test; **Figures 5B,C**).

By comparing the metabolic connectivity of the RSCd core network during CFC between the vehicle and inhibitor groups, a significant decrease in multiple connections associated with hippocampus was observed in the RSCd inhibition group, specifically, the connections Hip–RSCd, Hip–RSCg, Hip–Amy, and Hip–Pir ($p < 0.05$; permutation test; **Figures 4D,E**). However, metabolic connectivity of hippocampus was not observed significant reduction in the core network of RSCg inhibitor group ($p < 0.05$; permutation test; **Figures 5D,E**).

DISCUSSION

The present study examined the effects of RSCd and RSCg on the formation of contextual fear memory in rats and explored their underlying metabolic network mechanisms. Behaviorally, rats with disturbed RSCd showed 5-h and 24-h retrieval impairments, while those with disturbed RSCg did not. Network node degree centrality analysis revealed that both RSCd and RSCg, together with several key structures related to memory and spatial cognition, play hub roles in brain-wide metabolic network during CFC. However, rats with disturbed RSCd showed significantly reduced network connectivity of the hippocampal–amygdalar circuit, while subjects with disturbed RSCg did not.

Previous studies have demonstrated the RSC, as a whole functional entity investigated, is necessary in both formation and retrieval of contextual fear memory (Corcoran et al., 2011; Cowansage et al., 2014). Our findings also seem to be consistent with these reports, rats with disturbed RSCd showing impaired 5-h and 24-h retrieval. More importantly, our findings show that RSCd and RSCg, the major two main constituents of RSC, differ in the effects of rats on CFC behavior. The 5-h and 24-h tests were used to examine the results of memory formation and recent retrieval. For animals with pharmacologically inactivated RSCd before the 5-h test, their freezing periods were significantly decreased than those of controls and animals with suppressed RSCg. For 24-h tests without pharmacological interference, which means that neural correlates for retrieval should not be disturbed, animals also showed a significantly reduced freezing level. These results implicated that memory impairment might

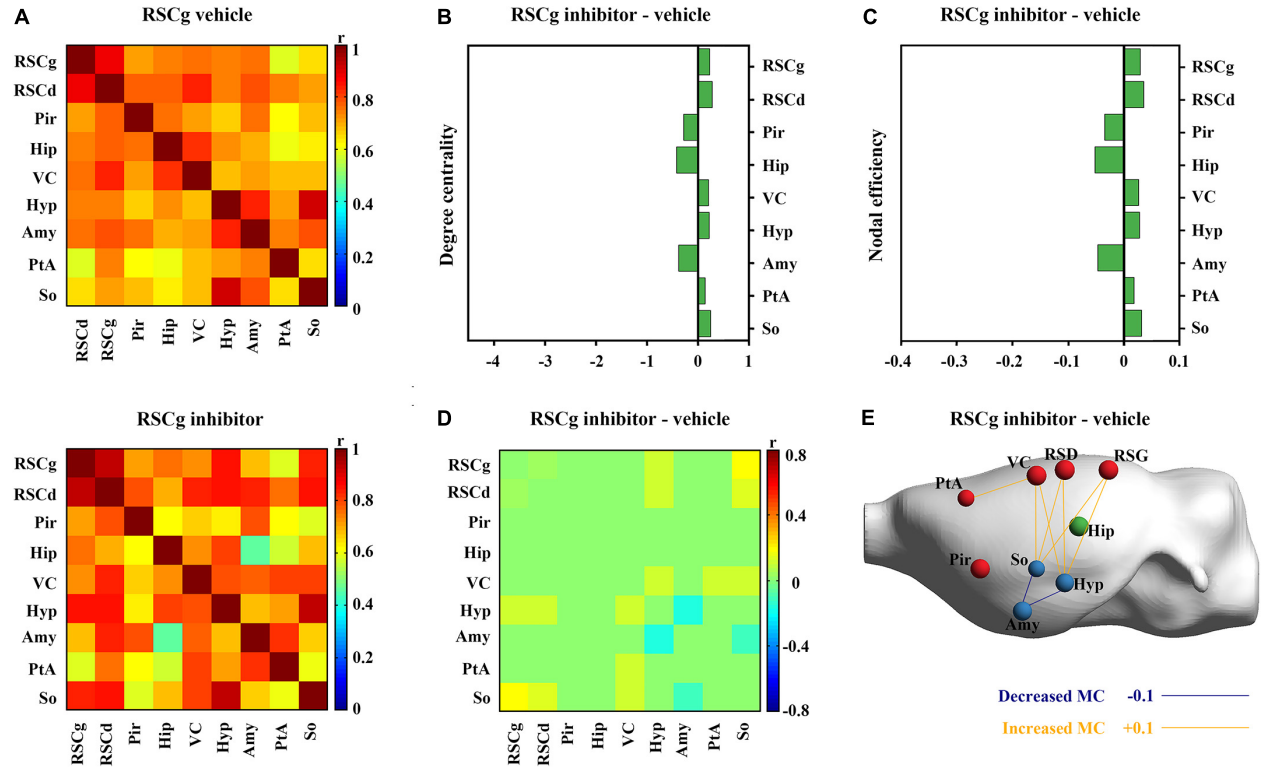

FIGURE 5 | Effects of suppressed RSCg on its core metabolic networks during CFC. **(A)** Core metabolic network of RSCg vehicle and inhibitor groups during CFC. **(B)** Degree centrality and **(C)** nodal efficiency of nodes in RSCg core network do not alter significantly in rats with suppressed RSCg. **(D)** 10,000 permutation tests reveal that the metabolic correlations of the hippocampus with other nodes also do not alter significantly in rats with suppressed RSCg. **(E)** The links that changed significantly in metabolic connectivity between nodes of rat brain with suppressed RSCd. MC, metabolic connectivity. RSCg vehicle group $n = 35$, RSCg inhibitor group $n = 32$. $p < 0.05$ was considered statistically significant.

be contributed to the disturbed memory information process, not the retrieval phase. While animals with suppressed RSCg before conditioning, neither the 5-h nor 24-h test showed memory impairments. These results suggested that the RSC might mainly rely on the RSCd, not RSCg, to play its role in the contextual fear memory formation process.

The brain-wide metabolic network constructed for control rats showed the neural collections involved in the processes of memory formation. Particularly, some structures viewed as high degree nodes (or hubs) with greater connectivity were identified, which were thought to exert greater effect on network function (Vetere et al., 2017). These regions included the hippocampus, amygdala, RSC (RSCd and RSCg), and VC, happening to be the key brain sites involved in episodic memory and spatial cognition processes. Notably, RSC was one of the most prominent sites, suggesting its global importance and supporting the notion that the RSC might be a pivotal hub of the whole brain (Vann et al., 2009). The very richness of structural connections with other regions provides the basis for the role of RSC in a whole brain range. In both primates and rodents, extensive connections of RSC with numerous other cortices and subcortical nuclei, especially with thalamus, hippocampus, and forebrain, make its potential roles in various memory-related cognition tasks (Vangroen and Wyss, 1990; Kobayashi and Amaral, 2000, 2003, 2007; van Groen and Wyss, 2003). After pharmacologically inactivated, regions influenced by disturbed RSCg and RSCd are different. Under disturbed RSCd condition, a significantly decreased nodal degree occurred in the Pir, the hippocampus, the amygdala, and RSCg, while only the hippocampal degree was decreased in the RSCg situation. This finding suggested that the RSCd influenced the key memory-related structures, hippocampus and amygdala, more significantly than the RSCg. Moreover, disturbed RSCd affected RSCg, not vice versa, suggesting that there was a possible directly functional dependency of RSCg on RSCd during encoding processing of contextual conditioning, given their structural coupling.

Furthermore, the analysis for the core metabolic networks involved in RSCd/RSCg during CFC gave more specifically metabolic connectivity insight to the mechanism by which they play roles through interactions with other structures. Regions with high connectivity with RSCd and RSCg, respectively, are almost the same ones, including the Pir, hippocampus, amygdala, VC, and hypothalamus, and they largely overlap with the hub regions of brain-wide network. However, under pharmacological inference conditions, their effect on network properties of other regions differed significantly. Disturbed RSCd caused a decreased connecting strength between itself and the hippocampus,

hippocampus and the Pir, and hippocampus and amygdala nuclei. While in the disturbed RSCg situation, the decrease in connecting strength occurred only between the hypothalamus and the amygdala nuclei, and the supraoptic region and the amygdala nuclei. The hippocampal–amygdalar system is viewed as one core mechanism for the information of contextual fear memory, in which the amygdala nuclei is responsible for coupling of conditioning stimuli and unconditioning stimuli and the hippocampus is engaged in encoding and recent storage processing (Ciocchi et al., 2010; Fanselow and Dong, 2010; Strange et al., 2014). Decreased connectivity between these two structures would directly lead to the failure of contextual fear memory formation. One possible mechanism is that, contrasted to RSCg, the RSCd is particularly involved in spatial information processing associated with the environment due to its heavy connection with the VC (Vogt and Miller, 1983). Because of the possible perturbed information flow of contextual information, the hippocampal–amygdala memory formation circuit was not evoked.

Another notable finding is that the disturbed RSCd also reduced the connectivity between the hippocampus and the Pir, while the RSCg did not. In animals, contrasted to human beings, contextual memory for environmental odors plays a vital role in their life and regulates many behaviors crucial to living, in which the Pir/olfactory cortex are always involved by their direct connections with the hippocampus and the amygdala nuclei (Chu and Downes, 2002; Willander and Larsson, 2007). Whether this olfactory learning mechanism is generally engaged in contextual memory or only triggered under certain specific conditions needs further investigation. Taken together, our findings suggest that the RSCd might play its role in the formation of contextual memory by triggering the evocation of the hippocampal–amygdalar system.

In summary, the present study demonstrated the rat RSC might play its role in contextual fear memory formation processes mainly relying on its RSCd constituent rather than the RSCg part, which might be performed by calling the hippocampal–amygdala system. These findings may also provide a useful target for pharmacotherapeutic treatments of some disorders with retrograde amnesia syndrome as well as PTSD with persistent fear. And metabolic network approaches provide an efficient means by which concerning neural correlates under particular tasks can be investigated *in vivo*.

DATA AVAILABILITY STATEMENT

The raw data supporting the conclusions of this study are available on request to the corresponding authors.

ETHICS STATEMENT

The animal study was reviewed and approved by all protocols were approved by the Institutional Animal Care and Use Committee of Kunming Institute of Zoology, Chinese Academy of Sciences (ID: SMKX-20190820-195).

AUTHOR CONTRIBUTIONS

T-TP and HL: conceptualization and writing, review, and editing. T-TP, CL, and Q-XZ: investigation. T-TP, B-BN, T-HZ, WZ, and S-LZ: software and formal analysis. G-HZ, LX, and B-BN: resources. T-TP, CL, and HL: writing – original draft. LX, G-HZ, and D-ML: supervision. LX, B-BN, Q-XZ, and T-HZ: funding acquisition. All authors contributed to the article and approved the submitted version.

FUNDING

This work was supported by the National Natural Science Foundation of China (12175268, 32071029, and 31861143037); China Postdoctoral Science Foundation (No. 2021T140668); and Strategic Priority Research Program of the Chinese Academy of Sciences (XDB32020000).

ACKNOWLEDGMENTS

We thank Jun-Bo Sun, Gui-Fen Xie, and Pei-Yu Zhang for their excellent technical assistance in the conduct of animal experiments.

SUPPLEMENTARY MATERIAL

The Supplementary Material for this article can be found online at: https://www.frontiersin.org/articles/10.3389/fnins.2022.886858/full#supplementary-material

REFERENCES

Alexandra Kredlow, M., Fenster, R. J., Laurent, E. S., Ressler, K. J., and Phelps, E. A. (2022). Prefrontal cortex, amygdala, and threat processing: implications for PTSD. *Neuropsychopharmacology* 47, 247–259. doi: 10.1038/s41386-021-01155-7

Berger, T. W., Weikart, C. L., Bassett, J. L., and Orr, W. B. (1986). Lesions of the retrosplenial cortex produce deficits in reversal-learning of the rabbit nictitating membrane response: implications for potential interactions between hippocampal and cerebellar brain systems. *Behav. Neurosci.* 100, 802–809. doi: 10.1037/0735-7044.100.6.802

Brunello, N., Davidson, J. R. T., Deahl, M., Kessler, R. C., Mendlewicz, J., Racagni, G., et al. (2001). Posttraumatic stress disorder: diagnosis and epidemiology, comorbidity and social consequences, biology and treatment. *Neuropsychobiology* 43, 150–162. doi: 10.1159/000054884

Choi, H., Kim, Y. K., Kang, H., Lee, H., Im, H.-J., Hwang, D. W., et al. (2014). Abnormal metabolic connectivity in the pilocarpine-induced epilepsy rat model: a multiscale network analysis based on persistent homology. *Neuroimage* 99, 226–236. doi: 10.1016/j.neuroimage.2014.05.039

Chu, S., and Downes, J. J. (2002). Proust nose best: odors are better cues of autobiographical memory. *Mem. Cogn.* 30, 511–518. doi: 10.3758/bf03194952

Ciocchi, S., Herry, C., Grenier, F., Wolff, S. B. E., Letzkus, J. J., Vlachos, I., et al. (2010). Encoding of conditioned fear in central amygdala inhibitory circuits. *Nature* 468, 277–U239. doi: 10.1038/nature09559

Cooper, B. G., and Mizumori, S. J. Y. (2001). Temporary inactivation of the retrosplenial cortex causes a transient reorganization of spatial coding in the hippocampus. *J. Neurosci.* 21, 3986–4001. doi: 10.1523/jneurosci.21-11-03986.2001

Corcoran, K. A., Donnan, M. D., Tronson, N. C., Guzman, Y. F., Gao, C., Jovasevic, V., et al. (2011). NMDA receptors in retrosplenial cortex are necessary for retrieval of recent and remote context fear memory. *J. Neurosci.* 31, 11655–11659. doi: 10.1523/jneurosci.2107-11.2011

Corcoran, K. A., Yamawaki, N., Leaderbrand, K., and Radulovic, J. (2018). Role of retrosplenial cortex in processing stress-related context memories. *Behav. Neurosci.* 132, 388–395. doi: 10.1037/bne0000223

Cowansage, K. K., Shuman, T., Dillingham, B. C., Chang, A., Golshani, P., and Mayford, M. (2014). Direct reactivation of a coherent neocortical memory of context. *Neuron* 84, 432–441. doi: 10.1016/j.neuron.2014.09.022

Fanselow, M. S., and Dong, H.-W. (2010). Are the dorsal and ventral hippocampus functionally distinct structures? *Neuron* 65, 7–19. doi: 10.1016/j.neuron.2009.11.031

Gabriel, M., Lambert, R. W., Foster, K., Orona, E., Sparenborg, S., and Maiorca, R. R. (1983). Anterior thalamic lesions and neuronal activity in the cingulate and retrosplenial cortices during discriminative avoidance behavior in rabbits. *Behav. Neurosci.* 97, 675–696. doi: 10.1037/0735-7044.97.5.675

Huang, Q., Zhang, J., Zhang, T., Wang, H., and Yan, J. (2020). Age-associated reorganization of metabolic brain connectivity in Chinese children. *Eur. J. Nucl. Med. Mol. Imaging* 47, 235–246. doi: 10.1007/s00259-019-04508-z

Izquierdo, I., Furini, C. R. G., and Myskiw, J. C. (2016). Fear memory. *Physiol. Rev.* 96, 695–750. doi: 10.1152/physrev.00018.2015

Jovasevic, V., Corcoran, K. A., Leaderbrand, K., Yamawaki, N., Guedea, A. L., Chen, H. J., et al. (2015). GABAergic mechanisms regulated by miR-33 encode state-dependent fear. *Nat. Neurosci.* 18:1265. doi: 10.1038/nn.4084

Keane, T. M., Marshall, A. D., and Taft, C. T. (2006). Posttraumatic stress disorder: etiology, epidemiology, and treatment outcome. *Annu. Rev. Clin. Psychol.* 2, 161–197. doi: 10.1146/annurev.clinpsy.2.022305.095305

Keene, C. S., and Bucci, D. J. (2008). Contributions of the retrosplenial and posterior parietal cortices to cue-specific and contextual fear conditioning. *Behav. Neurosci.* 122, 89–97. doi: 10.1037/0735-7044.122.1.89

Kobayashi, Y., and Amaral, D. G. (2000). Macaque monkey retrosplenial cortex: I. Three-dimensional and cytoarchitectonic organization. *J. Comp. Neurol.* 426, 339–365. doi: 10.1002/1096-9861(20001023)426:3<339::aid-cne1>3.0.co;2-8

Kobayashi, Y., and Amaral, D. G. (2003). Macaque monkey retrosplenial cortex: II. Cortical afferents. *J. Comp. Neurol.* 466, 48–79. doi: 10.1002/cne.10883

Kobayashi, Y., and Amaral, D. G. (2007). Macaque monkey retrosplenial cortex: III. Cortical efferents. *J. Comp. Neurol.* 502, 810–833. doi: 10.1002/cne.21346

Leaderbrand, K., Chen, H. J., Corcoran, K. A., Guedea, A. L., Jovasevic, V., Wess, J., et al. (2016). Muscarinic acetylcholine receptors act in synergy to facilitate learning and memory. *Learn. Mem.* 23, 631–638. doi: 10.1101/lm.043133.116

Leech, R., and Sharp, D. J. (2014). The role of the posterior cingulate cortex in cognition and disease. *Brain* 137, 12–32. doi: 10.1093/brain/awt162

Liberzon, I., Taylor, S. F., Amdur, R., Jung, T. D., Chamberlain, K. R., Minoshima, S., et al. (1999). Brain activation in PTSD in response to trauma-related stimuli. *Biol. Psychiatry* 45, 817–826. doi: 10.1016/s0006-3223(98)00246-7

Lukoyanov, N. V., and Lukoyanova, E. A. (2006). Retrosplenial cortex lesions impair acquisition of active avoidance while sparing fear-based emotional memory. *Behav. Brain Res.* 173, 229–236. doi: 10.1016/j.bbr.2006.06.026

Mergenthaler, P., Lindauer, U., Dienel, G. A., and Meisel, A. (2013). Sugar for the brain: the role of glucose in physiological and pathological brain function. *Trends Neurosci.* 36, 587–597. doi: 10.1016/j.tins.2013.07.001

Nie, B., Chen, K., Zhao, S., Liu, J., Gu, X., Yao, Q., et al. (2013). A rat brain MRI template with digital stereotaxic atlas of fine anatomical delineations in paxinos space and its automated application in voxel-wise analysis. *Hum. Brain Mapp.* 34, 1306–1318. doi: 10.1002/hbm.21511

Nie, B., Liu, H., Chen, K., Jiang, X., and Shan, B. (2014). A statistical parametric mapping toolbox used for voxel-wise analysis of FDG-PET Images of Rat Brain. *PLoS One* 9:e108295. doi: 10.1371/journal.pone.0108295

Paxinos, G., and Watson, C. (2005). *The Rat Brain in Stereotaxic Coordinates*, 5th Edn. New York, NY: Academic Press.

Pothuizen, H. H. J., Davies, M., Albasser, M. M., Aggleton, J. P., and Vann, S. D. (2009). Granular and dysgranular retrosplenial cortices provide qualitatively different contributions to spatial working memory: evidence from immediate-early gene imaging in rats. *Eur. J. Neurosci.* 30, 877–888. doi: 10.1111/j.1460-9568.2009.06881.x

Schacter, D. L., and Addis, D. R. (2007). The cognitive neuroscience of constructive memory: remembering the past and imagining the future. *Philos. Trans. R. Soc. B Biol. Sci.* 362, 773–786. doi: 10.1098/rstb.2007.2087

Strange, B. A., Witter, M. P., Lein, E. S., and Moser, E. I. (2014). Functional organization of the hippocampal longitudinal axis. *Nat. Rev. Neurosci.* 15, 655–669. doi: 10.1038/nrn3785

van Groen, T., and Wyss, J. M. (2003). Connections of the retrosplenial granular b cortex in the rat. *J. Comp. Neurol.* 463, 249–263. doi: 10.1002/cne.10757

Vangroen, T., and Wyss, J. M. (1990). Connections of the retrosplenial antigranulocytes a cortex in the rat. *J. Comp. Neurol.* 300, 593–606. doi: 10.1002/cne.903000412

Vann, S. D., and Aggleton, J. P. (2002). Extensive cytotoxic lesions of the rat retrosplenial cortex reveal consistent deficits on tasks that tax allocentric spatial memory. *Behav. Neurosci.* 116, 85–94. doi: 10.1037//0735-7044.116.1.85

Vann, S. D., Aggleton, J. P., and Maguire, E. A. (2009). What does the retrosplenial cortex do? *Nat. Rev. Neurosci.* 10, 792–802. doi: 10.1038/nrn2733

Vetere, G., Kenney, J. W., Tran, L. M., Xia, F., Steadman, P. E., Parkinson, J., et al. (2017). Chemogenetic interrogation of a brain-wide fear memory network in mice. *Neuron* 94, 363–374.e4. doi: 10.1016/j.neuron.2017.03.037

Vogt, B. A., and Miller, M. W. (1983). Cortical connections between rat cingulate cortex and visual, motor, and postsubicular cortices. *J. Comp. Neurol.* 216, 192–210. doi: 10.1002/cne.902160207

Vogt, B. A., Vogt, L., Farber, N. B., and Bush, G. (2005). Architecture and neurocytology of monkey cingulate gyrus. *J. Comp. Neurol.* 485, 218–239. doi: 10.1002/cne.20512

Weiner, M. W., Veitch, D. P., Aisen, P. S., Beckett, L. A., Cairns, N. J., Green, R. C., et al. (2017). Recent publications from the Alzheimer's disease neuroimaging initiative: reviewing progress toward improved AD clinical trials. *Alzheimers Dement.* 13, E1–E85. doi: 10.1016/j.jalz.2016.11.007

Willander, J., and Larsson, M. (2007). Olfaction and emotion: the case of autobiographical memory. *Mem. Cogn.* 35, 1659–1663. doi: 10.3758/bf03193499

Yakushev, I., Drzezga, A., and Habeck, C. (2017). Metabolic connectivity: methods and applications. *Curr. Opin. Neurol.* 30, 677–685. doi: 10.1097/wco.0000000000000494

Zhang, T., Huang, Q., Jiao, C., Liu, H., Nie, B., Liang, S., et al. (2019). Modular architecture of metabolic brain network and its effects on the spread of perturbation impact. *Neuroimage* 186, 146–154. doi: 10.1016/j.neuroimage.2018.11.003

Zhou, H., Xiong, G.-J., Jing, L., Song, N.-N., Pu, D.-L., Tang, X., et al. (2017). The interhemispheric CA1 circuit governs rapid generalisation but not fear memory. *Nat. Commun.* 8:2190. doi: 10.1038/s41467-017-02315-4

Conflict of Interest: The authors declare that the research was conducted in the absence of any commercial or financial relationships that could be construed as a potential conflict of interest.

Publisher's Note: All claims expressed in this article are solely those of the authors and do not necessarily represent those of their affiliated organizations, or those of the publisher, the editors and the reviewers. Any product that may be evaluated in this article, or claim that may be made by its manufacturer, is not guaranteed or endorsed by the publisher.

frontiers | Frontiers in Neuroscience

ORIGINAL RESEARCH
published: 02 June 2022
doi: 10.3389/fnins.2022.894720

Increased Resting-State Functional Connectivity of the Hippocampus in Rats With Sepsis-Associated Encephalopathy

Yue Yao[1†], Chunqiang Lu[2†], Jiu Chen[3], Jie Sun[4], Cuihua Zhou[1], Cheng Tan[1], Xian Xian[1], Jianhua Tong[5] and Hao Yao[1]**

[1] Cardiovascular Surgery Center, The Second Affiliated Hospital of Nanjing Medical University, Nanjing, China, [2] Department of Radiology, Zhongda Hospital, Medical School of Southeast University, Nanjing, China, [3] Institute of Brain Functional Imaging, The Affiliated Brain Hospital of Nanjing Medical University, Nanjing, China, [4] Department of Anesthesiology, Zhongda Hospital, Medical School of Southeast University, Nanjing, China, [5] Department of Anesthesiology, The Second Affiliated Hospital of Nanjing Medical University, Nanjing, China

OPEN ACCESS

Edited by:
Jie Wang,
Wuhan Institute of Physics and Mathematics (CAS), China

Reviewed by:
Shengxiang Liang,
Fujian University of Traditional Chinese Medicine, China
Xuxia Wang,
Innovation Academy for Precision Measurement Science and Technology (CAS), China

***Correspondence:**
Jianhua Tong
tongjh1982@163.com
Hao Yao
yaohao@njmu.edu.cn

†These authors have contributed equally to this work and share first authorship

Specialty section:
This article was submitted to Brain Imaging Methods, a section of the journal Frontiers in Neuroscience

Received: 12 March 2022
Accepted: 11 May 2022
Published: 02 June 2022

Citation:
Yao Y, Lu C, Chen J, Sun J, Zhou C, Tan C, Xian X, Tong J and Yao H (2022) Increased Resting-State Functional Connectivity of the Hippocampus in Rats With Sepsis-Associated Encephalopathy. Front. Neurosci. 16:894720. doi: 10.3389/fnins.2022.894720

Background: Sepsis-associated encephalopathy (SAE) has been identified as a frequent complication of sepsis, featured by an aberrant level of cognitive and affective functions. The present study is designed to explore the changes in functional connectivity (FC) of the hippocampus in rats with SAE utilizing resting-state functional magnetic resonance imaging (rs-fMRI).

Methods: Sprague-Dawley rats were randomly assigned to the SAE and control groups. We acquired rs-fMRI data using a 7T MRI to evaluate hippocampal network functional differences between the two groups with a seed-based approach. Behavioral performance was assessed using the open field test and forced swimming test. Statistical analysis was undertaken to evaluate the correlation between the hippocampal FC and behavioral findings.

Results: Compared with the control group, the SAE group showed increased FC between the bilateral hippocampus and thalamus, septum, bed nuclei stria terminalis (BNST), left primary forelimb somatosensory cortex (S1FL), primary motor cortex (M1), and inferior colliculus. Increased FC between the left hippocampus and thalamus, septum, BNST, left S1FL, and inferior colliculus was observed. While with the right hippocampus, FC in thalamus, septum, left S1FL and inferior colliculus was enhanced. Additionally, positive correlations were found between the hippocampal FC and the immobility time in the forced swimming test.

Conclusion: Hippocampus-related brain networks have significant alterations in rats with SAE, and the elevated hippocampal resting-state FC was positively related to affective deficits. Changes in FC between the hippocampus and other brain regions could be a potential neuroimaging biomarker of cognitive or mental disorders triggered by SAE.

Keywords: sepsis-associated encephalopathy, hippocampus, functional magnetic resonance imaging, functional network, functional connectivity

INTRODUCTION

Around 70% of patients with sepsis develop sepsis-associated encephalopathy (SAE), a generalized malfunction of the brain caused by infections that occur outside of the central nervous system (Andonegui et al., 2018; Chen et al., 2020). Patients with SAE usually manifest as severe and long-term cognitive impairment in the chronic phase (Semmler et al., 2013). In addition to cognitive damage, survivors also have a higher rate of psychiatric illnesses, such as depression, anxiety, post-traumatic stress disorder, and a proclivity to self-harm, than the general population. Long-term cognitive deficits and negative emotions provoked by SAE are clearly detrimental to the patients' quality of life. However, the pathophysiology of SAE is intricate and the mechanisms causing neurological dysfunction are still inconclusive. Relevant studies have shown that SAE may be related to neuroinflammation, impaired vascular function, neuroendocrine dysfunction, neurotransmission disturbances, and other mechanisms (Sharshar et al., 2003; Semmler et al., 2007; Goodson et al., 2018). These aberrant processes are especially susceptible to specific brain regions involved in arousal, autonomic regulation, determining behavioral response to stress, and more sophisticated cognitive tasks. Therefore, the pathological alterations in or between these brain regions and corresponding behavioral changes in SAE patients have always been hot and difficult issues in clinical research.

Resting-state functional magnetic resonance imaging (rs-fMRI) is a promising application for exploring brain networks, which has been widely employed in both healthy and pathological states to research the brain and its functional structure (Lee et al., 2010; Hutchison et al., 2012; Lei et al., 2014). The resting-state functional connectivity (FC) measures the temporal dependency between neuronal activity patterns across anatomically distinct brain regions, and it sheds new light on how functional brain networks relate to human behavior (Qiu et al., 2016). A similar method can be used in rats to acquire translational measurements in models of neuropsychiatric disorders. Previous imaging studies demonstrate that the FC within the default-mode network (DMN) was significantly increased in rats with SAE, which promoted the pathophysiological understanding of cognitive and affective impairment in SAE from the perspective of neuroimaging (Ji et al., 2018).

The hippocampus is known to exist as the primary site of nerve formation in the adult brain, which participates in mediating cognition and emotion (Jinno, 2011). There is some evidence to suggest that abnormal hippocampal neurogenesis is an essential pathogenic trait of SAE (Yin et al., 2020). Furthermore, molecular targets are modified in animal models of sepsis, which have a predominant impact on the hippocampus (Comim et al., 2010; Steckert et al., 2017). Pathological changes in the hippocampus caused by SAE may lay the groundwork for the occurrence of cognitive dysfunction and affective disorders. Nonetheless, it remains unknown how the hippocampus interacts with other related brain regions, as well as its relationship with impairment of cognitive or emotional functions in individuals with SAE. Considering the pronounced vulnerability of hippocampal functional organization to the complex neuropathological processes of sepsis-related injury, we picked the hippocampus as the region of interest (ROI) and assumed that the hippocampal FC would be altered in SAE rats.

The objective of this research is to investigate the features of hippocampus-related brain networks in rats with SAE, and to further explore the relationships between the altered FC and cognitive and affective disorders. Our findings may provide a new key reference for comprehension of the neural mechanisms underlying SAE.

MATERIALS AND METHODS

Animals and Modeling

The experimental procedures were approved by the Ethics Committee of the Second Affiliated Hospital of Nanjing Medical University and carried out in compliance with the guidelines for Care and Use of Laboratory Animals in China. Thirty male Sprague-Dawley rats (300–380 g) obtained from Nanjing Medical University were housed in a temperature-, light/dark-controlled animal care facility with unlimited access to chow and water. All rats were assigned to control and SAE groups at random (n = 15 per group). The rats in the SAE group were given a single dose of 5 mg/kg lipopolysaccharide (LPS) intraperitoneally. Controls were administered intraperitoneally with an equal volume of normal saline. To avoid circadian variations, all the injections were performed between 9:00 a.m. and 10:00 a.m.

Behavioral Studies

The open field test (OFT) and forced swimming test (FST) were conducted to evaluate cognitive function and affective behaviors in the rats after 48 h of modeling. Rats were randomly divided into the SAE group and the control group to counterbalance potential order effects. Each rat was evaluated independently, with no other rats' performance in the next tasks being seen. There was an interval of 1 day between tests to reduce the possible impact of prior testing.

Open Field Test

A dark gray plastic box ($60 \times 60 \times 40$ cm^3) was utilized as the apparatus. Each test lasted 5 min and each rat was positioned in the reaction chamber's central area. Ethovision software (version 11.5) was used to track and quantify the total distance traveled and center time. The exploration time of rats in the center zone which is 25×25 cm square, was calculated as the center time. The device will be cleaned before the next test.

Forced Swimming Test

We used an 80-cm-high transparent glass circular cylinder with a 40-cm inner circumference. The water in the cylinder was kept at a height of 30 cm and a temperature in the range of 23–25°C. It was difficult to modify the effects of the forced swim through behavioral adaptation since they couldn't simply stand at the bottom of the container at a depth of 30 cm. Each test lasted 6 min after the rats were individually placed. In the remaining 4 min, the rat's immobility time was analyzed

and documented by the monitoring system. The water will be replaced before the next test.

Magnetic Resonance Imaging Acquisition

All MR images were acquired with a 7.0 T MRI scanner (Bruker-Biospin, Ettlingen, Germany) with a four-channel phase array rat head coil after 24 h of modeling. 5% isoflurane in oxygen and air was used to produce anesthesia, and dexmedetomidine (0.015 mg/kg) was injected subcutaneously. The rats were then placed in a prone posture on a small animal MRI scan bed and their heads were fixed with dental hooks and ear bars to reduce head movements. We employed an anesthetic regimen that included a subcutaneous delivery of dexmedetomidine (0.03 mg/kg) followed by inhalational isoflurane for anesthesia maintenance. Throughout the scanning period, the degree of anesthesia was maintained by modulating the isoflurane concentration (0.2–0.5%) to preserve the respiration rate of 80–100 breaths per minute and oxygen saturation of 95–100%. Magnetic resonance scanning was started after the respiration, heart rate and saturation of rats were observed to be stable. Functional images were obtained using a single-shot gradient-echo EPI sequence (TR = 2,000 ms, TE = 19 ms, FOV = 3.2 × 3.2 cm^2, matrix size = 64 × 64, slice thickness = 1.0 mm, slice gap = 0, voxel size = 0.5 × 0.5 × 1 mm^3, repetition = 180).

Image Processing and Data Analysis

Raw rat EPI datasets were firstly converted to 32-bit NIFTI format using Bruker2Analyze Converter and MRIcron.[1] The voxel size of rat images was scaled by ten times (5 mm × 5 mm × 10 mm) to facilitate processing. Preprocessing of the rs-fMRI data were performed using Statistical Parametric Mapping (SPM 12). The first 10 volumes of functional data were eliminated for signal equilibrium. The remaining volumes were adjusted for slice timing correction, head movement correction, and spatial normalization to a standard rat brain template (resampled to 3 mm × 3 mm × 3 mm) and smoothed with kernel of full width at half maximum (FWHM) of 4 mm. The normalization method was the same as our previous study (Lu et al., 2021). Exclusion criteria were defined at 0.1 mm and 1 degree in maximum head movement. Further analysis includes band-pass filtering, seed region selection, and calculation of FC maps. The time courses of all voxels were subjected to band-pass filtering (0.01–0.1 Hz). Based on a standard rat brain atlas of Paxinos (Valdes-Hernandez et al., 2011), seed ROIs were chosen in the bilateral hippocampus, left hippocampus, and right hippocampus, respectively. Pearson's correlation coefficients were determined between the mean time course of every seed region and other brain voxels. A Fisher's r to z transformation was used to convert whole-brain FC maps into normally distributed data.

One sample *t*-tests of zFC (fisher's z transformed) images in the FC analysis were performed to show brain areas significantly connected to seed ROIs. Then two-sample *t*-tests of zFC images were performed between the SAE group and control group within the masks generated by the union of statistically significant areas in the one-sample *t*-tests of the two groups. A Gaussian Random Field correction method with a voxel defining threshold $P = 0.001$, corresponding to a cluster level of $P = 0.05$ (two tails) was used for the multi-comparison correction. Data analysis was performed using SPSS for Windows software (version 26.0). Results are presented as mean ± SD. The Kolmogorov-Smirnov test was applied to ensure normal distribution of all data. Data were analyzed with two-sample *t*-tests. Pearson's correlations were employed to assess the relationship between the FC values and behavioral performance. Statistical significance was defined as a *P*-value of less than 0.05. FDR ($q = 0.05$) was used to rectify multiple comparisons in correlation analysis.

[1] http://people.cas.sc.edu/rorden/mricro/

RESULTS

Behavioral Test Results

In the open field test, rats with SAE had a shorter total distance ($P < 0.01$, **Figure 1A**) and longer center time ($P < 0.05$, **Figure 1B**) compared with the control group. The immobility time of the SAE group was significantly prolonged in the forced swimming test ($P < 0.001$, **Figure 1C**).

Results of Seed-Based FC Analysis

One sample *t*-tests images showed brain regions significantly connected to the hippocampus (**Figure 2**). The pattern of the FC map connected to the hippocampus resembles the pattern of the DMN demonstrated in our previous and other researchers' studies (Lu et al., 2012, 2021). This result verified that the hippocampus is one of the nodes in the DMN. Compared to the control group, the SAE group has higher FC between the bilateral hippocampus and thalamus, septum, bed nuclei stria terminalis (BNST), left primary forelimb somatosensory cortex (S1FL), primary motor cortex (M1), and inferior colliculus (**Figure 3**). FC analysis selecting the left hippocampus as the seed point showed significantly increased FC in thalamus, septum, BNST, left S1FL, and inferior colliculus in the SAE group (**Figure 4**). With the right hippocampus as the seed brain region, we found that the FC between the thalamus, septum, left S1FL and inferior colliculus was enhanced in the SAE group (**Figure 5**). **Table 1** showed coordinates (anterior commissure serve as origin) of peak significance from higher FC selecting the hippocampus as the seed between the SAE and control groups.

Correlation Analysis

The mean zFC values within clusters that revealed a substantial difference between the two groups were extracted. The mean zFC values between the hippocampus and thalamus is positively correlated with the immobility time in the forced swimming test (**Figures 6A–D**).

DISCUSSION

To the best of our knowledge, this is the first study to reveal the altered FC of the hippocampus in rats with SAE. Specifically, the

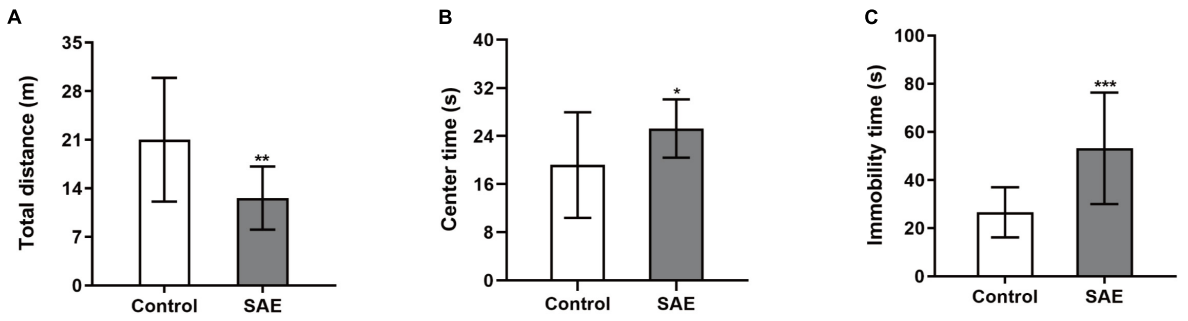

FIGURE 1 | (A–C) Rats with SAE showed a decreased total distance and increased center time in the open field test while they displayed prolonged immobility time in the forced swimming test. *$P < 0.05$, ** $P < 0.01$, ***$P < 0.001$.

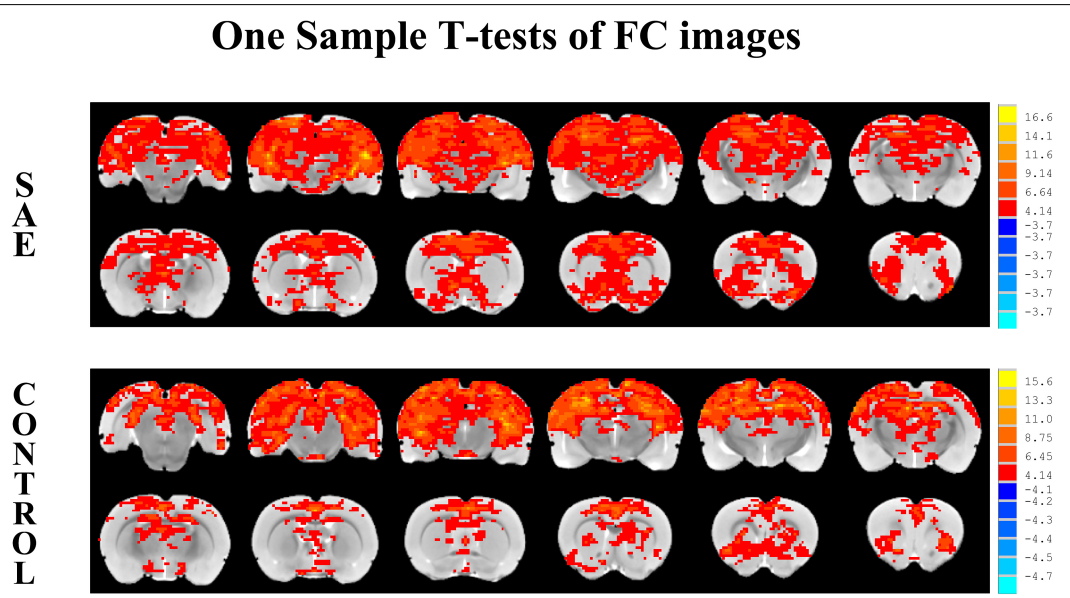

FIGURE 2 | Illustration of one-sample *t*-tests results of the hippocampus functional connectivity (FC) maps in the SAE and control groups, the seed is the bilateral hippocampus.

hippocampus-related brain regions with significant differences in FC are thalamus, septum, BNST, S1FL, M1, and inferior colliculus. Moreover, mental disorders reflected by the behavioral test positively correlated with the FC of the hippocampus-thalamus.

In our study, rats with SAE exhibited some cognitive deterioration and emotional disorders such as depression and anxiety, which agreed with the findings of many clinical trials. Neuroimaging studies of the hippocampus in individuals with either depression or anxiety disturbances reveal that hippocampal structural and functional plasticity exists abnormalities. In addition, defects in hippocampal neurogenesis have been proposed to cause cognitive impairment and depression- and anxiety-like behaviors (Kim et al., 2015; Fang et al., 2020). It might explain the common incidence of cognitive dysfunction in affective disorders, as well as the depression and anxiety seen in patients with or at risk for cognitive decline. The detailed underlying mechanism remains to be further elucidated.

We discovered that the thalamus showed increased connectivity to the hippocampus in the model of SAE. As a critical structure in cognitive and mood networks, the thalamus absorbs and integrates information from the basal ganglia, limbic system, and cerebellum before relaying it to the hippocampus and the neocortex (Wolff and Vann, 2019). Injury to the thalamus which sends and receives bi-directional fibers to and from the hippocampus subiculum can induce the related networks to malfunction. The connectivity between the hippocampus and thalamus has been regarded as an important pathway for cognition (Aggleton et al., 2010). Mousavi et al. (2017) found the abnormal FC of the hippocampus-thalamus could have relevance for study into the processes driving cognitive problems in patients with absence epilepsy. Baumgartner et al. (2018) detected that cognitive deficits imposed by stroke were closely related to disruption of hippocampal-thalamic connectivity. Furthermore, a fMRI study of a highly anxious population indicated aberrant connectivity of the left hippocampus and

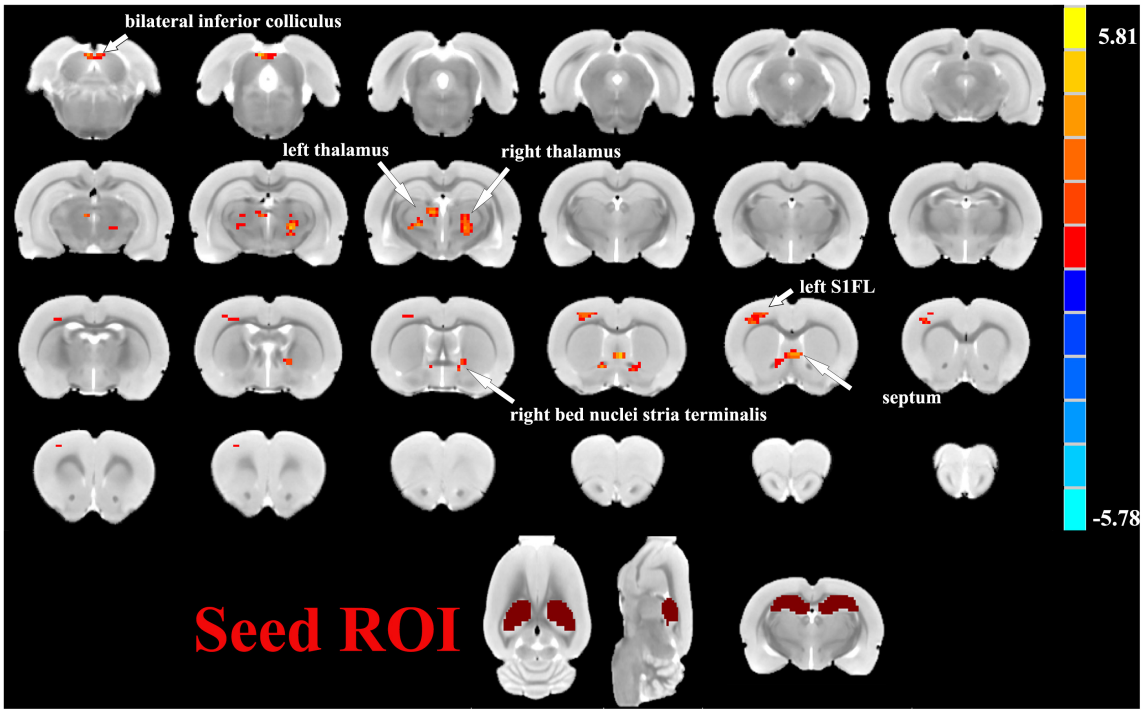

FIGURE 3 | Two sample *t*-test functional connectivity (FC) analysis selecting the bilateral hippocampus as seed between the SAE and control groups. Compared to the control group, FC was higher between the bilateral hippocampus and thalamus, septum, bed nuclei stria terminalis (BNST), left primary forelimb somatosensory cortex (S1FL), primary motor cortex (M1), and inferior colliculus in the SAE group.

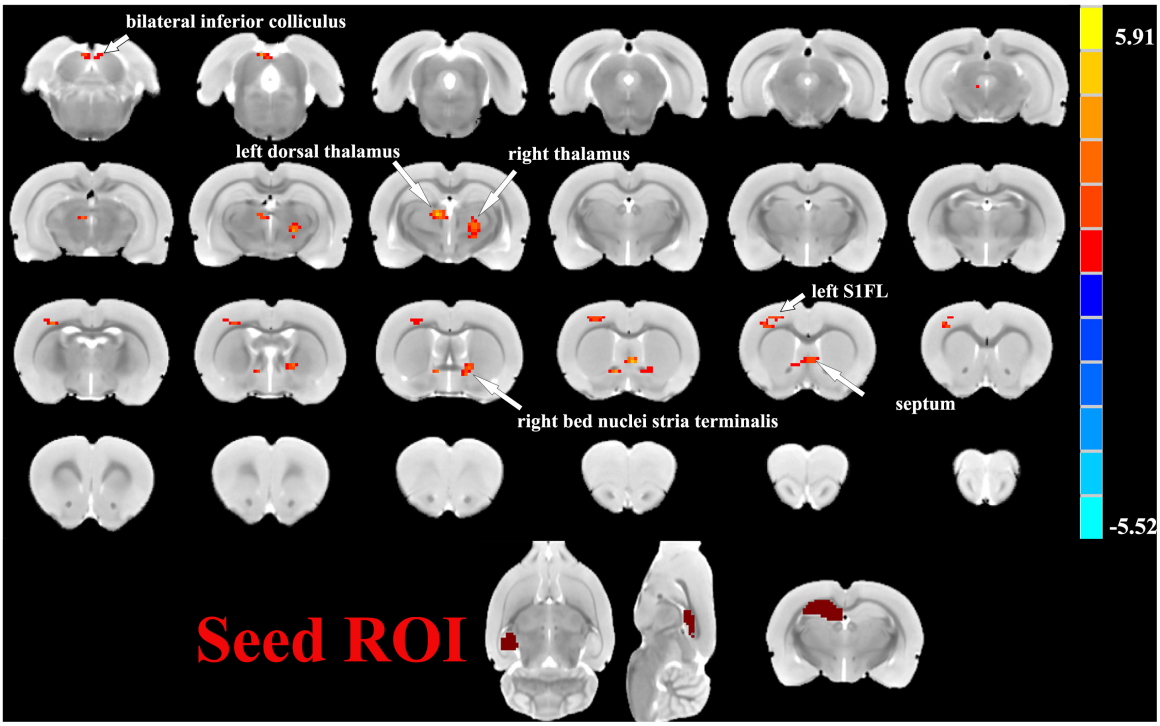

FIGURE 4 | Two sample *t*-test functional connectivity (FC) analysis selecting the left hippocampus as seed between the SAE and control groups. Within the SAE group, FC analysis selecting the left hippocampus as the seed point showed significantly increased FC in thalamus, septum, bed nuclei stria terminalis (BNST), left primary forelimb somatosensory cortex (S1FL) and inferior colliculus.

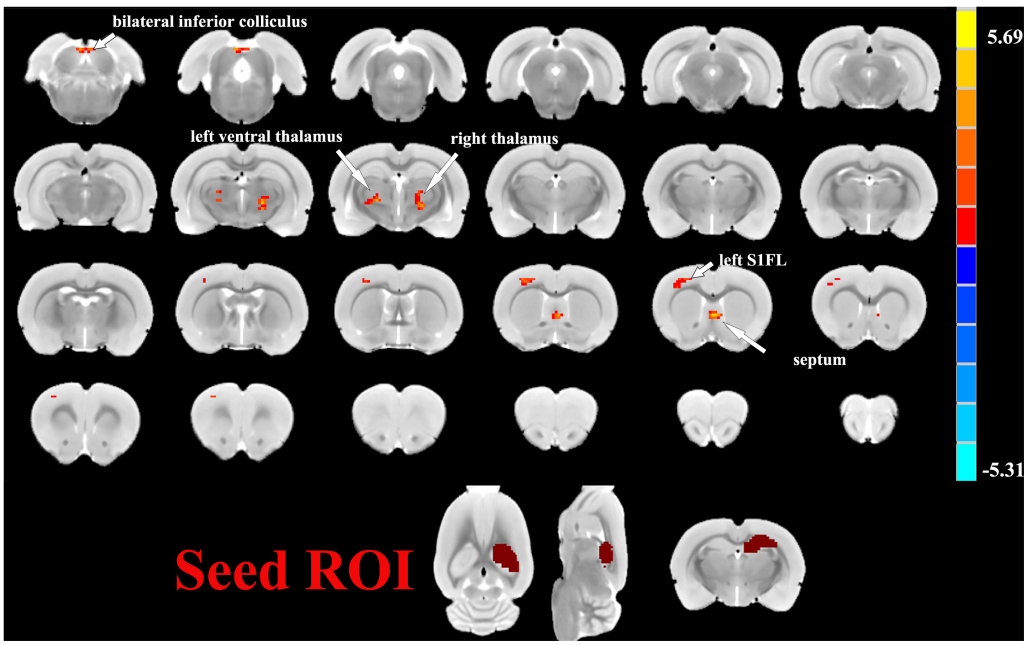

FIGURE 5 | Two sample *t*-test functional connectivity (FC) analysis selecting the right hippocampus as seed between the SAE and control groups. With the right hippocampus as the seed brain region, the SAE group displayed enhanced FC between the right hippocampus and thalamus, septum, left primary forelimb somatosensory cortex (S1FL), and inferior colliculus.

thalamus (Yang et al., 2019). Research has demonstrated that the connectivity between the hippocampus and thalamus affects depression to a large degree (Im et al., 2021). In our study, the thalamus was shown to have enhanced connectivity with the hippocampus, and the enhanced FC values between the two regions were negatively correlated with behavioral performance in rats with SAE. Our results were consistent with previous studies showing that the destroyed connectivity of the thalamo-hippocampus may be associated with cognitive deficits and mood disorders (Yang et al., 2019). These findings were interpreted as implying the existence of neural self-compensation or cerebral reserve (Li et al., 2020). Increased FC between the hippocampus and thalamus may also result from elevated external somatosensory stimuli to the central nervous system, especially to the hippocampus or thalamic nuclei from the systemic inflammatory response in SAE rats.

Our data also showed the increased FC between the hippocampus and septum in rats with SAE. The hippocampus and the septum are at the heart of the limbic system, managing motivated behavior and regulating numerous cognitive tasks. Complex reciprocal connectivity in anatomy and function has been demonstrated between the hippocampus and septum (Okada and Okaichi, 2010). These connections form the hippocampo-septal and septo-hippocampal pathways which are linked to cognitive functions (Niewiadomska et al., 2009). In line with several study findings, the oscillations in the septo-hippocampal network are influenced by depression and engaged in its symptoms (Hajos et al., 2003; Kang et al., 2010). Anxiety-related activities are thought to be bound up with theta oscillations in the septo-hippocampal circuits (Caliskan and Stork, 2019). One possible explanation is that in our study, the enhanced FC of these regions in SAE rats is a compensatory mechanism as cognition or emotion becomes

TABLE 1 | FC analysis selecting the hippocampus as the seed.

Brain region	Peak coordinate (Anterior commissure as origin, unit: 0.1 mm)			Volume (voxels)	T-peak
	x	*y*	*z*		
Bilateral hippocampal FC					
Left thalamus	27	6	−39	66	5.1308
Right thalamus	−18	3	−39	73	5.5627
Septum; left BNST	0	9	9	57	5.8070
Right BNST	−12	−6	3	34	5.1342
Left S1FL; M1	30	48	9	110	4.8684
Inferior colliculus	9	42	−81	39	5.2872
Left hippocampal FC					
Left thalamus	15	18	−36	51	5.2352
Right thalamus	−21	6	−39	56	5.1748
Septum; left BNST	0	6	6	51	5.3491
Right BNST	−12	−3	3	43	4.9559
Left S1FL	30	48	9	96	4.5596
Inferior colliculus	12	42	−78	30	4.8301
Right hippocampal FC					
Left thalamus	27	6	−39	31	5.1277
Right thalamus	−18	3	−39	58	5.5843
Septum	0	9	9	39	5.3961
Left S1FL	30	48	9	79	4.5682
Inferior colliculus	9	42	−81	35	5.2091

For converting to PAXINOS & WATSON stereotaxic coordinate, just add y to 70 (y + 70). FC, functional connectivity; BNST, bed nuclei stria terminalis; S1FL, primary forelimb somatosensory cortex; M1, primary motor cortex.

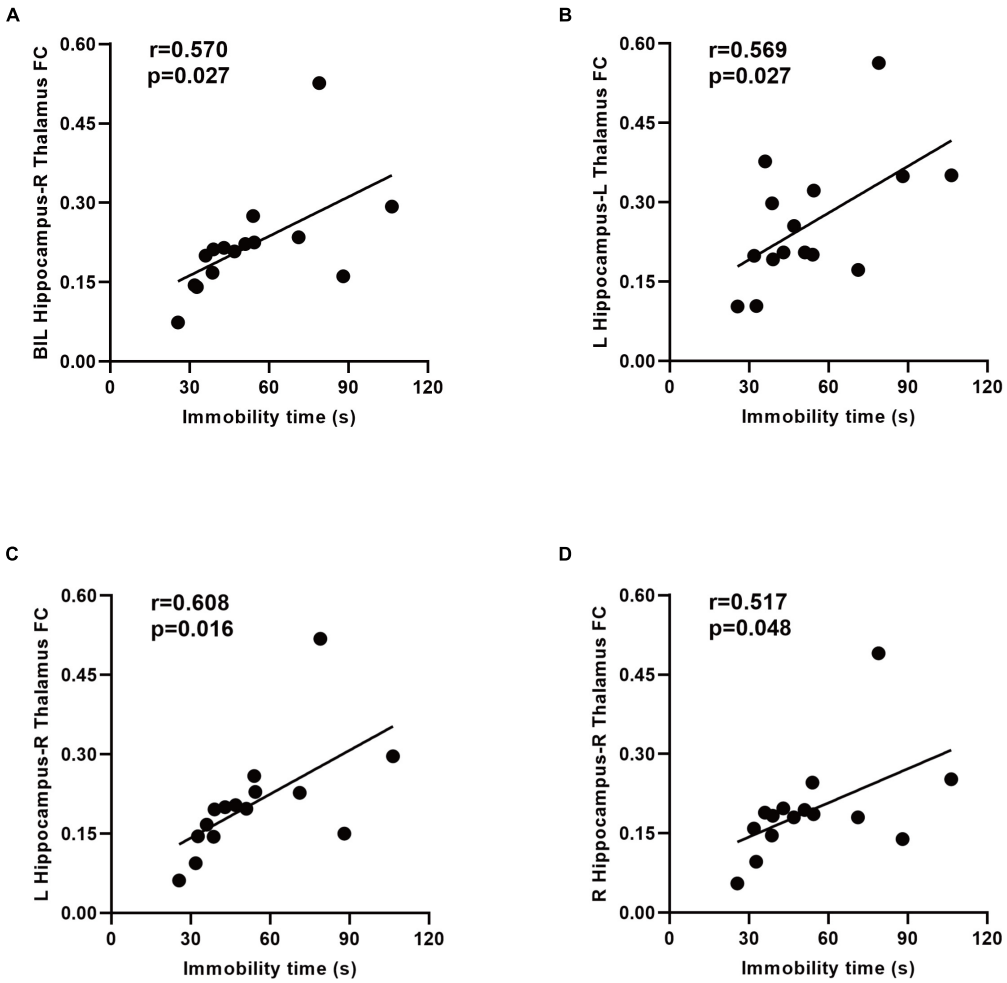

FIGURE 6 | Relationship between the immobility time and functional connectivity (FC) in the SAE group. A positive correlation between the immobility time and zFC values between the bilateral hippocampus and right thalamus was found **(A)**. There was a positive correlation between the immobility time and zFC values between the left hippocampus and thalamus **(B,C)**. Increased connectivity between the right hippocampus and right thalamus associated with the immobility time in the forced swimming test **(D)**. BIL, bilateral; L, left; R, right; FC, functional connectivity.

impaired. The increased resting-state hippocampal connectivity to the septum may be interpreted to mobilize additional neural resources to maintain cognitive or affective status in SAE patients.

The BNST, which is a complex cluster of neuronal nuclei situated in the basal forebrain, has been implicated in the negative affective state or psychiatric disease (Lebow and Chen, 2016). With strong connectivity to the hippocampus, the BNST is localized more specifically to the anterior CA region that is involved in anxiety reactions and motivation processing (Torrisi et al., 2015). We observed both the bilateral hippocampus and left hippocampus showed increased FC with the BNST, suggesting that it might be the potential mechanism of depression- and anxiety-like behaviors due to SAE.

Located in the postcentral gyrus, the primary somatosensory cortex (S1) is closely linked to the thalamus both structurally and functionally (Zhang et al., 2010). The S1 is regarded as a sensory signal structure for acquisition and transformation; nonetheless, its role in controlling and regulating associative learning behavior has also become increasingly evident (Galvez et al., 2006; Chau et al., 2013). (Kang et al. (2018) found that increased S1-thalamic FC in individuals with major depressive disorder was linked to cognitive function and affective experience. As shown in previous research, reduced synchronization between the hippocampus and S1, in particular, correlates with cognitive and memory impairment in aged rats (Xie et al., 2013; Ash et al., 2016). Our results add to the growing body of evidence indicating the hyper-connectivity between the two is crucial. This discovery might lead to more information that disrupted functional networks between the hippocampus and S1 underlie the defective cognitive and emotional ability of SAE patients. Since the M1 is located adjacent to the S1FL region in the rat brain, our result may be falsely positive due to technical issues such as inadequate registration or normalization. Nevertheless, the increased connectivity between the bilateral hippocampus and M1 may be interpreted as the compensatory effects after the motor or cognitive-affective function was impaired, or the

connectivity changed after the activity in M1 was affected by SAE, and the specific mechanism required further study.

In addition to the findings presented above, we detected the increased connectivity between the hippocampus and inferior colliculus in the SAE group. The inferior colliculus serves as a pivotal relay station for auditory pathway (De Martino et al., 2013). Schwenzer et al. (2012) revealed that auditory impairment could be a sign of depression. Studies on elderly individuals with sensory deficits found that the damaged auditory function was linked to an increased incidence of depressed and anxious symptoms (Simning et al., 2019). Our work demonstrated alterations in FC between the hippocampus and inferior colliculus, which might be related to the disordered emotions or auditory cognitive defects seen in rats with SAE.

Our research has several limitations. First, although the spontaneous activity of rats decreases when they are depressed, it is undeniable that the increased immobility time of the SAE rats might be associated with a decrease in motor function. Second, we employed a seed-based analysis, which has an underlying methodological constraint caused by *a priori* hypothesis about the seed region for the extraction of BOLD time-courses to assess the temporal correlation with the time series of other voxels in the brain. The hippocampus could be more finely divided into different subregions according to diverse functions, however, we did not subdivide it more accurately when choosing ROIs. Lastly, our study prevented us from investigating causal relationships or the role of change in hippocampus-related brain function on the evolution of cognitive or emotional deterioration in rats with SAE. Other unmeasured variables could be responsible for the correlation between them, thus more research is needed.

In summary, the current study provides evidence that the increased activity in the hippocampus functional network likely contributes to cognitive and emotional deficits in the SAE rat model. The hippocampus-related brain function may be an effective imaging target for cognitive disturbances and affective experience in SAE. The specific altered region could provide a valuable reference for further understanding the etiology of SAE.

DATA AVAILABILITY STATEMENT

The original contributions presented in this study are included in the article/supplementary material, further inquiries can be directed to the corresponding author/s.

ETHICS STATEMENT

The animal study was reviewed and approved by the Ethics Committee of The Second Affiliated Hospital of Nanjing Medical University.

AUTHOR CONTRIBUTIONS

YY and CL conceived the experiments, analyzed the data, and wrote the first draft of the manuscript. YY, JS, CZ, CT, and XX performed the experiments. JC, JT, and HY contributed to the conception and design of the study and revised the manuscript. All authors contributed to the article and approved the submitted version.

FUNDING

This work was funded by the National Nature Science Foundation of China (NSFC, grant no. 82001779), the Nature Science Foundation of Jiangsu Province (grant no. BK20200368), and the Postgraduate Research and Practice Innovation Program of Jiangsu Province (SJCX21_0649).

REFERENCES

Aggleton, J. P., O'Mara, S. M., Vann, S. D., Wright, N. F., Tsanov, M., and Erichsen, J. T. (2010). Hippocampal-anterior thalamic pathways for memory: uncovering a network of direct and indirect actions. *Eur. J. Neurosci.* 31, 2292–2307. doi: 10.1111/j.1460-9568.2010.07251.x

Andonegui, G., Zelinski, E. L., Schubert, C. L., Knight, D., Craig, L. A., Winston, B. W., et al. (2018). Targeting inflammatory monocytes in sepsis-associated encephalopathy and long-term cognitive impairment. *JCI Insight* 3:e99364. doi: 10.1172/jci.insight.99364

Ash, J. A., Lu, H., Taxier, L. R., Long, J. M., Yang, Y., Stein, E. A., et al. (2016). Functional connectivity with the retrosplenial cortex predicts cognitive aging in rats. *Proc. Natl. Acad. Sci. U.S.A.* 113, 12286–12291.

Baumgartner, P., El Amki, M., Bracko, O., Luft, A. R., and Wegener, S. (2018). Sensorimotor stroke alters hippocampo-thalamic network activity. *Sci. Rep.* 8:15770. doi: 10.1038/s41598-018-34002-9

Caliskan, G., and Stork, O. (2019). Hippocampal network oscillations at the interplay between innate anxiety and learned fear. *Psychopharmacology* 236, 321–338. doi: 10.1007/s00213-018-5109-z

Chau, L. S., Davis, A. S., and Galvez, R. (2013). Neocortical synaptic proliferation following forebrain-dependent trace associative learning. *Behav. Neurosci.* 127, 285–292. doi: 10.1037/a0031890

Chen, S., Tang, C., Ding, H., Wang, Z., Liu, X., Chai, Y., et al. (2020). Maf1 ameliorates sepsis-associated encephalopathy by suppressing the NF-kB/NLRP3 inflammasome signaling pathway. *Front. Immunol.* 11:594071. doi: 10.3389/fimmu.2020.594071

Comim, C. M., Cassol, O. J. Jr., Constantino, L. C., Petronilho, F., Constantino, L. S., Stertz, L., et al. (2010). Depressive-like parameters in sepsis survivor rats. *Neurotox. Res.* 17, 279–286. doi: 10.1007/s12640-009-9101-6

De Martino, F., Moerel, M., van de Moortele, P. F., Ugurbil, K., Goebel, R., Yacoub, E., et al. (2013). Spatial organization of frequency preference and selectivity in the human inferior colliculus. *Nat. Commun.* 4:1386.

Fang, Y., Shi, B., Liu, X., Luo, J., Rao, Z., Liu, R., et al. (2020). Xiaoyao pills attenuate inflammation and nerve injury induced by lipopolysaccharide in hippocampal neurons in vitro. *Neural Plast.* 2020:8841332. doi: 10.1155/2020/8841332

Galvez, R., Weiss, C., Weible, A. P., and Disterhoft, J. F. (2006). Vibrissa-signaled eyeblink conditioning induces somatosensory cortical plasticity. *J. Neurosci.* 26, 6062–6068. doi: 10.1523/JNEUROSCI.5582-05.2006

Goodson, C. M., Rosenblatt, K., Rivera-Lara, L., Nyquist, P., and Hogue, C. W. (2018). Cerebral blood flow autoregulation in sepsis for the intensivist: why its monitoring may be the future of individualized care. *J. Intensive Care Med.* 33, 63–73. doi: 10.1177/0885066616673973

Hajos, M., Hoffmann, W. E., Robinson, D. D., Yu, J. H., and Hajos-Korcsok, E. (2003). Norepinephrine but not serotonin reuptake inhibitors

enhance theta and gamma activity of the septo-hippocampal system. *Neuropsychopharmacology* 28, 857–864. doi: 10.1038/sj.npp.1300116

Hutchison, R. M., Womelsdorf, T., Gati, J. S., Leung, L. S., Menon, R. S., and Everling, S. (2012). Resting-state connectivity identifies distinct functional networks in macaque cingulate cortex. *Cereb. Cortex* 22, 1294–1308. doi: 10.1093/cercor/bhr181

Im, S., Lee, J., and Kim, S. (2021). Preliminary comparison of subcortical structures in elderly subclinical depression: structural analysis with 3T MRI. *Exp. Neurobiol.* 30, 183–202. doi: 10.5607/en20056

Ji, M., Xia, J., Tang, X., and Yang, J. (2018). Altered functional connectivity within the default mode network in two animal models with opposing episodic memories. *PLoS One* 13:e0202661. doi: 10.1371/journal.pone.0202661

Jinno, S. (2011). Decline in adult neurogenesis during aging follows a topographic pattern in the mouse hippocampus. *J Comp. Neurol.* 519, 451–466. doi: 10.1002/cne.22527

Kang, H. M., Jin, J., Lee, S., Ryu, J., and Park, C. (2010). A novel method for olfactory bulbectomy using photochemically induced lesion. *Neuroreport* 21, 179–184. doi: 10.1097/WNR.0b013e328334884c

Kang, L., Zhang, A., Sun, N., Liu, P., Yang, C., Li, G., et al. (2018). Functional connectivity between the thalamus and the primary somatosensory cortex in major depressive disorder: a resting-state fMRI study. *BMC Psychiatry* 18:339. doi: 10.1186/s12888-018-1913-6

Kim, J. Y., Lee, J. H., Kim, D., Kim, S. M., Koo, J., and Jahng, J. W. (2015). Beneficial effects of highly palatable food on the behavioral and neural adversities induced by early life stress experience in female rats. *Int. J. Biol. Sci.* 11, 1150–1159. doi: 10.7150/ijbs.12044

Lebow, M. A., and Chen, A. (2016). Overshadowed by the amygdala: the bed nucleus of the stria terminalis emerges as key to psychiatric disorders. *Mol. Psychiatry* 21, 450–463.

Lee, J. N., Hsu, E. W., Rashkin, E., Thatcher, J. W., Kreitschitz, S., Gale, P., et al. (2010). Reliability of fMRI motor tasks in structures of the corticostriatal circuitry: implications for future studies and circuit function. *Neuroimage* 49, 1282–1288. doi: 10.1016/j.neuroimage.2009.09.072

Lei, X., Wang, Y., Yuan, H., and Mantini, D. (2014). Neuronal oscillations and functional interactions between resting state networks. *Hum. Brain Mapp.* 35, 3517–3528. doi: 10.1002/hbm.22418

Li, M. G., He, J. F., Liu, X. Y., Wang, Z. F., Lou, X., and Ma, L. (2020). structural and functional thalamic changes in Parkinson's disease with mild cognitive impairment. *J. Magn. Reson. Imaging* 52, 1207–1215. doi: 10.1002/jmri.27195

Lu, C. Q., Zeng, C. H., Cui, Y., Meng, X. P., Luan, Y., Xu, X. M., et al. (2021). An investigation of the impacts of three anesthetic regimens on task-functional magnetic resonance imaging and functional connectivity resting-state functional magnetic resonance imaging in sprague Dawley and Wistar rats. *Brain connect.* 12, 74–84. doi: 10.1089/brain.2020.0875

Lu, H., Zou, Q., Gu, H., Raichle, M. E., Stein, E. A., and Yang, Y. (2012). Rat brains also have a default mode network. *Proc. Natl. Acad. Sci. U.S.A.* 109, 3979–3984. doi: 10.1073/pnas.1200506109

Mousavi, S. R., Arcaro, J. A., Leung, L. S., Tenney, J. R., and Mirsattari, S. M. (2017). Functional connectivity of the hippocampus to the thalamocortical circuitry in an animal model of absence seizures. *Epilepsy Res.* 137, 19–24. doi: 10.1016/j.eplepsyres.2017.08.004

Niewiadomska, G., Baksalerska-Pazera, M., and Riedel, G. (2009). The septo-hippocampal system, learning and recovery of function. *Prog. Neuropsychopharmacol. Biol. Psychiatry* 33, 791–805. doi: 10.1016/j.pnpbp.2009.03.039

Okada, K., and Okaichi, H. (2010). Functional cooperation between the hippocampal subregions and the medial septum in unreinforced and reinforced spatial memory tasks. *Behav. Brain Res.* 209, 295–304. doi: 10.1016/j.bbr.2010.02.007

Qiu, L. L., Ji, M. H., Zhang, H., Yang, J. J., Sun, X. R., Tang, H., et al. (2016). NADPH oxidase 2-derived reactive oxygen species in the hippocampus might contribute to microglial activation in postoperative cognitive dysfunction in aged mice. *Brain Behav. Immun.* 51, 109–118. doi: 10.1016/j.bbi.2015.08.002

Schwenzer, M., Zattarin, E., Grozinger, M., and Mathiak, K. (2012). Impaired pitch identification as a potential marker for depression. *BMC Psychiatry* 12:32. doi: 10.1186/1471-244X-12-32

Semmler, A., Frisch, C., Debeir, T., Ramanathan, M., Okulla, T., Klockgether, T., et al. (2007). Long-term cognitive impairment, neuronal loss and reduced cortical cholinergic innervation after recovery from sepsis in a rodent model. *Exp. Neurol.* 204, 733–740. doi: 10.1016/j.expneurol.2007.01.003

Semmler, A., Widmann, C. N., Okulla, T., Urbach, H., Kaiser, M., Widman, G., et al. (2013). Persistent cognitive impairment, hippocampal atrophy and EEG changes in sepsis survivors. *J. Neurol. Neurosurg. Psychiatry* 84, 62–69. doi: 10.1136/jnnp-2012-302883

Sharshar, T., Gray, F., de la Grandmaison, G. L., Hopklnson, N. S., Ross, E., Dorandeu, A., et al. (2003). Apoptosis of neurons in cardiovascular autonomic centres triggered by inducible nitric oxide synthase after death from septic shock. *Lancet* 362, 1799–1805. doi: 10.1016/s0140-6736(03)14899-4

Simning, A., Fox, M. L., Barnett, S. L., Sorensen, S., and Conwell, Y. (2019). Depressive and anxiety symptoms in older adults with auditory, vision, and dual sensory impairment. *J. Aging Health* 31, 1353–1375. doi: 10.1177/0898264318781123

Steckert, A. V., Dominguini, D., Michels, M., Abelaira, H. M., Tomaz, D. B., Sonai, B., et al. (2017). The impact of chronic mild stress on long-term depressive behavior in rats which have survived sepsis. *J. Psychiatr. Res.* 94, 47–53. doi: 10.1016/j.jpsychires.2017.06.006

Torrisi, S., O'Connell, K., Davis, A., Reynolds, R., Balderston, N., Fudge, J. L., et al. (2015). Resting state connectivity of the bed nucleus of the stria terminalis at ultra-high field. *Hum. Brain Mapp.* 36, 4076–4088. doi: 10.1002/hbm.22899

Valdes-Hernandez, P. A., Sumiyoshi, A., Nonaka, H., Haga, R., Aubert-Vasquez, E., Ogawa, T., et al. (2011). An in vivo MRI template set for morphometry, tissue segmentation, and fMRI localization in rats. *Front. Neuroinform.* 5:26. doi: 10.3389/fninf.2011.00026

Wolff, M., and Vann, S. D. (2019). The cognitive thalamus as a gateway to mental representations. *J. Neurosci.* 39, 3–14. doi: 10.1523/JNEUROSCI.0479-18.2018

Xie, P., Yu, T., Fu, X., Tu, Y., Zou, Y., Lui, S., et al. (2013). Altered functional connectivity in an aged rat model of postoperative cognitive dysfunction: a study using resting-state functional MRI. *PLoS One* 8:e64820. doi: 10.1371/journal.pone.0064820

Yang, C., Zhang, Y., Lu, M., Ren, J., and Li, Z. (2019). White matter structural brain connectivity of young healthy individuals with high trait anxiety. *Front. Neurol.* 10:1421. doi: 10.3389/fneur.2019.01421

Yin, J., Shen, Y., Si, Y., Zhang, Y., Du, J., Hu, X., et al. (2020). Knockdown of long non-coding RNA SOX2OT downregulates SOX2 to improve hippocampal neurogenesis and cognitive function in a mouse model of sepsis-associated encephalopathy. *J. Neuroinflammation* 17:320. doi: 10.1186/s12974-020-01970-7

Zhang, D., Snyder, A. Z., Shimony, J. S., Fox, M. D., and Raichle, M. E. (2010). Noninvasive functional and structural connectivity mapping of the human thalamocortical system. *Cereb. Cortex* 20, 1187–1194.[endref] doi: 10.1093/cercor/bhp182

Conflict of Interest: The authors declare that the research was conducted in the absence of any commercial or financial relationships that could be construed as a potential conflict of interest.

Publisher's Note: All claims expressed in this article are solely those of the authors and do not necessarily represent those of their affiliated organizations, or those of the publisher, the editors and the reviewers. Any product that may be evaluated in this article, or claim that may be made by its manufacturer, is not guaranteed or endorsed by the publisher.

frontiers | Frontiers in Neuroscience

ORIGINAL RESEARCH
published: 23 June 2022
doi: 10.3389/fnins.2022.938674

Assessment of Rat Sciatic Nerve Using Diffusion-Tensor Imaging With Readout-Segmented Echo Planar Imaging

Yueyao Chen[1†], Zhongxian Pan[1†], Fanqi Meng[1], Qian Xu[1], Leyu Huang[1], Xuejia Pu[1], Xuewen Yu[2], Yanglei Wu[3], Hanqing Lyu[1] and Xiaofeng Lin[4*]*

[1] Department of Radiology, Shenzhen Traditional Chinese Medicine Hospital, The Fourth Clinical Medical College of Guangzhou University of Chinese Medicine, Shenzhen, China, [2] Department of Pathology, Shenzhen Traditional Chinese Medicine Hospital, The Fourth Clinical Medical College of Guangzhou University of Chinese Medicine, Shenzhen, China, [3] Siemens Healthineers, Beijing, China, [4] Department of Nuclear Medicine, The Seventh Affiliated Hospital, Sun Yat-sen University, Shenzhen, China

OPEN ACCESS

Edited by:
Shengxiang Liang,
Fujian University of Traditional Chinese Medicine, China

Reviewed by:
Xiangchuang Kong,
Huazhong University of Science and Technology, China
Wenshu Qian,
National Institutes of Health (NIH), United States

***Correspondence:**
Hanqing Lyu
13510269808@139.com
Xiaofeng Lin
linxf22@mail.sysu.edu.cn

[†] These authors have contributed equally to this work and share first authorship

Specialty section:
This article was submitted to Brain Imaging Methods, a section of the journal Frontiers in Neuroscience

Received: 07 May 2022
Accepted: 30 May 2022
Published: 23 June 2022

Citation:
Chen Y, Pan Z, Meng F, Xu Q, Huang L, Pu X, Yu X, Wu Y, Lyu H and Lin X (2022) Assessment of Rat Sciatic Nerve Using Diffusion-Tensor Imaging With Readout-Segmented Echo Planar Imaging. Front. Neurosci. 16:938674. doi: 10.3389/fnins.2022.938674

Objectives: This study aimed to compare readout-segmented-3, readout-segmented-5, and readout-segmented-7 echo-planar imaging (RS3-EPI, RS5-EPI, and RS7-EPI) of DTI in the assessment of rat sciatic nerve at 3T MR.

Methods: Eight male adult healthy Sprague-Dawley rats were scanned at 3T MR with RS-3 EPI, RS5-EPI, and RS-7 EPI DTI. The image quality of RS-3 EPI, RS-5 EPI, and RS-7 EPI in terms of the nerve morphology, distortions of the nearby femur, muscles, and homogeneity of neuromuscular were evaluated by two experienced radiologists. The correlations between the histopathological and DTI parameters, including fractional anisotropy (FA) and radial diffusivity (RD), were calculated, respectively, and compared in RS-3, RS-5, and RS-7 EPI. The image quality scores for RS-3 EPI, RS-5 EPI, and RS-7 EPI were compared using the Wilcoxon rank-sum test. The correlation between DTI and histopathological parameters was calculated using the Pearson correlation coefficient.

Results: RS-5 EPI yielded the best SNR-values corrected for the acquisition time compared to RS3-EPI and RS7-EPI. The image quality scores of RS-5 EPI were superior to those of RS-3 and RS-7 EPI (P = 0.01–0.014) and lower artifacts of the ventral/dorsal margin and femur (P = 0.008–0.016) were shown. DTT analysis yielded a significantly higher number of tracts for RS5-EPI compared to RS3-EPI (P = 0.007) but no significant difference with RS7-EPI (P = 0.071). For the three sequences, FA and RD were well-correlated with the myelin-related histopathological parameters (|r| 0.709–0.965, P = 0.001–0.049). The overall correlation coefficients of FA and RD obtained from RS-5 EPI were numerically higher than that with both RS3-EPI and RS7-EPI.

Conclusion: For the rat sciatic nerve DTI imaging, RS-5 EPI offered the best image quality and SNR-values corrected for the acquisition time. The FA and RD derived from the RS-5 EPI were the most sensitive quantitative biomarkers to detect rat sciatic nerve histopathological change.

Keywords: magnetic resonance imaging, diffusion tensor imaging, peripheral nerve, readout-segmented echo-planar imaging, sciatic nerve

INTRODUCTION

Diffusion tensor imaging (DTI) has been widely recognized for its value in the central nervous system, such as fiber tracking, assessing fiber continuity, evaluating white matter fiber tract injury, and degeneration of cranial nerve fibers (Mori and Zhang, 2006). DTI technique was subsequently routinely used to determine the integrity of the peripheral nerves, especially in experimental animal studies of nerve injury. Many preclinical and animal studies have proven that DTI is one of the most valuable functional sequences in evaluating peripheral nerve injury repair and function (Guggenberger et al., 2012; Jeon et al., 2018; Zheng et al., 2021). Parameters such as FA and RD derived from DTI are strongly correlated with myelin-related pathological parameters and are considered to be the sensitive biomarkers for detecting early peripheral nerve dysfunction, degeneration, and regeneration (Chen et al., 2017; Farinas et al., 2020; Zheng et al., 2021).

Generally, DTI is performed by using single-shot echo-planar imaging (SS-EPI) sequence for its faster speed. However, this technique is vulnerable to geometric distortion around tissue interface and signal-intensity dropout, primarily because of slow traversal through k-space along the phase-encoding direction (Porter and Heidemann, 2009). Recently, DWI based on readout-segmented echo-planar imaging (RS-EPI), in which the k-space is divided into several segments along the readout direction, has been suggested as an alternative approach to overcome the limitations of the SS-EPI technique (Porter and Heidemann, 2009). Most of the current clinical studies show that RS-EPI has the better image quality and lesion detection, thereby improving the diagnostic performance of DTI (Kida et al., 2016), including in skull base and orbit (Yeom et al., 2013; Chen et al., 2020), breast (Bogner et al., 2012), kidney (Friedli et al., 2017), pelves (Thian et al., 2014), and sacroiliac joint (Zhang et al., 2021). To our knowledge, the application of RS-EPI DWI has not been previously described for the sciatic nerve, especially rat sciatic nerve, which was very small in size and had a relatively high signal in fat set T2WI, presenting challenges in DTI.

Single-shot echo-planar imaging is prone to susceptibility artifacts that manifest as geometric distortion, image blurring, and ghosting artifacts (Drake-Pérez et al., 2018). With the increased numbers of readout segments, although RS-EPI has a more remarkable ability to reduce artifacts and a higher signal-to-noise ratio (SNR), but becomes more vulnerable to motion artifacts and more time-consuming. This pattern is demonstrated in our preliminary study. We found that the image quality of the rat sciatic nerve from DTI with a higher segmented number (e.g., the RS7-EPI) was not better than DTI with a lower segmented number (e.g., the RS3-EPI) and sacrificed more time. In addition, the small and sharp contrast tissue with longer T2 relaxation time, such as nerve tissue, is prone to produce motion-induced deterioration effects (Zaitsev et al., 2015). What's more, deep and prolonged anesthesia significantly increases the risk of animal death during *in vivo* MRI studies. This further suggests that the image quality does not simply increase with the increasing segmented number but requires a trade-off between the SNR, nerve artifact, and acquisition time. Therefore, the number of readout segments needs to be carefully considered *in vivo* DTI study of rat sciatic nerve. The comparison of the different performance of different readout-segment numbers in RS-EPI DWI has not been previously described for the rat sciatic nerve.

Diffusion tensor imaging parameters such as FA and RD values were considered the sensitive and invasive biomarkers in the monitoring of nerve repair (Chen et al., 2017). However, severe image artifacts and distortion of the nerve can directly affect the region of interest (ROI) drawing and the accuracy of the measured values (Atkinson et al., 2000). In our study, in addition to the evaluation of nerve image quality, we analyzed the correlation between the DTI and pathological parameters related to nerve repair.

Thus, the purposes of the study were, first, to compare the image quality of RS-3 EPI, RS-5 EPI, and RS-7 EPI of DTI of the rat sciatic nerve, and, second, to evaluate the FA and RD values derived from which readout-segment number could provide more accurate pathological information in *in vivo* peripheral nerve monitoring by DTI.

MATERIALS AND METHODS

Subjects

All interventions and animal care procedures were performed by the Guidelines and Policies for Animal Surgery and were approved by the Institutional Animal Use and Care Committee. All animals were obtained from the Animal Experiment Center of Guangdong province. The animals were housed in a standard animal facility with 12-h on/off light conditions and free access to standard food and water. A total of eight male adult healthy Sprague-Dawley rats weighing 250 ± 20 g were used in this study.

Magnetic Resonance Imaging

All eight healthy adult male Sprague-Dawley rats were anesthetized to deep sleep (7% chloralhydrate, 5 ml/kg, intraperitoneal injection, the rats can deep sleep at least 90 min) and scanned at a 3T scanner (MAGNETOM Prisma, Siemens Healthcare, Erlangen, Germany). After anesthesia, each rat was placed prone in a rat coil (6-cm diameter, eight-channel, Suzhou Medcoil Healthcare Co., Ltd., Suzhou Industrial Park, Suzhou, China) with the limbs fixed with medical adhesive tape to prevent movement further. Both hind limbs were positioned symmetrically.

In our pre-experiments, the acquisition times for readout segment numbers 3, 5, 7, and 9 were 6:12, 10:12, 14:12, and 18:12 min, respectively. To control the overall scan time and reduce the anesthesia risk to a minimum, 18:12 min of readout

Abbreviations: DTI, diffusion tensor imaging; FA, fractional anisotropy; RD, radial diffusivity; POAA, percentage of axon area; POMA, percentage of myelin area; TOM, the thickness of myelin; DOMF, diameter of myelinated fibers; SS, single-shot; RS, readout-segmented; EPI, echo-planar imaging; ROI, region of interest; SI, signal intensity; SD, standard deviation; SNR, signal-to-noise ratio; ICC, intraclass correlation coefficient.

segment 9 is beyond our tolerance time. Thus, readout segment numbers 3, 5, and 7 were chosen in our study.

Three axial DTI sequences (RS-3 EPI, RS-5 EPI, and RS-7 EPI) were performed perpendicular to the sciatic nerve with comparable imaging parameters. For the three DTI sequences of RS-3 EPI, RS-5 EPI, and RS-7 EPI: the number of readout segments = 3, 5, and 7, respectively. TE = 75, 63, and 58 ms, respectively; Echo spacing = 0.94, 0.66, and 0.32 ms, respectively. Unified parameters include the following: TR = 4000 ms; slice thickness/gap = 1.5 mm/0 mm; b value = 0, 800 s/mm^2; diffusion directions = 20; EPI factor = 48; FOV = 70 × 70 mm^2; Matrix = 100 × 100; No. of sections = 20. A coronal fat-suppressed T2-weighted image was obtained to display the morphology of bilateral sciatic nerves and ensure the correct ROI position for DTI parameters measurement in the sciatic nerve (**Figure 1**).

Signal-to-Noise Ratio Measurements

The signal-to-noise ratio (SNR) was defined as the ratio between the mean signal intensity of the sciatic nerve (SI_{Nerve}) and the standard deviation of the background noise ($SD_{Background}$) (**Figure 2**). Using the following equations (Bogner et al., 2012), images and corresponding noise data were post-processed individually (*via* MATLAB MRIqual version 1.2.3), yielding voxel-based SNR maps (**Figures 2A–F**). Using the following formulas, SNR was calculated from DW images (b = 800 s/mm2). ROIs covering each sciatic nerve were manually drawn on the adjacent three slices of the sciatic nerve trunk. The three measurements were averaged, and corresponding SNR values were extracted. The ROI of the background noise was placed in the same phase encoding direction with the sciatic nerve and close to the edge of the image. The size of ROI is uniformly 1 cm^2.

$$SNR = \frac{SI_{Nerve}}{SD_{Background}}$$

Signal-to-Noise Ratio Correction Due to Sequence-Specific Differences in Acquisition Time

To determine the SNR efficiency of a particular acquisition scheme, the measured SNR was divided by the square root of the respective acquisition time (S):

$$SNR\,(TA) = \frac{SNR_{Nerve}}{\sqrt{TA}}$$

where TA is the total acquisition duration (Manoliu et al., 2017).

Qualitative Image Evaluation

Two independent readers performed image analysis (Reader 1, a radiologist with 10 years of experience in DTI of the nerve; Reader 2, with 4 years of experience in DTI of the nerve). Both readers were blinded to the histopathologic results. The three DTI sequence data were transferred to the workstation (Syngo *Via* 2, Siemens) for image quality evaluation and DTI parameters measurement. DTI images, including b = 0, 800 s/mm^2, FA, and RD maps were generated simultaneously in Neuro 3D modules. The image quality was assessed qualitatively on DWI b = 800 images based on the following factors: sharpness of nerve margin, artifacts of nerve, artifacts of the femur, artifacts of ventral margin, artifacts of dorsal margin, homogeneity of neuromuscular (**Figure 3**). All images were scored using a 5-point system: 5 means that the images are artifact-free images without distortion and artifact and with great anatomic details of the bilateral sciatic nerve, muscle, and femur; and 1 means impossible to differentiate the anatomic details because of image quality that has been severely distorted by artifacts or low SNR.

Quantitative Analysis of Diffusion Tensor Imaging Parameters and Diffusion Tensor Tractography

Quantitative analysis of the acquired diffusion data was performed using the syngo.*via* Neuro 3D tool (version 2, Siemens

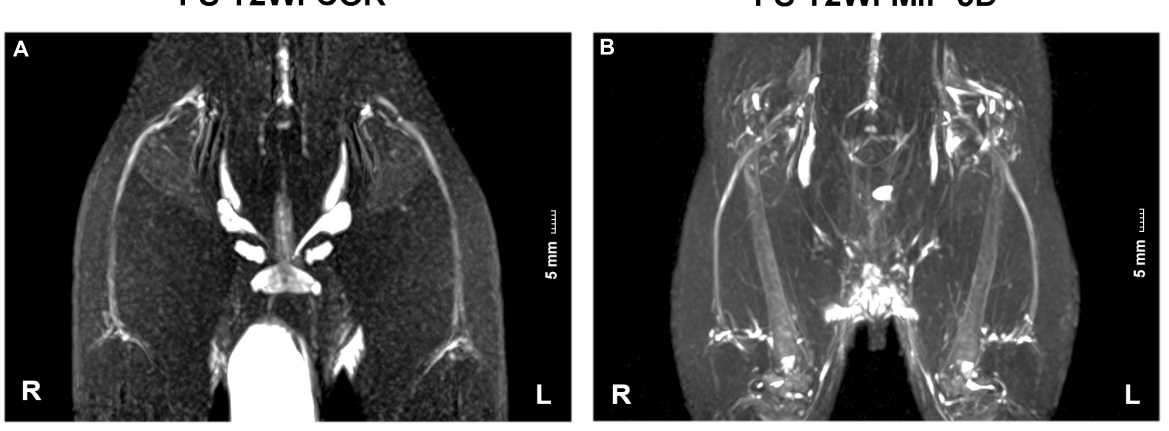

FIGURE 1 | FS T2WI COR and MIP 3D images of sciatic nerves. **(A,B)** T2WI coronal view displayed the morphology of bilateral sciatic nerves. They split above the knee joint into tibial and peroneal nerves. R, right hind limb; L, left hind limb. Scale: 5 mm.

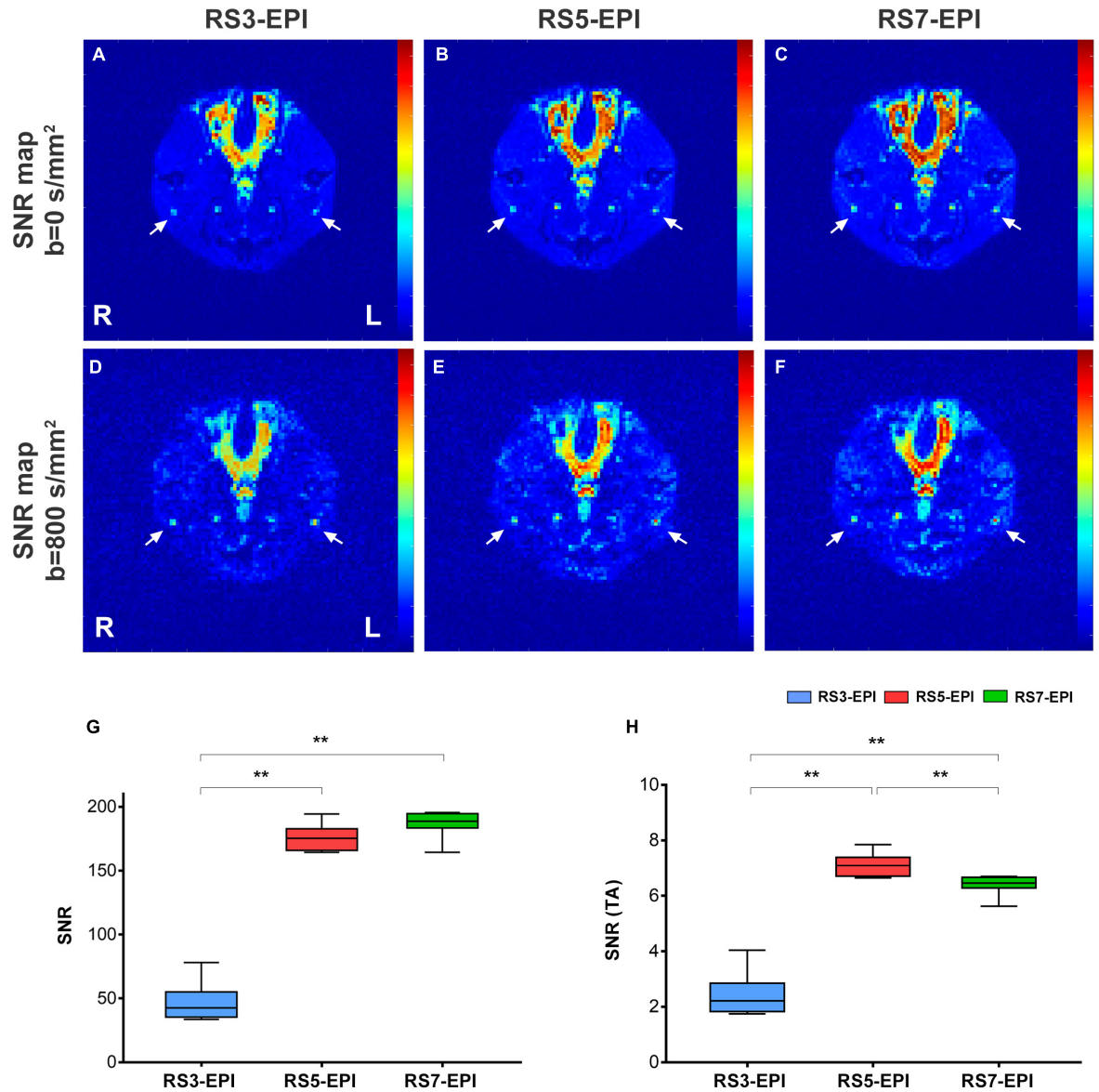

FIGURE 2 | SNR maps **(A–F)**, SNR value **(G)**, and SNR (TA) value **(H)** for RS3-EPI, RS5-EPI, and RS7-EPI. The measured SNR value increases with increasing segmented **(G)** for the three EPI sequences. Regarding SNR-values corrected for the acquisition time, RS5-EPI yielded significantly higher SNR than RS3-EPI and RS7-EPI **(H)**. SNR, signal-to-noise ratio; SNR(TA), SNR Correction due to sequence-specific differences in acquisition time **(H)**. $^{**}P \leq 0.017$, *post hoc* analysis with Bonferroni corrected.

Healthcare). The diffusion tensor parameters (FA and RD) were measured and calculated. ROIs of approximately 3 mm^2 were manually drawn on the adjacent three slices of the sciatic nerve. The three measurements were averaged for data analysis. Special attention was paid to position the ROIs to minimize the partial volume effect. Transverse DTI images were linked with coronal T2-weighted images to ensure the correct and consistent position of ROIs in the sciatic nerve. Tractography was obtained on the same workstation *via*. A multiple ROI method was used to reconstruct diffusion tensor tractography (DTT). The threshold of FA was set to be 0.15, the maximum fiber angle was 35°, and the minimum fiber length was 15 mm (Chen et al., 2017). The DTT numbers generated by different segmented EPI were calculated and recorded.

Histopathologic Assessment

Animals were executed after MR imaging by transcardial perfusion with PBS followed by 4% paraformaldehyde in 0.1 M PBS (pH 7.4). The middle stumps of the sciatic nerves were harvested and post-fixed in 4% glutaraldehyde. Transverse semi-thin sections (1 μm thickness) were prepared and stained with toluidine blue to detect nerve myelin. For quantifying toluidine blue staining, sections of the middle stumps were analyzed morphometrically. In brief, an objective magnification of ×1000

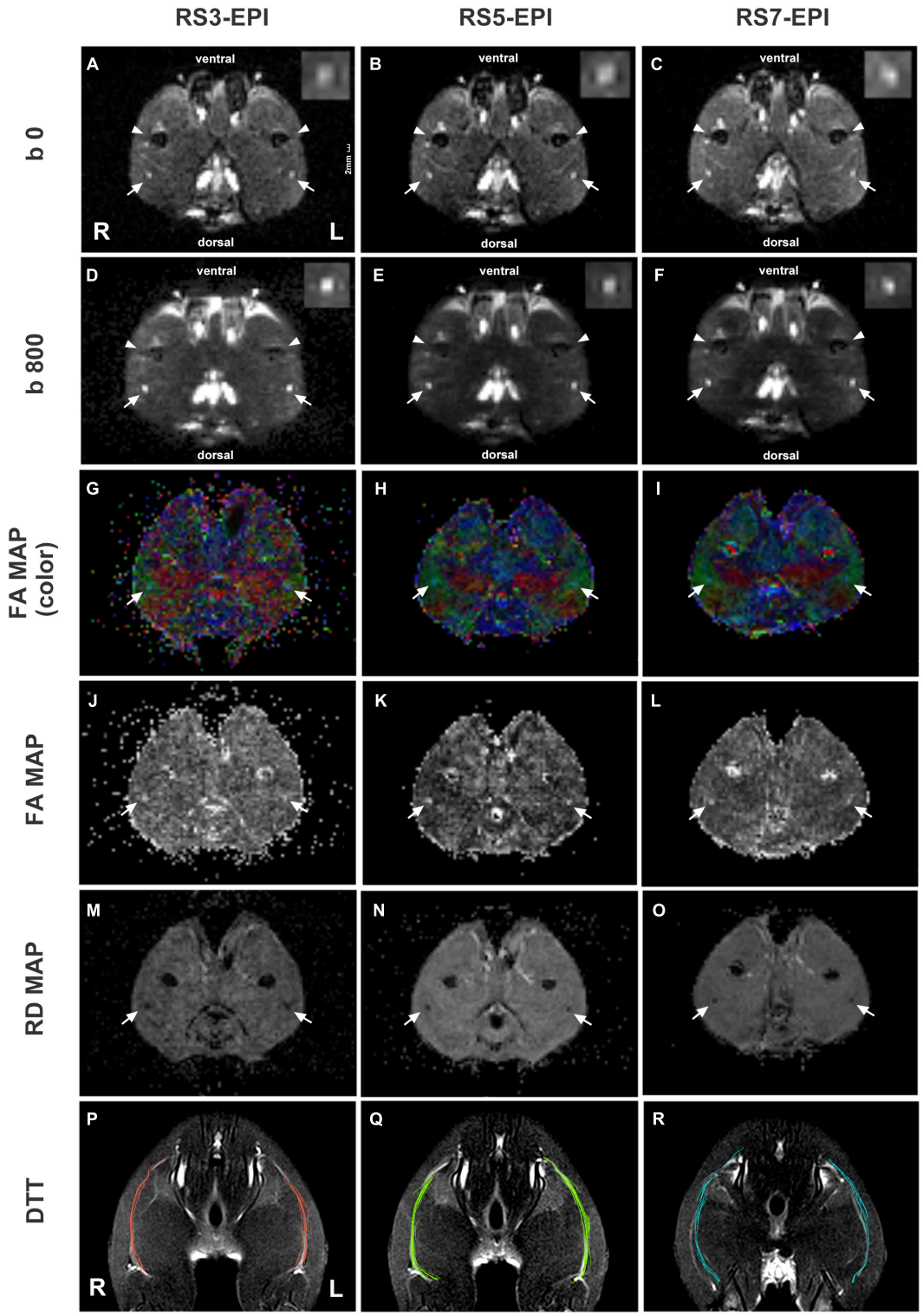

FIGURE 3 | DTI images and DTT of sciatic nerves for RS3-EPI, RS5-EPI, and RS7-EPI. The RS5-EPI images displayed clearer nerve boundaries and minimum nerve distortion, while RS7-EPI showed severe nerve distortion and blurred nerve boundaries **(A–F)**. The FA maps **(G–L)** and RD maps **(M–O)** showed blurred boundaries of RS3-EPI due to poor SNR **(G,J,M)** and of RS5-EPI due to severe nerve distortion **(I,L,O)**. The ventral and dorsal margin artifacts and background noise for RS3-EPI were more pronounced **(D,G,J)**. DTT: RS5-EPI DTI can generate more fibers than RS3-EPI and RS7-EPI and display nerve fibers with a more condensed bundle and realistic architecture **(P–R)**. Conversely, fibers generated by RS3-EPI and RS7-EPI DTI were sparse and discrete, some of which were deviated and in random order. R: right hind limb; L: left hind limb. Scale: 2 mm.

was used to take digital images of the entire cross-sectional area of the nerve (60 × 40 μm, 13.7 pixels/μm) on a microscope (Olympus BX60, Japan) for detailed histological quantification. Of these images, five randomly selected measured images (per image area, 240 μm^2; total area, 1200 μm^2 of different regions per nerve segment and animal) were analyzed, as previously described. ImageJ software[1] was used to perform analysis to determine the percentage of axon area (POAA), percentage of myelin area (POMA), thickness of myelin (TOM), and diameter of myelinated fibers (DOMF). The final value used for statistical analysis represents the mean of five measuring images per nerve segment and animal.

Statistical Analysis

Inter-reader agreement was assessed by using a linear-weighted inter-rater agreement (Kappa) test for the image quality scores at several aspects (sharpness of nerve margin, artifacts of nerve, artifacts of femur, artifacts of ventral muscles, artifacts of dorsal muscles, homogeneity of neuromuscular). The values of Kappa over 0.75, from 0.4 to 0.75, and below 0.4 were regarded as excellent, fair to good, and poor, respectively. Normal distribution of FA, RD, DTT fiber number, SNR, and SNR(TA) was evaluated using the Shapiro–Wilk's test. To assess potential between-group effects, ANOVA was performed for interval-scaled variables [FA, RD, DTT fiber number, SNR, and SNR(TA)], and Friedman tests were performed for ordinal scaled variables (sharpness of nerve margin, artifacts of nerve, artifacts of femur, artifacts of ventral muscles, artifacts of dorsal muscles, homogeneity of neuromuscular). To evaluate potential differences between RS3-EPI and RS5-EPI, RS3-EPI and RS7-EPI, and RS5-EPI and RS7-EPI, *post hoc* two-sample *t*-tests were performed for interval-scaled variables, and *post hoc* Wilcoxon signed-rank tests were performed for ordinal scaled variables. All statistical tests were Bonferroni corrected for *post hoc* analysis. The degree of association between DTI and histopathological parameters was calculated using the Pearson correlation coefficient. A two-sided *P*-value of 0.05 or less indicated a significant result, and the significance level was $P \leq 0.017$ for *post hoc* analysis. Statistical analysis was performed by using SPSS (version 23, IBM SPSS, Chicago, IL, United States) and MedCalc (version 19.1.2, MedCalc Software bv, Ostend, Belgium), and plots were created by using GraphPad Prism (version 7) and RStudio (version 1.4.1717).

RESULTS

Morphology of Rat Sciatic Nerve

The bilateral sciatic nerve was best displayed on the coronal view of T2WI STIR (**Figure 1**). They split above the knee joint into tibial and peroneal nerves, and two to three sub-branches can be shown downward. In our study, the thickness of the average rat sciatic nerve trunk ranged from 1 to 2 mm.

[1]https://imagej.net

Signal-to-Noise Ratio Analysis

Figure 2 and **Table 1** show the SNR and SNR(TA) values for RS3-EPI, RS5-EPI, and RS7-EPI. For the three EPI sequences, Measured SNR increases with increasing segmented. To account for sequence-specific differences in scan duration, correction factors were calculated for the acquisition time. Regarding SNR-values corrected for the acquisition time, RS5-EPI yielded significantly higher SNR than RS3-EPI and RS7-EPI.

Qualitative Image Evaluation

The image quality scores of the three DTI images for the sharpness of nerve margin, artifacts of nerve, artifacts of the femur, artifacts of ventral muscles, artifacts of dorsal muscles, and homogeneity of neuromuscular are shown in **Table 2** and **Figures 3**, **4**. The interobserver agreement between the two independent radiologists was excellent (Kappa = 0.753–0.971). **Figure 4** shows the image quality scores rated by reader 1 (the more senior radiologist). For reader 1, the Friedman test revealed a significant between-group effect for the image quality scores (all $P = 0.001$). Furthermore, for the sharpness of nerve margin and artifacts of the nerve, the *post hoc* analysis revealed significantly higher image quality scores for RS5-EPI compared to RS3-EPI ($P = 0.011$–0.014) and RS7-EPI ($P = 0.01$–0.011), and significant higher image quality scores for RS3-EPI compared to RS7-EPI (both $P = 0.016$). For artifacts of the ventral muscles, the *post hoc* analysis yielded significantly higher image quality scores for RS5-EPI compared to RS3-EPI ($P = 0.011$) and RS7-EPI ($P = 0.008$) and significant higher image quality scores for RS7-EPI compared to RS3-EPI ($P = 0.016$). For artifacts of the femur, artifacts of dorsal muscles, and homogeneity of the neuromuscular, *post hoc* analysis revealed significantly lower image quality scores for RS3-EPI compared to RS5-EPI ($P = 0.009$–0.01) and RS7-EPI ($P = 0.008$–0.01), and no significant differences were found between RS5-EPI and RS7-EPI (all $P > 0.017$).

Quantitative Analysis of Diffusion Tensor Imaging Parameters and Diffusion Tensor Tractography

Figure 5 show the FA, RD, and DTT fiber number for RS3-EPI, RS5-EPI, and RS7-EPI. ANOVA yielded a significant group effect for FA ($P < 0.001$), RD ($P < 0.001$), and DTT fiber number ($P = 0.023$). The *post hoc* analysis yielded significantly higher FA for RS5-EPI compared to RS7-EPI ($P = 0.001$) and lower RD for RS5-EPI compared to both RS3-EPI ($P = 0.001$) and RS7-EPI ($P < 0.001$), and higher FA for RS3-EPI compared to RS7-EPI ($P = 0.001$). In addition, DTT analysis yielded a significantly higher number of tracts for RS5-EPI than RS3-EPI ($P = 0.007$) but no significant difference with RS7-EPI ($P = 0.071$).

Correlation Between Diffusion Tensor Imaging Parameters and Histopathological Parameters

Table 3 and **Figure 6** show the correlation coefficients between DTI parameters (FA, RD) and histopathological parameters (POAA, POMA, TOM, DOMF) for RS3-EPI, RS5-EPI, and RS7-EPI. For the three sequences, FA was correlated with

TABLE 1 | SNR and quantitative DTI analysis.

	RS3-EPI	RS5-EPI	RS7-EPI	*P*-value			
				ANOVA	RS3 vs. RS5	RS3 vs. RS7	RS5 vs. RS7
SNR	47.106 ± 14.858	175.896 ± 10.563	186.490 ± 10.188	<0.001*	<0.001**	<0.001**	0.093
SNR(TA)	2.443 ± 0.768	7.110 ± 0.425	6.389 ± 0.349	<0.001*	<0.001**	<0.001**	0.015**
FA	0.626 ± 0.007	0.647 ± 0.018	0.607 ± 0.009	<0.001*	0.035	0.001**	0.001**
RD (μm^2/msec)	0.665 ± 0.021	0.621 ± 0.027	0.693 ± 0.018	<0.001*	0.001**	0.023	<0.001**
DTT fiber number	6.375 ± 4.104	13.375 ± 3.292	8.875 ± 6.266	0.023*	0.007**	0.302	0.071

*DTI, diffusion tensor imaging; RS3, No. of readout segments = 3; RS5, No. of readout segments = 5; RS7, No. of readout Segments = 7; SNR, signal-to-noise ratio; SNR(TA), SNR correction due to sequence-specific differences in acquisition time; FA, fractional anisotropy; RD, radial diffusivity; DTT, diffusion tensor tractography; *P ≤ 0.05; **P ≤ 0.017, post hoc analysis with Bonferroni corrected.*

TABLE 2 | Qualitative image evaluation.

Image quality evaluation	RS3 Median (range)	RS5 Median (range)	RS7 Median (range)	*P*-value				Kappa (95% CI) of Reader 1 vs. Reader 2
				Friedman	RS3 vs. RS5	RS3 vs. RS7	RS5 vs. RS7	
Reader 1								
Sharpness of the nerve margin	4 (2–5)	5 (4–5)	2 (1–4)	0.001*	0.011**	0.016**	0.011**	0.753 (0.526–0.980)
Artifacts of the nerve	3 (2–4)	4 (4–5)	2 (1–3)	0.001*	0.014**	0.016**	0.010**	0.793 (0.648–0.938)
Artifacts of the femur	2 (1–3)	4.5 (4–5)	5 (3–5)	0.001*	0.009**	0.009**	1.000	0.970 (0.915–1.000)
Artifacts of the ventral margin	2 (1–3)	5 (4–5)	4 (3–4)	0.001*	0.011**	0.016**	0.008**	0.967 (0.903–1.000)
Artifacts of the dorsal margin	2 (1–2)	4.5 (4–5)	4 (3–5)	0.001*	0.009**	0.010**	0.480	0.971 (0.914–1.000)
Homogeneity of the neuromuscular region	2 (1–3)	4.5 (4–5)	4 (4–5)	0.001*	0.010**	0.008**	0.157	0.967 (0.908–1.000)
Reader 2								
Sharpness of the nerve margin	4 (2–5)	5 (4–5)	3.5 (2–4)	0.007*	0.020**	0.260	0.017**	\
Artifacts of the nerve	3.5 (2–4)	4 (4–5)	2.5 (1–3)	0.002*	0.038	0.054	0.010**	\
Artifacts of the femur	2 (1–3)	4.5 (4–5)	5 (3–5)	0.001*	0.008**	0.008**	1.000	\
Artifacts of the ventral margin	2 (1–3)	5 (4–5)	4 (3–5)	0.001*	0.011**	0.014**	0.034	\
Artifacts of the dorsal margin	2 (1–2)	4.5 (4–5)	4.5 (3–5)	0.001*	0.009**	0.010**	0.705	\
Homogeneity of the neuromuscular region	2 (2–3)	4.5 (4–5)	4 (4–5)	0.001*	0.009**	0.007**	0.157	\

*RS3: No. of readout segments = 3; RS5: No. of readout segments = 5; RS7: No. of readout segments = 7; CI: confidence interval; *P ≤ 0.05; **P ≤ 0.017, post hoc analysis with Bonferroni corrected.*

almost all of the histopathological parameters (r = 0.751 to 0.851 for RS3-EPI, r = 0.886 to 0.953 for RS5-EPI, and r = 0.741 to 0.897 for RS7-EPI, $P \leq$ 0.001–0.036), except the DOMF for both RS3-EPI (r = 0.664, P = 0.073) and RS7-EPI (r = 0.623, P = 0.099), and RD was correlated with almost all of the histopathological parameters (r = −0.764 to −0.816 for RS3-EPI, r = −0.876 to −0.964 for RS5-EPI, and r = −0.709 to −0.812 for RS7-EPI, $P \leq$ 0.001−0.049), except the POAA for RS7-EPI (r = −0.691, P = 0.058). The overall correlation coefficients of FA and RD obtained with RS5-EPI were numerically higher than that with both RS3-EPI and RS7-EPI. The overall correlation coefficients of FA and RD obtained with RS3-EPI were numerically higher than that with RS7-EPI, except for the correlation coefficients between FA and POAA and between RD and POMA.

DISCUSSION

To evaluate the feasibility of segment-number 3, 5, and 7 of RS-EPI for DWI/DTI of rat sciatic nerve, we assessed qualitative data using image quality scoring in several detailed aspects on axial DWI images, and quantitative data using SNR, SNR(TA), number of tracts, FA, and RD value together with their correlation with pathologic parameters for each sciatic nerve in eight healthy rats. We found that referring to the rat sciatic nerve, RS5-EPI yielded optimal image quality, SNR(TA), pathology-correlated FA and RD value, and the richest number of fiber tracts compared to the RS7-EPI as well as RS3-EPI. Therefore, the current results demonstrate that DWI/DTI imaging of the rat sciatic nerve, RS5-EPI, is feasible, and the DTI parameters derived

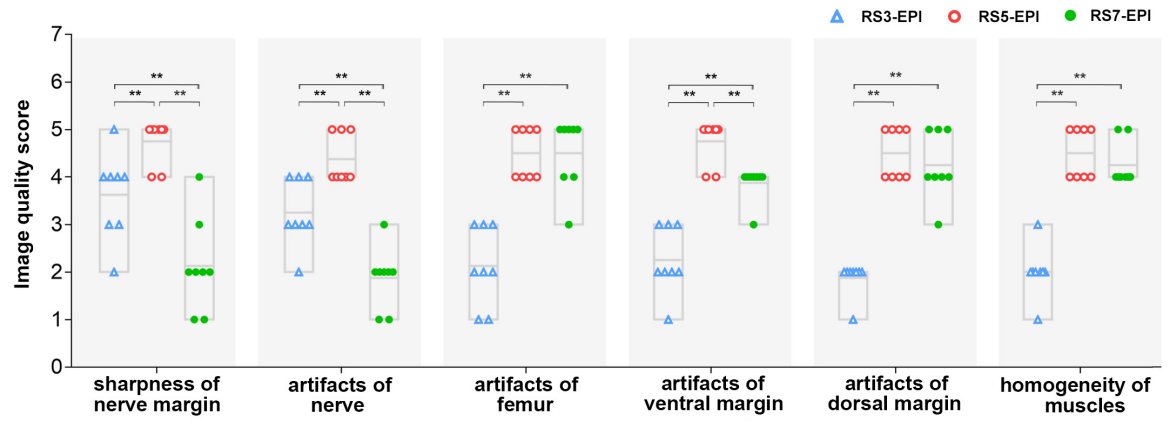

FIGURE 4 | Image quality scores for RS-3 EPI, RS-5 EPI, and RS-7 EPI. The chart showed the image quality scores rated by reader 1 (the more senior radiologist). The image quality scores of RS-5 EPI were superior to those of RS-3 and RS-7 EPI for better display of the nerve and lower artifacts of the ventral/dorsal margin and femur. $^{**}P \leq 0.017$, *post hoc* analysis with Bonferroni corrected.

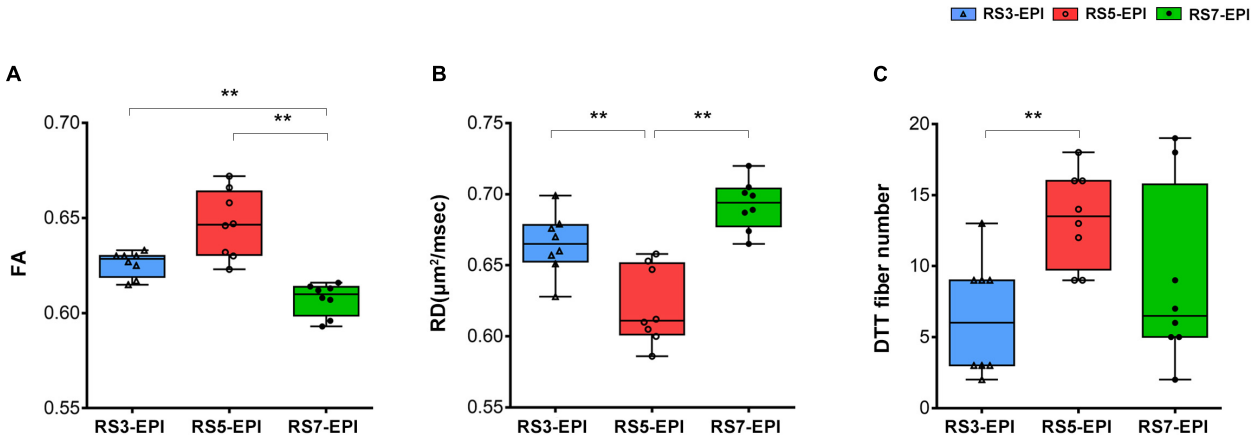

FIGURE 5 | Box plot comparing FA, RD, and DTT fiber numbers for RS3-EPI, RS5-EPI, and RS7-EPI. RS5-EPI yielded higher FA and lower RD than RS3-EPI and RS7-EPI **(A,B)**. The DTT fiber number generated by RS5-EPI was significantly higher than RS3-EPI **(C)**. $^{**}P \leq 0.017$, *post hoc* analysis with Bonferroni corrected.

TABLE 3 | Correlation coefficients between DTI parameters and histopathological parameters.

	FA			RD		
	RS3-EPI	**RS5-EPI**	**RS7-EPI**	**RS3-EPI**	**RS5-EPI**	**RS7-EPI**
POAA	$r = 0.851$ ($P = 0.007$*)	0.911 (0.002*)	0.897 (0.003*)	−0.816 (0.013*)	−0.882 (0.004*)	−0.691 (0.058)
POMA	0.799 (0.017*)	0.944 (<0.001*)	0.769 (0.026*)	−0.764 (0.027*)	−0.964 (<0.001*)	−0.812 (0.014*)
TOM	0.751 (0.032*)	0.953 (<0.001*)	0.741 (0.036*)	−0.808 (0.015*)	−0.922 (<0.001*)	−0.709 (0.049*)
DOMF	0.664 (0.073)	0.886 (0.003*)	0.623 (0.099)	−0.765 (0.027*)	−0.876 (0.004*)	−0.716 (0.046*)

*DTI, diffusion tensor imaging; FA, fractional anisotropy; RD, radial diffusivity. Histopathological parameters: POAA, percentage of axon area; POMA, percentage of myelin area; TOM, thickness of myelin; DOMF, diameter of myelinated fiber. r value, correlation coefficient value. P-value in parentheses, the result of correlation. *$P \leq 0.05$.*

from RS5-EPI showed a stronger linear correlation with histopathological parameters.

In our study, the SNR tended to increase with an increased segment number. The SNR for RS5-EPI and RS7-EPI were significantly higher than SNR for RS3-EPI. This difference may be because RS-EPI samples subsets of k-space points in the readout direction in each shot, thereby permitting a substantial reduction in echo spacing, TE, and T2* signal blurring. Multishot approaches typically can accommodate higher spatial resolution and possess higher SNR (Porter and Heidemann, 2009). As the increases of segment number, the acquisition time increases significantly (Atkinson et al., 2000). In our study, although RS7-EPI yielded the highest SNR originally, regarding SNR-values corrected for the acquisition time, RS5-EPI yielded higher

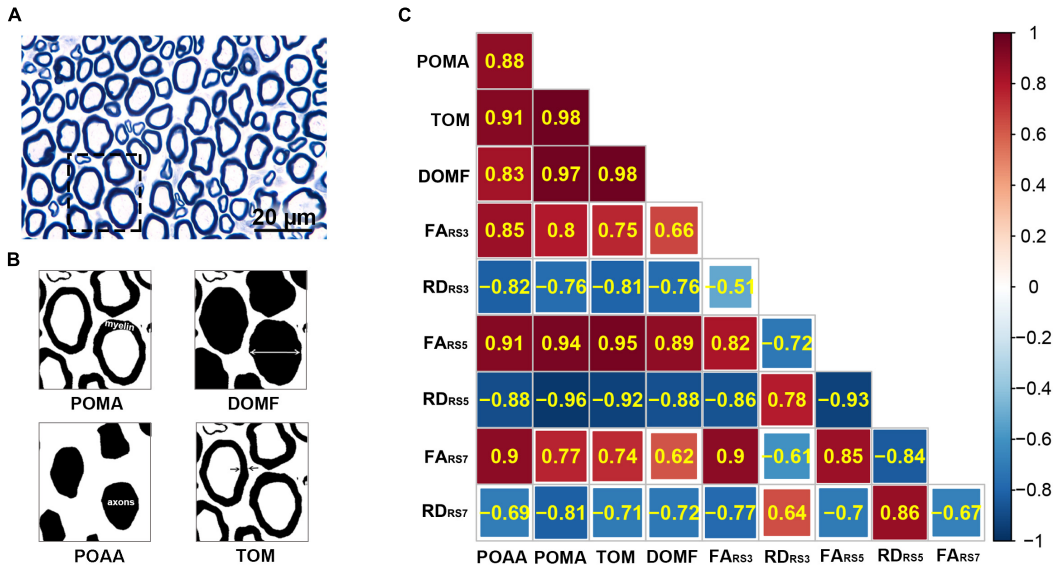

FIGURE 6 | Heatmap of correlation between DTI and histopathological parameters in RS3-EPI, RS5-EPI, and RS7-EPI. **(A)** Correlation coefficients between DTI parameters and histopathological parameters. **(B)** Toluidine blue myelin staining of the sciatic nerves (×1000). Scale: 20 μm. **(C)** Toluidine blue myelin staining was analyzed by ImageJ software to determine the quantitative pathological parameters, including POAA, percentage of axon area; POMA, percentage of myelin area; TOM, the thickness of myelin; DOMF, diameter of myelinated fibers.

SNR(TA) than both RS3-EPI and RS7-EPI. This shows that the SNRs of RS5-EPI and RS7-EPI are very close, but RS5-EPI requires a lower time cost and has a better application value.

In our study, the RS5-EPI sequence showed better image quality of the rat sciatic nerve compared with both RS3-EPI and RS7-EPI, displaying clearer margin and fewer artifacts of the rat sciatic nerve. RS5-EPI performed better than RS3-EPI because RS-EPI samples subsets of k-space points in the readout direction in each shot, and the resulting shorter echo spacing reduces susceptibility artifacts, geometric distortion, and T2* blurring by accelerating the k-space traversal along the direction of the readout. At the same time, the SNR has been improved. RS-EPI incorporated a 2D navigator-based reacquisition technique, which corrects motion-induced phase errors (Zaitsev et al., 2015). Unexpectedly, although RS7-EPI had the most subsets, the longest acquisition time, and the highest SNR, it yielded the lowest image quality scores of the rat sciatic nerve of the three RS-EPI. The most important reasons are that although multi-shot techniques acquire only a segment of k-space after each diffusion sensitization and enable higher resolution and reduced susceptibility artifacts. Motion during the diffusion sensitization leads to phase changes and k-space offsets. These differ between segments in multi-shot sequences, which can lead to severe image artifacts if uncorrected (Atkinson et al., 2000). Motion as a function of the k-space position is the most relevant parameter for the appearance of artifacts. In the case of interleaved multishot k-space acquisitions, such as the RS-EPI DTI, even slow continuous drifts produce significant ghosting; for example, the gradual relaxation of the neck muscles in head imaging or of the muscles around the sciatic nerve after anesthesia in our study (Zaitsev et al., 2015). With the increase of readout segments, RS-EPI becomes more vulnerable to motion artifacts. To reduce these motion artifacts, a nonlinear phase correction and reacquisition technique based on navigation echoes is used in RS-EPI (Nguyen et al., 1998; Porter and Mueller, 2004). However, the correction would fail for severely corrupted data sets since the reacquisition is time-limited (only 20% of the standard measurement time) (Porter and Heidemann, 2009). Meanwhile, with the increase of segments, the scanning time of RS-EPI increases multiply (Friedli et al., 2017; McKay et al., 2020), and the corrupted data due to motion increases either. It would be difficult to reacquire all the corrupted data in a limited time, resulting in partial data loss. This explains the heavier motion artifacts and geometric distortion of the RS-7 EPI than the RS-5 EPI. The corrupted data was still in time to be corrected with a high probability. What's more, it is essential wherein k-space fast motion occurs, as data corruption near the center of the k-space produces stronger artifacts than data corruption near the k-space periphery (Zaitsev et al., 2015). This is why the RS7-EPI scores in all aspects were more discrete than in the other two sequences in our study. When the motion occurs near the k-space periphery, the correction would be successful; while the motion occurs near the k-space center, the correction would be failed. In our study, due to the small size of the rat coil and the smaller voxel size with higher resolution, the signal strength is stronger, and the motion artifacts are more substantial (Gruber et al., 2018; Vergara Gomez et al., 2019). In addition to the extreme sensitivity to motion, the unsatisfied nerve image quality of RS7-EPI resulted from some other reasons. The sharp contrast tissue with a longer T2 relaxation time, such as nerve tissue, can produce motion-induced deterioration effects, which appear as a blurred border or geometric distortion (Chavhan et al., 2014). Conversely, the bone cortex and muscles with shorter T2 relaxation time have stronger resistance to motion artifacts than

neural tissues. This explains why for the RS7-EPI, which is most sensitive to motion artifacts, the image quality of femoral and muscle scored excellent while the sciatic nerve scored poorly.

In our study, in terms of the artifacts of ventral margin and dorsal margin, both RS5-EPI and RS7-EPI performed very well. This is because in areas with more susceptibility artifacts, such as the ventral and dorsal margin (adjacent to the air), the readout segmented EPI becomes very dominant in reducing geometric distortion caused by susceptibility artifacts (Bogner et al., 2012; Yeom et al., 2013; Zaitsev et al., 2015). Moreover, we found that the performance of RS7-EPI at the ventral margin was not as good as that at the dorsal border, which may be due to the presence of the scrotum, bladder, and intestine, which are water-containing organs on the ventral side, indicating that RS7-EPI is more prone to motion artifacts for tissues with high T2, which is also consistent with the fact that neural tissues with high T2 signal are more prone to motion artifacts at RS7-EPI (Chavhan et al., 2014). The superior homogeneity of the muscles yielded by RS5-EPI and RS7-EPI due to their excellent SNR compared with RS3-EPI. In our study, RS-5 EPI generated more DTT fiber numbers and displayed a more condensed bundle and realistic architecture. This is first due to the superior SNR of RS5-EPI and second related to the stronger resistance to motion artifact.

In summary, RS5-EPI not only has the best SNR (TA) and best resists motion-induced artifacts and nerve display but also has fewer artifacts in the peripheral edge region and shows good muscle homogeneity, allowing the best image quality to be acquired in the DTI scan of the rat sciatic nerve.

Diffusion tensor imaging offers quantitative information on the structure and orientation features to assess peripheral nerve diseases. Among these DTI metrics, FA and RD were thought to be the most stable and sensitive biomarkers for evaluating peripheral nerve regeneration (Naraghi et al., 2015; Chen et al., 2017). FA can reflect the packing density of axons within a voxel. At the same time, RD quantifies the diffusion perpendicular to the axonal orientation and is supposed to reflect myelin-related information (Jeon et al., 2018). Previously, peripheral nerve repair-related studies have shown that in the process of nerve fiber regeneration, with the density and integrality of myelin increases, FA value increases while RD value decreases (Chen et al., 2017; Farinas et al., 2020; Zheng et al., 2021). Similarly, in the peripheral nerve degeneration process of healthy aging people, nerve anisotropy (FA) decreases and RD increases with the decrease of the number of myelinated fibers (Jeon et al., 2018). Therefore, FA and RD value are sensitive biomarkers to detect minor myelin. In our study, the overall correlation coefficients of FA and RD obtained with RS5-EPI were numerically higher than that with both RS3-EPI and RS7-EPI. The FA and RD values for the three RS EPI were correlated differently with almost all the myelin-related pathological parameters of the rat sciatic nerve. Therefore, this indicated that referring to rat sciatic nerve, RS-5 EPI can acquire better image quality and provide more sensitive and accurate histological information compared to RS3-EPI and RS7-EchangesPI.

Our study had limitations. First, healthy adult rats were used in this study. The differences in DTI parameters for monitoring pathological changes in the sciatic nerve of healthy rats were minor. Future comparative studies on the rat sciatic nerve injury model will be more meaningful. Second, we did not include the comparison of single short EPI in our research. Despite the severe magnetic sensitivity artifacts at the edges of EPI, the single short EPI might yield good image quality of the nerve because of the longer TE, stronger resistance to motion artifacts, and shorter acquisition time. It would be interesting to compare RS-EPI and SS-EPI in the sciatic nerve in the future.

In conclusion, for the rat sciatic nerve DTI imaging, the RS-5 EPI sequence was more robust to motion artifacts and offered a shorter scanning time than the RS-7 EPI sequence. Regarding SNR-values corrected for the acquisition time, RS5-EPI yielded significantly higher SNR than RS3-EPI and RS7-EPI. The FA and RD derived from the RS-5 EPI sequence might be highly sensitive quantitative biomarkers to detect rat sciatic nerve histopathological change. These findings will also inform the DTI sequence optimization in MRI basic research for peripheral nerves.

DATA AVAILABILITY STATEMENT

The original contributions presented in this study are included in the article/supplementary material, further inquiries can be directed to the corresponding authors.

ETHICS STATEMENT

The animal study was reviewed and approved by the Institutional Animal Care and Use Committee of Jennio Biotech Co., Ltd. Written informed consent was obtained from the owners for the participation of their animals in this study.

AUTHOR CONTRIBUTIONS

YC: data collection and analysis, experiment design, and writing of the manuscript. ZP: statistical analysis of data and creation of statistical charts. FM: rat MRI scan, sequence optimization, and technical assistance. QX: pathological staining and analysis. LH: image processing. XP: MRI data acquisition. XY: pathological staining. YW: discussion and revision of the manuscript. XL and HL: full access to all the data in the study and responsible for the integrity of the data and the accuracy of the data analysis. All authors contributed to the article and approved the submitted version.

FUNDING

This research was supported by the National Natural Science Foundation of China (Grant code: 81903960) and the Natural Science Foundation of Guangdong Province (Grant code: 2020A1515010732).

REFERENCES

Atkinson, D., Porter, D. A., Hill, D. L., Calamante, F., and Connelly, A. (2000). Sampling and reconstruction effects due to motion in diffusion-weighted interleaved echo planar imaging. *Magn. Reson. Med.* 44, 101–109. doi: 10.1002/1522-2594(200007)44:1<101::aid-mrm15>3.0.co;2-s

Bogner, W., Pinker-Domenig, K., Bickel, H., Chmelik, M., Weber, M., Helbich, T. H., et al. (2012). Readout-segmented echo-planar imaging improves the diagnostic performance of diffusion-weighted MR breast examinations at 3.0 T. *Radiology* 263, 64–76. doi: 10.1148/radiol.12111494

Chavhan, G. B., Alsabban, Z., and Babyn, P. S. (2014). Diffusion-weighted imaging in pediatric body MR imaging: principles, technique, and emerging applications. *Radiographics* 34, E73–E88. doi: 10.1148/rg.343135047

Chen, H. H., Hu, H., Chen, W., Cui, D., Xu, X. Q., Wu, F. Y., et al. (2020). Thyroid-Associated orbitopathy: evaluating microstructural changes of extraocular muscles and optic nerves using readout-segmented echo-planar imaging-based diffusion tensor imaging. *Korean J. Radiol.* 21, 332–340. doi: 10.3348/kjr.2019.0053

Chen, Y. Y., Zhang, X., Lin, X. F., Zhang, F., Duan, X. H., Zheng, C. S., et al. (2017). DTI metrics can be used as biomarkers to determine the therapeutic effect of stem cells in acute peripheral nerve injury. *J. Magn. Reson. Imaging* 45, 855–862. doi: 10.1002/jmri.25395

Drake-Pérez, M., Boto, J., Fitsiori, A., Lovblad, K., and Vargas, M. I. (2018). Clinical applications of diffusion weighted imaging in neuroradiology. *Insights Imaging* 9, 535–547.

Farinas, A. F., Manzanera Esteve, I. V., Pollins, A. C., Cardwell, N. L., Kaoutzanis, C., Nussenbaum, M. E., et al. (2020). Diffusion magnetic resonance imaging predicts peripheral nerve recovery in a rat sciatic nerve injury model. *Plast. Reconstr. Surg.* 145, 949–956. doi: 10.1097/PRS.0000000000006638

Friedli, I., Crowe, L. A., de Perrot, T., Berchtold, L., Martin, P. Y., de Seigneux, S., et al. (2017). Comparison of readout-segmented and conventional single-shot for echo-planar diffusion-weighted imaging in the assessment of kidney interstitial fibrosis. *J. Magn. Reson. Imaging* 46, 1631–1640. doi: 10.1002/jmri.25687

Gruber, B., Froeling, M., Leiner, T., and Klomp, D. (2018). RF coils: a practical guide for nonphysicists. *J. Magn. Reson. Imaging* 48, 590–604. doi: 10.1002/jmri.26187

Guggenberger, R., Markovic, D., Eppenberger, P., Chhabra, A., Schiller, A., Nanz, D., et al. (2012). Assessment of median nerve with MR neurography using diffusion-tensor imaging: normative and pathologic diffusion values. *Radiology* 265, 194–203. doi: 10.1148/radiol.12111403

Jeon, T., Fung, M. M., Koch, K. M., Tan, E. T., and Sneag, D. B. (2018). Peripheral nerve diffusion tensor imaging: Overview, pitfalls, and future directions. *J. Magn. Reson. Imaging* 47, 1171–1189. doi: 10.1002/jmri.25876

Kida, I., Ueguchi, T., Matsuoka, Y., Zhou, K., Stemmer, A., and Porter, D. (2016). Comparison of diffusion-weighted imaging in the human brain using readout-segmented EPI and PROPELLER turbo spin echo with single-shot EPI at 7 T MRI. *Invest. Radiol.* 51, 435–439. doi: 10.1097/RLI.0000000000000248

Manoliu, A., Ho, M., Piccirelli, M., Nanz, D., Filli, L., Dappa, E., et al. (2017). Simultaneous multislice readout-segmented echo planar imaging for accelerated diffusion tensor imaging of the mandibular nerve: A feasibility study. *J. Magn. Reson. Imaging* 46, 663–677. doi: 10.1002/jmri.25603

McKay, J. A., Church, A. L., Rubin, N., Emory, T. H., Hoven, N. F., Kuehn-Hajder, J. E., et al. (2020). A comparison of methods for high-spatial-resolution diffusion-weighted imaging in breast MRI. *Radiology* 297, 304–312. doi: 10.1148/radiol.2020200221

Mori, S., and Zhang, J. (2006). Principles of diffusion tensor imaging and its applications to basic neuroscience research. *Neuron* 51, 527–539. doi: 10.1016/j.neuron.2006.08.012

Naraghi, A. M., Awdeh, H., Wadhwa, V., Andreisek, G., and Chhabra, A. (2015). Diffusion tensor imaging of peripheral nerves. *Semin. Musculoskelet. Radiol.* 19, 191–200.

Nguyen, Q., Clemence, M., and Ordidge, R. (1998). "The use of intelligent re-acquisi tion to reduce scan time in MRI degraded by motion," in *Proceedings of the 6th Annual Meeting of ISMRM*, Sydney.

Porter, D., and Mueller, E. (2004). "Multi-shot diffusion-weighted EPI with readout mosaic segmentation and 2D navigator correction," in *Proceedings of the 12th Annual Meeting of ISMRM*, Kyoto.

Porter, D. A., and Heidemann, R. M. (2009). High resolution diffusion-weighted imaging using readout-segmented echo-planar imaging, parallel imaging and a two-dimensional navigator-based reacquisition. *Magn. Reson. Med.* 62, 468–475. doi: 10.1002/mrm.22024

Thian, Y. L., Xie, W., Porter, D. A., and Weileng Ang, B. (2014). Readout-segmented echo-planar imaging for diffusion-weighted imaging in the pelvis at 3T-A feasibility study. *Acad. Radiol.* 21, 531–537. doi: 10.1016/j.acra.2014.01.005

Vergara Gomez, T. S., Dubois, M., Glybovski, S., Larrat, B., de Rosny, J., Rockstuhl, C., et al. (2019). Wireless coils based on resonant and nonresonant coupled-wire structure for small animal multinuclear imaging. *NMR Biomed.* 32:e4079. doi: 10.1002/nbm.4079

Yeom, K. W., Holdsworth, S. J., Van, A. T., Iv, M., Skare, S., Lober, R. M., et al. (2013). Comparison of readout-segmented echo-planar imaging (EPI) and single-shot EPI in clinical application of diffusion-weighted imaging of the pediatric brain. *AJR Am. J. Roentgenol.* 200, W437–W443. doi: 10.2214/AJR.12.9854

Zaitsev, M., Maclaren, J., and Herbst, M. (2015). Motion artifacts in MRI: A complex problem with many partial solutions. *J. Magn. Reson. Imaging* 42, 887–901. doi: 10.1002/jmri.24850

Zhang, H., Huang, H., Zhang, Y., Tu, Z., Xiao, Z., Chen, J., et al. (2021). Diffusion-Weighted MRI to assess sacroiliitis: improved image quality and diagnostic performance of readout-segmented echo-planar imaging (EPI) over conventional single-shot EPI. *AJR Am. J. Roentgenol.* 217, 450–459.

Zheng, C., Yang, Z., Chen, S., Zhang, F., Rao, Z., Zhao, C., et al. (2021). Nanofibrous nerve guidance conduits decorated with decellularized matrix hydrogel facilitate peripheral nerve injury repair. *Theranostics* 11, 2917–2931. doi: 10.7150/thno.50825

Conflict of Interest: YW was employed by Siemens Healthcare (China).

The remaining authors declare that the research was conducted in the absence of any commercial or financial relationships that could be construed as a potential conflict of interest.

frontiers | Frontiers in Neuroscience

TYPE Review
PUBLISHED 15 July 2022
DOI 10.3389/fnins.2022.938665

OPEN ACCESS

EDITED BY
Yen-Yu Ian Shih,
University of North Carolina at Chapel Hill, United States

REVIEWED BY
Cornelius Faber,
University Hospital Münster, Germany
Patricia Pais-Roldán,
Helmholtz Association of German Research Centres (HZ), Germany

*CORRESPONDENCE
Lauren Kosten
lauren.kosten@uantwerpen.be
Georgios A. Keliris
georgios.keliris@outlook.com

SPECIALTY SECTION
This article was submitted to Brain Imaging Methods, a section of the journal Frontiers in Neuroscience

RECEIVED 07 May 2022
ACCEPTED 28 June 2022
PUBLISHED 15 July 2022

CITATION
Kosten L, Emmi SA, Missault S and Keliris GA (2022) Combining magnetic resonance imaging with readout and/or perturbation of neural activity in animal models: Advantages and pitfalls.
Front. Neurosci. 16:938665.
doi: 10.3389/fnins.2022.938665

Combining magnetic resonance imaging with readout and/or perturbation of neural activity in animal models: Advantages and pitfalls

Lauren Kosten[1]*, Serena Alexa Emmi[1], Stephan Missault[1] and Georgios A. Keliris[1,2]*

[1]Bio-Imaging Lab, Department of Biomedical Sciences, University of Antwerp, Antwerp, Belgium, [2]Foundation for Research & Technology – Hellas, Heraklion, Greece

One of the main challenges in brain research is to link all aspects of brain function: on a cellular, systemic, and functional level. Multimodal neuroimaging methodology provides a continuously evolving platform. Being able to combine calcium imaging, optogenetics, electrophysiology, chemogenetics, and functional magnetic resonance imaging (fMRI) as part of the numerous efforts on brain functional mapping, we have a unique opportunity to better understand brain function. This review will focus on the developments in application of these tools within fMRI studies and highlight the challenges and choices neurosciences face when designing multimodal experiments.

KEYWORDS

multimodal imaging, fMRI, neural activity, hemodynamic response, optical imaging

Introduction and state-of-the-art

Functional magnetic resonance imaging (fMRI) is a powerful neuroimaging tool that since its inception in 1990 (Ogawa et al., 1990) has revolutionized human as well as non-human neuroscience and biomedical research. FMRI's global brain coverage and relatively good spatial and temporal resolution can provide invaluable insights into whole-brain activity and network organization. Moreover, its non-invasive nature without ionizing radiation allow repeated and longitudinal *in vivo* acquisitions in the same subjects and thus evaluation and follow-up of disease progression and/or therapeutic outcome.

Functional magnetic resonance imaging relies on the coupling between neural activity and hemodynamic responses, known as neurovascular coupling (NVC) (Ingvar and Lassen, 1962). In its most common application, fMRI detects the blood-oxygen-level-dependent (BOLD) signal, which reflects changes in the relative levels of oxygenated and deoxygenated hemoglobin driven by changes in cerebral blood flow, blood volume, and blood oxygenation, which are coupled to neural activity by NVC

(Buxton and Frank, 1997; Logothetis and Wandell, 2004). Hence, fMRI provides an indirect measure of neural activity. More specifically, neural activity has higher energy demands met by oxidative metabolism and that requires increases in oxygen consumption. The brain's vascular system responds to this demand by increases in cerebral blood flow (CBF), termed as "functional hyperemia," and cerebral blood volume (CBV) resulting in a local markedly increased ratio of oxygenated hemoglobin (HbO) over deoxygenated hemoglobin (HbR) (Attwell and Iadecola, 2002). The differences in magnetic properties of HbO (weakly diamagnetic) and HbR (strongly paramagnetic) result in measurable changes in MRI BOLD signal when their ratio is altered allowing the detection of activated brain areas. The capability of neuronal activity to trigger metabolic responses *via* the NVC became clear when autoradiography studies using the 2-[^{14}C]-deoxyglucose (2DG) approach had been conducted (Sokoloff et al., 1977). Since then, the NVC has received much attention in the literature and the acquired knowledge has underlined its high level of complexity. Further, thanks to the research conducted by Chance et al. (1962) and Jöbsis (1977), it was shown that neuronal activity is not only able to trigger changes in CBF and CBV but also in oximetric signals detectable *via* optical imaging. The NVC is governed by several mechanisms and signaling pathways that are still far from being understood (Lok et al., 2007). Thus, although a link between neural activity and hemodynamic responses is established, their exact relationship is still an open research query. It is of importance to shed light on these phenomena not only to correctly interpret fMRI data but also to provide a better understanding of pathological conditions such as stroke or neurodegenerative diseases that are characterized, among other features, by the disruption of the NVC (Girouard and Iadecola, 1985; Jonckers et al., 2015). Currently, different fMRI methods are in use, including resting state [rsfMRI, Jonckers et al. (2015)], stimulus-evoked [st-fMRI, Barry et al. (2021)], and pharmacological fMRI [phMRI, Zhao et al. (2021)]. Respectively, these techniques permit the assessment of functional connectivity between brain regions during rest (measured by the correlation between low frequency fluctuations in the BOLD signal) as well as brain activation triggered by sensory stimulation or a pharmacological challenge. Each of these methods pinpoints different aspects of neuronal activity, making it a technique suitable to investigate different aspects of brain function.

In order to obtain full advantage from the application of fMRI, its strengths and weaknesses should be taken into consideration, together with the potential of other neural activity readout and neuromodulation approaches (**Figure 1**). It is essential to recognize what fMRI can and cannot do (Logothetis, 2008). On the one hand, fMRI is characterized by relatively high three-dimensional spatial resolution of the whole brain, but on the other hand, it is affected by a relatively low temporal resolution, given that it relies on the NVC that is slower in nature (order of seconds) in comparison to neuronal spiking activity that demonstrates millisecond resolution (Logothetis and Pfeuffer, 2004). As previously mentioned, fMRI is only an indirect measure of neuronal activity. The controversy surrounding the BOLD response and the interpretation of fMRI data is mainly related to it being a "surrogate" signal resulting from hemodynamic changes and therefore not a direct readout of neuronal activity (Logothetis and Pfeuffer, 2004).

Combining fMRI with additional readouts of neural activity provides a powerful tool to gain insights into the NVC and the interpretation of fMRI findings. The most widely used probe for neural activity in experimental neuroscience has been electrophysiological recordings (Hubel, 1957; Wiesel, 1959; Rubaiy, 2017). More recently, the advent of novel technologies such as the development of (genetically encoded) calcium imaging dyes with relatively fast dynamics able to follow neural activity, introduced a stark competitor to electrophysiology. During the last decades, there has been a marked shift from electrophysiological approaches to optical imaging in combination with fMRI in the study of neuronal activity and NVC (Scanziani and Häusser, 2009). Each of these techniques provides a different approach in the study of neuronal activity in combination with fMRI and the use of one rather than another mainly depends on the aim of the study and on the type of neuronal activity investigation that has to be done.

This review compares electrophysiological with optical approaches that can be used in combination with MRI imaging. The focus is to provide an examination of the main features of these methods, including their implementation, costs and MRI compatibility starting from electrophysiology and ending with the most recent state-of-the-art optical techniques. By highlighting the pros and cons of each technique, we aim to guide scientists toward the most suitable technique for their goals.

Coupling the blood-oxygen-level-dependent signal to the electrical neuronal activity: Simultaneous functional magnetic resonance imaging and electrophysiology

Since its inception, electrophysiology has been considered the "gold standard" to probe electrical neuronal activity (Galvani, 1791; Piccolino, 1997, 1998). Its strength relies on its remarkable sensitivity and temporal resolution in investigating, in the order of milliseconds, the electrical features of neurons by means of electrodes made of different materials (glass, metal, silicon). In particular, it provides

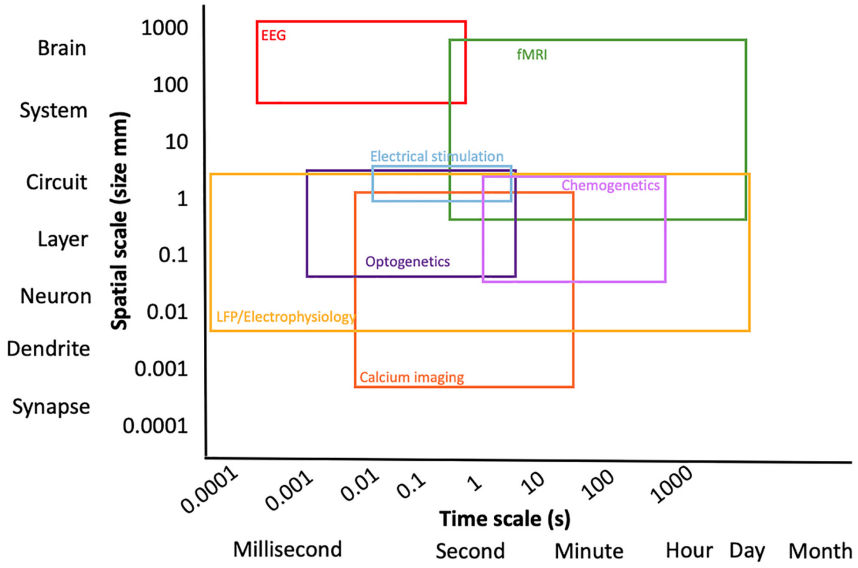

FIGURE 1
Overview of multimodal techniques expanding the spatial and temporal resolution of the experiment.

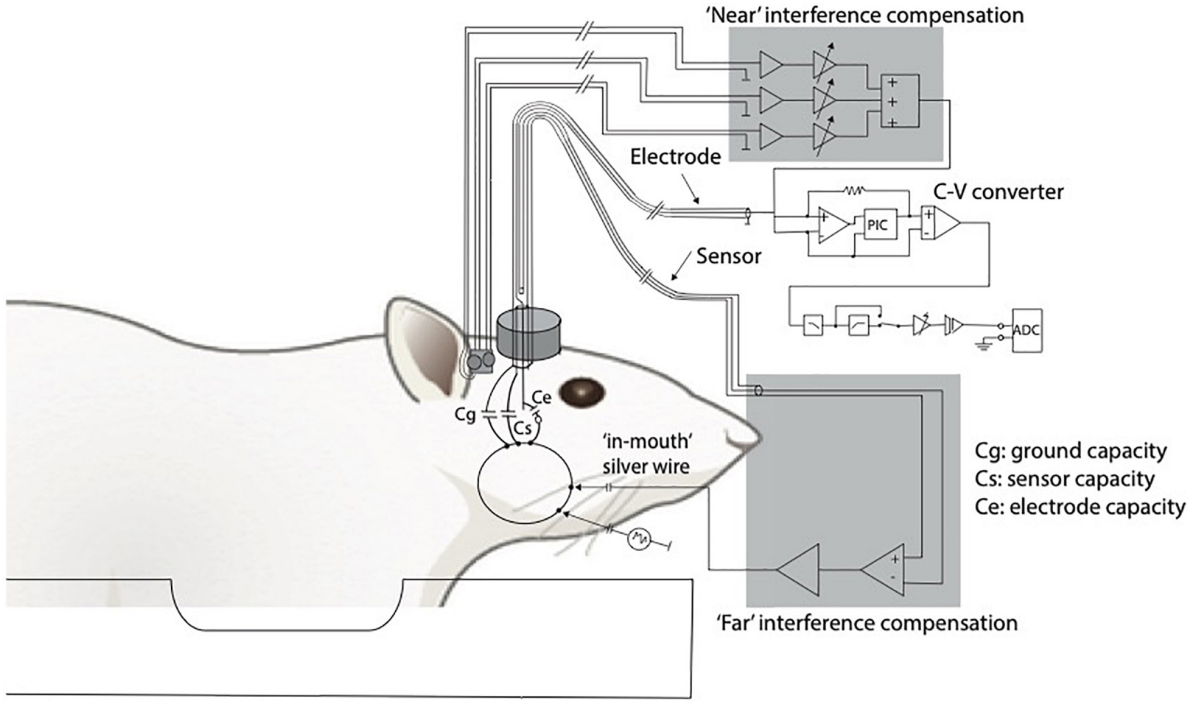

FIGURE 2
Adapted from Logothetis et al. (2001). Diagram of the recording and compensation circuitry. The animal can be conceived as being capacitively connected to any metal contact, including connections to ground (Cg), sensor (Cs), and electrode (Ce). Because of the finite animal-to-ground capacity, a fraction of the interference currents flow through the electrode. To compensate for such currents, a sensor is built into the electrode holder (current sensor). Interference originating near the electrode tip or within the electrode holder and the cables is compensated for by using three small, orthogonally oriented identical coils positioned near the electrode (magnetic field sensor). C-V, current to voltage converter.

direct and precise measurements of electrical currents and voltage changes at different scales, from single ion channels to small neuronal populations, with a high signal-to-noise ratio. However, electrophysiology shows disadvantages as well. While it offers high temporal resolution and precision (single neurons can be measured), it has limited spatial coverage, meaning that recordings of electrical signals are limited to neuronal groups and cannot be extended to the whole neuronal network and thus difficult to do whole-brain recordings. At the macroscale, indirect measurement of large areas of the brain's activity is achieved *via* electroencephalography (EEG), at the mesoscale the development of microelectrode arrays (MEAs) has increased the number of neurons that can be recorded both *in vivo* and *in vitro*. They are however invasive in an *in vivo* setting and limited to the brain region of implantation and most importantly, they potentially record undefined signals coming from the areas surrounding the array (Obien et al., 2015).

The lack of a one-to-one correspondence between spontaneous electrophysiological and hemodynamic measures suggests that electrophysiology might be able to reveal properties of spatial patterns in spontaneous activity that are undetectable with fMRI. For example, the much better temporal resolution of electrophysiology enables researchers to answer questions about networks such as whether one brain area 'leads' while another one in the network "follows." Measuring correlations between spontaneous signal fluctuations, be it in electrophysiology or in fMRI, has grown to be a much-used way to probe brain functional connectivity during rest. These so-called resting-state networks commonly found in fMRI seem to possess analogous electrophysiological patterns over the cortical surface (Schölvinck et al., 2013). At the same time, the wealth of spectral, spatial, and temporal scales afforded by electrophysiological measurements has begun to put the spotlight on the meaning and value of correlation-based concepts such as functional connectivity and functional networks (Schölvinck et al., 2013). To overcome the disadvantages related to both fMRI and electrophysiology and to achieve their maximum efficiency, they can be advantageously combined to shed light on the neuronal basis of the BOLD signal: while the BOLD signal at the basis of fMRI gives an indirect measure of neuronal activity, electrophysiology provides a direct measure of it (Logothetis and Wandell, 2004), hence becoming the starting technique to elucidate the neural basis of the BOLD signal. To help with interpretation of the neural basis of rsfMRI connectivity, Wang et al. (2019) utilized a multi-modal approach including rsfMRI, optogenetic stimulation (more on this in section Optogenetically modulating neuronal activity using light) and multi-depth cortical electrophysiology recording to examine whether and how the somatosensory thalamus contributes to cortical interhemispheric rsfMRI connectivity. They demonstrated that low frequency activities in the thalamo-cortical network contribute to brain-wide rsfMRI connectivity, highlighting the thalamus as a pivotal region that underlies rsfMRI connectivity. Both techniques are however, susceptible to electromagnetic interference, thus compromising each other in terms of signal and data acquisition when used in simultaneous setups. For example, electrophysiology electrodes can distort the magnetic field and jeopardize the MR image quality. Concurrently, the strong magnetic field can hamper the proper amplification of weak electrophysiological signals recorded inside the magnet. As a consequence, several features of the electrophysiology set-up must be modified to guarantee its functioning in the MRI scanner without compromising the quality of each measurement, therefore demanding a series of technical adaptations such as the use of nonmagnetic electrodes.

Logothetis and colleagues have played a major role in the development and improvement of these adjustments. One of these is the establishment of an interference compensation system able to compensate the interference to the electrophysiological signals generated by the alternation of the field gradients used for image generation during echo-planar imaging (EPI) (Oeltermann et al., 2007; **Figure 2**). Their research that sheds light on the neural origin of the BOLD signal *via* simultaneous electrophysiological recordings of local field potentials (LFPs) and spiking activity of neurons of the primary visual cortex and fMRI measurements in anesthetized non-human primates (*Macaca mulatta*) while visually stimulated using contrast gratings is considered fundamental for our understanding of the relationship of BOLD with neural activity (Logothetis et al., 2001). With the obtained results, they provided overwhelming evidence that the BOLD signal strongly correlates with the underlying LFPs, which are more accurately described as a combination of post- and pre-synaptic activity at multiple neurons ("peri"synaptic). This study had a considerable impact because, for the first time, it was demonstrated by means of electrophysiology and fMRI that a spatially localized increase in the BOLD signal directly and monotonically reflects an increase of the neural activity. As such, the BOLD signal is more closely related to LFPs than the spiking activity. The same has been demonstrated when investigating the coupling between the BOLD signal and electrophysiological recordings in a different brain area of anesthetized macaque monkeys: the motion-sensitive area MT in the visual cortex (Lippert Michael et al., 2010). Later, consistent with these results, other studies confirmed that the BOLD signal is better predicted by LFPs, even in case of pharmacological dissociation of spiking activity and LFPs (Rauch et al., 2008), as well as in alert and behaving experimental conditions (Goense and Logothetis, 2008). In fact, it was necessary to investigate if the same results could be reported in alert, awake animals because of the well-known effect of anesthesia on both neuronal activity and vasculature, consequently affecting the NVC (Williams et al., 2010; Masamoto and Kanno, 2012; Jonckers et al., 2015).

Pan et al. (2010) approached the issue of electrodes distorting the MRI images and the MRI acquisition inducing noise in the electrical recordings through the use of glass microelectrodes rather than metal and implementation of a noise removal algorithm for the electrophysiology data in a rat model. Their modified method of electrode implantation minimizes influence on the image quality, and successfully combined the strengths of functional brain imaging with electrophysiology. Jaime et al. stated that their use of intracortical implantation of a multichannel microelectrode array resulted in minimal distortion and signal loss in fMRI images inside a 9.4T MRI scanner. Due to nanomanufacturing advances permitting the production of MRI-compatible microelectrode arrays with 16 or more channels, multimodal research is widely extended. The methodology even permits longitudinal data collection of LFP and rsMRI (Jaime et al., 2018; Zaldivar et al., 2018). Other successful attempts at MRI compatible recordings include the use of carbon fiber electrodes placed on the skull or surface of the brain (Opdam et al., 2002; Austin et al., 2003; Nersesyan et al., 2004; Mirsattari et al., 2005; David et al., 2008) calomel electrodes anchored to the skull (Brinker et al., 1999), platinum wire electrodes covering the scalp (Sumiyoshi et al., 2011), saline-filled (Canals et al., 2009; Moreno et al., 2016) or carbon fiber-threaded (Shyu et al., 2004) glass micropipettes inserted into the brain. Duffy et al. took it a step further by developing carbon fiber optrodes (optical fiber and electrode hybrid devices), which can be utilized in chronic longitudinal studies (Duffy et al., 2015). It is evident that electrodes often cause susceptibility artifacts and could compromise fMRI outcomes. Some studies often show considerable artifacts nearby the electrodes (Walton et al., 2021). The use of tungsten microwires was an initial improvement (Chao et al., 2014; Lai et al., 2015; van den Berge et al., 2017), and further advanced with for example graphene fiber electrodes (Zhao et al., 2020) and advanced imaging sequences to obtain susceptibility artifact free fMRI data such as the 3D radial MRI pulse sequence "Multi-Band SWeep Imaging with Fourier Transformation (MB-SWIFT)" (Lehto et al., 2017).

Taken together, these findings and methodological adaptations allow to compare results coming from human fMRI studies with plenty of electrophysiological data obtained not only from anesthetized animals but also from animals in alert and behaving conditions (Keliris et al., 2007, 2019).

While adaptations for MRI compatibility are not widespread, there are excellent commercial *in vivo* recording systems available such as Smart Ephys to record, amplify, and analyze signals from freely moving or anesthetized animals (Multi Channel Systems MCS GmbH, 2020). Similarly, commercially available probes such as NeuroNexus or ATLAS Neuroengineering are widely used in literature, however, these systems still need adaptations for multimodal use. When it comes to commercially available MRI compatible systems, Blackrock has a unit named MagRes, which is an MRI compatible headstage that will allow small animal researchers to directly correlate neural activity with hemodynamic changes detected on MRI for awake and responsive subjects (Blackrock Neurotech, 2021).

In terms of translation to human studies, EEG and fMRI are two of the fundamental non-invasive methods for identifying brain activity. Multimodal methods have sought to combine the high temporal resolution of EEG with the spatial coverage of fMRI, but the complexity of this approach is still in need of improvement. Nguyen et al. (2018) recently described a method for better EEG and fMRI integration using a spatiotemporal fMRI constrained source analysis method. Similarly, Klein et al. (2015) published a study in 2015 focusing on the influence of the EEG on morphometric measurements of T1-weighted MRI data, recommending against using the structural images obtained during simultaneous EEG-MRI recordings for further anatomical data analysis, despite the benefit of time and as long as no final solution is found for correcting the artifacts caused by the EEG setup.

From electrons to photons: Magnetic resonance imaging combined with optical imaging as a readout

The scientific community is experiencing a replacement of electrophysiological techniques by optical techniques, mainly because optical imaging offers greater advantages in probing neural activity in terms of both spatial resolution and target specificity by means of genetic approaches (Luo et al., 2008). While electrophysiology is spatially limited (only able to record electrical signals from neurons within a circumscribed brain region surrounding the recording electrodes), optical imaging allows simultaneous recordings from a whole neuronal population of interest at high spatial resolution. Contrary to electrophysiological recordings, optical imaging allows to record neuronal activity without invasive contact with the tissue because light can be transmitted through. Most optical imaging methods make use of (fluorescent) reporters to record neural activity, which, in the last decade, have been subject to continuous improvements. Ultimately, optical approaches have gained use over electrophysiological approaches, revolutionizing research into neuronal activity. Optical measurements of membrane voltage [e.g., *via* voltage-sensitive dyes (VSDs) or *via* genetically encoded voltage sensors (GEVIs)] is however, limited by averaging. Consequently, the detection of single action potentials through optical reporters is still challenging. It is also possible to perform label-free optical imaging of the membrane potential, avoiding the need for exogenous chromophores. However, this technique is still

at an early stage, though first demonstrated 70 years ago, and is challenged by the relatively small signals generated by the intrinsic optical properties (Lee et al., 2019). Instead of membrane voltage, intracellular calcium changes can be monitored using fluorescent calcium-sensitive dyes as an indirect measure of neural activity (see Calcium signal as a readout of neuronal activity: Magnetic resonance imaging and fiber-optic calcium recordings). Another complementary technique is intrinsic (signal) optical imaging, which allows scientists to indirectly record cortical neural activity by measuring hemodynamic changes in the brain, and is thus based on the NVC like fMRI (Morone et al., 2017). This method also avoids the need for a fluorescent reporter and there is no need for a cranial window or thinning the skull in small animals. However, these intrinsic signals are much weaker than changes measured through the skull with calcium indicators and have lower spatial resolution. The temporal resolution is limited by the hemodynamic response (Juavinett et al., 2017).

For simultaneous readouts with functional MRI, fiber photometry is ideally suited. An optical fiber can guide the laser beam into the MR bore, while the signal is detected by equipment placed outside of the magnetic field, so that the two methods do not interfere with each other. An array of fibers can be implanted so as to target multiple brain regions of interest (Sych et al., 2019). An important pitfall to be aware of however, is potential heating caused by the laser. This heating can impact the MR signals causing T1 and T2* changes (Christie et al., 2013). Schmid et al. executed control experiments to rule out heat-induces apparent BOLD signal upon stimulation with blue light and propose this may be used as a standard control experiment in opto-fMRI. Occurrence of apparent BOLD is dependent on the energy deposited in the tissue, which is determined by the intensity, duration, and frequency of the stimulation pulses (Schmid et al., 2017). Further things to consider are light propagation in tissue becoming diffusive and therefore losing spatial information (Ioanas et al., 2022b), and correction for absorption of fluorescence light by blood (Zhang et al., 2021).

Opto-fMRI of excitatory vs. inhibitory neurons has also deepened our understanding of BOLD itself. It is assumed that the BOLD fMRI response reflects changes in excitatory neural activity. However, the contribution of inhibitory neurons to BOLD fMRI is unclear. The group of Seong Gi-Kim has published some interesting work in this regard. They selectively modulated inhibitory and excitatory neuronal activity in the somatosensory cortex by 20-s optogenetic stimulation of VGAT-ChR2 and CaMKII-ChR2 mice, respectively, to provide insights into the neurovascular coupling of excitatory and inhibitory neurons and the interpretation of BOLD fMRI signals (Moon et al., 2021). One of their other studies provides useful insights into how perfusion signals of different epileptic states are related in terms of NVC by conducting real-time *in vivo* measurements of cerebral blood flow (CBF), vessel diameter, and excitatory and inhibitory neuronal calcium signals during recurrent focal seizures (Lim et al., 2021).

Calcium signal as a readout of neuronal activity: Magnetic resonance imaging and fiber-optic calcium recordings

Calcium is a reporter of neuronal activity: changes in intracellular calcium concentration reflect changes in voltage membrane (Grienberger and Konnerth, 2012). Calcium is an important second messenger in eukaryotic cells and it is of central importance to mammalian neurons (Brini et al., 2014). In fact, it plays a crucial role in several neuronal mechanisms at different levels: presynaptically, calcium influx determines the release of neurotransmitter packed in synaptic vesicles (Neher and Sakaba, 2008); postsynaptically, a temporary increase of calcium at the level of the dendritic spines is responsible for activity-dependent synaptic plasticity (Zucker, 1999). Calcium ions are also involved in the regulation of gene transcription at the subcellular level (Lyons and West, 2011). As opposed to fMRI, calcium indicators provide an accurate and direct measure of neuronal activity with a high signal to noise ratio. More specifically, neuronal activity is measured as changes in the intracellular calcium concentration reflected by altered emitted fluorescence of the calcium indicator (Wachowiak et al., 2002).

Calcium indicators may be classified into three different types, each one characterized by distinct features: (1) the bioluminescent calcium indicator aequorin (Ohmiya and Hirano, 1996); (2) chemical calcium indicators; (3) genetically encoded calcium indicators (GECIs). The bioluminescent calcium indicator aequorin is extracted from marine organisms. When calcium binds its calcium binding sites, aequorin undergoes a conformational change that results in the emission of a photon (Ohmiya and Hirano, 1996). This calcium indicator does not require external illumination, thus providing several advantages including avoidance of phototoxicity, photobleaching, autofluorescence, and induction of light-dependent biological processes. On the other hand, aequorin can perform only one photon emission per cycle and it has to be loaded into single cells using a micropipette. Moreover, aequorin does not represent the best choice in terms of quantum yield and protein stability. On the contrary, chemical calcium indicators (e.g., Fluo-3, Calcium Green-1, and Oregon Green BAPTA) can be loaded into the brain with different approaches such as multicell bolus loading (Stosiek et al., 2003; Schulz et al., 2012) and bulk electroporation (Nagayama et al., 2007). Moreover, there are several types of chemical calcium indicators with differential calcium affinity and spectral properties that can be simultaneously used. The last category, GECIs (e.g., GCaMP6, RCaMP) entered the stage of calcium imaging more

than a decade ago and are currently widely used in neuroscience. They are characterized by high target specificity since they can exclusively be expressed in neuronal subpopulations of interest by means of viral constructs injected into brain areas of choice. Compared with chemical indicators (Paredes et al., 2008), they show reduced toxicity and are functional in neurons for longer periods of time, thus making them most suitable for longitudinal studies (Grienberger and Konnerth, 2012).

Calcium-based optical fiber photometry allows to investigate circuit-specific activity dynamics recording bulk changes in calcium fluorescence signals in genetically defined neurons in a relatively simple and artifact-free manner through an optical fiber implanted in the animal's head (Schlegel et al., 2018). Proper fiber implantation is important for the success of the recordings. Because of the optical fiber, this technique allows to penetrate deeper brain regions (subcortical regions) in comparison with the older two-photon calcium imaging but at the same time it lacks in cellular resolution. To overcome this limitation, it can be alternatively combined with two-photon microscopy that, on the contrary, gives excellent spatial resolution (Resendez and Stuber, 2015). Two-photon-imaging in combination with novel calcium indicators (e.g., GCamp7) allows the recording of large networks of neurons (hundreds of cells) with high timing accuracy (single spike detection), yet in a complementary manner rather than simultaneously. Unlike electrophysiology, it does not require MRI sensitive components such as metal wires, hence it does not interfere with fMRI acquisition due to the lack of radiofrequency interference. fMRI and calcium-based optical photometry can be combined to correlate neuronal activity of specific neuronal networks to whole-brain activity and functional connectivity (Yu, 2017; **Figure 3**). Recently, MRI-compatible microscopes are being developed for optical readout during fMRI with the potential to provide a resolution superior to MR resolution and to highlight particular structures (Wapler et al., 2021).

To date, calcium-based optical fiber photometry represents an important milestone in the study of the correlation between neuronal activity and hemodynamics determining the BOLD signal.

The first paper reporting *in vivo* studies using calcium indicators in mammals (GCaMP3) was published in 2009 (Tian et al., 2009). Subsequently, many studies have been published using fiber photometry in combination with other techniques (e.g., fMRI, optogenetics), expanding the palette of multimodal imaging techniques. Schulz et al. (2012) demonstrated the feasibility of coupling fiber-optic calcium recording and fMRI to simultaneously acquire calcium-specific fluorescence emitted by chemical calcium indicators (OGB-1, Rhod-2, and Fluo-4) and BOLD signals in a forepaw stimulation paradigm and to reveal the complexity of the BOLD signal that involves not only neuronal but also glial activity. A similar approach was used by Schmid et al. (2016), who additionally manipulated neuronal activity with optogenetics. Independent of the type of stimulation (sensory or optogenetic), the calcium response was identical.

A major disadvantage of calcium dyes as opposed to GECIs is that longitudinal studies are more challenging due to their shorter decay time, loading approach and limited cell-type specificity. To overcome these limiting factors, it is possible to use GECIs and in particular, the improved generation of GECIs (Chen et al., 2013). Liang et al. (2017) used an improved version of GECIs, namely GCaMP6f, to demonstrate the feasibility of simultaneous calcium and BOLD signals recordings in order to elucidate the neural basis of the BOLD signal. The adopted approach was validated with a visual stimulation paradigm: upon visual stimulation, a robust increase of calcium and BOLD signals was detected. The importance of this study relies on the establishment of a setup that allows longitudinal and simultaneous GCaMP6-based fiber photometry and fMRI in rats, thus setting new perspectives to investigate the NVC. Recently, even more insights into the BOLD signal have been revealed by coupling fiber-optic calcium recordings to fMRI. He and colleagues have developed single-vessel resting-state fMRI to delineate vessel-specific fluctuations in the BOLD signal (He et al., 2018). Combining this technique with simultaneous intracellular calcium recordings, they have been able to investigate whether neuronal activity is correlated with fluctuations in the cerebral vasculature. This method has allowed to determine the temporal dynamic features of neurovascular fluctuations and to define the spatial distribution of these fluctuations in the BOLD signal in the neurovascular network. The data show that neural activity and intrinsic vascular fluctuations are correlated. Although emerging evidence suggests that the hemodynamic response function (HRF) can vary by brain region and species, a single, canonical, human-based HRF is widely used in animal studies. Therefore, the development of flexible, accessible, brain-region specific HRF calculation approaches is paramount as hemodynamic animal studies become increasingly popular. Chao et al. calculated empirical HRFs for various rat brain regions, by simultaneously measuring neuronal activity *via* GECI GCaMP6f, local cerebral blood volume (CBV) from intravenous Rhodamine B dye, and whole brain CBV *via* fMRI with the Feraheme contrast agent. Empirical HRFs were calculated with GCaMP6f and Rhodamine B recordings from rat brain regions during resting-state and task-based paradigms, resulting in each HRF faster and narrower than the canonical HRF and no significant difference between these regions. When used in general linear model analyses of corresponding fMRI data, the empirical HRFs showed better detection performance than the canonical HRF (Chao et al., 2022).

It is evident that a multimodal approach in which fMRI is simultaneously coupled with calcium optical fiber recording is of exceptional utility and validity. Last but not least, the use of simultaneous fMRI and GCaMP-mediated Ca^{2+} optical fiber recording has allowed to discover the role of the astrocytic Ca^{2+}

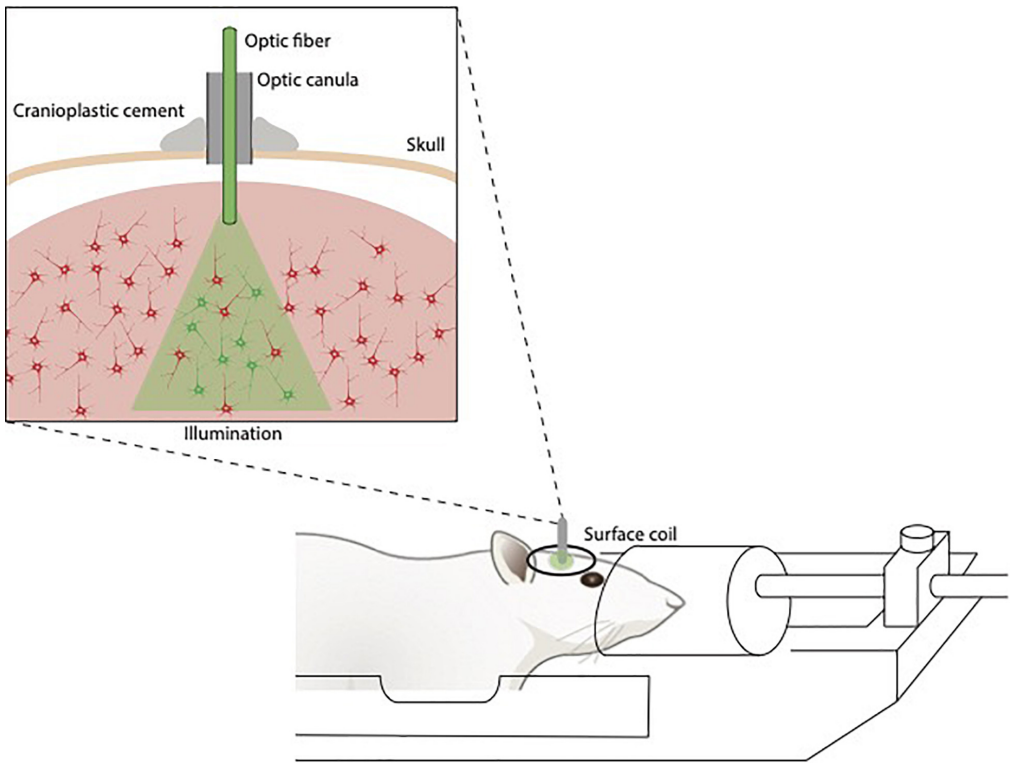

FIGURE 3
Illustration of fiberoptics/fMRI setup. The optic fibers are implanted above the opsin/calcium indicator-stained area, fixed to the skull, guided through the coil and connected to the stimulation/detection unit.

		fMRI	fMRI + Electrophysiology	Opto-fMRI	fMRI + Calcium-based optical fiber photometry	Simultaneous opto-fMRI and Calcium-based optical fiber photometry
Invasiveness		Non invasive	Invasive	Invasive	Invasive	Invasive
Longitudinal		Yes	Depending on chronic implant	Depending on chronic implant	Depending on chronic implant	Depending on chronic implant
Resolution	**Spatial**	High (whole brain 3D)	Localized	Localized	Localized	Localized
	Temporal	Low	High	Low (fMRI)	Limited (fast-spiking neurons)	
Target		Indirect • Neuronal activity	Direct • Multi- and single unit activity	Direct • Modulation targeted neuronal populations	Direct • Deep brain region neuronal activity	Direct • Modulation targeted neuronal populations • Neuronal activity recording
EM interference		Susceptible	Susceptible	None	None	None
Signal		Within a voxel (All vasculature contributing)	Not averaged/Averaged depending on electrode impedance	Within voxel	Averaging	Averaging
MRI Compatibility			Must be ensured	Must be ensured	Must be ensured	Must be ensured
Pitfalls			• Interference correction	• Fiber implantation • Laser power • Opsin's expression • Heating artifacts • Light propagation	• Fiber implantation • GECI expression • Hemodynamic artifacts	• Fiber implantation • Laser power • Opsin/GECI expression • Spectra overlap • Fiber saturation

FIGURE 4
Comparative overview of specifications for multimodal imaging approaches.

signal in the modulation (vasodilatation/constriction) of the neurovascular network and its influence on thalamic regulation of cortical states. Interestingly, it has been found that sensory-evoked and intrinsic astrocytic Ca^{2+} signals were, respectively, coupled with positive and negative BOLD signals, giving rise to specific NVC events (Wang et al., 2018). In this regard, the work of Lake et al. is of interest as well, highlighting MR-compatible optical calcium imaging approached by concurrent wide-field optical and functional MRI (Lake et al., 2020). Pais-Roldán et al. (2020) went a step further to combine both simultaneous fMRI and fiber-optic calcium recordings with pupillometry to enable tracking of brain-state dependent pupil dynamics and identifying unique cross-scale neuronal dynamic patterns under anesthesia. This study suggested that the pupil dynamics observed during anesthesia in rats are directly linked to the global fMRI signal fluctuation, as well as to the cortical population activity observed as neuronal calcium transient oscillations, and perfectly exemplifies the successful combination of imaging modalities. A recent study consisting fiber-based optical recordings in animals expressing the genetically encoded calcium sensor Twitch-2B combined with fMRI elucidated the pitfall of hemodynamic artifacts and how to correct them (Lambers et al., 2022). The authors identified prominent effects of hemodynamic artifacts in the timecourses of fluorescence and fMRI signals and applied an MR parameter-based correction algorithm to yield results consistent with expected signal changes.

In recent years, the development of multimodal nanoprobes has been growing. An example of these nanostructures is a bimodal system based on quantum dots and low molecular weight Gd^{3+} chelates, prepared for MRI and optical analyses (Albuquerque et al., 2021). Non-covalent nanosystems range in size from 7 to 160 nm, and a relaxivity value of 4.5 (at 1.5 T) to 31.5 (at 35 MHz) $mM^{-1}s^{-1}$ per Gd^{3+}. Covalent nanosystems can range from 8 to 45 nm diameter, and relaxivity values from 1.6 (at 3 T) to 24 (at 1.5 T) $mM^{-1}s^{-1}$ per Gd^{3+}. It can be concluded that the preparation method is independent of both the final nanoprobe size and their relaxivity values. Studies about the nanoprobe stability and inertness in the presence of endogenous metals in mammals are still required.

Neural perturbation: Combining magnetic resonance imaging with neuronal excitation or inhibition

Electrical stimulation

While electrical neural activity can be probed by means of electrophysiology as described above, targeted brain regions can also be stimulated through electrodes in a technique known as deep brain stimulation (DBS). DBS has developed over the last 20 years into a highly effective evidenced-based treatment option for neurological disorders. Moreover, it has become a fascinating tool to provide illustrative insights into the functioning of brain networks. Similar to electrophysiological recordings, brain stimulation is achieved by means of stereotactically implanting electrodes into specific targets in the brain, and delivering constant or intermittent electric currents from an implanted battery source (Gonzalez-Escamilla et al., 2020).

Non-invasive brain circuit tracing, using fMRI, allows the exploration of direct clinical effects of DBS. However, fMRI studies on patients implanted with DBS electrodes are limited because of safety concerns and imaging artifacts (Tagliati et al., 2009; Kahan et al., 2015), therefore, animal models typically are used with these aims. A technique by Tolias et al. (2005) to record brain activity using the blood oxygen level dependent (BOLD) signal while applying electrical microstimulation to the primate brain, demonstrated its utility in uncovering *in vivo* functional connectivity maps.

In non-human primates, subthalamic nucleus (STN)-DBS increases BOLD activation in the sensorimotor cortex, supplementary motor area, caudate nucleus, pedunculopontine nucleus, cingulate, insular cortex, and cerebellum (Min et al., 2014). Similarly, increased BOLD responses in motor, somatosensory, and cingulate cortices to STN- and internal global pallidus (GPi)-DBS are found in rats (Lai et al., 2014). In pigs, DBS targeting of the STN and the entopeduncular nucleus, the non-primate analogue of the primate GPi, induces increased BOLD activity in the ipsilateral sensorimotor network, including the premotor, primary motor, and primary somatosensory cortices, as well as dorsolateral prefrontal and anterior cingulate and insular cortices. The network activations showed differential, target-specific, non-motor network effects (Min et al., 2012).

Neurons can be stimulated electrically through metal or MRI compatible glass electrodes, but electrical stimulation is nonspecific regarding cell-type and allows to directly trigger neuronal activity only in single or a small group of neurons dependent on the position of the stimulating electrode.

Optogenetically modulating neuronal activity using light

In addition to neuronal activity measurements, light can also be used to modulate neuronal activation. More promising than the electrical stimulation described above is the relatively new technique known as optogenetics, which guarantees higher genetic, temporal and spatial specificity (Nagel et al., 2003; Zhang et al., 2007). The use of light is paving the way to a more specific and effective control and investigation of neuronal networks' activity.

Optogenetics represents a technique of choice to modulate neuronal activity using light. Its implementation results from the need to establish a method that can be used to pinpoint how different neuronal subtypes cooperate to carry out thoughts, feelings, movements and how their activity is affected in brain pathology. Optogenetics has revolutionized the field of neuroscience because it allows, as opposed to classical electrical brain stimulation techniques, a real-time direct optical manipulation of specific neuronal subtypes, ensuring both excellent spatial and temporal resolution in various animal models (Yizhar et al., 2011). For this technique, target cells are genetically modified to express light-activated ion channels like channelrhodopsins (ChR), halorhodopsin and light-gated ionotropic glutamate receptors (Lin, 2011). In this way, their activity can be triggered or inhibited by light on a millisecond time scale. Microbial opsins can be selectively expressed in target neurons using viral vectors (Yizhar et al., 2011). Optogenetics does have some possible caveats that should be taken into account when planning optogenetic experiments (Guru et al., 2015): (1) opsins' expression and light delivery is not uniform in all targeted neurons; (2) fiber placement is of importance: if the fiber is just slightly displaced, the success of the experiment could be impeded; (3) the delivered light indiscriminately modulates all the neurons of the targeted neuronal population, shadowing individual neuronal activity patterns; (4) opsins' expression can alter the physiological activity of neurons, including their cellular machinery due to the expression of "additional" ion channels in the cellular membrane; and (5) the specificity of light excitatory modulation can be impaired because direct delivery of light on the axonal membrane can also result in the excitation of terminals projecting to other brain areas which are not of interest.

Although the history of the methodological development can be traced to the 1970s, one of the most important milestones in the implementation of this technique was not achieved until 2005, when Karl Deisseroth's group conducted the expression of channelrhodopsin-2 (ChR2) in neuronal cells (rat hippocampal cultured cells) to identify light-evoked neuronal activity (Boyden et al., 2005). Nowadays, this breakthrough technique permits to achieve a virtually complete neural circuit mapping, thus providing a causal link between brain activity and behavior in healthy and pathological conditions (Tye and Deisseroth, 2012). From its appearance until now, implementation of optogenetics has been made much easier thanks to the growing literature dealing with several technical aspects of this technique such as opsins' choice, light source (lasers, LEDs) and delivery (intensity, depth of illumination), genetic targeting specificity and stimulation/inhibition protocols.

Optogenetics can be combined with fMRI resulting in what is known as optogenetic fMRI (opto-fMRI). Opto-fMRI combines the precision of optogenetic manipulation and the high spatial resolution at the whole-brain level of fMRI that enable the examination of activity and functional connectivity of specific neural networks at the whole-brain level without electromagnetic interference with the radiofrequency signal. Opto-fMRI allows to indirectly measure neuronal activity in the whole brain at high spatial resolution, independently from the site of stimulation (Lee et al., 2010). Specifically, this method allows to determine the effects of activation/inhibition of a specific target neuronal population on whole-brain activity and functional connectivity. To combine both techniques, some precautions should be taken. Importantly, the optical fiber and implanted cannula used to deliver light into the brain must be MRI compatible. Further, the laser power and fiber implantation have to be carefully established to avoid false BOLD responses. In fact, a negative BOLD response has been observed in the area under the fiber tip during high laser power stimulations (Desai et al., 2011). In 2013, Christie and colleagues have again noticed that fMRI responses are influenced by laser power, which acts as a possible confounding factor in opto-fMRI studies. Indeed, prolonged (30s) blue light exposure of naïve brains of dead rats has caused a temperature increase and has impacted the MR signal in terms of temperature dependent changes in the relaxation times T1 and T2* (Christie et al., 2013).

While taking these caveats into consideration, some important research has been done using opto-fMRI. Lee et al. (2010) published a paper that has proven that optogenetics can be used together with high-field MRI to study the BOLD signal evoked by optical stimulation of specific brain areas in anesthetized rats. In particular, opto-fMRI was used to explore the role of local excitatory neurons in the induction of the BOLD signal. To this aim, ChR2 was expressed under regulation of the Ca2+/calmodulin-dependent protein kinase II (CAMKII) promoter in the primary motor cortex (M1) of adult rats by means of an AAV vector. Upon optical stimulation, light-activated neurons elicited a BOLD response not only in the illuminated area (M1) but also in the non-optically stimulated thalamus. This study is important not only for its findings related to the nature of the BOLD signal but also because it underlines crucial features characterizing opto-fMRI. The most relevant is the opportunity to globally map the effect of the manipulation (light stimulation) of a specific neuronal population on the whole-brain activity in rodents, rendering information about the networks recruited by local neuronal populations.

Abe et al. (2012) used opto-fMRI in a 2012 study to explore the neuronal connectivity of the hippocampal formation utilizing a rat strain that expressed ChR2-venus protein. After optical stimulation at the dentate gyrus, they obtained a BOLD response not only in the dentate gyrus, but also in CA3, and they also detected the longitudinal-axis activation of the hippocampal formation. The authors state that these results may accelerate the search for dynamical functional brain mapping, as well as increasing our understanding of hippocampal networks. More importantly though, it further establishes opto-fMRI as a powerful tool for neuroscience.

More recently, Christie et al. (2017) conducted the first three-dimensional study of spatial correlations of NVC using single pulse opto-fMRI, a technique based on the delivery of only one brief and short light stimulus. This approach ensures (1) a well-defined modulation of the volume of activated neurons in a determined brain region, spatially confining the recruitment of neural activity; (2) minimization of vascular and neuronal adaptation; and (3) prevention of heating artifacts. It provides a unique view of the spatial features of the NVC. ChR2 was expressed in cortical glutamatergic neurons of anesthetized rats, which then were illuminated with a single 10 ms pulse of blue light (inter-stimulus interval 20 s) of gradually increasing intensities to manipulate the spatial extent of the stimulus. Simultaneously, a 3D-mapping of functional hyperemia was done in order to estimate the volume of neural and hemodynamic correlations. As previously reported (Leithner and Royl, 2014), the spatial extent of the BOLD response is way more extended than the estimated volume of neuronal activation. However, a major limitation was that the spatial extent of neuronal activation was not directly measured but only estimated on the basis of the scattering and absorption features of blue light in the brain. A very recent study by the Grandjean group used opto-fMRI to show enhanced fMRI signal within several projection areas following optogenetic activation of the entorhinal cortex 3xTgAD mice (Mandino et al., 2022).

A major hurdle for making full use of the versatility of optogenetics, and thus of opto-fMRI, and GECI, is the application in species with low or no availability of transgenic lines in species such as primates (Gerits and Vanduffel, 2013). The highly flexible Cre-LoxP/adeno-associated viral (AAV) vector delivery method is usually dependent of transgenic lines expressing Cre recombinase under the desired cell-type-specific promoter, or alternatively of co-injection of an AAV vector expressing Cre recombinase under the desired cell-type-specific promoter (Gompf et al., 2015). Large libraries of such transgenic lines are available for rat and mouse models (Han, 2012), yet for other animal models there is no comparable availability, and consequently, opto-fMRI applications in these settings generally make use of more unwieldy custom lentiviral vectors, as well as close consideration of the trade-off between promoter length and expression characteristics.

One key feature of optogenetics is the ability to selectively modulate cells closely relevant to specific neurotransmitter systems. Prominent studies of neurochemical systems with fMRI include dopamine modulation (Decot et al., 2017; Lohani et al., 2017; Ioanas et al., 2022a), with findings suggesting that large-scale brain-wide activity dynamics, measured across many distinct neuroanatomical regions, are also directly or indirectly regulated by the activity of VTA dopaminergic neurons *in vivo* (Decot et al., 2017), and that mesolimbic and non-limbic basal ganglia dopamine circuits are functionally connected (Lohani et al., 2017). Ioanas et al. (2022a) present a comprehensive assay producing the first whole-brain opto-fMRI map of dopaminergic activation in the mouse, and show that VTA dopaminergic system function is consistent with its structural VTA projections.

New frontiers in small animal imaging: Simultaneous fiber-optic calcium recordings and opto-functional magnetic resonance imaging

While technically challenging, it is possible to combine fiber-optic calcium imaging together with opto-fMRI to simultaneously modulate genetically targeted neuronal populations, record their neuronal activity and acquire whole-brain activity and functional connectivity data. This would be utterly difficult with electrophysiology instead of calcium imaging/optogenetics because it does not allow to record or modulate neuronal activity from hundreds of genetically identified neurons at the same time. As previously discussed for opto-fMRI and fiber-optic calcium recordings combined with fMRI, all the set-up components must be MRI compatible or at least positioned outside the scanner room. Importantly, both opsins and calcium indicators need to have non-overlapping spectra in order to avoid potential cross-talk (Akerboom et al., 2013). If optogenetics and fiber-optic calcium recordings are performed in the same brain area using the same excitation wavelength, the detecting fiber can be saturated by fluorescence. This phenomenon can be prevented in two ways: by using different wavelengths for opsin and calcium indicators or by spatially separating the area of the opsin's excitation and the region of neuronal activity detection (e.g., the light used to excite the opsin is delivered in the medial septum and the detection of calcium indicators' fluorescence is done in the hippocampus). If the second solution is adopted, the excitatory fiber and the detecting fiber have to be precisely positioned to ensure that excitation and detection happen in their exact locations. Further, before starting the experiment, the laser power has to be defined in order to avoid tissue heating and false MRI signal. The stimulation duration is important as well: while short pulses (in the order of millisecond) are sufficient to activate opsins such as ChR2, a longer stimulation is required for BOLD measurements. It has been demonstrated that a BOLD response can be evoked by a single 10 ms pulse of excitatory light (Christie et al., 2017) or with consecutive shorter pulses (1 ms) lasting several seconds (Albers et al., 2018). Chen X. et al., 2019 verified the multi-modal fMRI platform in combination with both optogenetic stimulation and simultaneous Ca^{2+} recordings to map optogenetically-driven single-vessel fMRI with concurrent neuronal calcium recordings in the rat hippocampus. By implementing simultaneous optogenetic single-vessel fMRI and optical fiber Ca^{2+} recordings, distinct hemodynamic spatiotemporal patterns across the hippocampal vasculature could be directly characterized based on concurrent neuronal

Ca^{2+} signals for the first time. It is worth noting that in labs with a specialized infrastructure, it is possible to monitor the positioning of the optical fiber with MRI feedback to ensure that the recording or stimulation is done in the optimal place. In this regard, Chen et al. described an MRI-guided robotic arm as a flexible positioning system to assist optical fiber brain intervention in real time in a study involving optogenetic fMRI with concurrent Ca2+ recording (Chen Y. et al., 2019).

Perturbation of neural activity using chemogenetics

Altered neural signaling can also be achieved using a chemogenetic approach, the most commonly used being Designer Receptors Exclusively Activated by Designer Drugs or DREADDs. DREADDs are extremely useful research tools that allow a targeted manipulation of certain pathways in the brain. DREADDs are genetically modified G protein coupled receptors (GPCRs) that only respond to an exogenous drug and not to any endogenous molecule, activating one of three major GPCR signaling pathways, ultimately leading to activation or inhibition of the DREADD-expressing cells. Using DREADDs, one can unravel the specific role of different pathways in the brain. Compared with optogenetics, DREADDs have the advantage that they can be activated by systemic administration of a pharmacological compound and that they have less temporal restrictions, which renders them more attractive for therapeutic purposes. Although the temporal precision and control of chemogenetics is lower than optogenetics, it has been proven to be an invaluable tool in modern neuroscience allowing cell-type-specific modulations, bidirectional control of cells, and mapping of functional networks.

In vivo, DREADDs expression in specific cell types is typically achieved by using transgenic mouse models or focal viral vector injections targeting selected brain areas. Various transgenic mouse models have been developed to specifically express DREADDs in selected cell populations by using specific promoters (Guettier et al., 2009; Farrell et al., 2013), the transcriptional Tet-On/Off system (Alexander et al., 2019) or the Cre-recombinase system (Zhu et al., 2016). On the other hand, DREADDs can also be expressed using a completely virally mediated method. In this case, a viral construct is intracranially injected and the cellular transduction and expression of the DREADDs is determined by the viral vector's serotype (of genome and capsid) and promoter gene (Aschauer et al., 2013). After successful expression of the designer receptors, they can be activated by administration of a designer drug, such as clozapine-*N*-oxide [CNO, Armbruster et al. (2007)] or JHU37160 (Bonaventura et al., 2019).

Our lab has recently made progress studying targeted cholinergic stimulation in rodents using pharmacological fMRI (phMRI) (Peeters et al., 2020a,c). The study of this chemogenetic manipulation with phMRI is a method without any interference to the MRI hardware, as no external hardware is necessary for targeted brain stimulation. In literature, DREADDs stimulation combined with MRI has been used to capture the effect of selective activation of certain neuronal populations. Baslow et al. (2016) used functional magnetic resonance spectroscopy to evaluate alterations in local neuronal *N*-acetyl-aspartate as well as a BOLD fMRI to assess changes in neuronal activity. In this study, a viral delivery method was used to express excitatory hM3Dq-DREADDs in medial prefrontal cortex neurons. CNO injection elicited a focal decrease in the *N*-acetyl-aspartate signal and an increased BOLD response. In addition, local field potentials were recorded as a direct measure of neural activity and confirmed that CNO could increase neural activity through activation of hM3Dq, supporting the utility of DREADDs *in vivo* (Baslow et al., 2016). Roelofs et al. expressed hM3Dq receptors in the mesolimbic and mesocortical pathway in rats. Significantly increased BOLD responses were observed in the ventral tegmental area, nucleus accumbens, and medial prefrontal cortex after CNO injection. DREADDs stimulation not only induced activation in the mesocorticolimbic regions but also drove BOLD response alterations at the whole-brain level. In contrast to the altered neural activity, the functional connectivity remained stable after CNO injection (Roelofs et al., 2017). Giorgi et al. (2017) highlighted the advantage of chemogenetics combined with fMRI to causally link the activity of specific neuronal populations with whole-brain functional activity. The stimulation of serotonergic neurons upon CNO injection in transgenic mice expressing excitatory DREADDs in serotonergic neurons, resulted in a significantly increased relative cerebral blood volume in connected regions encompassing corticohippocampal and ventrostriatal regions while the administration of the selective serotonin reuptake inhibitor citalopram globally decreased the relative cerebral blood volume (Giorgi et al., 2017).

Another neurochemical system studied with a chemogenetic-fMRI approach is the norepinephrine system. Zerbi et al. (2019) used a mouse model to study the effect of locus coeroleus (LC) stimulation on large-scale functional connectivity and showed that LC activation rapidly interrupts ongoing behavior and strongly increases brain-wide connectivity, with the most profound effects in the salience and amygdala networks. Oyarzabal et al. (2022) reported that chemogenetic-induced tonic LC activity decreased cerebral blood volume (CBV) and glucose uptake and increased synchronous low-frequency fMRI activity within the frontal cortices of the DMN.

For a full review of the combination of chemogenetics with *in vivo* imaging modalities, we refer to Peeters et al., 2020b.

In contrast to optogenetics, chemogenetics allow for remote and longer lasting activation/inhibition of neuronal activity without the need for an optic fiber implantation. *In vivo* imaging will allow non-invasive, longitudinal monitoring of disease progression and therapy response in patients that will undergo DREADD-based neuromodulatory therapy.

Conclusion and future directions

Advancements in neuroscience and specifically in the investigation of NVC are essentially owed to the recent technical improvements developed in the field of multimodal MRI. Above all, a major role is played by the development and combination of techniques such as fMRI, optogenetics and fiber-optic calcium imaging that are able to efficiently manipulate not only individual cells, but also neuronal networks at a whole-brain resolution. **Figure 4** summarizes strengths and caveats that need to be considered when combining techniques in a simultaneous recording setup.

In short, if the main focus of the experiment is to acquire direct and not averaged recordings of neuronal activity of single neurons or at least a limited number of them, electrophysiology still remains the best choice, whereas if the scientist aims to investigate/modulate neuronal activity of genetically identified neuronal types at a network level, optical techniques are recommended. However, as is the case with any newly developed methodology, one must also be wary of the caveats. Recently, Christophe Bernard reviewed some confounding factors that should be taken into account when interpreting optogenetic effects (Bernard, 2020), such as brain dynamics, cell dynamics, possible perturbations by inserted channelrhodopsins, possibility of the light perturbing native proteins and modifications triggered by the viral vectors. We have to always be aware of what this means for data interpretation.

Today's systems neuroscientists face a choice. While the animals they study engage in some behavioral task, how should they monitor neural activity? Should they use electrodes? Should they introduce into their neurons of interest a molecule that will signal activity and image it? Should they monitor whole-brain activity or use localized techniques? The main goal of multimodal MRI is to simultaneously combine fMRI with other different methods to take advantage of their technical strengths while compensating for possible weaknesses. It represents a powerful tool to investigate the link between neuronal activity and vascular network dynamics from single cell or circuit level to the whole brain with a multiscale approach. Electrophysiology and MRI have been considered the opening chords of a revolution characterized by a shift from electrons to photons and from the application of single techniques (e.g., electrophysiology, fMRI) to the simultaneous combination of fMRI with techniques able to modulate and measure neuronal activity.

Although the described techniques complement each other well, additional technical improvements are critical. These advancements may pave the way for longitudinal brain imaging studies providing single-cell and network resolutions as well as specific control of neuronal activity. For example, a huge effort has been done to further improve the optogenetics' toolbox as well as the variety of calcium indicators. In fact, many variants of opsins (Lin, 2011; Lin et al., 2013) and calcium dyes (Zhao et al., 2011) have been developed. Currently, attention is focused on the development of red-shifted calcium indicators (Wu et al., 2013; Rose et al., 2014) that, unlike the blue emitting indicators: (1) can be expressed together with ChR2 or blue-emitting calcium indicators allowing multi-labeling without the risk of spectra overlapping; and (2) are characterized by reduced light scattering, thus giving higher tissue penetration with reduced excitation power. However, kinetics and spectral response remain to be improved.

A new frontier in deep brain stimulation using light is presented in the paper of Chen and colleagues where they have demonstrated the ability to perform deep brain stimulation using upconversion nanoparticles (UCNPs) (Chen et al., 2018). UCNPs are specialized nanoparticles able to upconvert the absorbed near-infrared (NIR) light to visible blue light. Innovative is the attempt to solve the invasiveness of inserting a laser in the brain to activate light-sensitive channels: targeted deep brain areas can be non-invasively stimulated through tissue-penetrating NIR light shined from outside the brain. Further, transgenic rodents have been generated to guarantee the cell-type specific expression of opsins (Zhao et al., 2011; Madisen et al., 2012) as well as of GECIs (Dana et al., 2014; Sato et al., 2015). The use of transgenic lines helps to overcome limitations characterizing the viral expression systems where gene delivery is mediated *via* brain injection of a viral vector, such as limited labeling of target neurons and problematic access of the virus to determined brain areas. Additionally, a more stable, reproducible and homogeneous expression over a longer period of time can be achieved. Even if these techniques are continuously improved as new technologies arise, there are still a few technical issues affecting multimodal imaging that need to be addressed in the near future to allow remarkable steps forward in the field of small animal imaging.

Author contributions

GK led the review. LK finalized the manuscript, undertook part of the systematic review, and designed the figures. SE drafted the first manuscript and undertook part of the systematic review. SM made critical comments on the manuscript and reviewed the final report. All authors contributed to the article and approved the submitted version.

Funding

This study was supported by the Research Foundation Flanders (FWO) (grant agreement G048917N to GK). SM was a postdoctoral fellow of the Research Foundation Flanders (FWO) (12W1619N).

Conflict of interest

The authors declare that the research was conducted in the absence of any commercial or financial relationships that could be construed as a potential conflict of interest.

The handling editor declared a past co-authorship with authors GK and SM.

Publisher's note

References

Abe, Y., Sekino, M., Terazono, Y., Ohsaki, H., Fukazawa, Y., Sakai, S., et al. (2012). Opto-fMRI analysis for exploring the neuronal connectivity of the hippocampal formation in rats. *Neurosci. Res.* 74, 248–255. doi: 10.1016/j.neures.2012.08.007

Akerboom, J., Calderón, N. C., Tian, L., Wabnig, S., Prigge, M., Tolö, J., et al. (2013). Genetically encoded calcium indicators for multi-color neural activity imaging and combination with optogenetics. *Front. Mol. Neurosci.* 6:2. doi: 10.3389/fnmol.2013.00002

Albers, F., Wachsmuth, L., van Alst, T. M., and Faber, C. (2018). Multimodal functional neuroimaging by simultaneous BOLD fMRI and fiber-optic calcium recordings and optogenetic control. *Mol. Imaging Biol.* 20, 171–182.

Albuquerque, G. M., Souza-Sobrinha, I., Coiado, S. D., Santos, B. S., Fontes, A., Pereira, G. A. L., et al. (2021). Quantum dots and Gd 3+ chelates: advances and challenges towards bimodal nanoprobes for magnetic resonance and optical imaging. *Top. Curr. Chem. (Cham)* 379:12. doi: 10.1007/s41061-021-00325-x

Alexander, S. P. H., Fabbro, D., Kelly, E., Mathie, A., Peters, J. A., Veale, E. L., et al. (2019). The concise guide to pharmacology 2019/20: enzymes. *Br. J. Pharmacol.* 176 Suppl 1(Suppl 1), S297–S396.

Armbruster, B. N., Li, X., Pausch, M. H., Herlitze, S., and Roth, B. L. (2007). Evolving the lock to fit the key to create a family of G protein-coupled receptors potently activated by an inert ligand. *Proc. Natl. Acad. Sci. U.S.A.* 104, 5163–5168. doi: 10.1073/pnas.0700293104

Aschauer, D. F., Kreuz, S., and Rumpel, S. (2013). Analysis of transduction efficiency, tropism and axonal transport of AAV serotypes 1, 2, 5, 6, 8 and 9 in the mouse brain. *PLoS One* 8:e76310. doi: 10.1371/journal.pone.0076310

Attwell, D., and Iadecola, C. (2002). The neural basis of functional brain imaging signals. *Trends Neurosci.* 25, 621–625.

Austin, V. C., Blamire, A. M., Grieve, S. M., O'Neill, M. J., Styles, P., Matthews, P. M., et al. (2003). Differences in the BOLD fMRI response to direct and indirect cortical stimulation in the rat. *Magn. Reson. Med.* 49, 838–847.

Barry, R. L., Conrad, B. N., Maki, S., Watchmaker, J. M., McKeithan, L. J., Box, B. A., et al. (2021). Multi-shot acquisitions for stimulus-evoked spinal cord BOLD fMRI. *Magn. Reson. Med.* 85, 2016–2026. doi: 10.1002/mrm.28570

Baslow, M. H., Cain, C. K., Sears, R., Wilson, D. A., Bachman, A., Gerum, S., et al. (2016). Stimulation-induced transient changes in neuronal activity, blood flow and N-acetylaspartate content in rat prefrontal cortex: a chemogenetic fMRS-BOLD study. *NMR Biomed.* 29, 1678–1687. doi: 10.1002/nbm.3629

Bernard, C. (2020). Optogenetics: keep interpretations light. *eNeuro* 7:ENEURO.0091-20.2020. doi: 10.1523/ENEURO.0091-20.2020

Blackrock Neurotech (2021). *MagRes Headstage IFU – Blackrock Neurotech*. Available online at: https://blackrockneurotech.com/downloads/magres-head-ifu/ [Accessed April 20, 2022].

Bonaventura, J., Eldridge, M. A. G., Hu, F., Gomez, J. L., Sanchez-Soto, M., Abramyan, A. M., et al. (2019). High-potency ligands for DREADD imaging and activation in rodents and monkeys. *Nat. Commun.* 10, 1–12. doi: 10.1038/s41467-019-12236-z

Boyden, E. S., Zhang, F., Bamberg, E., Nagel, G., and Deisseroth, K. (2005). Millisecond-timescale, genetically targeted optical control of neural activity. *Nat. Neurosci.* 8, 1263–1268.

Brini, M., Calì, T., Ottolini, D., and Carafoli, E. (2014). Neuronal calcium signaling: function and dysfunction. *Cell. Mol. Life Sci.* 71, 2787–2814.

Brinker, G., Bock, C., Busch, E., Krep, H., Hossmann, K. A., and Hoehn-Berlage, M. (1999). Simultaneous recording of evoked potentials and T2*-weighted MR images during somatosensory stimulation of rat. *Magn. Reson. Med.* 41, 469–473. doi: 10.1002/(sici)1522-2594(199903)41:3<469::aid-mrm7>3.0.co;2-9

Buxton, R. B., and Frank, L. R. (1997). A model for the coupling between cerebral blood flow and oxygen metabolism during neural stimulation. *J. Cereb. Blood Flow Metab.* 17, 64–72. doi: 10.1097/00004647-199701000-00009

Canals, S., Beyerlein, M., Merkle, H., and Logothetis, N. K. (2009). Functional MRI evidence for LTP-induced neural network reorganization. *Curr. Biol.* 19, 398–403. doi: 10.1016/j.cub.2009.01.037

Chance, B., Cohen, P., Jobsis, F., and Schoener, B. (1962). Intracellular oxidation-reduction states in vivo. *Science* 137, 499–508.

Chao, T. H. H., Chen, J. H., and Yen, C. T. (2014). Repeated bold-fMRI imaging of deep brain stimulation responses in rats. *PLoS One* 9:e97305. doi: 10.1371/journal.pone.0097305

Chao, T. H. H., Zhang, W. T., Hsu, L. M., Cerri, D. H., Wang, T. W. W., and Shih, Y. Y. I. (2022). Computing hemodynamic response functions from concurrent spectral fiber-photometry and fMRI data. *Neurophotonics* 9:032205. doi: 10.1117/1.NPh.9.3.032205

Chen, S., Weitemier, A. Z., Zeng, X., He, L., Wang, X., Tao, Y., et al. (2018). Near-infrared deep brain stimulation via upconversion nanoparticle-mediated optogenetics. *Science* 359, 679–684. doi: 10.1126/science.aaq1144

Chen, T. W., Wardill, T. J., Sun, Y., Pulver, S. R., Renninger, S. L., Baohan, A., et al. (2013). Ultrasensitive fluorescent proteins for imaging neuronal activity. *Nature* 499, 295–300.

Chen, X., Sobczak, F., Chen, Y., Jiang, Y., Qian, C., Lu, Z., et al. (2019). Mapping optogenetically-driven single-vessel fMRI with concurrent neuronal calcium recordings in the rat hippocampus. *Nat. Commun.* 10:5239. doi: 10.1038/s41467-019-12850-x

Chen, Y., Pais-Roldan, P., Chen, X., Frosz, M. H., and Yu, X. (2019). MRI-guided robotic arm drives optogenetic fMRI with concurrent Ca 2+ recording. *Nat. Commun.* 10:2536. doi: 10.1038/s41467-019-10450-3

Christie, I. N., Wells, J. A., Kasparov, S., Gourine, A. V., and Lythgoe, M. F. (2017). Volumetric spatial correlations of neurovascular coupling studied using single pulse opto-fMRI. *Sci. Rep.* 7:41583. doi: 10.1038/srep41583

Christie, I. N., Wells, J. A., Southern, P., Marina, N., Kasparov, S., Gourine, A. V., et al. (2013). fMRI response to blue light delivery in the naïve brain: implications for combined optogenetic fMRI studies. *Neuroimage* 66, 634–641. doi: 10.1016/j.neuroimage.2012.10.074

Dana, H., Chen, T. W., Hu, A., Shields, B. C., Guo, C., Looger, L. L., et al. (2014). Thy1-GCaMP6 transgenic mice for neuronal population imaging in vivo. *PLoS One* 9:e108697. doi: 10.1371/journal.pone.0108697

David, O., Guillemain, I., Saillet, S., Reyt, S., Deransart, C., Segebarth, C., et al. (2008). Identifying neural drivers with functional MRI: an electrophysiological validation. *PLoS Biol.* 6:2683–2697. doi: 10.1371/journal.pbio.0060315

Decot, H. K., Namboodiri, V. M. K., Gao, W., McHenry, J. A., Jennings, J. H., Lee, S. H., et al. (2017). Coordination of brain-wide activity dynamics by dopaminergic neurons. *Neuropsychopharmacology* 42:615. doi: 10.1038/npp.2016.151

Desai, M., Kahn, I., Knoblich, U., Bernstein, J., Atallah, H., Yang, A., et al. (2011). Mapping brain networks in awake mice using combined optical neural control and fMRI. *J. Neurophysiol.* 105, 1393–1405. doi: 10.1152/jn.00828.2010

Duffy, B. A., Choy, M. K., Chuapoco, M. R., Madsen, M., and Lee, J. H. (2015). MRI compatible optrodes for simultaneous LFP and optogenetic fMRI investigation of seizure-like afterdischarges. *Neuroimage* 123, 173–184. doi: 10.1016/j.neuroimage.2015.07.038

Farrell, M. S., Pei, Y., Wan, Y., Yadav, P. N., Daigle, T. L., Urban, D. J., et al. (2013). A Gαs DREADD mouse for selective modulation of cAMP production in striatopallidal neurons. *Neuropsychopharmacology* 38, 854–862. doi: 10.1038/npp.2012.251

Galvani, L. (1791). *De viribus Electricitatis In Motu Musculari Commentarius*. Bologna: Typographia Instituti Scientiarium.

Gerits, A., and Vanduffel, W. (2013). Optogenetics in primates: a shining future? *Trends Genet.* 29, 403–411.

Giorgi, A., Migliarini, S., Galbusera, A., Maddaloni, G., Mereu, M., Margiani, G., et al. (2017). Brain-wide mapping of endogenous serotonergic transmission via chemogenetic fMRI. *Cell Rep.* 21, 910–918. doi: 10.1016/j.celrep.2017.09.087

Girouard, H., and Iadecola, C. (1985). Neurovascular coupling in the normal brain and in hypertension, stroke, and Alzheimer disease. *J. Appl. Physiol.* 100, 328–335.

Goense, J. B. M., and Logothetis, N. K. (2008). Neurophysiology of the BOLD fMRI signal in awake monkeys. *Curr. Biol.* 18, 631–640.

Gompf, H. S., Budygin, E. A., Fuller, P. M., and Bass, C. E. (2015). Targeted genetic manipulations of neuronal subtypes using promoter-specific combinatorial AAVS in wild-type animals. *Front. Behav. Neuroscienc.* 9:152. doi: 10.3389/fnbeh.2015.00152

Gonzalez-Escamilla, G., Muthuraman, M., Ciolac, D., Coenen, V. A., Schnitzler, A., and Groppa, S. (2020). Neuroimaging and electrophysiology meet invasive neurostimulation for causal interrogations and modulations of brain states. *Neuroimage* 220:117144. doi: 10.1016/j.neuroimage.2020.117144

Grienberger, C., and Konnerth, A. (2012). Imaging calcium in neurons. *Neuron* 73, 862–885.

Guettier, J. M., Gautam, D., Scarselli, M., de Azua, I. R., Li, J. H., Rosemond, E., et al. (2009). A chemical-genetic approach to study G protein regulation of beta cell function in vivo. *Proc. Natl. Acad. Sci. U.S.A.* 106, 19197–19202. doi: 10.1073/pnas.0906593106

Guru, A., Post, R. J., Ho, Y. Y., and Warden, M. R. (2015). Making sense of optogenetics. *Int. J. Neuropsychopharmacol.* 18:yv079.

Han, X. (2012). In vivo application of optogenetics for neural circuit analysis. *ACS Chem. Neurosci.* 3, 577–584.

He, Y., Wang, M., Chen, X., Pohmann, R., Polimeni, J. R., Scheffler, K., et al. (2018). Ultra-slow single-vessel bold and cbv-based FMRI spatiotemporal dynamics and their correlation with neuronal intracellular calcium signals. *Neuron* 97, 925–939.e5. doi: 10.1016/j.neuron.2018.01.025

Hubel, D. H. (1957). Tungsten microelectrode for recording from single units. *Science* 125, 549–550.

Ingvar, D. H., and Lassen, N. A. (1962). Regional blood flow of the cerebral cortex determined by krypton85. *Acta Physiol. Scand.* 54, 325–338. doi: 10.1161/01.str.15.6.1017

Ioanas, H. I., Schlegel, F., Skachokova, Z., Schroeter, A., Husak, T., and Rudin, M. (2022b). Hybrid fiber optic-fMRI for multimodal cell-specific recording and manipulation of neural activity in rodents. *Neurophotonics* 9: 032206. doi: 10.1117/1.NPh.9.3.032206

Ioanas, H. I., Saab, B. J., and Rudin, M. (2022a). Whole-brain opto-fMRI map of mouse VTA dopaminergic activation reflects structural projections with small but significant deviations. *Transl. Psychiatry* 12:60. doi: 10.1038/s41398-022-01812-5

Jaime, S., Cavazos, J. E., Yang, Y., and Lu, H. (2018). Longitudinal observations using simultaneous fMRI, multiple channel electrophysiology recording, and chemical microiontophoresis in the rat brain. *J. Neurosci. Methods* 306, 68–76. doi: 10.1016/j.jneumeth.2018.05.010

Jöbsis, F. F. (1977). Noninvasive, infrared monitoring of cerebral and myocardial oxygen sufficiency and circulatory parameters. *Science* 198, 1264–1266. doi: 10.1126/science.929199

Jonckers, E., Shah, D., Hamaide, J., Verhoye, M., and van der Linden, A. (2015). The power of using functional fMRI on small rodents to study brain pharmacology and disease. *Front. Pharmacol.* 6:231. doi: 10.3389/fphar.2015.00231

Juavinett, A. L., Nauhaus, I., Garrett, M. E., Zhuang, J., and Callaway, E. M. (2017). Automated identification of mouse visual areas with intrinsic signal imaging. *Nat. Protoc.* 12:32.

Kahan, J., Papadaki, A., White, M., Mancini, L., Yousry, T., Zrinzo, L., et al. (2015). The Safety of using body-transmit mri in patients with implanted deep brain stimulation devices. *PLoS One* 10:e0129077. doi: 10.1371/journal.pone.0129077

Keliris, G. A., Li, Q., Papanikolaou, A., Logothetis, N. K., and Smirnakis, S. M. (2019). Estimating average single-neuron visual receptive field sizes by fMRI. *Proc. Natl. Acad. Sci. U.S.A.* 116, 6425–6434. doi: 10.1073/pnas.1809612116

Keliris, G. A., Shmuel, A., Ku, S. P., Pfeuffer, J., Oeltermann, A., Steudel, T., et al. (2007). Robust controlled functional MRI in alert monkeys at high magnetic field: effects of jaw and body movements. *Neuroimage* 36, 550–570. doi: 10.1016/j.neuroimage.2007.02.057

Klein, C., Hänggi, J., Luechinger, R., and Jäncke, L. (2015). MRI with and without a high-density EEG cap–what makes the difference? *Neuroimage* 106, 189–197. doi: 10.1016/j.neuroimage.2014.11.053

Lai, H. Y., Albaugh, D. L., Kao, Y. C. J., Younce, J. R., and Shih, Y. Y. I. (2015). Robust deep brain stimulation functional MRI procedures in rats and mice using an MR-compatible tungsten microwire electrode. *Magn. Reson. Med.* 73, 1246–1251. doi: 10.1002/mrm.25239

Lai, H. Y., Younce, J. R., Albaugh, D. L., Kao, Y. C. J., and Shih, Y. Y. I. (2014). Functional MRI reveals frequency-dependent responses during deep brain stimulation at the subthalamic nucleus or internal globus pallidus. *Neuroimage* 84:11.

Lake, E. M. R., Ge, X., Shen, X., Herman, P., Hyder, F., Cardin, J. A., et al. (2020). Simultaneous cortex-wide fluorescence Ca2+ imaging and whole-brain fMRI. *Nat. Methods* 17:1262.

Lambers, H., Wachsmuth, L., Thomas, D., Boumezbeur, F., Hoesker, V., Pradier, B., et al. (2022). Fiber-based lactate recordings with fluorescence resonance energy transfer sensors by applying an magnetic resonance-informed correction of hemodynamic artifacts. *Neurophotonics* 9:032212. doi: 10.1117/1.NPh.9.3.032212

Lee, H. J., Jiang, Y., and Cheng, J. X. (2019). Label-free optical imaging of membrane potential. *Curr. Opin. Biomed. Eng.* 12, 118–125.

Lee, J. H., Durand, R., Gradinaru, V., Zhang, F., Goshen, I., Kim, D. S., et al. (2010). Global and local fMRI signals driven by neurons defined optogenetically by type and wiring. *Nature* 465, 788–792. doi: 10.1038/nature09108

Lehto, L. J., Idiyatullin, D., Zhang, J., Utecht, L., Adriany, G., Garwood, M., et al. (2017). MB-SWIFT functional MRI during deep brain stimulation in rats. *Neuroimage* 159:443.

Leithner, C., and Royl, G. (2014). The oxygen paradox of neurovascular coupling. *J. Cereb. Blood Flow Metab.* 34, 19–29.

Liang, Z., Ma, Y., Watson, G. D. R., and Zhang, N. (2017). Simultaneous GCaMP6-based fiber photometry and fMRI in rats. *J. Neurosci. Methods* 289, 31–38. doi: 10.1016/j.jneumeth.2017.07.002

Lim, H. K., You, N., Bae, S., Kang, B. M., Shon, Y. M., Kim, S. G., et al. (2021). Differential contribution of excitatory and inhibitory neurons in shaping neurovascular coupling in different epileptic neural states. *J. Cereb. Blood Flow Metab.* 41:1145. doi: 10.1177/0271678X20934071

Lin, J. Y. (2011). A user's guide to channelrhodopsin variants: features, limitations and future developments. *Exp. Physiol.* 96, 19–25. doi: 10.1113/expphysiol.2009.051961

Lin, J. Y., Knutsen, P. M., Muller, A., Kleinfeld, D., and Tsien, R. Y. (2013). ReaChR: a red-shifted variant of channelrhodopsin enables deep transcranial optogenetic excitation. *Nat. Neurosci.* 16, 1499–1508. doi: 10.1038/nn.3502

Lippert Michael, T. M. T., Steudel, T., Ohl, F., Logothetis, N. K., and Kayser, C. (2010). Coupling of neural activity and fMRI-BOLD in the motion area MT. *Magn. Reson. Imaging* 28, 1087–1094. doi: 10.1016/j.mri.2009.12.028

Logothetis, N. K. (2008). What we can do and what we cannot do with fMRI. *Nature* 453, 869–878.

Logothetis, N. K., and Pfeuffer, J. (2004). On the nature of the BOLD fMRI contrast mechanism. *Magn. Reson. Imaging* 22, 1517–1531.

Logothetis, N. K., and Wandell, B. A. (2004). Interpreting the BOLD signal. *Annu. Rev. Physiol.* 66, 735–769.

Logothetis, N. K., Pauls, J., Augath, M., Trinath, T., and Oeltermann, A. (2001). Neurophysiological investigation of the basis of the fMRI signal. *Nature* 412, 150–157.

Lohani, S., Poplawsky, A. J., Kim, S. G., and Moghaddam, B. (2017). Unexpected global impact of VTA dopamine neuron activation as measured by opto-fMRI. *Mol. Psychiatry* 22, 585–594. doi: 10.1038/mp.2016.102

Lok, J., Gupta, P., Guo, S., Kim, W. J., Whalen, M. J., van Leyen, K., et al. (2007). Cell-cell signaling in the neurovascular unit. *Neurochem. Res.* 32, 2032–2045.

Luo, L., Callaway, E. M., and Svoboda, K. (2008). Genetic dissection of neural circuits. *Neuron* 57, 634–660.

Lyons, M. R., and West, A. E. (2011). Mechanisms of specificity in neuronal activity-regulated gene transcription. *Prog. Neurobiol.* 94, 259–295.

Madisen, L., Mao, T., Koch, H., Zhuo, J. M., Berenyi, A., Fujisawa, S., et al. (2012). A toolbox of Cre-dependent optogenetic transgenic mice for light-induced activation and silencing. *Nat. Neurosci.* 15, 793–802. doi: 10.1038/nn.3078

Mandino, F., Yeow, L. Y., Bi, R., Sejin, L., Bae, H. G., Baek, S. H., et al. (2022). *The Lateral Entorhinal Cortex Is A Hub For Local And Global Dysfunction In Early Alzheimer's Disease State*. Available online at: https://journals.sagepub.com/doi/10.1177/0271678X221082016 [Accessed May 6, 2022].

Masamoto, K., and Kanno, I. (2012). Anesthesia and the quantitative evaluation of neurovascular coupling. *J. Cereb. Blood Flow Metab.* 32, 1233–1247. doi: 10.1038/jcbfm.2012.50

Min, H. K., Hwang, S. C., Marsh, M. P., Kim, I., Knight, E., Striemer, B., et al. (2012). Deep brain stimulation induces BOLD activation in motor and non-motor networks: an fMRI comparison study of STN and EN/GPi DBS in large animals. *Neuroimage* 63, 1408–1420. doi: 10.1016/j.neuroimage.2012.08.006

Min, H. K., Ross, E. K., Lee, K. H., Dennis, K., Han, S. R., Jeong, J. H., et al. (2014). Subthalamic nucleus deep brain stimulation induces motor network BOLD activation: use of a high precision MRI guided stereotactic system for nonhuman primates. *Brain Stimul.* 7, 603–607. doi: 10.1016/j.brs.2014.04.007

Mirsattari, S. M., Ives, J. R., Bihari, F., Leung, L. S., Menon, R. S., and Bartha, R. (2005). Real-time display of artifact-free electroencephalography during functional magnetic resonance imaging and magnetic resonance spectroscopy in an animal model of epilepsy. *Magn. Reson. Med.* 53, 456–464. doi: 10.1002/mrm.20357

Moon, H. S., Jiang, H., Vo, T. T., Jung, W. B., Vazquez, A. L., and Kim, S. G. (2021). Contribution of excitatory and inhibitory neuronal activity to BOLD fMRI. *Cereb. Cortex (New York, NY)* 31, 4053.

Moreno, A., Morris, R. G. M., and Canals, S. (2016). Frequency-dependent gating of hippocampal-neocortical interactions. *Cereb. Cortex* 26, 2105–2114. doi: 10.1093/cercor/bhv033

Morone, K. A., Neimat, J. S., Roe, A. W., and Friedman, R. M. (2017). Review of functional and clinical relevance of intrinsic signal optical imaging in human brain mapping. *Neurophotonics* 4:031220. doi: 10.1117/1.NPh.4.3.031220

Multi Channel Systems MCS GmbH (2020). *Smart Ephys*. Available online at: https://www.smart-ephys.com/home/extracellular-in-vivo-electrophysiology/ [Accessed Aprir 20, 2022].

Nagayama, S., Zeng, S., Xiong, W., Fletcher, M. L., Masurkar, A. V., Davis, D. J., et al. (2007). In vivo simultaneous tracing and Ca(2+) imaging of local neuronal circuits. *Neuron* 53, 789–803. doi: 10.1016/j.neuron.2007.02.018

Nagel, G., Szellas, T., Huhn, W., Kateriya, S., Adeishvili, N., Berthold, P., et al. (2003). Channelrhodopsin-2, a directly light-gated cation-selective membrane channel. *Proc. Natl. Acad. Sci. U.S.A.* 100, 13940–13945.

Neher, E., and Sakaba, T. (2008). Multiple roles of calcium ions in the regulation of neurotransmitter release. *Neuron* 59, 861–872.

Nersesyan, H., Hyder, F., Rothman, D. L., and Blumenfeld, H. (2004). Dynamic fMRI and EEG recordings during spike-wave seizures and generalized tonic-clonic seizures in WAG/Rij rats. *J. Cereb. Blood Flow Metab.* 24, 589–599. doi: 10.1097/01.WCB.0000117688.98763.23

Nguyen, T., Potter, T., Karmonik, C., Grossman, R., and Zhang, Y. (2018). Concurrent EEG and functional MRI recording and integration analysis for dynamic cortical activity imaging. *J. Vis. Exp.* 136:56417.

Obien, M. E. J., Deligkaris, K., Bullmann, T., Bakkum, D. J., and Frey, U. (2015). Revealing neuronal function through microelectrode array recordings. *Front. Neurosci.* 8:423.

Oeltermann, A., Augath, M. A., and Logothetis, N. K. (2007). Simultaneous recording of neuronal signals and functional NMR imaging. *Magn. Reson. Imaging* 25, 760–774.

Ogawa, S., Lee, T. M., Kay, A. R., and Tank, D. W. (1990). Brain magnetic resonance imaging with contrast dependent on blood oxygenation. *Proc. Natl. Acad. Sci. U.S.A.* 87, 9868–9872.

Ohmiya, Y., and Hirano, T. (1996). Shining the light: the mechanism of the bioluminescence reaction of calcium-binding photoproteins. *Chem. Biol.* 3, 337–347. doi: 10.1016/s1074-5521(96)90116-7

Opdam, H. I., Federico, P., Jackson, G. D., Buchanan, J., Abbott, D. F., Fabinyi, G. C. A., et al. (2002). A sheep model for the study of focal epilepsy with concurrent intracranial EEG and functional MRI. *Epilepsia* 43, 779–787. doi: 10.1046/j.1528-1157.2002.04202.x

Oyarzabal, E. A., Hsu, L. M., Das, M., Chao, T. H. H., Zhou, J., Song, S., et al. (2022). Chemogenetic stimulation of tonic locus coeruleus activity strengthens the default mode network. *Sci. Adv.* 8:9898. doi: 10.1126/sciadv.abm9898

Pais-Roldán, P., Takahashi, K., Sobczak, F., Chen, Y., Zhao, X., Zeng, H., et al. (2020). Indexing brain state-dependent pupil dynamics with simultaneous fMRI and optical fiber calcium recording. *Proc. Natl. Acad. Sci. U.S.A.* 117, 6875–6882. doi: 10.1073/pnas.1909937117

Pan, W. J., Thompson, G., Magnuson, M., Majeed, W., Jaeger, D., and Keilholz, S. (2010). Simultaneous FMRI and electrophysiology in the rodent brain. *J. Vis. Exp.* 42:1901.

Paredes, R. M., Etzler, J. C., Watts, L. T., Zheng, W., and Lechleiter, J. D. (2008). Chemical calcium indicators. *Methods* 46, 143–151.

Peeters, L. M., Hinz, R., Detrez, J. R., Missault, S., de Vos, W. H., Verhoye, M., et al. (2020a). Chemogenetic silencing of neurons in the mouse anterior cingulate area modulates neuronal activity and functional connectivity. *Neuroimage* 220:117088. doi: 10.1016/j.neuroimage.2020.117088

Peeters, L. M., van den Berg, M., Hinz, R., Majumdar, G., Pintelon, I., and Keliris, G. A. (2020c). Cholinergic modulation of the default mode like network in rats. *iScience* 23:101455. doi: 10.1016/j.isci.2020.101455

Peeters, L. M., Missault, S., Keliris, A. J., and Keliris, G. A. (2020b). Combining designer receptors exclusively activated by designer drugs and neuroimaging in experimental models: A powerful approach towards neurotheranostic applications. *Br. J. Pharmacol.* 177, 992–1002. doi: 10.1111/bph.14885

Piccolino, M. (1997). Luigi Galvani and animal electricity: two centuries after the foundation of electrophysiology. *Trends Neurosci.* 20, 443–448. doi: 10.1016/s0166-2236(97)01101-6

Piccolino, M. (1998). Animal electricity and the birth of electrophysiology: the legacy of Luigi Galvani. *Brain Res. Bull.* 46, 381–407. doi: 10.1016/s0361-9230(98)00026-4

Rauch, A., Rainer, G., and Logothetis, N. K. (2008). The effect of a serotonin-induced dissociation between spiking and perisynaptic activity on BOLD functional MRI. *Proc. Natl. Acad. Sci. U.S.A.* 105, 6759–6764. doi: 10.1073/pnas.0800312105

Resendez, S. L., and Stuber, G. D. (2015). In vivo calcium imaging to illuminate neurocircuit activity dynamics underlying naturalistic behavior. *Neuropsychopharmacology* 40, 238–239. doi: 10.1038/npp.2014.206

Roelofs, T. J. M., Verharen, J. P. H., van Tilborg, G. A. F., Boekhoudt, L., van der Toorn, A., de Jong, J. W., et al. (2017). A novel approach to map induced activation of neuronal networks using chemogenetics and functional neuroimaging in rats: a proof-of-concept study on the mesocorticolimbic system. *Neuroimage* 156, 109–118. doi: 10.1016/j.neuroimage.2017.05.021

Rose, T., Goltstein, P. M., Portugues, R., and Griesbeck, O. (2014). Putting a finishing touch on GECIs. *Front. Mol. Neurosci.* 7:88. doi: 10.3389/fnmol.2014.00088

Rubaiy, H. N. A. (2017). Short guide to electrophysiology and ion channels. *J. Pharm. Pharm. Sci.* 20, 48–67.

Sato, M., Kawano, M., Ohkura, M., Gengyo-Ando, K., Nakai, J., and Hayashi, Y. (2015). Generation and imaging of transgenic mice that express g-camp7 under a tetracycline response element. *PLoS One* 10:e0125354. doi: 10.1371/journal.pone.0125354

Scanziani, M., and Häusser, M. (2009). Electrophysiology in the age of light. *Nature* 461, 930–939.

Schlegel, F., Sych, Y., Schroeter, A., Stobart, J., Weber, B., Helmchen, F., et al. (2018). Fiber-optic implant for simultaneous fluorescence-based calcium recordings and BOLD fMRI in mice. *Nat. Protoc.* 13, 840–855. doi: 10.1038/nprot.2018.003

Schmid, F., Wachsmuth, L., Albers, F., Schwalm, M., Stroh, A., and Faber, C. (2017). True and apparent optogenetic BOLD fMRI signals. *Magn. Reson. Med.* 77, 126–136. doi: 10.1002/mrm.26095

Schmid, F., Wachsmuth, L., Schwalm, M., Prouvot, P. H., Jubal, E. R., Fois, C., et al. (2016). Assessing sensory versus optogenetic network activation by combining (o)fMRI with optical Ca2+ recordings. *J. Cereb. Blood Flow Metab.* 36, 1885–1900. doi: 10.1177/0271678X15619428

Schölvinck, M. L., Leopold, D. A., Brookes, M. J., and Khader, P. H. (2013). The contribution of electrophysiology to functional connectivity mapping. *Neuroimage* 80, 297–306.

Schulz, K., Sydekum, E., Krueppel, R., Engelbrecht, C. J., Schlegel, F., Schröter, A., et al. (2012). Simultaneous BOLD fMRI and fiber-optic calcium recording in rat neocortex. *Nat. Methods* 9, 597–602.

Shyu, B. C., Lin, C. Y., Sun, J. J., Chen, S. L., and Chang, C. (2004). BOLD response to direct thalamic stimulation reveals a functional connection between the medial thalamus and the anterior cingulate cortex in the rat. *Magn. Reson. Med.* 52, 47–55. doi: 10.1002/mrm.20111

Sokoloff, L., Reivich, M., Kennedy, C., Rosiers, M. H. D., Patlak, C. S., Pettigrew, K. D., et al. (1977). The [14c]deoxyglucose method for the measurement of local cerebral glucose utilization: theory, procedure, and normal values in the conscious and anesthetized albino rat1. *J. Neurochem.* 28, 897–916.

Stosiek, C., Garaschuk, O., Holthoff, K., and Konnerth, A. (2003). In vivo two-photon calcium imaging of neuronal networks. *Proc. Natl. Acad. Sci. U.S.A.* 100, 7319–7324.

Sumiyoshi, A., Riera, J. J., Ogawa, T., and Kawashima, R. (2011). A mini-cap for simultaneous EEG and fMRI recording in rodents. *Neuroimage* 54, 1951–1965. doi: 10.1016/j.neuroimage.2010.09.056

Sych, Y., Chernysheva, M., Sumanovski, L. T., and Helmchen, F. (2019). High-density multi-fiber photometry for studying large-scale brain circuit dynamics. *Nat. Methods* 16, 553–560. doi: 10.1038/s41592-019-0400-4

Tagliati, M., Jankovic, J., Pagan, F., Susatia, F., Isaias, I. U., and Okun, M. S. (2009). Safety of MRI in patients with implanted deep brain stimulation devices. *Neuroimage* 47 Suppl 2(Suppl. 2), T53–T57.

Tian, L., Hires, S. A., Mao, T., Huber, D., Chiappe, M. E., Chalasani, S. H., et al. (2009). Imaging neural activity in worms, flies and mice with improved GCaMP calcium indicators. *Nat. Methods* 6, 875–881. doi: 10.1038/nmeth.1398

Tolias, A. S., Sultan, F., Augath, M., Oeltermann, A., Tehovnik, E. J., Schiller, P. H., et al. (2005). Mapping cortical activity elicited with electrical microstimulation using FMRI in the macaque. *Neuron* 48, 901–911.

Tye, K. M., and Deisseroth, K. (2012). Optogenetic investigation of neural circuits underlying brain disease in animal models. *Nat. Rev. Neurosci.* 13, 251–266.

van den Berge, N., Albaugh, D. L., Salzwedel, A., Vanhove, C., van Holen, R., Gao, W., et al. (2017). Functional circuit mapping of striatal output nuclei using simultaneous deep brain stimulation and fMRI. *Neuroimage* 146:1050. doi: 10.1016/j.neuroimage.2016.10.049

Wachowiak, M., Falk, C. X., Cohen, L. B., and Zochowski, M. R. (2002). "Voltage and calcium imaging of brain activity: examples from the turtle and the mouse," in *Brain Mapping: The Methods*, 2nd Edn, Vol. 877, eds A. W. Toga and J. C. Mazziotta (Amsterdam: Academic Press), 77–95.

Walton, L. R., Verber, M., Lee, S. H., Chao, T. H. H., Wightman, R. M., and Shih, Y. Y. I. (2021). Simultaneous fMRI and fast-scan cyclic voltammetry bridges evoked oxygen and neurotransmitter dynamics across spatiotemporal scales. *Neuroimage* 244:118634. doi: 10.1016/j.neuroimage.2021.118634

Wang, M., He, Y., Sejnowski, T. J., and Yu, X. (2018). Brain-state dependent astrocytic Ca2+ signals are coupled to both positive and negative BOLD-fMRI signals. *Proc. Natl. Acad. Sci. U.S.A.* 115, E1647–E1656. doi: 10.1073/pnas.1711692115

Wang, X., Leong, A. T. L., Chan, R. W., Liu, Y., and Wu, E. X. (2019). Thalamic low frequency activity facilitates resting-state cortical interhemispheric MRI functional connectivity. *Neuroimage* 201:115985. doi: 10.1016/j.neuroimage.2019.06.063

Wapler, M. C., Testud, F., Hucker, P., Leupold, J., vonElverfeldt, D., Zaitsev, M., et al. (2021). MR-compatible optical microscope for in-situ dual-mode MR-optical microscopy. *PLoS One* 16:e0250903. doi: 10.1371/journal.pone.0250903

Wiesel, T. N. (1959). Recording inhibition and excitation in the cat's retinal ganglion cells with intracellular electrodes. *Nature* 183, 264–265. doi: 10.1038/183264a0

Williams, K. A., Magnuson, M., Majeed, W., LaConte, S. M., Peltier, S. J., Hu, X., et al. (2010). Comparison of alpha-chloralose, medetomidine and isoflurane anesthesia for functional connectivity mapping in the rat. *Magn. Reson. Imaging* 28, 995–1003. doi: 10.1016/j.mri.2010.03.007

Wu, J., Liu, L., Matsuda, T., Zhao, Y., Rebane, A., Drobizhev, M., et al. (2013). Improved orange and red Ca2± indicators and photophysical considerations for optogenetic applications. *ACS Chem. Neurosci.* 4, 963–972. doi: 10.1021/cn400012b

Yizhar, O., Fenno, L. E., Davidson, T. J., Mogri, M., and Deisseroth, K. (2011). Optogenetics in neural systems. *Neuron* 71, 9–34.

Yu, X. (2017). "When photons meet protons: optogenetics, calcium signal detection, and FMRI in small animals," in *Small Animal Imaging*, eds F. Kiessling, B. Pichler, and P. Hauff (Cham: Springer), 773–791.

Zaldivar, D., Rauch, A., Logothetis, N. K., and Goense, J. (2018). Two distinct profiles of fMRI and neurophysiological activity elicited by acetylcholine in visual cortex. *Proc. Natl. Acad. Sci. U.S.A.* 115, E12073–E12082. doi: 10.1073/pnas.1808507115

Zerbi, V., Floriou-Servou, A., Markicevic, M., Vermeiren, Y., Sturman, O., Privitera, M., et al. (2019). Rapid reconfiguration of the functional connectome after chemogenetic locus coeruleus activation. *Neuron* 103, 702–718.e5. doi: 10.1016/j.neuron.2019.05.034

Zhang, F., Aravanis, A. M., Adamantidis, A., de Lecea, L., and Deisseroth, K. (2007). Circuit-breakers: optical technologies for probing neural signals and systems. *Nat. Rev. Neurosci.* 8, 577–581. doi: 10.1038/nrn2192

Zhang, W. T., Harry Chao, T. H., Yang, Y., Wang, T. W., Lee, S. H., Oyarzabal, E. A., et al. (2021). Spectral fiber-photometry derives hemoglobin-absorption changes for accurate measurement of fluorescent sensor activity. *bioRxiv* [Preprint] bioRixv: 2021.08.23.457372.

Zhao, S., Li, G., Tong, C., Chen, W., Wang, P., Dai, J., et al. (2020). Full activation pattern mapping by simultaneous deep brain stimulation and fMRI with graphene fiber electrodes. *Nat. Commun.* 11:1788. doi: 10.1038/s41467-020-15570-9

Zhao, S., Ting, J. T., Atallah, H. E., Qiu, L., Tan, J., Gloss, B., et al. (2011). Cell type–specific channelrhodopsin-2 transgenic mice for optogenetic dissection of neural circuitry function. *Nat. Methods* 8, 745–755.

Zhao, Y., Rütgen, M., Zhang, L., and Lamm, C. (2021). Pharmacological fMRI provides evidence for opioidergic modulation of discrimination of facial pain expressions. *Psychophysiology* 58:e13717. doi: 10.1111/psyp.13717

Zhu, H., Aryal, D. K., Olsen, R. H. J., Urban, D. J., Swearingen, A., Forbes, S., et al. (2016). Cre-dependent DREADD (designer receptors exclusively activated by designer drugs) mice. *Genesis* 54, 439–446.

Zucker, R. S. (1999). Calcium- and activity-dependent synaptic plasticity. *Curr. Opin. Neurobiol.* 9, 305–313.

frontiers | Frontiers in Neuroscience

TYPE Methods
PUBLISHED 28 July 2022
DOI 10.3389/fnins.2022.954237

OPEN ACCESS

EDITED BY
Shengxiang Liang,
Fujian University of Traditional Chinese Medicine, China

REVIEWED BY
Chuanli Cheng,
Shenzhen Institutes of Advanced Technology (CAS), China
Haitao Zhu,
Peking University, China
Qiu Huang,
Shanghai Jiao Tong University, China

*CORRESPONDENCE
Binbin Nie
niebb@ihep.ac.cn

†These authors have contributed equally to this work

SPECIALTY SECTION
This article was submitted to Brain Imaging Methods, a section of the journal Frontiers in Neuroscience

RECEIVED 27 May 2022
ACCEPTED 05 July 2022
PUBLISHED 28 July 2022

CITATION
Bao Z, Zhang T, Pan T, Zhang W, Zhao S, Liu H and Nie B (2022) Automatic method for individual parcellation of manganese-enhanced magnetic resonance imaging of rat brain. *Front. Neurosci.* 16:954237. doi: 10.3389/fnins.2022.954237

Automatic method for individual parcellation of manganese-enhanced magnetic resonance imaging of rat brain

Zhiguo Bao[1†], Tianhao Zhang[2,3†], Tingting Pan[2,4†], Wei Zhang[2,3], Shilun Zhao[2,3], Hua Liu[2,3] and Binbin Nie[2,3*]

[1]First Affiliated Hospital of Henan University, Kaifeng, China, [2]Beijing Engineering Research Center of Radiographic Techniques and Equipment, Institute of High Energy Physics, Chinese Academy of Sciences, Beijing, China, [3]School of Nuclear Science and Technology, University of Chinese Academy of Sciences, Beijing, China, [4]Physical Science and Technology College, Zhengzhou University, Zhengzhou, China

Aims: To construct an automatic method for individual parcellation of manganese-enhanced magnetic resonance imaging (MEMRI) of rat brain with high accuracy, which could preserve the inherent voxel intensity and Regions of interest (ROI) morphological characteristics simultaneously.

Methods and results: The transformation relationship from standardized space to individual space was obtained by firstly normalizing individual image to the Paxinos space and then inversely transformed. On the other hand, all the regions defined in the atlas image were separated and resaved as binary mask images. Then, transforming the mask images into individual space *via* the inverse transformations and reslicing using the 4th B-spline interpolation algorithm. The boundary of these transformed regions was further refined by image erosion and expansion operator, and finally combined together to generate the individual parcellations. Moreover, two groups of MEMRI images were used for evaluation. We found that the individual parcellations were satisfied, and the inherent image intensity was preserved. The statistical significance of case-control comparisons was further optimized.

Conclusions: We have constructed a new automatic method for individual parcellation of rat brain MEMRI images, which could preserve the inherent voxel intensity and further be beneficial in case-control statistical analyses. This method could also be extended to other imaging modalities, even other experiments species. It would facilitate the accuracy and significance of ROI-based imaging analyses.

KEYWORDS

individual parcellations, ROI-based analysis, manganese-enhanced magnetic resonance imaging (MEMRI), rat brain, stereotaxic template set

Introduction

Numerous studies have demonstrated the usefulness of magnetic resonance imaging (MRI) techniques in animal experiments, which is important for pathogenesis researches, drug developments, and so on (Bible et al., 2012; Kim et al., 2012; Wang et al., 2012, 2018; Li et al., 2015; Liang et al., 2020; Tu et al., 2020). Manganese-enhanced MRI (MEMRI), a new MRI technique, could detect the active neurons and trace neuronal pathway by monitoring manganese ions (Mn^{2+}) *in vivo* (Aoki et al., 2004; Koretsky and Silva, 2004). By tracing the deposition of Mn^{2+}, the active neurons would have high voxel intensity in MEMRI images, while other voxels have low intensity. Recently, the MEMRI technique has been widely used in various studies of the rodent brain (Ho et al., 2018; Perez et al., 2018; Gimenes et al., 2019; Yang et al., 2020; Bearer et al., 2022).

Imaging analysis is a prerequisite in MEMRI studies for quantitative interpretations of neuronal dysfunctions. Regions of interests (ROIs)-based analysis is one of the most frequently used methods in rat brain MEMRI studies (Spurny et al., 2019). Similar to other modalities of MRI, by spatially normalizing individual MEMRI images into a standard space, ROIs could be extracted *via* a corresponding atlas image automatically (Nie et al., 2013; Barriere et al., 2019). However, it has been found in functional studies that the brain sub-regions vary across individuals (Chong et al., 2017; Salehi et al., 2020; Reijonen et al., 2021). Moreover, because of image interpolations and transformations in spatial normalization, the inherent MEMRI intensity would be confused by adjacent voxels inevitably (Ashburner and Friston, 1999; Zhilkin and Alexander, 2004). Especially, the voxel intensity of active neurons would be affected, even decreased, by adjacent un-activated neurons, and the statistical significance of case-control studies would further be affected (Lv et al., 2021).

Alternatively, manually tracing ROIs in individual images is another important method in MEMRI studies, which could avoid the influences of image normalization and preserve the inherent voxel intensity (Jackson et al., 2011). However, this method has many disadvantages, such as low accuracy, labor-intensive, subjective and poor robustness, and so on. Therefore, it would be highly desirable to develop an automatic method for ROI parcellations in individual space of MEMRI images of rat brain.

In addition, more than a decade ago, our lab had constructed an automatic atlas-based method for tracing ROIs in individual space by registering the template images to individuals (Nie et al., 2010). However, as the resolution of individual images was often lower than the template, the accuracy of this image registration was always lower than spatial normalization, so that the subtle ROIs were hard to trace out precisely.

Therefore, the current study was aimed to introduce a new automatic method for individual parcellation of MEMRI images of rat brain with high accuracy, and both the inherent voxel intensity and ROI morphological characteristics could be preserved simultaneously. For evaluation, individual parcellations were performed on two groups of T2-weighted (T2WI) and MEMRI images, and further comparing with the parcellations in standardized space. Moreover, the method constructed in this study was packaged and available by contacting the corresponding author at niebb@ihep.ac.cn.

Materials and methods

The individual parcellation method

Parcellation of rat brain images in individual space could preserve the inherent voxel intensity and ROI morphological characteristics, which would further improve the statistical sensitivity in ROI-based analyses. The automatic individual parcellation method was performed based on the stereotaxic template sets of rat brain in Paxinos space (Liang et al., 2017). The flow chart was shown in Figure 1 and detailed as follows.

Firstly, the spatial transformation from individual space to Paxinos space was calculated by registering the MEMRI image to the stereotaxic template. This registration could be performed either by affine/nonlinear transformations based on the MEMRI template image (Figure 1-*Step 1a*) (Ashburner and Friston, 1999; Zhilkin and Alexander, 2004), or by DARTEL (diffeomorphic anatomical registration through exponentiated lie) algorithm (Mak et al., 2011) based on the tissue probability maps (TPM) (Figure 1-*Step 1b*). A transformation matrix was obtained *via* template way, named $Matrix_{sn}$, while a deformation field was obtained *via* TPM way, named $Deform_y$. The inverse transformation of $Matrix_{sn}$ or $Deform_y$ was then calculated to obtain the spatial transformation from Paxinos space to individual space (Ashburner et al., 2000), and saved as $InvMatrix_{sn}$ or $InvDeform_y$.

On the other hand, the atlas images in Paxinos space were preprocessed prior to registering with an individual image (Figure 1-*Step 2*). To avoid the influences between adjacent regions, all the ROIs defined in the atlas image were separated and resaved as single-ROI mask images. In another word, each ROI was resaved as a 3D binary image, and the image intensity of voxels inside the ROI was assigned 1 and outside was 0.

Finally, transforming the atlas images into individual space to create the parcellation of individual image (Figure 1-*Step 3*). In detail, all the separated ROI mask images were registered with individual image *via* the $InvMatrix_{sn}$/$InvDeform_y$ using the 4th B-spline interpolation algorithm. Then, the ROI contour of each registered mask image was identified, and further refined by image erosion and dilation using a disc operator with one voxel radius. Next, each refined ROI was given a unique integer as an index. At last, all the reassigned ROIs were combined together to generate the final individual parcellation image.

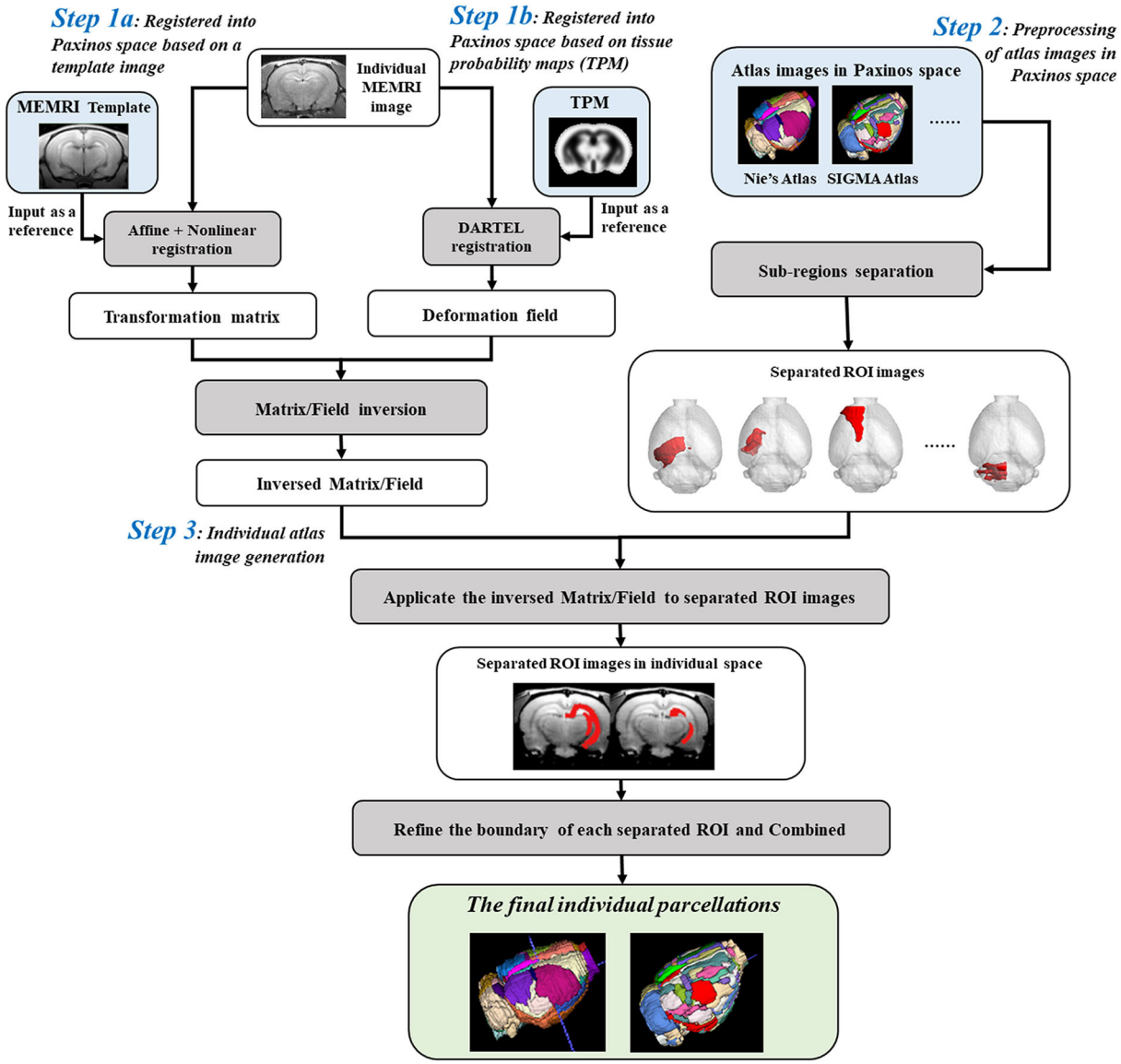

FIGURE 1
Flow chart for creating individual parcellations of manganese-enhanced magnetic resonance imaging (MEMRI) image of rat brain. *Step 1*: The individual MEMRI image was registered into Paxinos space either by affine/nonlinear transformations based on the MEMRI template image (*Step 1a*), or by DARTEL algorithm based on the tissue probability maps (TPM) (*Step 1b*), and the transformation matrix/deformation field was obtained, named as $Matrix_{sn}/Deform_{y}$. Inverse transformation of the $Matrix_{sn}/Deform_{y}$ was then calculated, named $InvMatrix_{sn}/InvDeform_{y}$. *Step 2*: All the regions of interests (ROIs) defined in atlas images in Paxinos space were firstly separated and resaved as single-ROI mask images. *Step 3*: The separated ROI mask images were transformed into individual space *via* the $InvMatrix_{sn}/InvDeform_{y}$ using 4th B-spline interpolation algorithm. The contour of each transformed ROI was identified and further refined by image erosion and expansion operator. Then, each refined ROI was given a unique integer as an index and then combined into a new atlas image. This combined atlas image was the final individual parcellations of MEMRI images.

Animals and MRI data acquisition for evaluation

Five healthy adult Sprague–Dawley (SD) rats (male, 5; age, 10–11 week old; weight, 250–300 g) and ten modal rats with smell damage (male, 10; age, 10–11 week old; and weight, 250–300 g) were used for method evaluation.

During MRI scan, all rats were anesthetized using inhaled isoflurane/O_2 (3% for induction and 1.5–2% for maintenance), and prostrated on a custom-made holder to minimize head motion while respiration was monitored at a rate of 50 breaths per min. For MEMRI study, all these rats were injected with manganese chloride (MnCl2·4H2O, Bio Basic Inc., Canada) dissolved in bicine [di(hydroxyethyl)glycine, Sigma-Ulrich, UK]

buffer pH 7.4 in doses of 13.95 mg/kg for continuous 7 days (Tang et al., 2016).

All datasets were acquired on a 7.0T animal MRI scanner (70/16 PharmaScan, Bruker Biospin GmbH, Germany) in Nanjing, using a 38-mm birdcage rat brain quadrature resonator for radiofrequency transmission and receiving. T_2-weighted (T2WI) data were obtained with a RARE sequence (RARE factor = 8, TR = 10493 ms, TE = 36 ms, matrix size 256*256*90, voxel size 0.14*0.14*0.3 mm, no slice gap). MEMRI data were obtained right after the last injection with a RAREVTR sequence (TR = 5500 ms, TE = 8 ms, matrix size 256*192*22, voxel size 0.14*0.18*1.2 mm^3, no slice gap) for six repetitions. All the Bruker original images were converted to DICOM format with programs (Paravision 5.0) in the scanner. All experiments were conducted in accordance with the National Institutes of Health Guide for the Care and Use of Laboratory Animals and were approved by the Jiang Su Animal Care and Use Committee.

Generation of individual parcellations of T2WI images

All the fifteen T2WI images were inspected and found equally of high quality in terms of the image contrast, noise level, and resolution. Firstly, all the individual T2WI images were registered into Paxinos space using DARTEL algorithm, and the corresponding $Deform_y$ of each rat was obtained. Then, all the $Deform_y$ were inversely transformed, and the corresponding $InvDeform_y$ of each rat was obtained. On the other hand, 66 functional ROIs defined in the 3D atlas image in Paxinos space were separated and resaved into 66 binary mask images. Next, all the 66 mask images were registered with each T2WI image *via* the corresponding $InvDeform_y$ repetitively using the 4th B-spline interpolation algorithm. Each registered ROI contour was identified and further refined. Finally, each refined ROI was given a unique integer as an index and combined together to generate the individual parcellations of each T2WI image.

Generation of individual parcellations of MEMRI images

All the fifteen MEMRI images were also inspected and found equally of high quality in terms of the image contrast, noise level, and resolution. Firstly, the MEMRI image series were realigned to remove the head movement, and a mean MEMRI image was created over the six realigned volumes. Next, the mean MEMRI image was registered into Paxinos space *via* the MEMRI template image of rat brain, and the corresponding $Matrix_{sn}$ of each rat was obtained. Then, all the $Matrix_{sn}$ were inversely transformed, and the corresponding $InvMatrix_{sn}$ of each rat was obtained. The preprocessing of the atlas image was the same with Section Generation of individual parcellations of T2WI images. Then, all the preprocessed ROI mask images were registered with individual mean MEMRI images *via* $InvMatrix_{sn}$, and the contour was refined. Finally, each refined ROI was given a unique integer as an index and combined together to generate the individual parcellations of each MEMRI image.

Statistical analysis of MEMRI images

For qualitative evaluation of the individual parcellations, the mean MEMRI values in dentate gyrus (*DG*) and hippocampus (*Hip*) of all the fifteen rats were extracted in individual space, respectively, and the time courses of each rat were plotted out. For qualitative comparison, all the fifteen MEMRI images were also normalized into the Paxinos space *via* the corresponding $Matrix_{sn}$ using the 4th B-spline interpolation algorithm, and resliced to 1*1*1.5 mm^3 (after zooming). The mean values in *DG* and *Hip* of normalized MEMRI images were also extracted and plotted out.

For quantitative evaluation of the individual parcellations, the mean values of the first MEMRI volume in *DG* and *Hip* were analyzed using SPSS software, version 19.0 (SPSS Inc. IBM, Armonk, NY, USA). The mean MEMRI values in ten modal and five healthy rats were compared by two-sample *t*-tests. Statistical significance was defined as a $p < 0.05$.

Furthermore, the accuracy of the individual parcellations was evaluated by a spatial index, named Dice similarity coefficient (*Dice*). It describes the similarity of the volume and position between the MEMRI image (*MEMRI*) and its corresponding individual parcellation image (*Parcellation*), named $Dice_{MePa}$, as shown in Equation (1).

$$Dice_{MePa} = 2 \times \frac{MEMRI \cap Parcellation}{MEMRI + Parcellation} \quad (1)$$

The derivation of the *Dice* is detailed previously (Gutierrez and Zaidi, 2012). The excellent agreement value of *Dice* is more than 80%. For comparison, the *Dice* was calculated between the template image and normalized MEMRI image, which was regarded as the golden standard, named $Dice_{TempMe}$. Moreover, the previous method proposed by our group was also executed (Nie et al., 2010). In detail, each individual MEMRI image was selected as the reference, and the template image was transformed to register with it. And the *Dice* between the MEMRI

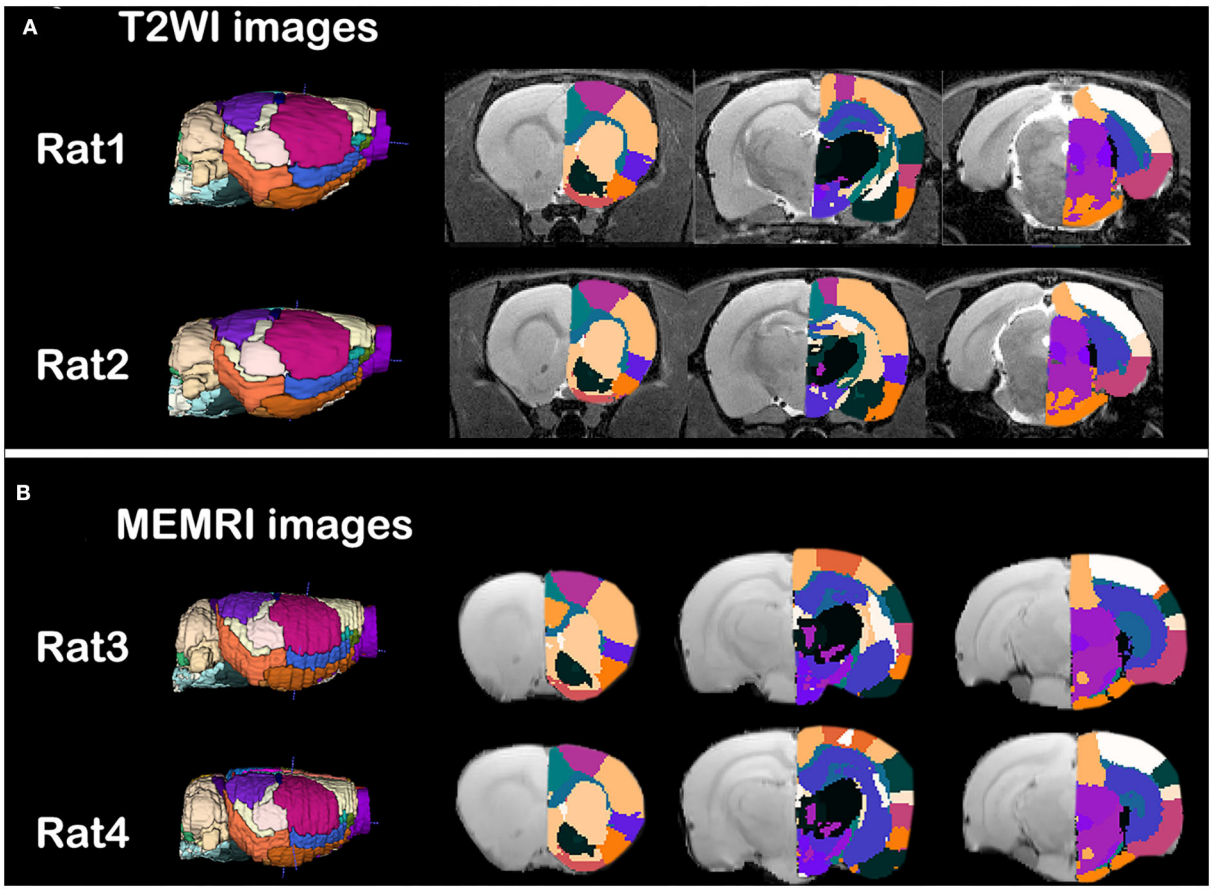

FIGURE 2
Qualitative evaluation of the individual parcellations of **(A)** T2WI images and **(B)** intercranial mean MEMRI images of rat brain. Four rats were randomly selected. Right side of the individual parcellations was shown in color scaled and superimposed on the corresponding MRI image. The T2WI/MEMRI MRI images were shown in gray scaled as background.

image and registered template image was also calculated, named $Dice_{MeTemp}$.

Results

Individual parcellations of MRI images

The individual parcellations of MRI images were shown in Figure 2. Two rats of T2WI images (Figure 2A) or MEMRI images (Figure 2B) were randomly selected. The individual parcellations were shown in color scale, while the MRI images were in gray scale. A 3D surface of individual parcellations was shown to the left, while three coronal slices were shown to the right. The individual parcellations were superimposed on the corresponding T2WI image (Figure 2A), or mean intracranial MEMRI image (Figure 2B). As illustrated in Figure 2, the parcellations were registered into the individual space accurately.

Quantitative evaluation of individual parcellations of MEMRI images

The evaluation of individual parcellations of two randomly selected MEMRI images was shown in Figure 3. Unilateral *DG* and *Hip* were superimposed on the first volume of MEMRI images (Figures 3A,B). The MEMRI time course in individual space was plotted out in blue color, while it in Paxinos space was in green (Figures 3C,D). As illustrated in Figure 3, although the downtrend of time courses was similar, the MEMRI voxel intensity in individual space was always higher than it in standardized space. It could be speculated that the inherent MEMRI signal could be persevered by individual parcellations.

The Dice similarity coefficients between the reference images and transformed images were listed in Table 1. The $Dice_{TempMe}$ between the template image and normalized MEMRI image was selected as the golden standard. As illustrated in Table 1, all the *Dice* coefficients were bigger than 80%. Compared with the $Dice_{MeTemp}$, the accuracy proposed in this study was higher.

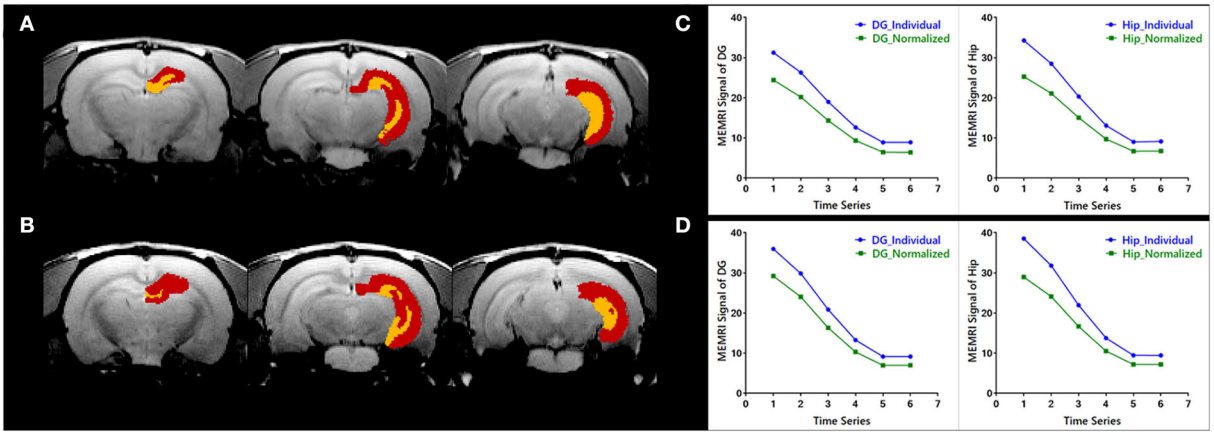

FIGURE 3
Quantitative evaluation of the individual parcellations of MEMRI images of **(A,C)** a modal rat and **(B,D)** a healthy rat. The individual parcellations were shown in color scaled in which the right dentate gyrus was yellow and the right hippocampus was red. The MEMRI images were shown in gray scaled as background. Based on the individual parcellations, the mean MEMRI signal in each ROI was extracted and the curve is shown in blue color **(C,D)**. As a comparison, the MEMRI images of these two rats were also standardized into Paxinos space, and the mean signal in each ROI was then extracted based on the atlas in Paxinos space. The signal curve extracted in traditional way was shown in green color **(C,D)**.

TABLE 1 Volumetric and spatial correspondence measures.

	$Dice_{TempMe}$ (%)	$Dice_{MeTemp}$ (%)	$Dice_{MePa}$ (%)
Whole brain	90.80 ± 0.39	89.42 ± 0.32	90.78 ± 0.20

$Dice_{TempMe}$ (%): Dice similarity coefficient between the template image and the normalized MEMRI image (the excellent agreement value is more than 80%).
$Dice_{MeTemp}$ (%): Dice similarity coefficient between the individual MEMRI image and the registered template image (the excellent agreement value is more than 80%).
$Dice_{MePa}$ (%): Dice similarity coefficient between the individual MEMRI image and the individual parcellation image (the excellent agreement value is more than 80%).

Statistical analysis of MEMRI images

The individual parcellations of MEMRI images were further applicate in ROI-based analyses of case-control studies. The statistical results were shown in Figure 4. The MEMRI signal of each group was presented as mean ± SD (standard deviation). The MEMRI signal in modal rats is significantly lower than the healthy rats in both *DG* ($p < 0.001$) and *Hip* ($p < 0.05$). Further studies of neural mechanisms would report in our coming article.

Discussion

In this study, the new automatic method for individual parcellation of rat brain MEMRI images was constructed. In our proposed procedure, the individual MEMRI images were remained untransformed, so the inherent voxel intensity could be preserved. It would further be beneficial to case-control ROI-based statistical analyses.

Compared with our previous work, the individual parcellation method proposed in this study could perform more precisely. Firstly, in this study, widespread image registration methods were adopted. Especially, by DARTEL algorithm, individual images could be normalized into the template space *via* a set of tissue probability maps iteratively (Zhang et al., 2022). However, it couldn't be adopted by our previous work, for the lacking of tissue probability maps in individual space. Therefore, although the DARTEL algorithm has been recognized as a more accurate method, it couldn't be used in transforming the standard space to an individual space. On the other hand, the template has also been regarded as a representative image, so transforming the individual image to register with the template would have higher accuracy.

In spatial normalization, the MEMRI images could be firstly normalized into the standardized space *via* both template way and DARTEL way, that there was also a preferential suggestion. When the individual MRI image has a nearly isotropic resolution, the DARTEL algorithm would perform better than the template way. Otherwise, the template-based method would be more suitable, for its higher arithmetic speed. In the current study, the time course of MEMEI was preferentially considered, so the image resolution was not better enough to use the DARTEL way. Therefore, for demonstration, the MEMRI images were performed in the template way, while the corresponding T2WI structural images were in the DARTEL way.

The parcellation boundary is a problem when transforming the atlas image. Traditionally, in order to protect the ROI index, the nearest neighbor interpolation method was frequently used in atlas image transformations, so that the parcellation boundary

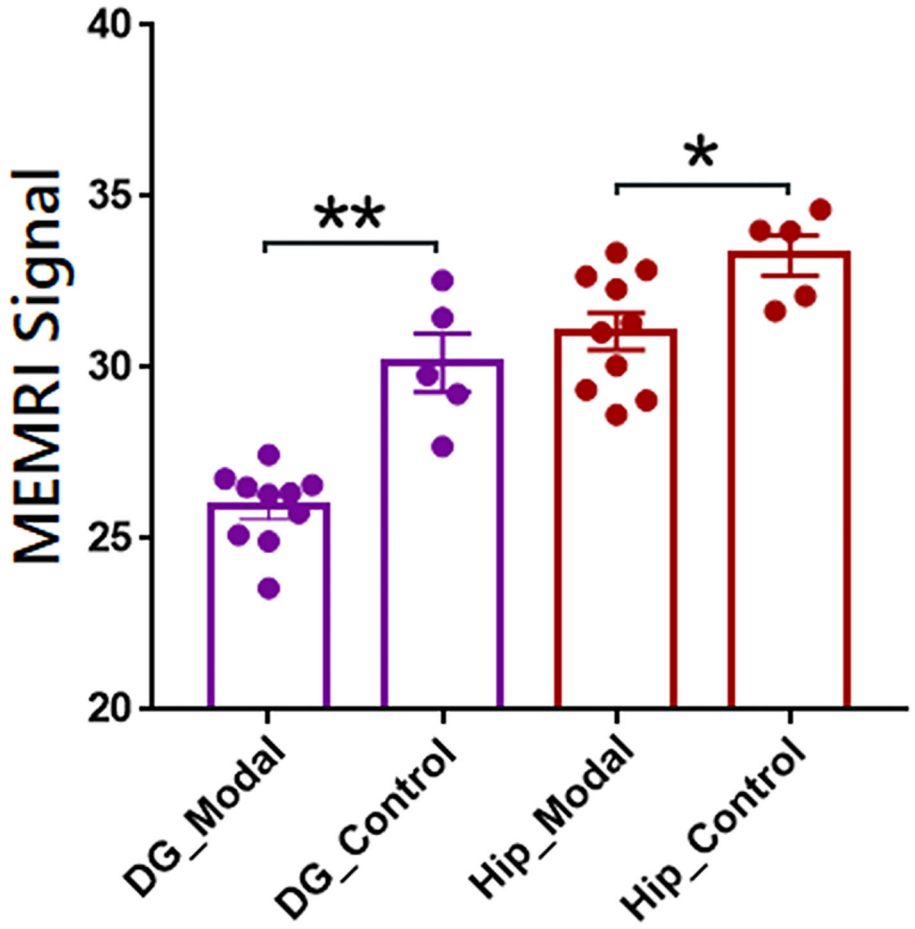

FIGURE 4
Regions of interest-based quantitative analysis results of MEMRI images between modal and healthy rats. The mean MEMRI signal in bilateral dentate gyrus (purple) and hippocampus (red) were shown as mean ± SE. $^{**}p < 0.001$; $^{*}p < 0.05$; DG, dentate gyrus; Hip, hippocampus.

was always dentate. To address this issue, we separated all the ROIs into a new binary mask image prior to transformation, and the 4th B-spline interpolation method was chosen. Moreover, the transformed boundary was further refined by erosion and expansion operators after transformation. By this strategy, our parcellation boundary in individual space would be smooth.

The usage and accuracy of a newly developed method are always evaluated by applications in various studies. In this study, a group of modal rats with smell damage was used, and two representative ROIs were selected. As demonstrated in the figures, compared with parcellations in standardized space, the inherent MEMRI intensity could be preserved in individual space, which was in line with the previous studies (Salehi et al., 2020; Reijonen et al., 2021; Wang et al., 2021). Image interpolation is ineluctable in image registration. However, the enhanced voxels are always subtle in MEMRI images, which would be influenced by adjacent un-enhanced voxels in image interpolation. Therefore, the image intensity in standard space is always lower than individual space. Moreover, although the downtrend of MEMRI time courses was similar, the slope is different.

Actually, the individual parcellation method proposed in this study could be applied to other imaging modalities of rat brain studies, such as functional MRI (fMRI), positron emission tomography (PET), diffusion tensor imaging (DTI), and so on. The operation was similar to MEMRI studies, except for choosing the corresponding modality template image (Figure 1-*Step 1a*). If the DARTEL algorithm was chosen (Figure 1-*Step 1b*), all the operations were the same with MEMRI studies.

Moreover, this method could also be generalized in data analyses of other species as long as there is a stereotaxic template set, such as human beings, monkeys, mice, tree shrews, and so on. In our released package, these species were all included based on our previous works of stereotaxic templates constructions.

Finally, there are some notes that should be pointed out. Firstly, the individual parcellations would be inaccurate if the

corresponding image could not be successfully registered into the standardized space. Secondly, the origin of individual images should be manually set to the same point as template, such as the D3V in rat brain studies (Nie et al., 2013). Thirdly, in rodent brain studies, the image voxel size should be enlarged ten times before spatial normalization. Finally, this individual parcellation method was not suitable in cerebral tumor or infarction imaging studies. Because the sub-anatomical structures are deformed, the traditional template or TPM cannot register the image into standardized space accurately.

Conclusions

In this study, we have constructed a new automatic method for individual parcellation of rat brain MEMRI images, which could preserve the inherent voxel intensity and further be beneficial to case-control statistical analyses. This method could also be extended to other imaging modalities, even other experiments species. It would facilitate the accuracy and significance of ROI-based imaging analyses.

Data availability statement

The raw data supporting the conclusions of this article will be made available by the authors, without undue reservation.

Ethics statement

The animal study was reviewed and approved by Jiang Su Animal Care and Use Committee.

Author contributions

BN led the project. ZB, TZ, and TP created the figures and wrote the manuscript. TZ established the software. TP carried out the MEMRI data analysis. WZ and SZ made substantial contributions to the manuscript and provided critical comments. All authors contributed to the article and approved the submitted version.

Funding

This work was financially supported by the National Natural Science Foundation of China (12175268 and 11975249).

Conflict of interest

The authors declare that the research was conducted in the absence of any commercial or financial relationships that could be construed as a potential conflict of interest.

Publisher's note

References

Aoki, I., Naruse, S., and Tanaka, C. (2004). Manganese-enhanced magnetic resonance imaging (MEMRI) of brain activity and applications to early detection of brain ischemia. *NMR Biomed.* 17, 569–580. doi: 10.1002/nbm.941

Ashburner, J., Andersson, J. L., and Friston, K. J. (2000). Image registration using a symmetric prior–in three dimensions. *Hum. Brain Mapp.* 9, 212–25. doi: 10.1002/(SICI)1097-0193(200004)9:4<212::AID-HBM3>3.0.CO;2-#

Ashburner, J., and Friston, K. J. (1999). Nonlinear spatial normalization using basis functions. *Hum. Brain Mapp.* 7, 254–66. doi: 10.1002/(SICI)1097-0193(1999)7:4<254::AID-HBM4>3.0.CO;2-G

Barriere, D. A., Magalhaes, R., Novais, A., Marques, P., Selingue, E., Geffroy, F., et al. (2019). The SIGMA rat brain templates and atlases for multimodal MRI data analysis and visualization. *Nat. Commun.* 10, 5699. doi: 10.1038/s41467-019-13575-7

Bearer, E. L., Zhang, X., and Jacobs, R. E. (2022). Studying axonal transport in the brain by manganese-enhanced magnetic resonance imaging (MEMRI). *Methods Mol. Biol.* 2431, 111–142. doi: 10.1007/978-1-0716-1990-2_6

Bible, E., Dell'Acqua, F., Solanky, B., Balducci, A., Crapo, P. M., Badylak, S. F., et al. (2012). Non-invasive imaging of transplanted human neural stem cells and ECM scaffold remodeling in the stroke-damaged rat brain by (19)F- and diffusion-MRI. *Biomaterials* 33, 2858–2871. doi: 10.1016/j.biomaterials.2011.12.033

Chong, M., Bhushan, C., Joshi, A. A., Choi, S., Haldar, J. P., Shattuck, D. W., et al. (2017). Individual parcellation of resting fMRI with a group functional connectivity prior. *Neuroimage* 156, 87–100. doi: 10.1016/j.neuroimage.2017.04.054

Gimenes, C., Malheiros, J. M., Battapady, H., Tannus, A., Hamani, C., and Covolan, L. (2019). The neural response to deep brain stimulation of the anterior nucleus of the thalamus: A MEMRI and c-Fos study. *Brain Res. Bull.* 147, 133–139. doi: 10.1016/j.brainresbull.2019.01.011

Gutierrez, D. F., and Zaidi, H. (2012). Automated analysis of small animal PET studies through deformable registration to an atlas. *Eur. J. Nucl. Med. Mol. Imaging* 39, 1807–1820. doi: 10.1007/s00259-012-2188-7

Ho, Y. J., Weng, J. C., Lin, C. L., Shen, M. S., Li, H. H., Liao, W. C., et al. (2018). Ceftriaxone treatment for neuronal deficits: a histological and MEMRI study in a rat model of dementia with lewy bodies. *Behav. Neurol.* 2018, 4618716. doi: 10.1155/2018/4618716

Jackson, S. J., Hussey, R., Jansen, M. A., Merrifield, G. D., Marshall, I., MacLullich, A., et al. (2011). Manganese-enhanced magnetic resonance imaging (MEMRI) of rat brain after systemic administration of MnCl(2): hippocampal signal enhancement without disruption of hippocampus-dependent behavior. *Behav. Brain Res.* 216, 293–300. doi: 10.1016/j.bbr.2010.08.007

Kim, Y. B., Kalthoff, D., Po, C., Wiedermann, D., and Hoehn, M. (2012). Connectivity of thalamo-cortical pathway in rat brain: combined diffusion

spectrum imaging and functional MRI at 11.7 T. *NMR Biomed.* 25, 943–952. doi: 10.1002/nbm.1815

Koretsky, A. P., and Silva, A. C. (2004). Manganese-enhanced magnetic resonance imaging (MEMRI). *NMR Biomed.* 17, 527–531. doi: 10.1002/nbm.940

Li, R., Liu, X., Sidabras, J. W., Paulson, E. S., Jesmanowicz, A., Nencka, A. S., et al. (2015). Restoring susceptibility induced MRI signal loss in rat brain at 9.4 T: a step towards whole brain functional connectivity imaging. *PLoS ONE* 10, e0119450. doi: 10.1371/journal.pone.0119450

Liang, S., Wu, S., Huang, Q., Duan, S., Liu, H., Li, Y., et al. (2017). Rat brain digital stereotaxic white matter atlas with fine tract delineation in Paxinos space and its automated applications in DTI data analysis. *Magn. Reson. Imaging* 43, 122–128. doi: 10.1016/j.mri.2017.07.011

Liang, S., Zhang, J., Zhang, Q., Li, L., Zhang, Y., Jin, T., et al. (2020). Longitudinal tracing of white matter integrity on diffusion tensor imaging in the chronic cerebral ischemia and acute cerebral ischemia. *Brain Res. Bull.* 154, 135–141. doi: 10.1016/j.brainresbull.2019.10.015

Lv, Q., Yan, M., Shen, X., Wu, J., Yu, W., Yan, S., et al. (2021). Normative analysis of individual brain differences based on a population MRI-based atlas of cynomolgus macaques. *Cereb. Cortex* 31, 341–355. doi: 10.1093/cercor/bhaa229

Mak, H. K., Zhang, Z., Yau, K. K., Zhang, L., Chan, Q., Chu, L. W., et al. (2011). Efficacy of voxel-based morphometry with DARTEL and standard registration as imaging biomarkers in Alzheimer's disease patients and cognitively normal older adults at 3.0 Tesla MR imaging. *J. Alzheimers Dis.* 23, 655–664. doi: 10.3233/JAD-2010-101659

Nie, B., Chen, K., Zhao, S., Liu, J., Gu, X., Yao, Q., et al. (2013). A rat brain MRI template with digital stereotaxic atlas of fine anatomical delineations in paxinos space and its automated application in voxel-wise analysis. *Hum. Brain Mapp.* 34, 1306–1318. doi: 10.1002/hbm.21511

Nie, B., Hui, J., Wang, L., Chai, P., Gao, J., Liu, S., et al. (2010). Automatic method for tracing regions of interest in rat brain magnetic resonance imaging studies. *J. Magn. Reson. Imaging* 32, 830–835. doi: 10.1002/jmri.22283

Perez, P. D., Hall, G., Zubcevic, J., and Febo, M. (2018). Cocaine differentially affects synaptic activity in memory and midbrain areas of female and male rats: an in vivo MEMRI study. *Brain Imaging Behav.* 12, 201–216. doi: 10.1007/s11682-017-9691-1

Reijonen, J., Kononen, M., Tuunanen, P., Maatta, S., and Julkunen, P. (2021). Atlas-informed computational processing pipeline for individual targeting of brain areas for therapeutic navigated transcranial magnetic stimulation. *Clin. Neurophysiol.* 132, 1612–1621. doi: 10.1016/j.clinph.2021.01.037

Salehi, M., Greene, A. S., Karbasi, A., Shen, X., Scheinost, D., Constable, R. T., et al. (2020). There is no single functional atlas even for a single individual: functional parcel definitions change with task. *Neuroimage* 208, 116366. doi: 10.1016/j.neuroimage.2019.116366

Spurny, B., Heckova, E., Seiger, R., Moser, P., Klobl, M., Vanicek, T., et al. (2019). Automated ROI-based labeling for multi-voxel magnetic resonance spectroscopy data using FreeSurfer. *Front. Mol. Neurosci.* 12, 28. doi: 10.3389/fnmol.2019.00028

Tang, X., Wu, D., Gu, L. H., Nie, B. B., Qi, X. Y., Wang, Y. J., et al. (2016). Spatial learning and memory impairments are associated with increased neuronal activity in 5XFAD mouse as measured by manganese-enhanced magnetic resonance imaging. *Oncotarget* 7, 57556–57570. doi: 10.18632/oncotarget.11353

Tu, T. W., Kovacs, Z. I., Sundby, M., Witko, J. A., Papadakis, G. Z., Reid, W. C., et al. (2020). Diffusion tensor imaging and chemical exchange saturation transfer MRI evaluation on the long-term effects of pulsed focused ultrasound and microbubbles blood brain barrier opening in the rat. *Front. Neurosci.* 14, 908. doi: 10.3389/fnins.2020.00908

Wang, H., Sun, J., Cui, D., Wang, X., Jin, J., Li, Y., et al. (2021). Quantitative assessment of inter-individual variability in fMRI-based human brain atlas. *Quant. Imaging Med. Surg.* 11, 810–822. doi: 10.21037/qims-20-404

Wang, J., Hao, Z., and Wang, H. (2018). Generation of individual whole-brain atlases with resting-state fMRI data using simultaneous graph computation and parcellation. *Front. Hum. Neurosci.* 12, 166. doi: 10.3389/fnhum.2018.00166

Wang, S., Tryggestad, E., Zhou, T., Armour, M., Wen, Z., Fu, D. X., et al. (2012). Assessment of MRI parameters as imaging biomarkers for radiation necrosis in the rat brain. *Int. J. Radiat. Oncol. Biol. Phys.* 83, e431–e436. doi: 10.1016/j.ijrobp.2011.12.087

Yang, J., Gao, J., Han, D., Li, Q., Liao, C., Li, J., et al. (2020). Hippocampal changes in inflammasomes, apoptosis, and MEMRI after radiation-induced brain injury in juvenile rats. *Radiat. Oncol.* 15, 78. doi: 10.1186/s13014-020-01525-3

Zhang, T., Nie, B., Liu, H., and Shan, B., Alzheimer's Disease Neuroimaging Initiative (2022). Unified spatial normalization method of brain PET images using adaptive probabilistic brain atlas. *Eur. J. Nucl. Med. Mol. Imaging* 49, 3073–3085. doi: 10.1007/s00259-022-05752-6

Zhilkin, P., and Alexander, M. E. (2004). Affine registration: a comparison of several programs. *Magn. Reson. Imaging* 22, 55–66. doi: 10.1016/j.mri.2003.05.004

frontiers | Frontiers in Neuroscience

TYPE Original Research
PUBLISHED 29 July 2022
DOI 10.3389/fnins.2022.968767

OPEN ACCESS

EDITED BY
Jie Wang,
Wuhan Institute of Physics and Mathematics (CAS), China

REVIEWED BY
Qi Huang,
Fudan University, China
Juan Li,
Chengdu University of Traditional Chinese Medicine, China

*CORRESPONDENCE
Jia Huang
jasmine1874@163.com

†These authors have contributed equally to this work

SPECIALTY SECTION
This article was submitted to Brain Imaging Methods, a section of the journal Frontiers in Neuroscience

RECEIVED 14 June 2022
ACCEPTED 11 July 2022
PUBLISHED 29 July 2022

CITATION
Lin B, Zhang L, Yin X, Chen X, Ruan C, Wu T, Liu Z and Huang J (2022) Modulation of entorhinal cortex–hippocampus connectivity and recognition memory following electroacupuncture on 3×Tg-AD model: Evidence from multimodal MRI and electrophysiological recordings. *Front. Neurosci.* 16:968767. doi: 10.3389/fnins.2022.968767

Modulation of entorhinal cortex–hippocampus connectivity and recognition memory following electroacupuncture on 3×Tg-AD model: Evidence from multimodal MRI and electrophysiological recordings

Bingbing Lin[1†], Lanlan Zhang[2†], Xiaolong Yin[1,3†], Xiaocheng Chen[1], Chendong Ruan[1], Tiecheng Wu[4], Zhizhen Liu[2] and Jia Huang[1*]

[1]College of Rehabilitation Medicine, Fujian University of Traditional Chinese Medicine, Fuzhou, China, [2]TCM Rehabilitation Research Center of State Administration of Traditional Chinese Medicine (SATCM), Fujian University of Traditional Chinese Medicine, Fuzhou, China, [3]National-Local Joint Engineering Research Center of Rehabilitation Medicine Technology, Fujian University of Traditional Chinese Medicine, Fuzhou, China, [4]Key Laboratory of Orthopedics & Traumatology of Traditional Chinese Medicine and Rehabilitation, Ministry of Education, Fuzhou, China

Memory loss and aberrant neuronal network activity are part of the earliest hallmarks of Alzheimer's disease (AD). Electroacupuncture (EA) has been recognized as a cognitive stimulation for its effects on memory disorder, but whether different brain regions or neural circuits contribute to memory recovery in AD remains unknown. Here, we found that memory deficit was ameliorated in 3×Tg-AD mice with EA-treatment, as shown by the increased number of exploring and time spent in the novel object. In addition, reduced locomotor activity was observed in 3×Tg-AD mice, but no significant alteration was seen in the EA-treated mice. Based on the functional magnetic resonance imaging, the regional spontaneous activity alterations of 3×Tg-AD were mainly concentrated in the accumbens nucleus, auditory cortex, caudate putamen, entorhinal cortex (EC), hippocampus, insular cortex, subiculum, temporal cortex, visual cortex, and so on. While EA-treatment prevented the chaos of brain activity in parts of the above regions, such as the auditory cortex, EC, hippocampus, subiculum, and temporal cortex. And then we used the whole-cell voltage-clamp recording to reveal the neurotransmission in the hippocampus, and found that EA-treatment reversed the synaptic spontaneous release. Since the hippocampus receives most of the projections of the EC, the hippocampus-EC circuit is one of the neural

circuits related to memory impairment. We further applied diffusion tensor imaging (DTI) tracking and functional connectivity, and found that hypo-connected between the hippocampus and EC with EA-treatment. These data indicate that the hippocampus–EC connectivity is responsible for the recognition memory deficit in the AD mice with EA-treatment, and provide novel insight into potential therapies for memory loss in AD.

KEYWORDS

Alzheimer's disease, electroacupuncture, recognition memory, functional connectivity, electrophysiology

Introduction

Alzheimer's disease (AD), the most common cause of dementia, is a progressive neurologic disorder that irreversible anatomical, cognitive, and behavioral deficits leading to affect a person's ability to function independently. As the disease processes, patients present with varying manifestations of cognitive decline including memory loss, thinking, reasoning skills, and language impairment (Wattmo and Wallin, 2017; Kamiya et al., 2018; Lane et al., 2018). The memory problem is a core symptom, notably, recognition memory is one of the first warning signatures of AD (Russo et al., 2017; Goldstein et al., 2019). Although there is no currently approved cure for AD, promising treatments emerge including trials aimed at preventing memory loss in early AD.

Increasing clinical and experimental studies have confirmed the efficacy of electroacupuncture (EA) on cognitive dysfunction (Wang et al., 2020; Yu et al., 2020; Yin et al., 2022). EA has been recognized as a crucial treatment in traditional Chinese medicine (TCM), which applies the inserted needles with an electric stimulating current to the acupoints. Clinical trials have shown that EA-treatment improved cognitive outcomes in early and mid-stage AD patients, and notably on memory function in AD prodromal patients (Deng and Wang, 2016; Jia et al., 2017; Lin et al., 2022). A review summarized that EA at acupoints such as Baihui (DU20), Shenting (DU24), and Neiguan (PC6) effectively improve the score of cognitive tests in patients with cognitive impairment, respectively (Yin et al., 2021). Our previous clinical study showed that EA at DU20/DU24 could effectively improve the score of MMSE and MoCA in patients with cognitive impairment (Jiang et al., 2016). Furthermore, animal studies also demonstrated altered behaviors in memory-loss rodents after EA-treatment (Huang et al., 2016). It has been described possible potential mechanisms such as regulation of synaptic plasticity and neuroinflammation in rodent models of AD. Besides, synaptic dysfunction is thought to lead to a chaos of functional brain activity in early AD (Sperling et al., 2011). Previous clinical and animal studies reported that EA-induced cognitive enhancement is closely related to the hippocampus (Hip) (Wang et al., 2014; Zheng et al., 2018, 2021; Li et al., 2021). Moreover, it could be speculated that in addition to hippocampal synaptic plasticity, EA-treatment could have other neuromodulation mechanisms that regulate memory function.

Compelling evidence demonstrated that altered recognition memory in both cognitive impairment patients and animals is potentially associated with changes in regional spontaneous activities and neural connectivity, including the hippocampal-cortex network (Matura et al., 2014; De Marco et al., 2017; Tanimizu et al., 2018; Salimi et al., 2022). Previous studies found that EA not only increased the neuronal activity of the hippocampus in mild cognitive impairment (MCI) patients but also enhanced the functional connections between brain regions (Tan et al., 2017). In addition to the functional connectivity (FC) and neuronal activity, the neuronal fiber connections revealed by diffusion tensor imaging (DTI) can also reflect the structural connectivity between brain regions. Studies showed that AD patients have lower nerve fiber density in the hippocampus than healthy elderly people, and it is positively correlated with memory behavior (Mayo et al., 2017, 2018). In the AD early stage, a gradual disruption of synapse and neuronal connections appear in parts of the brain regions dedicated to object recognition memory, particularly the entorhinal cortex (EC) and Hip (Braak et al., 2011). Evidence showed that functional and structural alterations in EC and Hip can be suggested as potential biomarkers for early AD (Devanand et al., 2007). Generally accepted that the EC–Hip

Abbreviations: AD, Alzheimer's disease; EA, electroacupuncture; Hip, hippocampus; MCI, mild cognitive impairment; DTI, diffusion tensor imaging; EC, entorhinal cortex; OFT, open field test; NORT, novel object recognition test; sEPSC, spontaneous postsynaptic currents; PCR, polymerase chain reaction; rs-fMRI, resting-state functional magnetic resonance imaging; T2WI, T2-weighted images; EPI, echo-planar imaging; FC, function connectivity; ROIs, regions of interest; ACSF, artificial cerebrospinal fluid; KCC, Kendall's coefficient of concordance.

interaction is pivotal for memory processing. However, the role of neuronal activities and neural connectivity alterations in the EC–Hip network in EA-induced memory recovery of AD remains unknown.

Therefore, the objective of the present study was to elucidate a comprehensive mechanism for the effects of EA on recognition memory deficits in AD. We hypothesized that EA treatment can regulate neuronal activities and neural connectivity in the EC–Hip network, and improve recognition memory. In this study, the open field test (OFT) and novel object recognition test (NORT) were performed after treatment, according to the time point of memory enhancement by EA-treatment in previous animal studies. We then employed 7.0 T resting-state functional magnetic resonance imaging (rs-fMRI) to observe where and to what extent neuronal activities take place in the brain after treatment. The hippocampus, which is thought to be the hub of memory-related networks in AD, showed changes with EA-treatment. To investigate if synaptic neurotransmission of the hippocampus was influenced by the EA-treatment, the spontaneous postsynaptic currents (sEPSC) recording at the hippocampal CA1 was measured. Finally, FC and DTI tracking were applied to detect the connections on hippocampal-related networks. The knowledge on how EA modulates neuronal activities and neural connectivity in AD mice will provide insight toward developing an effective strategy to overcome memory impairments.

Material and methods

Animals

Five months 3×Tg-AD mice and age-matched littermate wildtype-controls were used in the experiments (AD: n = 30, wildtype: n = 10). Male 3×Tg-AD transgenic mice express mutant human APPSwe, human PS1 (M146V) and mutant tau (P301L), thus mimicking pathological features of human AD. The offspring were genotyped by polymerase chain reaction (PCR) analysis using tail DNA to confirm the presence of mutant genes. The mice were housed in cages of up to 5 and kept in the standard environmental conditions, under a 12-h light/dark cycle and room temperature, with food and water provided *ad libitum*. All procedures using mice were approved by Fujian University of Traditional Chinese Medicine Animal Experiment Ethics Committee and Authority (ethical animal permission no. FJTCM IACUC2019031).

Electroacupuncture stimulation

The homozygous 3×Tg-AD mice were randomly assigned to three groups by the random digital table: EA-treated (EA group), non-acupoint EA-treated (Non-EA group), and control untreated mice (3×Tg AD group), age-matched littermate wildtype-controls was assigned to the WT group. The EA stimulation was performed with a disperse-dense-mode stimulation at an intensity level of 1 mA and a frequency of 1/20 Hz by using a stimulator (model G6805, Suzhou Medical Appliance Factory, Shanghai, China) for 30 min daily, 5 consecutive days weekly, 4 weeks. Before stimulation was initiated, the torso of the mice was fixed to restrict excessive mobility. EA stimulation was applied at either the DU20(Baihui)/DU24(Shenting) or the non-acupoints by inserting the 0.25 × 13 mm stainless steel acupuncture needle (Hwato, China) about 2–3 mm depth in each site. For the EA group, the mice received EA stimulation at DU20 and DU24 acupoints. The DU20 acupoint is located at the midline of the head, approximately midway on the line connecting the apices of the auricles. The DU24 acupoint is located at 2 mm directly above the midpoint of the mouse's eyes in **Supplementary Figure 1A**. For the Non-EA group, the EA stimulation was applied at non-acupoints for acupoint control, which were chosen to avoid the DU meridian and nearby acupoints. The bilateral non-acupoints are located at the bilateral hypochondrium, 2 cm above the posterior superior iliac spine and 3 cm lateral to the spine in **Supplementary Figure 1B**. The mice in the 3×Tg AD group and WT group (littermate controls) were fixed in the same way for 30 min without EA stimulation. The study timeline with all manipulations is presented in **Figure 1A**.

Behavioral and cognitive testing

The locomotor activity was determined by OFT. Recognition memory was assessed in a NORT that involves exploration activity that responds to novelty. The locomotor activity was assessed 1-day post-treatment, and NORT conduct 2-days post-treatment.

All the tests were recorded using a digital USB camera (Super HAD CCD; SONY, Japan). The video tracking was processed using a video tracking system and SuperMaze analysis system (XR-Xmaze, Shanghai Soft maze Information Technology Co., Ltd., China). The testing apparatuses of OFT and NORT were thoroughly cleaned with 10% ethanol between animals. The measurements were carried out in a quiet environment with the background noise controlled at ≤60 dB.

Locomotor activity

After habituation, the animal was placed into one corner of an open field arena (50 × 50 × 40 cm) that was divided into peripheral and central zones, and locomotor activity was measured for 5 min by total distance traveled and time spent in the central zones.

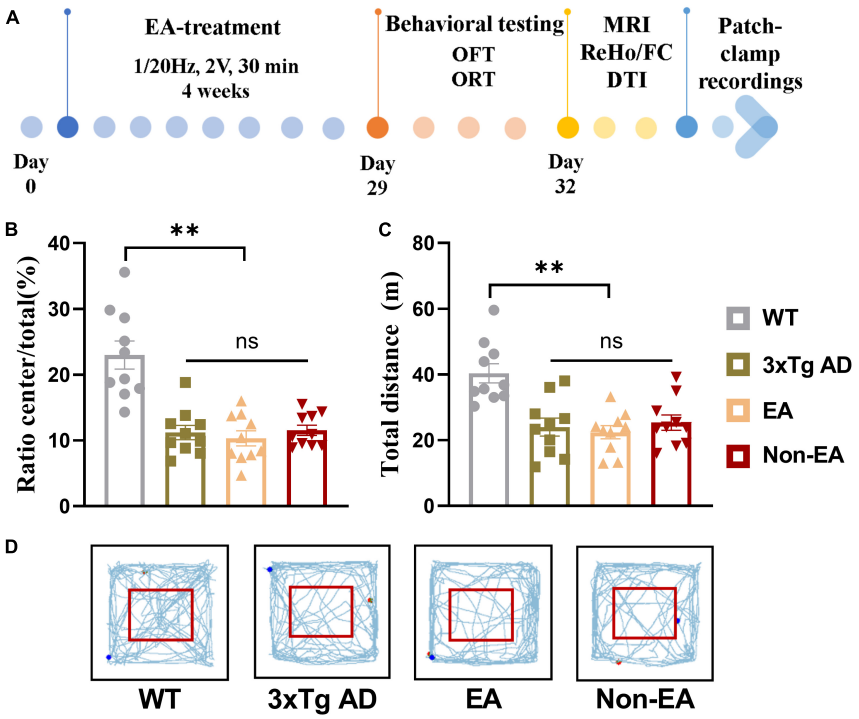

FIGURE 1
Effect of EA-treatment on locomotor activity in 3×Tg AD mice. **(A)** A schematic of the experimental design. Quantification of behavioral results in open field test (n = 10 in each group), involving **(B)** the percentage of time in the central zone, **(C)** the total distance traveled throughout the field, **(D)** and the trajectories of mice in the open field. All data represent the mean ± SEM. $^{**}P < 0.01$; ns, there was no significant difference.

Novel object recognition testing

Novel object recognition test was conducted in the arena where the OFT was performed the day before, and the habituation phase was considered negligible. During the training phase, the animal was familiarized with two identical objects for 10 min, and then was returned to its home cage for 24 h, after which the testing phase took place. During the recognition phase, the animal was placed back into the arena which contain one of familiar objects and a novel object for 10 min. The choice to explore the novel object was considered to be the use of learning and long-term recognition memory. Exploration times and times are counted for the nose/head or paws entering the object area (about 2 cm around the object). The recognition index (time) was calculated as time spent with the novel object/time spent with both objects. The recognition index (number) was calculated as number of exploring the novel object/numbers of exploring both objects ×100.

Magnetic resonance brain imaging protocols

Magnetic resonance imaging was acquired by Bruker 7.0T scanner (MiniMR-60 MRI system 7.0 T), and rs-fMRI and DTI were performed 10-day post-treatment. During the scan, an animal physiological detector (SurgiV et V3395TPR, Smiths Medical, United States) was used to monitor the body temperature, blood oxygen saturation and respiration of mice. The temperature control and ventilation system were used to maintain the stability of the physiological state throughout the experiment. Standardized anesthesia protocols and animal monitoring procedures were administered. Mice were initially anesthetized with 4% isoflurane (RWD, China) in a 1:4 O_2 air mixture for 4 min, and then were placed on an MRI-compatible stand equipped with a hot water flow bed to maintain the animal temperature at 36.5 ± 0.5°C throughout the measurements. Mice were immobilized with ear rods and mechanically ventilated by a ventilator at a rate of 80 beats/min at a flow rate of 1.8 ml/min and a flow rate of 0.5-0.75% isoflurane. The blood oxygen saturation was kept above 95% throughout the scan, and the respiratory rate was 80–120 beats/min. Data analysis was performed by an experimenter blind to group information.

Functional magnetic resonance imaging acquisition

The acquisition parameters were as follows: T2-weighted images (T2WI) using TurboRARE sequence: TR/TE = 4,200/35 ms, field of view = 20 × 20 mm, averages = 4, image size = 256 × 256, slices = 30, slice thickness = 0.5 mm;

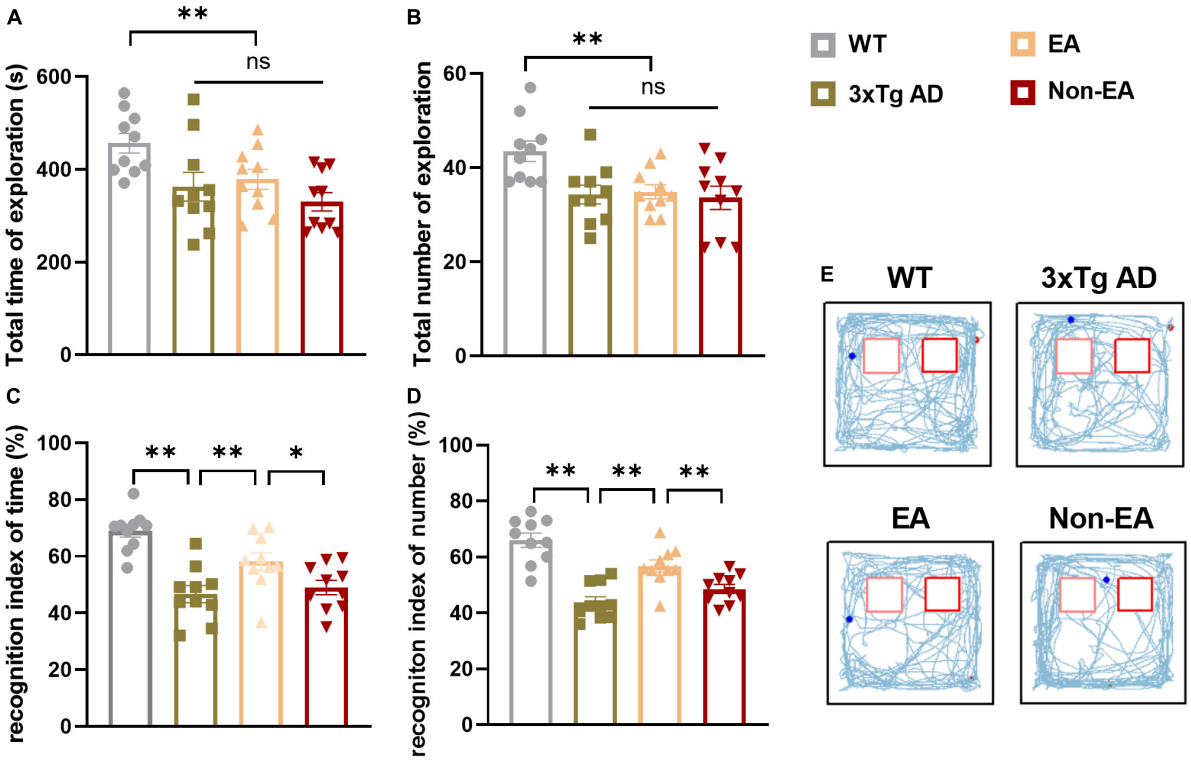

FIGURE 2
Effect of EA-treatment on recognition memory in 3×Tg-AD mice. Quantification of exploratory activity in ORT (n = 10 in each group), involving **(A)** the total time spent exploring, and **(B)** the total number of visits to both objects. Quantification of recognition memory, involving **(C)** the recognition index of time, **(D)** and the recognition index of number during probe test. **(E)** The trajectories of mice during probe test in the ORT. All data represent the mean ± SEM. *P < 0.05; **P < 0.01; ns, there was no significant difference.

rs-fMRI using an echo-planar imaging (EPI) sequence: TR/TE = 2,000/10.28 ms, field of view = 20 × 20 mm, repetitions = 200, image size = 64 × 64, slices = 30, slice thickness = 0.5 mm. The original image data was exported to DICOM format data by Paravision 6.0.1 software.

The rs-fMRI image data was carried out using Statistical Parametric Mapping (SPM8[1]) and the Data Processing Assistant for Resting-State fMRI (DPARSF[2]) software package (Wu et al., 2017). For the ReHo data, pre-processed with the following major steps: (1) The data of the first 10 time points were discarded for time calibration. (2) Time-slice correction. (3) Head movement correction. (4) Spatial standardization. (5) Detrend and filter: images were removed linear trend and the 0.01–0.08 Hz frequency band is used to perform time-space mean filtering on the data. The FC data preprocessing process is the same as that of ReHo, but spatial smoothing is performed in advance. Where the head movement translation is greater than 1.5 mm or the rotation angle exceeds 1.5°, the data is rejected.

1 http://www.fil.ion.ucl.ac.uk/spm
2 http://www.restfmri.net/forum/DPARSF

ReHo analysis

ReHo is a local measure of the temporal similarity between a particular voxel and its neighbors, and is used to assess the strength of functional synchronization in local brain regions (Zang et al., 2004). Use Kendall's coefficient of concordance (KCC) to define the ReHo value of the center voxel. Individual ReHo maps were generated by calculating the KCC value of the time series for a given voxel with its nearest neighbors, and smoothened by Gaussian kernel with a 1.5× voxel size Full Width of Half Maximum (FWHM) to improve the signal-to-noise ratio (SNR) for further statistical analysis. Voxel-wise statistics were performed with one-way analysis of variance (ANOVA) to determine the difference among all groups. The threshold for statistical significance was set at P = 0.005.

Seed-to-seed functional connectivity

According to the analysis results of ReHo, the bilateral EC and hippocampus were selected as regions of interest (ROIs). The average time series of the time series of all voxels in the region of interest was extracted, and then the correlation coefficient of the time series of signals between the EC and the hippocampus was calculated to obtain the FC strength, which was subjected to one-way ANOVA.

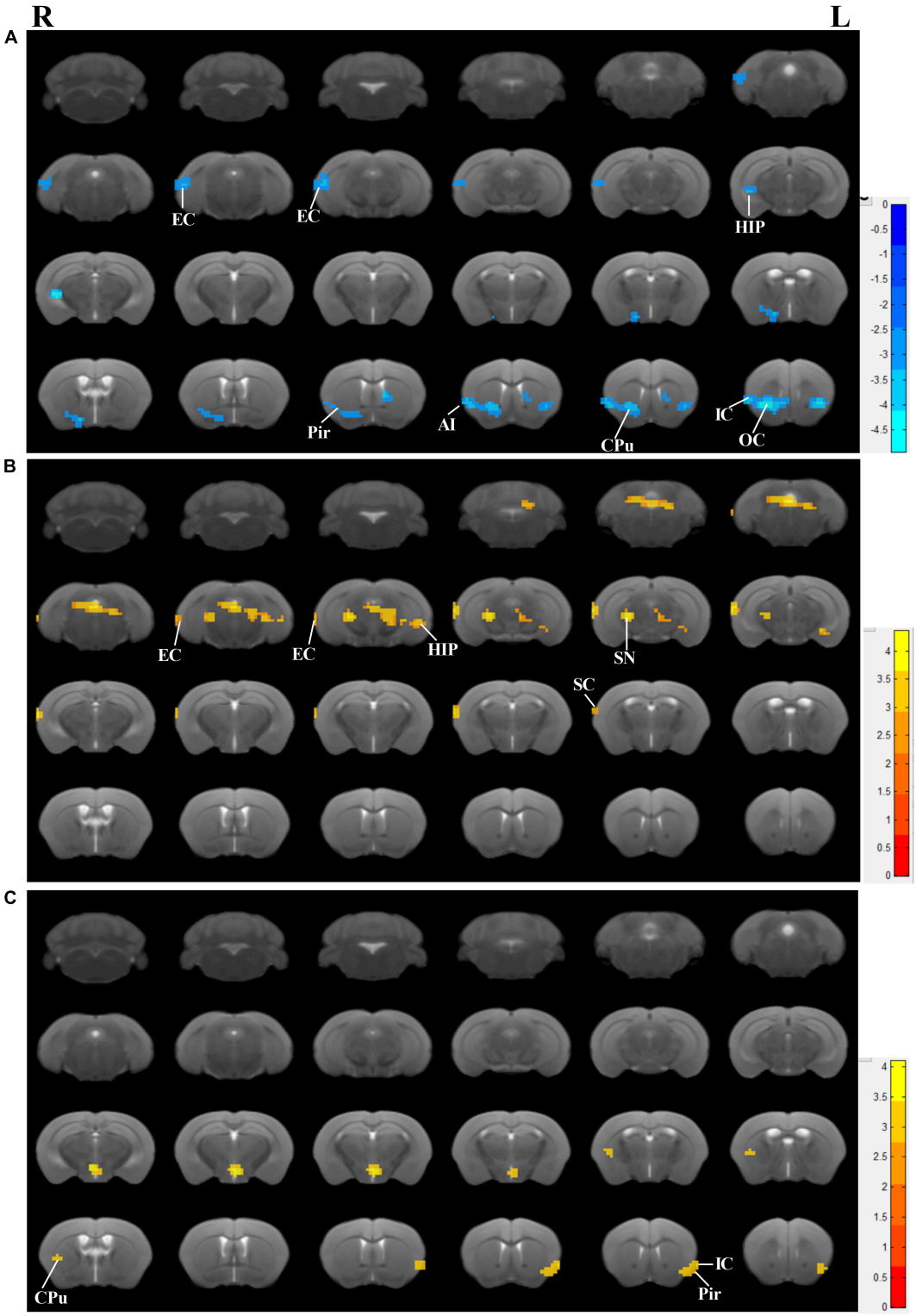

FIGURE 3
Effects of the EA-treatment on regional spontaneous activity. **(A)** Regions manifesting significant ReHo value differences between 3×Tg-AD mice and wildtype-control mice (blue, 3×Tg-AD < wildtype-control; color bar represents significance of difference), **(B)** between EA-treated and untreated 3×Tg-AD mice (red, untreated 3×Tg-AD < EA-treated; color bar represents significance of difference), and **(C)** between Non-EA-treated and untreated 3×Tg-AD mice (red, untreated 3×Tg-AD < Non-EA-treated; color bar represents significance of difference). EC, entorhinal cortex; HIP, hippocampus; Pir, piriform cortex; CPu, caudate putamen; OC, orbital cortex; IC, insular cortex; SC, somatosensory cortex; SN, substantia nigra.

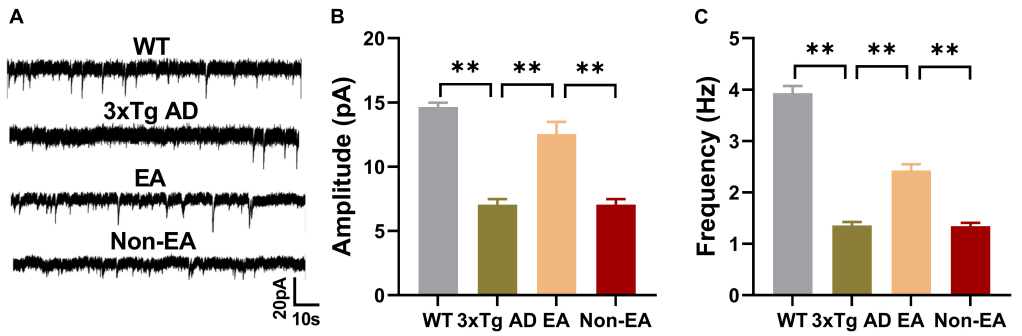

FIGURE 4
Effects of the EA-treatment on hippocampal synaptic neurotransmission. **(A)** Representative sEPSC traces of hippocampal CA1 from all mice by whole-cell voltage-clamp recording (n = 5 in each group). **(B)** The amplitude of sEPSC, and **(C)** the frequency of spontaneous firing of hippocampal CA1 were analyzed. Data are presented as the mean ± SEM. $^{**}P < 0.01$.

Diffusion tensor image acquisition

Diffusion tensor image scanning equipment and environment are the same as those of resting-state imaging. Unlike the resting-state imaging scans, the ventilator was mechanically ventilated at a rate of 80 beats/min with a flow rate of 3 ml/min and a flow rate of 1–1.5% isoflurane. The blood oxygen saturation was kept above 95% throughout the scan, and the respiratory rate was controlled at 60–90 beats/min to reduce head movement.

The acquisition parameters were as follows: a standard gradient-echo echo planar imaging sequence was used: TR = 12,000 ms, TE = 33 ms, averages = 2, FOV = 20 mm × 20 mm, image size = 96 × 96, slices = 30, slice thickness = 0.5 mm, b values = 1,000 s/mm^2, number of diffusion directions = 30.

DICOM format data was converted to NIfTI format data by MRIcron software. Fiber tracking was performed using the TrackVis image processing software and the FACT algorithm. By registering the mouse standard brain template to the b0 image, the conversion relationship from standard space to individual space is obtained. Using this transformation relationship, the mask images of the bilateral EC and bilateral hippocampus in the Paxinos atlas space were transformed into the individual space, that is, the corresponding EC and hippocampus mask images of each mouse individual space were obtained. They were then identified as ROIs, and the number of nerve fibers between the two ROIs in each group of mice was measured. The statistical analysis of nerve fibers among groups was subjected to one-way ANOVA.

Patch-clamp recordings

Mice were deeply anesthetized with isoflurane (RWD, China) and the brains were rapidly removed. The brain was placed in ice-cold artificial cerebrospinal fluid (ACSF) saturated with an oxygen gas mixture (95% O_2 + 5% CO_2) for 30 s. ACSF main components (in mM): 124 NaCl, 3.3 KCl, 1.2 KH_2PO_4, 26 $NaHCO_3$, 2.5 $CaCl_2$, 1.2 $MgSO_4$, 10 glucose (pH = 7.3). Coronal slices of 400 μm were cut with a vibrating slicer (VT 1000s; Leica) and kept at 20–25°C in ACSF saturated with 95% O_2/5% CO_2 for at least 1 h before recording.

The deep layer neurons in hippocampal CA1 neurons were viewed under a Nikon microscope equipped with a 40× water immersion objective and a high-performance charge-coupled device camera. The pipette (6–9 MΩ) was filled with an internal solution (in mM, 124 NaCl, 2.5 KCl, 1.2 NaH_2PO_4, 24 Na HCO_3, 5 HEPES, 12.5 D-glucose, 2.0 $CaCl_2$, 1.5 $MgSO_4$, QX-314 1.5 mmol/L). GABA receptor blocker (picrotoxin, 50 μM, Sigma) was added to the perfused ACSF. The sEPSC recordings were made at a holding membrane potential of −70 mV. Voltage and currents were recorded with a 700A Axon patch amplifier (Axon Instruments, United States). Data were digitized (Digidata 1322 digitizer; Molecular Devices, United States) and stored (Clampfit, version 10.6, Axon, United States). Off-line data of sEPSC analysis was performed using the Mini Analysis software (6.0, Synaptosoft, United States) and Origin 8.0 (OriginLab Corporation, United States). The amplitude and frequency of sEPSC were analyzed.

Statistical analysis

The data are presented as the mean ± standard error of mean (SEM). To compare discrepancies among groups, data from behavioral tests and sEPSC were performed statistical analysis by one-way ANOVA using SPSS 26.0, followed by the *post hoc* test. If the variances were homogeneous, the Turkey-Kramer HSD test was used as a *post hoc* test. If the variances were not homogeneous, the Dunnett's T3 test was used as a *post hoc* test. The data from ReHo, FC and DTI were tested for correlations with ORT data using Pearson

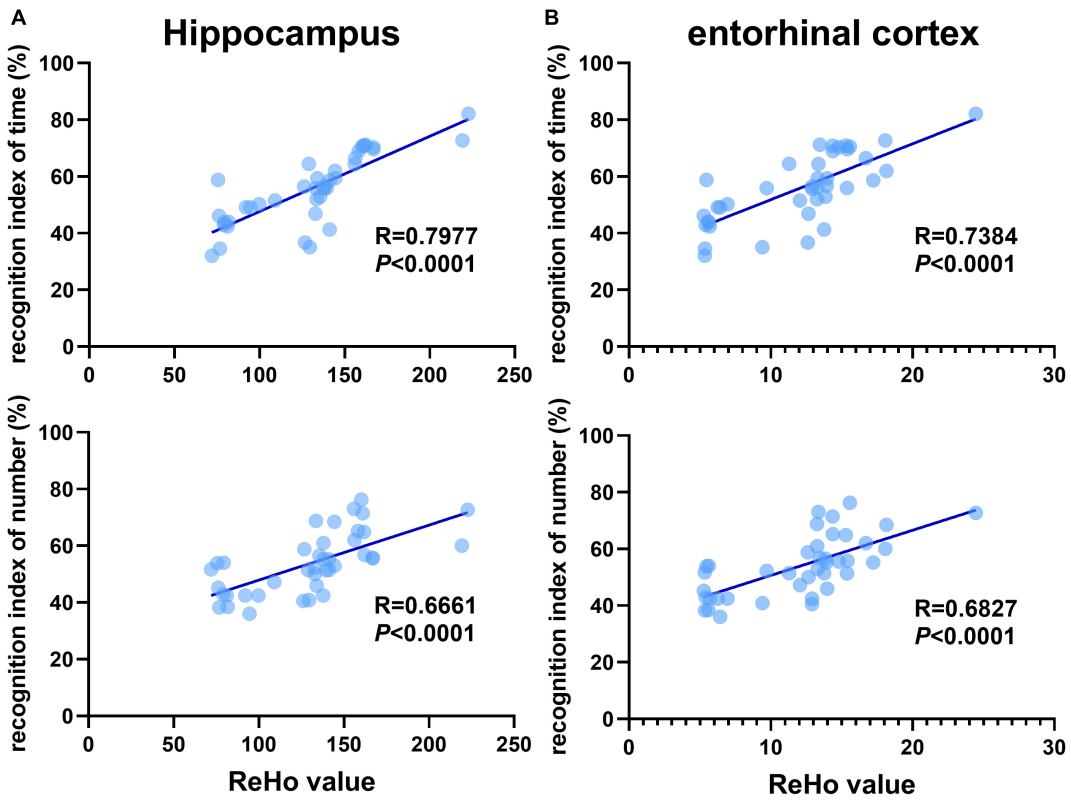

FIGURE 5
Recognition memory is correlated with aberrant ReHo across the hippocampus and entorhinal cortex. Correlational analysis between the recognition indexes (time/number) and ReHo value obtained from the **(A)** hippocampus, **(B)** entorhinal cortex (n = 10 in each group).

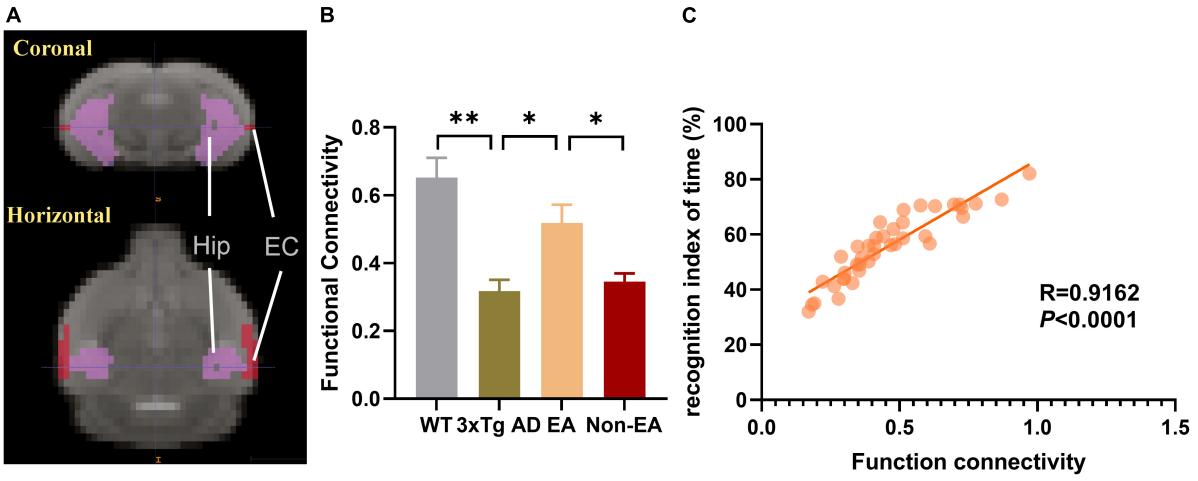

FIGURE 6
Effects of the EA-treatment on function connectivity between the hippocampus and entorhinal cortex. **(A)** Representative location image of hippocampus and entorhinal cortex. **(B)** Quantification of the function connectivity strength between the hippocampus and entorhinal cortex, **(C)** and the correlational analysis between the recognition index of time and function connectivity (n = 10 in each group). All data represent the mean ± SEM. $^{*}P < 0.05$; $^{**}P < 0.01$.

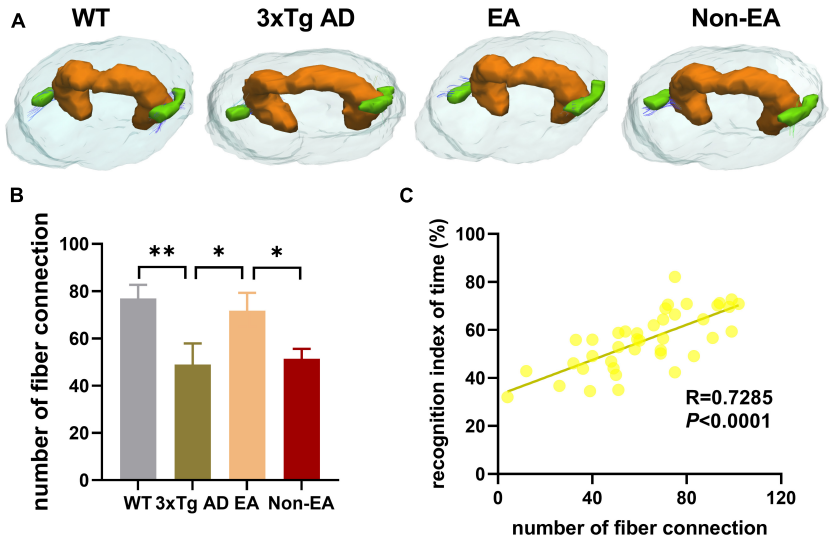

FIGURE 7
Effects of the EA-treatment on fiber connection between the hippocampus and entorhinal cortex. **(A)** Representative image of connected nerve fibers between hippocampus and entorhinal cortex in all group. **(B)** Quantification of the number of nerve fibers connection between the hippocampus and entorhinal cortex, **(C)** and the correlational analysis between the recognition index of time and the number of nerve fibers connection (n = 10 in each group). All data represent the mean ± SEM. $^{*}P < 0.05$; $^{**}P < 0.01$.

linear regression analysis, respectively. $P < 0.05$ was considered statistically significant.

Results

Effects of the electroacupuncture treatment on behavioral and cognitive impairments

As shown in Figure 1, the results obtained in the OFT 1-day post-treatment revealed a significant difference in the wildtype-control mice and untreated 3×Tg-AD mice. There was no significant difference between the untreated and treated 3×Tg-AD mice in exploratory activities, even EA or Non-EA treatment.

Analysis of recognition memory in the NORT performed 2–3-days post-treatment is summarized in Figure 2. The exploratory activity of the 3×Tg-AD mice was reduced, including the total time spent exploring and the total number of visits to both objects (Figures 2A,B). However, EA or Non-EA treatment did not affect it, supporting the results obtained in the OFT. As observed in a representative tracking figure during the test probe (Figure 2E), the wildtype-control mice remained for a longer period close to the novel object as compared with that of the untreated 3×Tg-AD mice. The time spent exploring the novel object and the number of visits presented a tendency to ameliorate with the EA-treatment. Furthermore, differences between the untreated and EA-treated 3×Tg-AD mice were significant but Non-EA-treatment presented no difference in the recognition indexes, which were calculated from the total time spent exploring two objects and the number of visits (Figures 2C,D).

Effects of the electroacupuncture treatment on regional spontaneous activity

Accompanied by cognitive alterations, ReHo value showed that there were brain region changes in untreated 3×Tg-AD mice compared to wildtype-control mice. A decreased regional spontaneous activity could be observed in untreated 3×Tg-AD mice in the accumbens nucleus, amygdala, anterior olfactory nucleus, auditory cortex, caudate putamen, EC, hippocampus, insular cortex, orbital cortex, piriform cortex, septal, somatosensory cortex, subiculum, temporal cortex, and visual cortex (Figure 3A).

Compared to untreated 3×Tg-AD mice, EA-treated 3×Tg-AD mice showed an increased regional spontaneous activity in the amygdala, auditory cortex, DG, dorsal raphe nucleus, EC, hippocampus, somatosensory cortex, subiculum, substantia nigra, temporal cortex, and ventral tegmental area (Figure 3B). Besides, Non-EA-treated 3×Tg-AD mice showed an increased regional spontaneous activity in the caudate putamen, insular cortex, motor cortex, orbital cortex, piriform cortex, and somatosensory cortex (Figure 3C). These

results could be concluded that AD-induced chaos of brain function was attenuated by EA-treatment, which brain regions including the auditory cortex, EC, hippocampus, subiculum, and temporal cortex.

Effects of the electroacupuncture treatment on hippocampal synaptic neurotransmission

The hippocampus, which is thought to be the hub of memory-related networks in AD mice, showed changes with EA-treatment. To investigate if synaptic neurotransmission of the hippocampus was influenced by the EA-treatment, we performed the whole-cell voltage-clamp recording. We compared the postsynaptic sEPSC between the 3×Tg-AD mice and wildtype-control mice by recording from hippocampus CA1, and found a significantly decreased sEPSC in the 3×Tg-AD mice, which suggested an enhanced spontaneous release of the neurotransmitter at the hippocampal terminals (**Figure 4**). And there was a significant difference between EA-treated and untreated 3×Tg-AD mice in the postsynaptic sEPSC of hippocampus CA1 (**Figure 4**), but Non-EA treatment does not affect it. The results suggested that the spontaneous release of the neurotransmitter was rescued with EA-treatment in 3×Tg-AD mice.

Recognition memory is correlated with aberrant ReHo across the hippocampus and entorhinal cortex

Previous studies have shown that 3×Tg-AD mice exhibit an accumulation of pathological inclusions and alterations of regional spontaneous activity in the hippocampus and EC. In addition, the hippocampus receives most of the inputs from the EC. Combining the above results, the quantitative analysis demonstrated a significantly positive correlation between differences in recognition index (time/number) and ReHo values of the hippocampus and EC, respectively (**Figure 5**).

Effects of the electroacupuncture treatment on connection between the hippocampus and entorhinal cortex

Based on the above results, we took the hippocampus and EC as ROIs, FC between those was calculated within each mouse, and the mean connectivity values are presented in **Figure 6**. Compared to wildtype-control mice, decreased connectivity between the hippocampus and EC was observed in untreated 3×Tg-AD mice (**Figure 6B**). There was significantly increased connectivity with the EA-treatment. Besides, the significantly changed connection showed a difference between EA-treated and Non-EA-treated 3×Tg-AD mice. **Figure 6C** showed a significantly positive correlation between difference in NORT performance (recognition index of time) and FC strength between the hippocampus and EC.

Furthermore, the number of nerve fiber connections was also tested using DTI fiber tracking. As **Figure 7** shown, the wildtype-control mice displayed more nerve fiber between the hippocampus and EC as compared with that of the untreated 3×Tg-AD mice. The number of nerve fiber connections between the hippocampus and EC showed an increase to ameliorate with the EA-treatment (**Figure 7B**). Difference between the untreated and EA-treated 3×Tg-AD mice was significant, but Non-EA-treatment presented no difference in the nerve fiber connection. **Figure 7C** showed a significantly positive correlation between difference in NORT performance (recognition index of time) and the number of nerve fiber connections between the hippocampus and EC.

Discussion

The current study explored the effects of EA-treatment on recognition memory and neural activity connections in 3×Tg-AD mice. The behavioral test showed that EA-treatment ameliorated recognition memory impairment in 3×Tg-AD mice. The regional homogeneity was measured by rs-fMRI and is known to reflect alterations in local neuronal integration. Our study showed that EA-treatment increased the ReHo value of local neuronal integration in the Hip, EC, and other brain regions. Besides, the local neuronal integration is thought to be caused by synaptic dysfunction in early AD. Further, we observed increased synaptic neurotransmission in hippocampal CA1 with EA-treatment. The EC-Hip is a critical circuit for object recognition memory. Moreover, we demonstrated that EA-induced recognition memory behavior was associated with aberrant local neuronal integration in the Hip and EC. Further analysis revealed that EA-treatment increased FC and the number of nerve fiber connections between the EC and Hip, suggesting hippocampus-cortex network modulation induced by EA.

3×Tg-AD mice express mutant alleles of human APP, PS1, and Tau genes that correspond to the coexistence of most APP and Tau genes in human AD currently found in clinical practice, which simulates the pathological process (Oddo et al., 2003). The mice investigated here in the early AD states, developed memory deficit, together with aberrant local neuronal integration and long-range connectivity (Liu et al., 2018; Manno et al., 2019). In the current study, the results we assessed

showed a decrease in locomotor and recognition memory in 3×Tg-AD mice. It can be considered that AD model mice have a deficit in memory encoding and/or storage at this stage, which is consistent with the clinical manifestation of AD patients. Compared with the healthy elderly, in previous studies, it was difficult to establish elaborative encoding of target information or context in the early AD populations (El Haj et al., 2015a,b).

Electroacupuncture treatment is recognized as an effective therapeutic of TCM to alleviate cognitive disorders. Previous animal experiments have suggested that EA-induced neuromodulation in AD model mice included regulation of Aβ protein, tau phosphorylation, neuroinflammation, brain plasticity, neuron apoptosis, mitochondrial activity, and blood–brain barrier function. However, the role of EA-treatment in preventing cognitive impairment in the early AD stage remains unclear. In our studies, we found that EA-treatment was able to improve the object recognition memory in 3×Tg-AD mice, which is in accordance with previous finds (Cai et al., 2019). Meanwhile, there is no alteration in locomotor activity with EA-treatment, which may be attributed to the specific role of acupoints inserted. According to the TCM theory, EA at DU20 and DU24 could enhance brain function and improve cognitive function. Previous clinical trials showed that the combination of DU20 with other acupoints downregulated the level of Aβ and cognitive function in AD patients (Yu et al., 2019). Besides, the role of the specific acupoints could also explain why our results showed no behavioral difference between the EA and Non-EA on AD mice, consistent with our previous studies (Lin et al., 2018; Li et al., 2020).

The synchronized neuronal activities and their network connectivity are essential for memory information transmission and processing, which are affected in AD populations (Uhlhaas and Singer, 2006; Shah et al., 2016). Besides, the Hip is consistently affected by neuronal degeneration, which is the hub of networks responsible for the early memory impairment in AD (Najm et al., 2019; Dong et al., 2021). The effect of EA-treatment on brain regions such as the hippocampus in AD patients has been confirmed to some extent. Clinical trials found significant neuronal activity changes in the right middle cingulate cortex, right inferior frontal gyrus, right hippocampus, and right inferior temporal gyrus of AD patients by EA (Zheng et al., 2018). Besides, our previous study found that EA at DU20 acupoint enhances glucose metabolism in the cortex, hippocampus, and other brain regions of AD mice (Liu et al., 2017). In the present study, our ReHo analysis revealed that EA-treatment increased synchronous activity in the Hip and brain regions (EC, subiculum, temporal cortex) known to be affected in AD patients, which is consistent with previous studies. In addition, brain regions including the subiculum, temporal cortex, and orbitofrontal cortex are closely associated with attention and decision-making, and the subiculum is regulated by the EC-Hip circuit. Moreover, researchers have confirmed the delay-dependent contribution of the CA1 region to object memory (Ásgeirsdóttir et al., 2020; Cinalli, et al., 2020). Our results revealed that spontaneous release of the neurotransmitter was rescued with EA-treatment in 3×Tg-AD mice. To summarize, we can speculate that the hippocampus is a key brain region for EA-treatment to improve memory function in AD model mice.

Furthermore, EC and Hip dysfunction are thought to be possible causes of initial memory symptoms (Van Hoesen et al., 1991). They are the earliest regions affected by AD, and the EC conveys spatial/contextual and object information to the hippocampus (van Strien et al., 2009; Knierim et al., 2014). Previous observations have revealed that coherent oscillatory activity in EC-Hip was correlated with object recognition memory performance (Salimi et al., 2022). Consistent with previous studies, the result in the present study has shown that EC and Hip are correlated with recognition memory performance. The clinical trials found that the connecting fibers between the hippocampus and related brain regions of AD patients were damaged and their functional connection strength decreased, which was closely related to the cognitive decline of AD (Quan et al., 2020; Dautricourt et al., 2021). Moreover, deep brain stimulation at EC affected increased resting-state FC and an obvious information flow from the EC to the Hip (Jiang et al., 2022). We found that the EA-treatment could increase the connecting fibers and functional connection strength between EC and Hip, indicating that the effects of EA-treatment might rely on EC–Hip network modulation mechanisms.

Importantly, there are important limitations and further investigation for the present study. Firstly, given the high incidence and earlier-onset features of AD cases in women, however, only male 3×Tg AD mice were used in our experiments, which limits our interpretation for both sexes. In addition, it is necessary to combine multiple high-resolution methods to detect the roles of different subregions of the hippocampus and EC, and the network connectivity between the hippocampus and other brain regions also needs to be further studied. Moreover, further experiments are necessary to determine the role of the EC -hippocampal circuit in recognition memory deficit in 3×Tg-AD mice with EA-treatment and to investigate the biomolecular mechanism(s) at work.

Conclusively, the data in the present work recapitulated that EA alleviated object recognition memory deficit associated with ameliorated neuronal activities and network connection in the 3×Tg-AD mice model. Our results suggested that the effect of EA- treatment may be dependent on the EC-Hip connection. EA may be a potentially translatable strategy for recognition memory impairment in AD patients.

Data availability statement

The raw data supporting the conclusions of this article will be made available by the authors, without undue reservation.

Ethics statement

The animal study was reviewed and approved by the Fujian University of Traditional Chinese Medicine Animal Experiment Ethics Committee and Authority.

Author contributions

JH and BL designed the study. JH, BL, and LZ wrote the manuscript. BL, XC, and LZ performed the experiments. XY, ZL, CR, and TW analyzed the data. All authors have read and approved the final manuscript.

Funding

This work was supported by the National Natural Science Fund of China (81774424).

Conflict of interest

The authors declare that the research was conducted in the absence of any commercial or financial relationships that could be construed as a potential conflict of interest.

Publisher's note

All claims expressed in this article are solely those of the authors and do not necessarily represent those of their affiliated organizations, or those of the publisher, the editors and the reviewers. Any product that may be evaluated in this article, or claim that may be made by its manufacturer, is not guaranteed or endorsed by the publisher.

Supplementary material

The Supplementary Material for this article can be found online at: https://www.frontiersin.org/articles/10.3389/fnins.2022.968767/full#supplementary-material

References

Ásgeirsdóttir, H. N., Cohen, S. J., and Stackman, R. W. Jr. (2020). Object and place information processing by CA1 hippocampal neurons of C57BL/6J mice. *J. Neurophysiol.* 123, 1247–1264. doi: 10.1152/jn.00278.2019

Braak, H., Thal, D. R., Ghebremedhin, E., and Del Tredici, K. (2011). Stages of the pathologic process in Alzheimer disease: age categories from 1 to 100 years. *J. Neuropathol. Exp. Neurol.* 70, 960–969. doi: 10.1097/NEN.0b013e318232a379

Cai, M., Lee, J. H., and Yang, E. J. (2019). Electroacupuncture attenuates cognition impairment via anti-neuroinflammation in an Alzheimer's disease animal model. *J. Neuroinflam.* 16:264. doi: 10.1186/s12974-019-1665-3

Cinalli, D. A. , Cohen, S. J., Guthrie, K., and Stackman, R. W. Jr. (2020). Object Recognition Memory: Distinct Yet Complementary Roles of the Mouse CA1 and Perirhinal Cortex. *Front. Mol. Neurosci.* 13:527543. doi: 10.3389/fnmol.2020.527543

Dautricourt, S., de Flores, R., Landeau, B., Poisnel, G., Vanhoutte, M., Delcroix, N., et al. (2021). Longitudinal changes in hippocampal network connectivity in Alzheimer's Disease. *Ann. Neurol.* 90, 391–406. doi: 10.1002/ana.26168

De Marco, M., Vallelunga, A., Meneghello, F., Varma, S., Frangi, A. F., and Venneri, A. (2017). ApoE ε4 allele related alterations in hippocampal connectivity in early Alzheimer's Disease support memory performance. *Curr. Alzheimer Res.* 14, 766–777. doi: 10.2174/1567205014666170206113528

Deng, M., and Wang, X. F. (2016). Acupuncture for amnestic mild cognitive impairment: a meta-analysis of randomised controlled trials. *Acupunct. Med.* 34, 342–348. doi: 10.1136/acupmed-2015-010989

Devanand, D. P., Pradhaban, G., Liu, X., Khandji, A., De Santi, S., Segal, S., et al. (2007). Hippocampal and entorhinal atrophy in mild cognitive impairment: prediction of Alzheimer disease. *Neurology* 68, 828–836. doi: 10.1212/01.wnl.0000256697.20968.d7

Dong, M., Xie, L., Das, S. R., Wang, J., Wisse, L. E. M., deFlores, R., et al. (2021). DeepAtrophy: Teaching a neural network to detect progressive changes in longitudinal MRI of the hippocampal region in Alzheimer's disease. *Neuroimage* 243:118514. doi: 10.1016/j.neuroimage.2021.118514

El Haj, M., Antoine, P., and Kapogiannis, D. (2015b). Similarity between remembering the past and imagining the future in Alzheimer's disease: Implication of episodic memory. *Neuropsychologia* 66, 119–125. doi: 10.1016/j.neuropsychologia.2014.11.015

El Haj, M., Antoine, P., and Kapogiannis, D. (2015a). Flexibility decline contributes to similarity of past and future thinking in Alzheimer's disease. *Hippocampus* 25, 1447–1455. doi: 10.1002/hipo.22465

Goldstein, F. C., Loring, D. W., Thomas, T., Saleh, S., and Hajjar, I. (2019). Recognition memory performance as a cognitive marker of prodromal Alzheimer's disease. *J. Alzheimers Dis.* 72, 507–514. doi: 10.3233/jad-190468

Huang, K. Y., Liang, S., Yu, M. L., Fu, S. P., Chen, X., and Lu, S. F. (2016). A systematic review and meta-analysis of acupuncture for improving learning and memory ability in animals. *BMC Comp. Altern. Med.* 16:297. doi: 10.1186/s12906-016-1298-3

Jia, Y., Zhang, X., Yu, J., Han, J., Yu, T., Shi, J., et al. (2017). Acupuncture for patients with mild to moderate Alzheimer's disease: a randomized controlled trial. *BMC Comp. Altern. Med.* 17:556. doi: 10.1186/s12906-017-2064-x

Jiang, C., Yang, S., Tao, J., Huang, J., Li, Y., Ye, H., et al. (2016). Clinical Efficacy of Acupuncture Treatment in Combination With RehaCom Cognitive Training for Improving Cognitive Function in Stroke: A 2 × 2 Factorial Design Randomized Controlled Trial. *J. Am. Med. Dir. Assoc.* 17, 1114–1122. doi: 10.1016/j.jamda.2016.07.021

Jiang, Y., Liu, D. F., Zhang, X., Liu, H. G., Zhang, C., and Zhang, J. G. (2022). Modulation of the rat hippocampal-cortex network and episodic-like memory performance following entorhinal cortex stimulation. *CNS Neurosci. Ther.* 28, 448–457. doi: 10.1111/cns.13795

Kamiya, M., Osawa, A., Kondo, I., and Sakurai, T. (2018). Factors associated with cognitive function that cause a decline in the level of activities of daily living in Alzheimer's disease. *Geriatr. Gerontol. Int.* 18, 50–56. doi: 10.1111/ggi.13135

Knierim, J. J., Neunuebel, J. P., and Deshmukh, S. S. (2014). Functional correlates of the lateral and medial entorhinal cortex: objects, path integration and

local-global reference frames. *Philos. Trans. R. Soc. Lond B Biol. Sci.* 369:20130369. doi: 10.1098/rstb.2013.0369

Lane, C. A., Hardy, J., and Schott, J. M. (2018). Alzheimer's disease. *Eur. J. Neurol.* 25, 59–70. doi: 10.1111/ene.13439

Li, J., Zhang, B., Jia, W., Yang, M., Zhang, Y., Zhang, J., et al. (2021). Activation of adenosine monophosphate-activated protein kinase drives the aerobic glycolysis in hippocampus for delaying cognitive decline following electroacupuncture treatment in APP/PS1 mice. *Front. Cell Neurosci.* 15:774569. doi: 10.3389/fncel.2021.774569

Li, L., Li, L., Zhang, J., Huang, S., Liu, W., Wang, Z., et al. (2020). Disease stage-associated alterations in learning and memory through the electroacupuncture modulation of the cortical microglial M1/M2 polarization in mice with Alzheimer's disease. *Neural. Plast.* 2020:8836173. doi: 10.1155/2020/8836173

Lin, C. J., Yeh, M. L., Wu, S. F., Chung, Y. C., and Lee, J. C. (2022). Acupuncture-related treatments improve cognitive and physical functions in Alzheimer's disease: a systematic review and meta-analysis of randomized controlled trials. *Clin. Rehabil.* 36, 609–635. doi: 10.1177/02692155221079117

Lin, R., Li, L., Zhang, Y., Huang, S., Chen, S., Shi, J., et al. (2018). Electroacupuncture ameliorate learning and memory by improving N-acetylaspartate and glutamate metabolism in APP/PS1 mice. *Biol. Res.* 51:21. doi: 10.1186/s40659-018-0166-7

Liu, D., Lu, H., Stein, E., Zhou, Z., Yang, Y., and Mattson, M. P. (2018). Brain regional synchronous activity predicts tauopathy in 3×TgAD mice. *Neurobiol. Aging* 70, 160–169. doi: 10.1016/j.neurobiolaging.2018.06.016

Liu, W., Zhuo, P., Li, L., Jin, H., Lin, B., Zhang, Y., et al. (2017). Activation of brain glucose metabolism ameliorating cognitive impairment in APP/PS1 transgenic mice by electroacupuncture. *Free Radic. Biol. Med.* 112, 174–190. doi: 10.1016/j.freeradbiomed.2017.07.024

Manno, F. A. M., Isla, A. G., Manno, S. H. C., Ahmed, I., Cheng, S. H., Barrios, F. A., et al. (2019). Early stage alterations in white matter and decreased functional interhemispheric hippocampal connectivity in the 3xTg mouse model of Alzheimer's disease. *Front. Aging Neurosci.* 11:39. doi: 10.3389/fnagi.2019.00039

Matura, S., Prvulovic, D., Butz, M., Hartmann, D., Sepanski, B., Linnemann, K., et al. (2014). Recognition memory is associated with altered resting-state functional connectivity in people at genetic risk for Alzheimer's disease. *Eur. J. Neurosci.* 40, 3128–3135. doi: 10.1111/ejn.12659

Mayo, C. D., Garcia-Barrera, M. A., Mazerolle, E. L., Ritchie, L. J., Fisk, J. D., and Gawryluk, J. R. (2018). Relationship between DTI metrics and cognitive function in Alzheimer's disease. *Front. Aging Neurosci.* 10:436. doi: 10.3389/fnagi.2018.00436

Mayo, C. D., Mazerolle, E. L., Ritchie, L., Fisk, J. D., and Gawryluk, J. R. (2017). Longitudinal changes in microstructural white matter metrics in Alzheimer's disease. *Neuroimage. Clin.* 13, 330–338. doi: 10.1016/j.nicl.2016.12.012

Najm, R., Jones, E. A., and Huang, Y. (2019). Apolipoprotein E4, inhibitory network dysfunction, and Alzheimer's disease. *Mol. Neurodegener.* 14:24. doi: 10.1186/s13024-019-0324-6

Oddo, S., Caccamo, A., Shepherd, J. D., Murphy, M. P., Golde, T. E., Kayed, R., et al. (2003). Triple-transgenic model of Alzheimer's disease with plaques and tangles: intracellular Abeta and synaptic dysfunction. *Neuron* 39, 409–421. doi: 10.1016/s0896-6273(03)00434-3

Quan, M., Zhao, T., Tang, Y., Luo, P., Wang, W., Qin, Q., et al. (2020). Effects of gene mutation and disease progression on representative neural circuits in familial Alzheimer's disease. *Alzheimers Res. Ther.* 12:14. doi: 10.1186/s13195-019-0572-2

Russo, M. J., Campos, J., Vázquez, S., Sevlever, G., and Allegri, R. F. (2017). Adding recognition discriminability index to the delayed recall is useful to predict conversion from mild cognitive impairment to Alzheimer's disease in the Alzheimer's disease neuroimaging initiative. *Front. Aging Neurosci.* 9:46. doi: 10.3389/fnagi.2017.00046

Salimi, M., Tabasi, F., Abdolsamadi, M., Dehghan, S., Dehdar, K., Nazari, M., et al. (2022). Disrupted connectivity in the olfactory bulb-entorhinal cortex-dorsal hippocampus circuit is associated with recognition memory deficit in Alzheimer's disease model. *Sci. Rep.* 12:4394. doi: 10.1038/s41598-022-08528-y

Shah, D., Praet, J., Latif Hernandez, A., Höfling, C., Anckaerts, C., Bard, F., et al. (2016). Early pathologic amyloid induces hypersynchrony of BOLD resting-state networks in transgenic mice and provides an early therapeutic window before amyloid plaque deposition. *Alzheimers Dement.* 12, 964–976. doi: 10.1016/j.jalz.2016.03.010

Sperling, R. A., Aisen, P. S., Beckett, L. A., Bennett, D. A., Craft, S., Fagan, A. M., et al. (2011). Toward defining the preclinical stages of Alzheimer's disease: recommendations from the National Institute on Aging-Alzheimer's Association workgroups on diagnostic guidelines for Alzheimer's disease. *Alzheimers Dement.* 7, 280–292. doi: 10.1016/j.jalz.2011.03.003

Tan, T. T., Wang, D., Huang, J. K., Zhou, X. M., Yuan, X., Liang, J. P., et al. (2017). Modulatory effects of acupuncture on brain networks in mild cognitive impairment patients. *Neural. Regen. Res.* 12, 250–258. doi: 10.4103/1673-5374.200808

Tanimizu, T., Kono, K., and Kida, S. (2018). Brain networks activated to form object recognition memory. *Brain Res. Bull.* 141, 27–34. doi: 10.1016/j.brainresbull.2017.05.017

Uhlhaas, P. J., and Singer, W. (2006). Neural synchrony in brain disorders: relevance for cognitive dysfunctions and pathophysiology. *Neuron* 52, 155–168. doi: 10.1016/j.neuron.2006.09.020

Van Hoesen, G. W., Hyman, B. T., and Damasio, A. R. (1991). Entorhinal cortex pathology in Alzheimer's disease. *Hippocampus* 1, 1–8. doi: 10.1002/hipo.450010102

van Strien, N. M., Cappaert, N. L., and Witter, M. P. (2009). The anatomy of memory: an interactive overview of the parahippocampal-hippocampal network. *Nat. Rev. Neurosci.* 10, 272–282. doi: 10.1038/nrn2614

Wang, L. Y., Pei, J., Zhan, Y. J., and Cai, Y. W. (2020). Overview of Meta-Analyses of Five Non-pharmacological Interventions for Alzheimer's Disease. *Front. Aging Neurosci.* 12:594432. doi: 10.3389/fnagi.2020.594432

Wang, Z., Liang, P., Zhao, Z., Han, Y., Song, H., Xu, J., et al. (2014). Acupuncture modulates resting state hippocampal functional connectivity in Alzheimer disease. *PLoS One* 9:e91160. doi: 10.1371/journal.pone.0091160

Wattmo, C., and Wallin, Å. K. (2017). Early- versus late-onset Alzheimer's disease in clinical practice: cognitive and global outcomes over 3 years. *Alzheimers Res. Ther.* 9:70. doi: 10.1186/s13195-017-0294-2

Wu, T., Grandjean, J., Bosshard, S. C., Rudin, M., Reutens, D., and Jiang, T. (2017). Altered regional connectivity reflecting effects of different anaesthesia protocols in the mouse brain. *Neuroimage* 149, 190–199. doi: 10.1016/j.neuroimage.2017.01.074

Yin, W., Lv, G., Li, C., and Sun, J. (2021). Acupuncture therapy for Alzheimer's disease: The effectiveness and potential mechanisms. *Anat. Rec.* 304, 2397–2411. doi: 10.1002/ar.24780

Yin, Z., Li, X., Wang, L., Sun, M., Zhao, L., and Liang, F. (2022). The comparative efficacy of multiple acupuncture for Alzheimer's Disease: a bayesian network meta-analysis. *Evid. Based Comp. Alternat. Med.* 2022:3288948. doi: 10.1155/2022/3288948

Yu, C. C., Du, Y. J., Wang, S. Q., Liu, L. B., Shen, F., Wang, L., et al. (2020). Experimental evidence of the benefits of acupuncture for Alzheimer's disease: an updated review. *Front. Neurosci.* 14:549772. doi: 10.3389/fnins.2020.549772

Yu, Z., Xu, J. C., Qin, Q. J., Ni, D. Y., and Zhang, Y. L. (2019). [Analysis on acupoint selection rules of acupuncture for Alzheimer's disease based on complex network]. *Zhongguo Zhen Jiu* 39, 551–555. doi: 10.13703/j.0255-2930.2019.05.025

Zang, Y., Jiang, T., Lu, Y., He, Y., and Tian, L. (2004). Regional homogeneity approach to fMRI data analysis. *Neuroimage* 22, 394–400. doi: 10.1016/j.neuroimage.2003.12.030

Zheng, W., Su, Z., Liu, X., Zhang, H., Han, Y., Song, H., et al. (2018). Modulation of functional activity and connectivity by acupuncture in patients with Alzheimer disease as measured by resting-state fMRI. *PLoS One* 13:e0196933. doi: 10.1371/journal.pone.0196933

Zheng, X., Lin, W., Jiang, Y., Lu, K., Wei, W., Huo, Q., et al. (2021). Electroacupuncture ameliorates beta-amyloid pathology and cognitive impairment in Alzheimer disease via a novel mechanism involving activation of TFEB (transcription factor EB). *Autophagy* 17, 3833–3847. doi: 10.1080/15548627.2021.1886720

frontiers | Frontiers in Neuroscience

TYPE Original Research
PUBLISHED 17 August 2022
DOI 10.3389/fnins.2022.964654

OPEN ACCESS

EDITED BY
Jie Wang,
Wuhan Institute of Physics and Mathematics (CAS), China

REVIEWED BY
Jie Zhuang,
Shanghai University of Sport, China
Jie Li,
Tongji University, China

*CORRESPONDENCE
Nian Wang
nianwang@iu.edu

SPECIALTY SECTION
This article was submitted to Brain Imaging Methods, a section of the journal Frontiers in Neuroscience

RECEIVED 08 June 2022
ACCEPTED 18 July 2022
PUBLISHED 17 August 2022

CITATION
Maharjan S, Tsai AP, Lin PB, Ingraham C, Jewett MR, Landreth GE, Oblak AL and Wang N (2022) Age-dependent microstructure alterations in 5xFAD mice by high-resolution diffusion tensor imaging.
Front. Neurosci. 16:964654.
doi: 10.3389/fnins.2022.964654

Age-dependent microstructure alterations in 5xFAD mice by high-resolution diffusion tensor imaging

Surendra Maharjan[1], Andy P. Tsai[2], Peter B. Lin[2], Cynthia Ingraham[2], Megan R. Jewett[1], Gary E. Landreth[2,3], Adrian L. Oblak[1,2] and Nian Wang[1,2]*

[1]Department of Radiology and Imaging Sciences, Indiana University, Indianapolis, IN, United States, [2]Stark Neurosciences Research Institute, Indiana University, Indianapolis, IN, United States, [3]Department of Anatomy, Cell Biology and Physiology, Indiana University, Indianapolis, IN, United States

Purpose: To evaluate the age-dependent microstructure changes in 5xFAD mice using high-resolution diffusion tensor imaging (DTI).

Methods: The 5xFAD mice at 4, 7.5, and 12 months and the wild-type controls at 4 months were scanned at 9.4T using a 3D echo-planar imaging (EPI) pulse sequence with the isotropic spatial resolution of 100 μm. The *b*-value was 3000 s/mm^2 for all the diffusion MRI scans. The samples were also acquired with a gradient echo pulse sequence at 50 μm isotropic resolution. The microstructure changes were quantified with DTI metrics, including fractional anisotropy (FA) and mean diffusivity (MD). The conventional histology was performed to validate with MRI findings.

Results: The FA values (p = 0.028) showed significant differences in the cortex between wild-type (WT) and 5xFAD mice at 4 months, while hippocampus, anterior commissure, corpus callosum, and fornix showed no significant differences for either FA and MD. FA values of 5xFAD mice gradually decreased in cortex (0.140 ± 0.007 at 4 months, 0.132 ± 0.008 at 7.5 months, 0.126 ± 0.013 at 12 months) and fornix (0.140 ± 0.007 at 4 months, 0.132 ± 0.008 at 7.5 months, 0.126 ± 0.013 at 12 months) with aging. Both FA (p = 0.029) and MD (p = 0.037) demonstrated significant differences in corpus callosum between 4 and 12 months age old. FA and MD were not significantly different in the hippocampus or anterior commissure. The age-dependent microstructure alterations were better captured by FA when compared to MD.

Conclusion: FA showed higher sensitivity to monitor amyloid deposition in 5xFAD mice. DTI may be utilized as a sensitive biomarker to monitor beta-amyloid progression for preclinical studies.

KEYWORDS

Alzheimer's disease, 5xFAD, MRI, DTI, diffusion MRI (dMRI)

Introduction

Alzheimer's disease (AD) is the most common cause of dementia with clinically characterized by age-dependent memory loss and cognitive dysfunction (Bush, 2003; Goedert and Spillantini, 2006). The primary characteristics of AD are the abnormal accumulation of extracellular β-amyloid (Aβ) and intracellular hyperphosphorylated tau proteins (Takahashi et al., 2010; Koss et al., 2016; Wang et al., 2016). Aβ plaque formation is considered as one of the earliest components, starting years, or even decades before clinical symptoms (Busciglio et al., 1995; Bloom, 2014). The capability to monitor the alterations in tissue microstructure caused by the accumulation of Aβ may provide an important biomarker to monitor disease progression or treatment response (Adlard et al., 2014; Thal et al., 2014).

Compared to the conventional volumetric MRI methods, diffusion MRI (dMRI) is more sensitive to the brain microstructural changes and has been widely used for the evaluation of white matter integrity (Bozzali et al., 2002; Mielke et al., 2009; Stebbins and Murphy, 2009; Wang et al., 2019b; Harrison et al., 2020; Veale et al., 2021). Patients with AD showed a significant reduction in the integrity of the associated white matter fiber tracts, including splenium of the corpus callosum, superior longitudinal fasciculus, and cingulum (Rose et al., 2000). Teipel et al. (2012) found a significant reduction of FA and a significant increase of MD in core areas of AD pathology including the corpus callosum, medial and temporal lobes, fornix, cingulate gyrus, precuneus, and prefrontal lobe white matter. The microstructure changes of patients with mild cognitive impairment have also been identified in the hippocampus using dMRI (Kantarci et al., 2005; Veale et al., 2021). More recently, dMRI studies have shown abnormalities in multiple neocortical areas at various stages of AD (Jacobs et al., 2013; Torso et al., 2021).

Despite the knowledge gained from human studies, transgenic animal models are an invaluable tool for studying pathogenic mechanisms and testing therapeutics of AD (Kitazawa et al., 2012; Jankowsky and Zheng, 2017; Sasaguri et al., 2017). The transgenic mouse model, 5xFAD, expresses human APP with three FAD mutations and human PSEN1 with two FAD mutations, and is commonly used to study the mechanisms of AD (Oakley et al., 2006; Forner et al., 2021). In 5xFAD mice, amyloid plaques are first observed between two and four months of age in the cortical layer V and in the subiculum of the hippocampal formation (Oblak et al., 2021). Different MRI techniques have been used to study the brain structure and function of 5xFAD mice (Mlynarik et al., 2012; Igarashi et al., 2020; Jullienne et al., 2022). Manganese-enhanced MRI (MEMRI) has been utilized as an activity-dependent contrast agent. Studies found that manganese could serve as a targeted contrast agent to visualize amyloid plaques in 5xFAD mice (Kim et al., 2021). The structural networks derived from dMRI exhibited higher path lengths in 6-month-old 5xFAD mice compared to controls (Kesler et al., 2018).

The 5xFAD transgenic mice have been acknowledged as a useful model for better understanding the pathogenesis of human AD (Girard et al., 2013). To the best of our knowledge, probing age-dependent tissue microstructure alterations in 5xFAD mice using high-resolution DTI has not been reported. In this study, we compared the microstructure alterations in cortex and hippocampus between wild-type (WT) and 5xFAD mice at 4 months of age. We further investigated the age-dependent microstructural variations in 5xFAD mice at three different ages (4, 7.5, and 12 months) throughout the whole brain (166 regions) (Wang et al., 2018a). The MRI findings were validated with Aβ plaque and NeuN staining.

Materials and methods

Animal preparation

Animal experiments were carried out in compliance with the Indiana University Institutional Animal Care and Use Committee. Six WT/six mice at the age of 4 months and eighteen 5xFAD (Jax #34848) mice at the ages of 4, 7.5, and 12 months (Jackson Laboratory, Bar Harbor, ME, United States) were sacrificed and perfused with the PBS solution. The mouse brains were immersed in buffered formalin for 24 h and then placed in a PBS solution of 0.5% Prohance (Bracco Diagnostics Inc., Princeton, NJ, United States) to shorten T1 and reduce scan time (Wang et al., 2019a).

MRI protocol

MR images of the specimens were acquired on a 30-cm bore 9.4T magnet (Bruker BioSpec 94/30, Billerica, MA, United States) with a maximum gradient strength of 660 mT/m on each axis. A high-sensitivity cryogenic RF surface receive-only coil was used for signal reception (Bruker CryoProbe). A multi-shot 3D EPI pulse sequence was used with the following parameters: matrix size = 180 × 128 × 76, FOV = 18.0 mm × 12.8 mm × 7.6 mm, 100 μm isotropic spatial resolution, TE = 22.3 ms, TR = 100 ms, 61 unique diffusion directions with *b*-value of 3000 s/mm^2 and six non-diffusion-weighted (b0) measurements (Crater et al., 2022). The gradient separation time was 4.4 ms and the diffusion gradient duration time was 9.8 ms.

A 3D gradient echo (GRE) pulse sequence was performed at the spatial resolution of 50 × 50 × 50 μm^3 with TE of 12 ms (Wang et al., 2018b). The parameters were as follows: matrix size = 360 × 256 × 152, FOV = 18.0 mm × 12.8 mm × 7.6 mm, flip angle = 45°, bandwidth (BW) = 125 kHz, and TR = 100 ms.

Data processing for diffusion tensor imaging

All the diffusion-weighted images (DWIs) were registered to the baseline images (b0) using linear affine registration. The scalar indices including FA, MD, axial diffusivity (AD), and

radial diffusivity (RD) were calculated based on the DTI model using DSI studio toolbox (Yeh et al., 2010). Each mouse brain was registered to the mouse brain atlas in Waxholm space using the Advanced Normalization Tools (ANTs) and then divided into 166 Region-of-interest (ROIs, **Supplementary Figure 1**; Wang et al., 2020a). The labels were mapped back to the individual brain space to calculate the values of DTI metrics in each ROI. A one-way analysis of variance (ANOVA) was performed to compare the statistically difference of DTI metrics between B6 and 5xFAD mice at the age of 4 months. To identify the age-dependent microstructure variations of 5xFAD mice, the DTI metrics were also compared at different ages: 4 months vs. 7.5 months, 4 months vs. 12 months. The statistical significance was determined at $p < 0.05$.

Histology

Histological examinations were performed on the mice brains as previous described (Oblak et al., 2021; Tsai et al., 2021). Thirty micron-thick sections were stained to visualize neuronal cell bodies and beta-amyloid plaques using antibodies directed against NeuN (Abcam #ab104225, 1:1000, Boston, MA) and 6E10 (BioLegend #803001, 1:1000). The slides were imaged using Leica DVM6 digital microscope.

Results

Figure 1 illustrates the T2*-weighted images of WT mice at 4 months and 5xFAD at different ages (4, 7.5, and 12 months, **Figures 1B–D,F–H**). As shown in the figure, numerous dark spots were evident in the cortex (red arrows) and hippocampus (white arrows) in 5xFAD mice. The hypointense signals were better observed under higher magnification, as displayed in the bottom row (**Figures 1E–H**). Such hypointense signals were not observed in the WT mouse (**Figures 1A–E**). The dark spot areas were gradually increased with age in the 5xFAD mice.

Figure 2 shows the representative FA (**Figures 2A,B**) and MD (**Figures 2C,D**) images of WT and 5xFAD mice at 4 months. Both WT and 5xFAD mice demonstrated very similar anatomy of the brain (**Figure 2A**). There are no apparent FA and MD differences in the corpus callosum (cc, yellow arrows) and hippocampus (Hc, blue arrows). The FA map showed darker (lower FA values) in the cortex (Cx) of 5xFAD compared to WT (red arrows). In contrast, the MD map depicted less variation between 5xFAD and WT mice.

The FA (**Figure 3b**) and MD (**Figure 3c**) values of different regions (**Figure 3a**) for both WT and 5xFAD mice at 4 months are shown in **Figure 3**. The different regions including Cx, Hc, anterior commissure (ac), cc, and fornix (fx) were rendered with different colors (**Figure 3a**). There were no significant differences in most of the brain regions, including Hc ($p = 0.269$ for FA; $p = 0.007$ for MD), ac ($p = 0.442$ for FA; $p = 0.126$ for MD), cc ($p = 0.168$ for FA; $p = 0.398$ for MD), and fx ($p = 0.366$ for FA; $p = 0.185$ for MD). In the cortex region, the FA exhibited a significant decrease between WT and 5xFAD mice ($p = 0.028$). In contrast, no significant difference was found for MD in the cortex region ($p = 0.052$).

To explore the age-dependent tissue microstructure change in different brain regions, the FA and MD values of 5xFAD mice at different ages (4, 7.5, and 12 months) were exhibited in **Figure 4**. The DTI metrics showed strong age-dependent variations in different areas of the brain (**Figures 4A–J**). The FA and MD revealed no significant differences between 4 and 7.5 months in Hc ($p = 0.375$ for FA, $p = 0.455$ for MD), ac ($p = 0.254$ for FA, $p = 0.180$ for MD), and cc ($p = 0.134$ for FA and $p = 0.429$ for MD) regions. In contrast, both FA and MD showed significant differences in fx ($p = 0.002$ for FA and $p = 0.045$ for MD). FA values had significant differences in Cx ($p = 0.044$); MD values showed no significant differences in Cx ($p = 0.320$). More regions showed significant differences between 4 and 12 months, including Cx ($p = 0.025$ for FA), cc ($p = 0.029$ for FA and $p = 0.037$ for MD), and fx ($p < 0.001$ for FA and $p = 0.005$ for MD).

To validate the MRI findings with conventional histology, the age-dependent FA (**Figures 5A,C**) and beta-amyloid staining (**Figures 5B,D**) images of 5xFAD mice are shown in **Figure 5**. The FA was gradually decreased with age in both upper layers (blue arrows in **Figure 5C**) and lower layers (black arrows in **Figure 5C**) of the cortex. The beta-amyloid staining was overlayed on the NeuN staining (**Figure 5D**). There were more plaques in the lower layers of the cortex regardless of the age. The plaques gradually increased with age in both lower and upper layers of the cortex. The representative FA slices at different ages (4, 7.5, and 12 m) are shown in **Supplementary Figure 2**.

The FA images (**Figures 6A,B**) and beta-amyloid staining (**Figure 6C**) at different ages of 5xFAD in the hippocampus are illustrated in **Figure 6**. The FA values showed strong age-dependent changes in the dentate gyrus (DG, blue arrows in **Figure 6B**), the dorsal subiculum (DS, purple arrows in **Figure 6B**), and the CA2 (white arrows). The plaques gradually increased with age in the hippocampus regions (**Figure 6C**). There were more plaques accumulated in the DG, DS, and CA2 regions, which was consistent with the reduction of FA.

The age-dependent whole-brain microstructure changes in 5xFAD mice were demonstrated in **Figure 7**. In general, FA exhibited higher sensitivity to the age effect than MD.

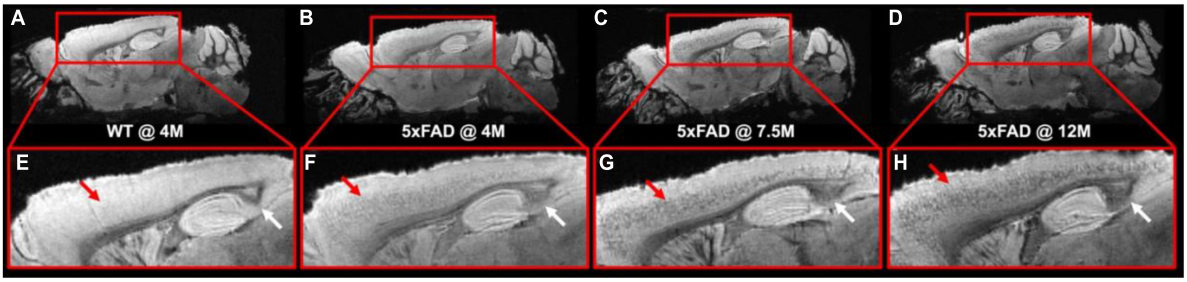

FIGURE 1
The T2*-weighted images of WT mice **(A,E)** at 4 months and 5xFAD at different ages (4, 7.5, and 12 months, **B–D**, **F–H**). Numerous dark spots were clearly evident in the cortex and hippocampus regions of the 5xFAD mice.

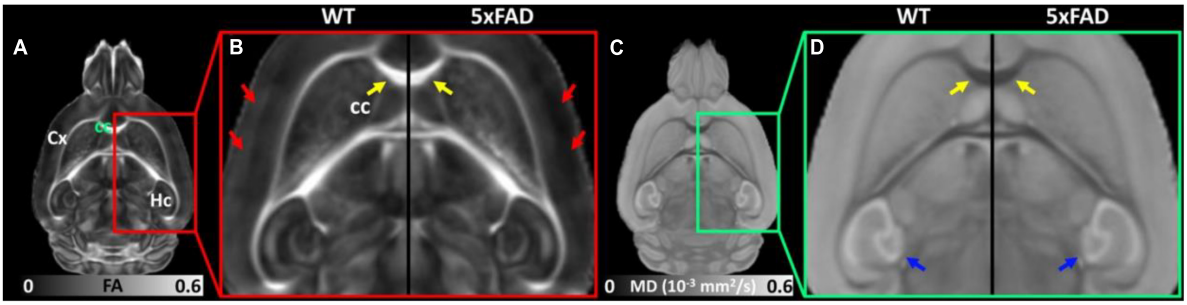

FIGURE 2
The representative FA **(A,B)** and MD **(C,D)** images of WT and 5xFAD mice at 4 months. There are no apparent FA and MD differences in the corpus callosum (cc, yellow arrows) and hippocampus (Hc, blue arrows) regions. The FA map showed darker (lower FA values) in the cortex (Cx) region of 5xFAD compared to WT (red arrows).

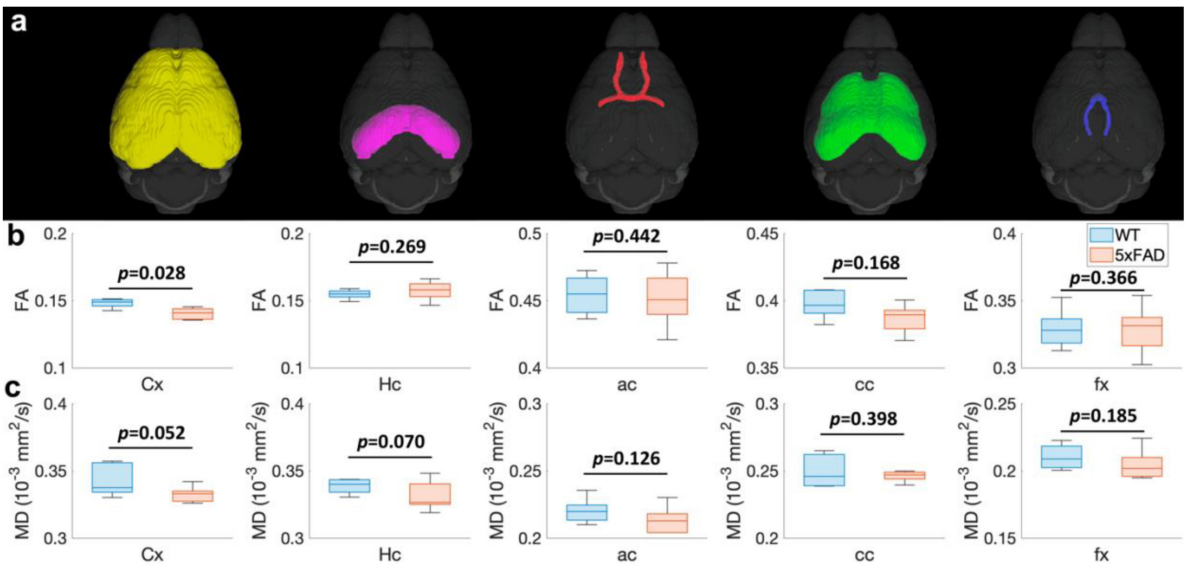

FIGURE 3
The FA **(B)** and MD **(C)** values at different regions (Cx, Hc, ac, cc, and fx, **A**) for both WT and 5xFAD mice at 4 months. Cx: cortex; Hc: hippocampus; ac: anterior commissure; cc: corpus callosum; fx: fornix.

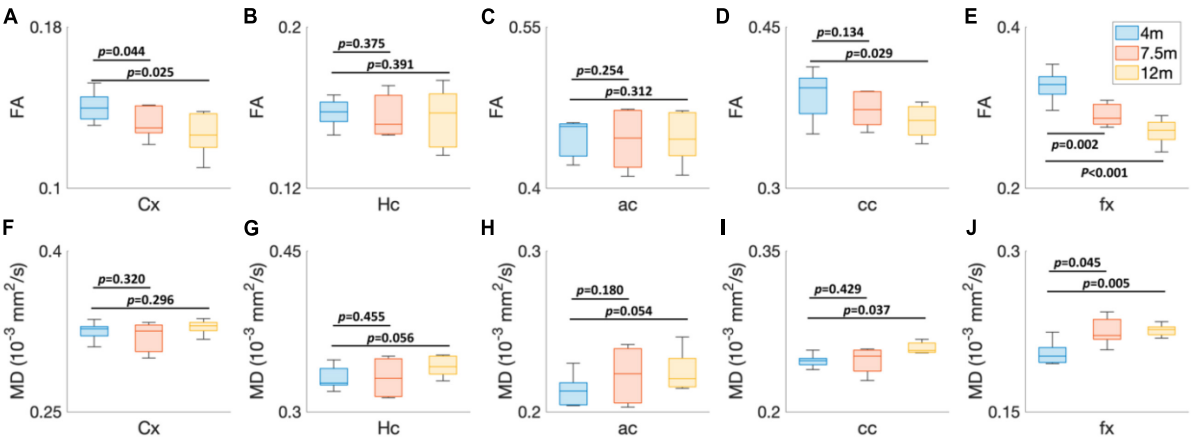

FIGURE 4
The age-dependent (4, 7.5, and 12 months) FA **(A–E)** and MD **(F–J)** values of 5xFAD mice at different brain regions. Cx, cortex; Hc, hippocampus; ac, anterior commissure; cc, corpus callosum; fx, fornix.

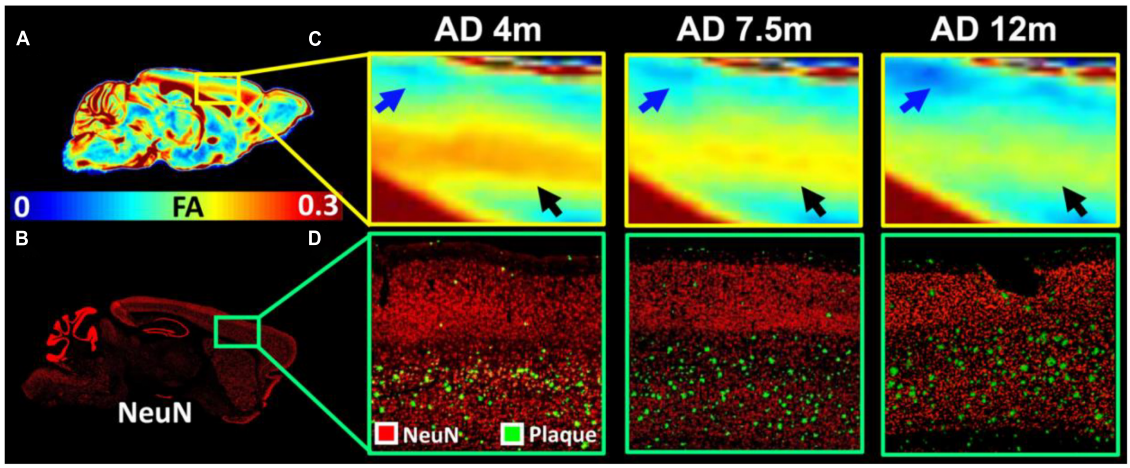

FIGURE 5
The age-dependent FA **(A,C)** and beta-amyloid staining images of 5xFAD mice **(B,D)**. The FA was gradually decreased with age in both upper layers (blue arrows in **C**) and lower layers (black arrows in **C**) of the cortex. The beta-amyloid staining was overlayed on the NeuN staining **(D)**.

The cortex regions including the insular cortex (Ins), primary visual cortex monocular area (V1M), secondary visual cortex lateral area (V2L), primary auditory cortex (Au1), and fornix showed significant differences in the FA statistical maps (4 vs. 7.5 months). There were more regions with significant differences between 4 and 12 months, including the primary motor cortex (M1), secondary motor cortex (M2), lateral orbital cortex (LO), secondary auditory cortex dorsal part (AuD), primary visual cortex binocular area (V1B), dorsal intermediate entorhinal cortex (DIEnt), corpus callosum (cc), and striatum (Cpu). Compared to the FA statistical maps, the MD statistical map showed fewer age-dependent alterations (4 vs. 7.5 months, 4 vs. 12 months). MD showed no significant differences in the cortex regions between 5xFAD at 4 and 7.5 months, MD showed significant differences in Cpu and cc between 5xFAD at 4 and 12 months. The fx showed significant differences in both comparisons (4 vs. 7.5 months, 4 vs. 12 months), while ac showed no significant differences among different ages.

Discussion

Diffusion tensor imaging is the most widely used dMRI technique to access neurodegenerative and pathophysiology diseases (Kantarci et al., 2010; Teipel et al., 2012). TDTI metrics including fractional anisotropy (FA) and mean diffusivity (MD) have been used as potential imaging biomarkers for the diagnosis of AD (Teipel et al., 2011; Nir et al.,

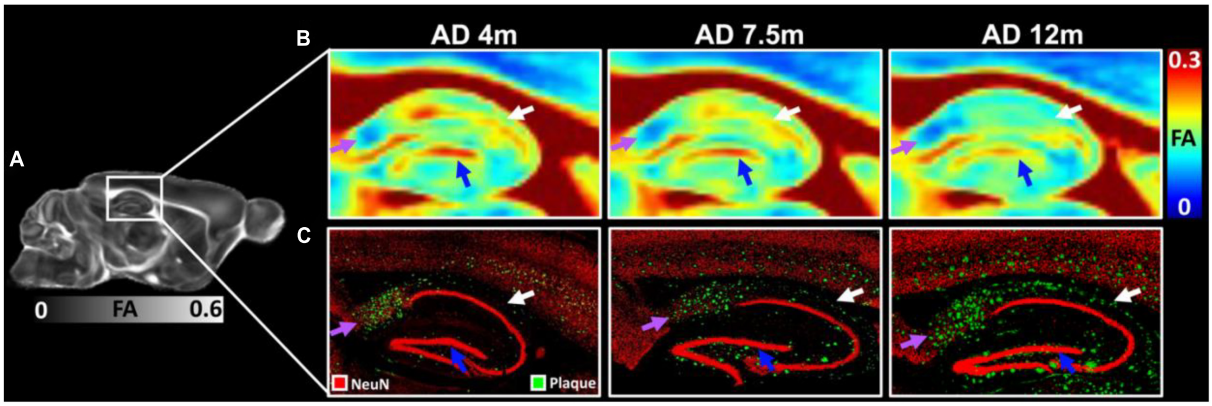

FIGURE 6
The FA images **(A,B)** and beta-amyloid staining **(C)** at different ages of 5xFAD in hippocampus region. The FA values showed strongly age-dependent in the dentate gyrus (DG, blue arrows), the dorsal subiculum (DS, purple arrows), and the CA2 (white arrows). The plaques gradually increased with age in the hippocampus regions **(C)**.

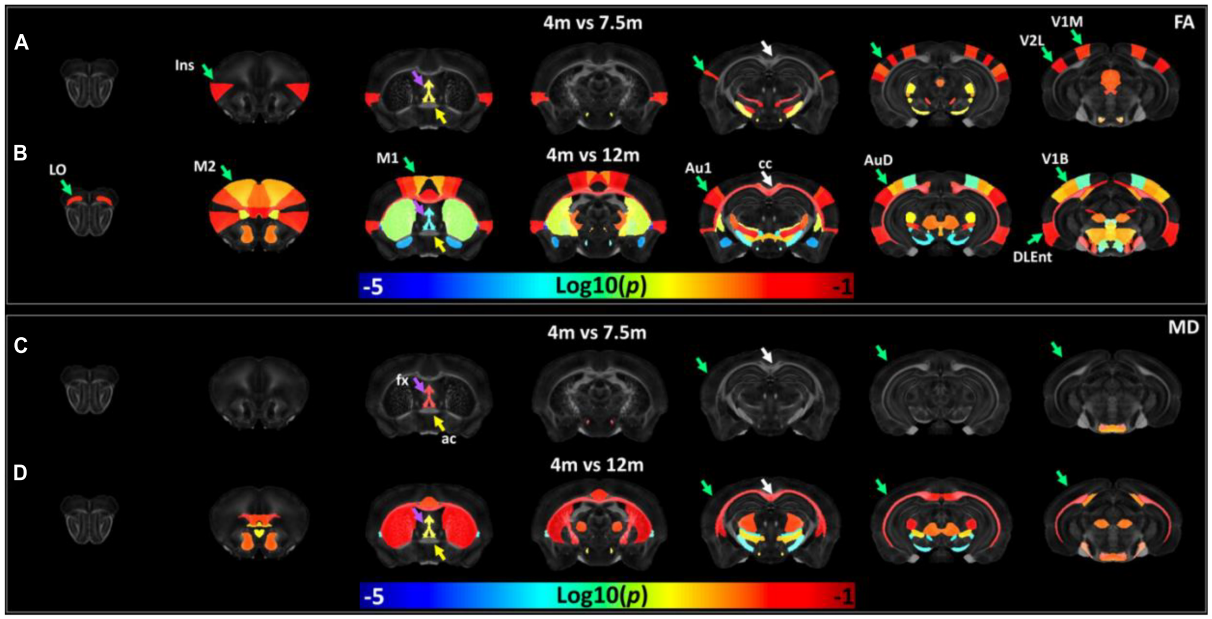

FIGURE 7
The age-dependent whole-brain microstructure changes in 5xFAD mice. The fractional anisotropy (FA) statistic maps (**A,B**) exhibited higher sensitivity to the age effect compared to mean diffusivity (MD) (**C,D**). Ins, insular cortex; V1M, primary visual cortex monocular area; V2L, secondary visual cortex lateral area; fx, fornix; M1, primary motor cortex; M2, secondary motor cortex; LO, lateral orbital cortex; Au1, primary auditory cortex; AuD, secondary auditory cortex dorsal part; V1B, primary visual cortex binocular area; DlEnt, dorsal intermediate entorhinal cortex; cc, corpus callosum; Cpu, striatum.

2013). The 5xFAD is one of the most common mouse models to study the beta-amyloid aspects of human AD, its microstructure change with age has not been investigated in detail (Oakley et al., 2006). In this study, we acquired whole-brain high-angular resolution dMRI at 100 μm^3 and investigated the age-dependent (4, 7.5, and 12 months) DTI metrics variations in different regions of the brain (166 ROIs).

The beta-amyloid plaques are a hallmark of AD that develop in its early stage (Reger et al., 2008). Non-invasive detection of these plaques would be invaluable for diagnosis and monitoring the treatment. The MRI signal has been enhanced by the MEMRI to visualize the Aβ plaques in transgenic rodent models of AD (Kim et al., 2021). Dudeffant et al. (2017) demonstrated that Gadolinium (Gd)-stained MRI can be used to detect the amyloid plaques in both mouse AD models and human-AD

brains. The Aβ plaques could also be detected in mouse AD models using a high-resolution T2-weighted spin-echo sequence (Jack et al., 2005). In this study, high-resolution GRE pulse sequence (50 μm isotropic) was applied to detect the AB plaques. The plaques showed hypointensity in MRI images and increased with age in both cortex and hippocampus regions, which is consistent with several previous findings (Higuchi et al., 2005; Meadowcroft et al., 2009). Distinguishing individual amyloid plaques by high-resolution MRI might provide a noninvasive estimate of plaque burden in transgenic AD mice that might be useful in assessing the efficacy of anti-amyloid therapies (Santin et al., 2016).

Several studies have demonstrated that DTI changes precede the anatomical changes on structural MRI for detecting the brain impairment in different mice models (Zhang et al., 2012; Muller et al., 2020). However, the observed DTI scalars are not consistent across studies, probably due to the dynamic microstructural change in different animal models. For instance, FA in the cortex was reported to increase in 3xTg AD mice (Snow et al., 2017; Manno et al., 2019), while the FA was showed reduced in APP transgenic mice (Muller et al., 2013; Qin et al., 2013). It's also suggested that DTI studies of AD models with marked neuron loss indicate increased MD, whereas those of a mild neuropathological phenotype without neuron loss tend to report decreased MD (Snow et al., 2017). Compared to MD, we demonstrated the reduction of FA in the cortex region can be detected as early as 4 months between WT and 5xFAD. The cortex area exhibited lower FA values and higher plaque loading in 5xFAD mice with age, which suggests that FA could be a sensitive imaging biomarker to detect the beta-amyloid pathology in the AD mice.

In the current study, we divided the whole brain into 166 different regions, in which more than 40 ROIs belong to isocortex (Wang et al., 2020a). It allows us to investigate the spatial–temporal pattern of the microstructure with the beta-amyloid progression in a well-established AD mouse model. At 7.5 months age, primary visual cortex and secondary visual cortex have already reduced the FA values significantly. At 12 months age, more cortex regions exhibited microstructure alterations, including the primary visual cortex, secondary auditory cortex, primary auditory cortex, dorsolateral entorhinal cortex, and motor cortex. In contrast, fewer cortex regions showed significant MD changes compared to FA values, which suggests that FA could be used to detect the inhomogeneous progression of beta-amyloid deposition at different regions of the cortex area.

Similar to the cortex, amyloid plaque loading is known to be high in hippocampus (Lazarov et al., 2002; Vyas et al., 2020). Reduced FA and increased MD in hippocampus were reported in many of these human studies, probably attributed to increased extracellular space volume and neurodegeneration (Muller et al., 2007; Cherubini et al., 2010; Hong et al., 2013; Nowrangi et al., 2013). It has been reported that only FA showed a significant increase in the hippocampus of APP/PS1 mice, compared to other DTI metrics (Shu et al., 2013). In contrast, decreased FA was detected in the hippocampus in the 12-14-month-old 3xTG AD mice (Snow et al., 2017). In the current study, both FA and MD showed no significant differences for the ROI-based analysis (whole hippocampus). The inconsistency may cause by different mouse models and different ages of mice in different studies. The heterogeneous FA alterations were observed in the subregions of the hippocampus, which may be associated primarily with the plaque deposition and related inflammation (Praet et al., 2018). It has been noted that the hippocampus exhibits complex microstructure and has been demonstrated to show laminar features due to layer-dependent FA values (Wang et al., 2020b). The higher spatial resolution dMRI with sub-region analysis should be performed in future studies to investigate the inhomogeneous microstructure alterations at different layers of the hippocampus (Wu et al., 2020).

Alzheimer's disease is classically considered a disease of gray matter; however, white matter abnormalities have been widely reported in the brains of incipient and mildly afflicted individuals (Sachdev et al., 2013). Advanced neuroimaging studies demonstrate that patients with preclinical AD have widespread white matter abnormalities at a stage similar to those reported in AD (Marquez and Yassa, 2019; Stone et al., 2021). White matter abnormalities, particularly axonal transport deficiencies, are also important components of AD (Klok et al., 2018). The fornix is a white matter bundle belonging to the medial diencephalon and serves a vital role in memory functions (Copenhaver et al., 2006; Nowrangi and Rosenberg, 2015). Fornix microstructural degradation, as measured by reduced FA, was prominent in both MCI and AD, and may provide evidence of degenerative white matter injury in AD (Lee et al., 2012). The age-dependent microstructural alterations of fx were demonstrated by both FA and MD in 5xFAD mice. In contrast, the ac showed no significant changes among different ages (4 m–12 m), which is consistent with a recent study using the P301L mouse model (Massalimova et al., 2021). Compared to other white matter bundles, fornix may play an important role in AD pathology and can be used as a disease biomarker for pharmacological therapeutics (Badea et al., 2016).

There are several limitations in our study. First, we only performed ROI-based analysis due to the limited sample size, the voxel-based analysis should be performed with larger sample size. Second, compared to *in vivo* studies, *ex vivo* MRI affords higher resolution and fewer motion artifacts, it may not accurately represent the tissue microstructures under normal physiological conditions due to the fixation. Third, only female 5xFAD mice were conducted in the study, the sex difference effect is warranted in future studies. In addition, transgenic models have been widely used to study AD risk

factors and mechanisms, but the degree of characteristics displayed in comparison with AD in humans is still limited (Elder et al., 2010).

Conclusion

We demonstrated that microstructure alterations are age-dependent using a model of progressive brain amyloidosis. We were able to detect the inhomogeneous FA alterations in different parts of cortex and hippocampus. The spatial–temporal pattern of the microstructure changes in the cortex region with the beta-amyloid progression has been generated. DTI metrics could be used to monitor the progression of beta-amyloid deposition and the efficiency of the anti-AD drugs.

Data availability statement

The original contributions presented in this study are included in the article/**Supplementary material**, further inquiries can be directed to the corresponding author.

Ethics statement

The animal study was reviewed and approved by Indiana University Institutional Animal Care and Use Committee.

Author contributions

SM and NW: study conception and design and draft manuscript preparation. AT, PL, CI, MJ, and NW: data collection. SM, GL, AO, and NW: analysis and interpretation of results. All authors reviewed the manuscript and approved the submitted version.

Funding

This work was supported by NIH R01NS125020, RF1AG068400, U54AG054345, and K01AG054753.

Acknowledgments

The authors thank Yu-Chien Wu and Erin Jarvis from Roberts Translational Imaging Facility and STARK Neuroscience Research Institute for resource support.

Conflict of interest

The authors declare that the research was conducted in the absence of any commercial or financial relationships that could be construed as a potential conflict of interest.

Publisher's note

All claims expressed in this article are solely those of the authors and do not necessarily represent those of their affiliated organizations, or those of the publisher, the editors and the reviewers. Any product that may be evaluated in this article, or claim that may be made by its manufacturer, is not guaranteed or endorsed by the publisher.

Supplementary material

The Supplementary Material for this article can be found online at: https://www.frontiersin.org/articles/10.3389/fnins.2022.964654/full#supplementary-material

References

Adlard, P. A., Tran, B. A., Finkelstein, D. I., Desmond, P. M., Johnston, L. A., Bush, A. I., et al. (2014). A review of beta-amyloid neuroimaging in Alzheimer's disease. *Front. Neurosci.* 8:327. doi: 10.3389/fnins.2014.00327

Badea, A., Kane, L., Anderson, R. J., Qi, Y., Foster, M., Cofer, G. P., et al. (2016). The fornix provides multiple biomarkers to characterize circuit disruption in a mouse model of Alzheimer's disease. *Neuroimage* 142, 498–511

doi: 10.1016/j.neuroimage.2016.08.014

Bloom, G. S. (2014). Amyloid-beta and tau the trigger and bullet in alzheimer disease pathogenesis. *JAMA Neurol.* 71, 505–508 doi: 10.1001/jamaneurol.2013.5847

Bozzali, M., Falini, A., Franceschi, M., Cercignani, M., Zuffi, M., Scotti, G., et al. (2002). White matter damage in Alzheimer's disease assessed in vivo using diffusion tensor magnetic resonance imaging. *J. Neurol. Neurosurg. Psychiatry* 72, 742–746 doi: 10.1136/jnnp.72.6.742

Busciglio, J., Lorenzo, A., Yeh, J., and Yankner, B. A. (1995). Beta-amyloid fibrils induce tau-phosphorylation and loss of microtubule-binding. *Neuron* 14, 879–888 doi: 10.1016/0896-6273(95)90232-5

Bush, A. I. (2003). The metallobiology of Alzheimer's disease. *Trends Neurosci.* 26, 207–214 doi: 10.1016/S0166-2236(03)00067-5

Cherubini, A., Peran, P., Spoletini, I., Di Paola, M., Di Iulio, F., Hagberg, G. E., et al. (2010). Combined volumetry and DTI in subcortical structures of mild cognitive impairment and Alzheimer's disease patients. *J. Alzheimers Dis.* 19, 1273–1282 doi: 10.3233/JAD-2010-091186

Copenhaver, B. R., Rabin, L. A., Saykin, A. J., Roth, R. M., Wishart, H. A., Flashman, L. A., et al. (2006). The fornix and mammillary bodies in older adults

with Alzheimer's disease, mild cognitive impairment, and cognitive complaints: A volumetric MRI study. *Psychiatry Res. Neuroimaging* 147, 93–103 doi: 10.1016/j.pscychresns.2006.01.015

Crater, S., Maharjan, S., Qi, Y., Zhao, Q., Cofer, G., Cook, J. C., et al. (2022). Resolution and b value dependent structural connectome in ex vivo mouse brain. *Neuroimage* 255:119199 doi: 10.1016/j.neuroimage.2022.119199

Dudeffant, C., Vandesquille, M., Herbert, K., Garin, C. M., Alves, S., Blanchard, V., et al. (2017). Contrast-enhanced MR microscopy of amyloid plaques in five mouse models of amyloidosis and in human Alzheimer's disease brains. *Sci. Rep.* 7:4955 doi: 10.1038/s41598-017-05285-1

Elder, G. A., Sosa, M. A. G., and De Gasperi, R. (2010). Transgenic mouse models of Alzheimer's disease. *Mount Sinai J. Med.* 77, 69–81 doi: 10.1002/msj.20159

Forner, S., Kawauchi, S., Balderrama-Gutierrez, G., Kramar, E. A., Matheos, D. P., Phan, J., et al. (2021). Systematic phenotyping and characterization of the 5xFAD mouse model of Alzheimer's disease. *Sci. Data* 8:270 doi: 10.1038/s41597-021-01054-y

Girard, S. D., Baranger, K., Gauthier, C., Jacquet, M., Bernard, A., Escoffier, G., et al. (2013). Evidence for early cognitive impairment related to frontal cortex in the 5xFAD mouse model of Alzheimer's disease. *J. Alzheimers Dis.* 33, 781–796 doi: 10.3233/JAD-2012-120982

Goedert, M., and Spillantini, M. G. (2006). A century of Alzheimer's disease. *Science* 314, 777–781 doi: 10.1126/science.1132814

Harrison, J. R., Bhatia, S., Tan, Z. X., Mirza-Davies, A., Benkert, H., Tax, C. M. W., et al. (2020). Imaging Alzheimer's genetic risk using diffusion MRI: A systematic review. *Neuroimage Clin.* 27:102359 doi: 10.1016/j.nicl.2020.102359

Higuchi, M., Iwata, N., Matsuba, Y., Sato, K., Sasamoto, K., and Saido, T. C. (2005). 19F and 1H MRI detection of amyloid beta plaques in vivo. *Nat. Neurosci.* 8, 527–533 doi: 10.1038/nn1422

Hong, Y. J., Yoon, B., Lim, S. C., Shim, Y. S., Kim, J. Y., Ahn, K. J., et al. (2013). Microstructural changes in the hippocampus and posterior cingulate in mild cognitive impairment and Alzheimer's disease: A diffusion tensor imaging study. *Neurol. Sci.* 34, 1215–1221 doi: 10.1007/s10072-012-1225-4

Igarashi, H., Ueki, S., Kitaura, H., Kera, T., Ohno, K., Ohkubo, M., et al. (2020). Longitudinal GluCEST MRI changes and cerebral blood flow in 5xFAD mice. *Contrast Media Mol. Imaging* 2020:8831936 doi: 10.1155/2020/8831936

Jack, C. R. Jr., Wengenack, T. M., Reyes, D. A., Garwood, M., Curran, G. L., et al. (2005). In vivo magnetic resonance microimaging of individual amyloid plaques in Alzheimer's transgenic mice. *J. Neurosci.* 25, 10041–10048 doi: 10.1523/JNEUROSCI.2588-05.2005

Jacobs, H. I., Van Boxtel, M. P., Gronenschild, E. H., Uylings, H. B., Jolles, J., and Verhey, F. R. (2013). Decreased gray matter diffusivity: A potential early Alzheimer's disease biomarker? *Alzheimers Dement.* 9, 93–97 doi: 10.1016/j.jalz.2011.11.004

Jankowsky, J. L., and Zheng, H. (2017). Practical considerations for choosing a mouse model of Alzheimer's disease. *Mol. Neurodegener.* 12:89 doi: 10.1186/s13024-017-0231-7

Jullienne, A., Trinh, M. V., and Obenaus, A. (2022). Neuroimaging of Mouse Models of Alzheimer's Disease. *Biomedicines* 10:305. doi: 10.3390/biomedicines10020305

Kantarci, K., Avula, R., Senjem, M. L., Samikoglu, A. R., Zhang, B., Weigand, S. D., et al. (2010). Dementia with lewy bodies and Alzheimer disease neurodegenerative patterns characterized by DTI. *Neurology* 74, 1814–1821 doi: 10.1212/WNL.0b013e3181e0f7cf

Kantarci, K., Petersen, R. C., Boeve, B. F., Knopman, D. S., Weigand, S. D., O'brien, P. C., et al. (2005). DWI predicts future progression to Alzheimer disease in amnestic mild cognitive impairment. *Neurology* 64, 902–904 doi: 10.1212/01.WNL.0000153076.46126.E9

Kesler, S. R., Acton, P., Rao, V., and Ray, W. J. (2018). Functional and structural connectome properties in the 5xFAD transgenic mouse model of Alzheimer's disease. *Netw. Neurosci.* 2, 241–258 doi: 10.1162/netn_a_00048

Kim, E., Di Censo, D., Baraldo, M., Simmons, C., Rosa, I., Randall, K., et al. (2021). In vivo multi-parametric manganese-enhanced MRI for detecting amyloid plaques in rodent models of Alzheimer's disease. *Sci. Rep.* 11:12419 doi: 10.1038/s41598-021-91899-5

Kitazawa, M., Medeiros, R., and Laferla, F. M. (2012). Transgenic mouse models of alzheimer disease: Developing a better model as a tool for therapeutic interventions. *Curr. Pharm. Des.* 18, 1131–1147 doi: 10.2174/138161212799315786

Klok, M. D., Bugiani, M., De Vries, S. I., Gerritsen, W., Breur, M., Van Der Sluis, S., et al. (2018). Axonal abnormalities in vanishing white matter. *Ann. Clin. Transl. Neurol.* 5, 429–444 doi: 10.1002/acn3.540

Koss, D. J., Jones, G., Cranston, A., Gardner, H., Kanaan, N. M., and Platt, B. (2016). Soluble pre-fibrillar tau and beta-amyloid species emerge in early human Alzheimer's disease and track disease progression and cognitive decline. *Acta Neuropathol.* 132, 875–895 doi: 10.1007/s00401-016-1632-3

Lazarov, O., Lee, M., Peterson, D. A., and Sisodia, S. S. (2002). Evidence that synaptically released beta-amyloid accumulates as extracellular deposits in the hippocampus of transgenic mice. *J. Neurosci.* 22, 9785–9793 doi: 10.1523/JNEUROSCI.22-22-09785.2002

Lee, D. Y., Fletcher, E., Carmichael, O. T., Singh, B., Mungas, D., Reed, B., et al. (2012). Sub-regional hippocampal injury is associated with fornix degeneration in Alzheimer's disease. *Front. Aging Neurosci.* 4:1 doi: 10.3389/fnagi.2012.00001

Manno, F. A. M., Isla, A. G., Manno, S. H. C., Ahmed, I., Cheng, S. H., Barrios, F. A., et al. (2019). Early stage alterations in white matter and decreased functional interhemispheric hippocampal connectivity in the 3xTg mouse model of Alzheimer's disease. *Front. Aging Neurosci.* 11:39 doi: 10.3389/fnagi.2019.00039

Marquez, F., and Yassa, M. A. (2019). Neuroimaging biomarkers for Alzheimer's disease. *Mol. Neurodegener.* 14:21 doi: 10.1186/s13024-019-0325-5

Massalimova, A., Ni, R. Q., Nitsch, R. M., Reisert, M., Von Elverfeldt, D., and Klohs, J. (2021). Diffusion tensor imaging reveals whole-brain microstructural changes in the P301L mouse model of tauopathy. *Neurodegener. Dis.* 20, 173–184 doi: 10.1159/000515754

Meadowcroft, M. D., Connor, J. R., Smith, M. B., and Yang, Q. X. (2009). MRI and histological analysis of beta-amyloid plaques in both human Alzheimer's disease and APP/PS1 transgenic mice. *J. Magnetic Resonance Imaging* 29, 997–1007 doi: 10.1002/jmri.21731

Mielke, M. M., Kozauer, N. A., Chan, K. C. G., George, M., Toroney, J., Zerrate, M., et al. (2009). Regionally-specific diffusion tensor imaging in mild cognitive impairment and Alzheimer's disease. *Neuroimage* 46, 47–55 doi: 10.1016/j.neuroimage.2009.01.054

Mlynarik, V., Cacquevel, M., Sun-Reimer, L., Janssens, S., Cudalbu, C., Lei, H. X., et al. (2012). Proton and phosphorus magnetic resonance spectroscopy of a mouse model of Alzheimer's disease. *J. Alzheimers Dis.* 31, S87–S99 doi: 10.3233/JAD-2012-112072

Muller, H. P., Kassubek, J., Vernikouskaya, I., Ludolph, A. C., Stiller, D., and Rasche, V. (2013). Diffusion tensor magnetic resonance imaging of the brain in app transgenic mice: A cohort study. *PLos One* 8:e67630. doi: 10.1371/journal.pone.0067630

Muller, H. P., Roselli, F., Rasche, V., and Kassubek, J. (2020). Diffusion tensor imaging-based studies at the group-level applied to animal models of neurodegenerative diseases. *Front. Neurosci.* 14:734. doi: 10.3389/fnins.2020.00734

Muller, M. J., Greverus, D., Weibrich, C., Dellani, P. R., Scheurich, A., Stoeter, P., et al. (2007). Diagnostic utility of hippocampal size and mean diffusivity in amnestic MCI. *Neurobiol. Aging* 28, 398–403 doi: 10.1016/j.neurobiolaging.2006.01.009

Nir, T. M., Jahanshad, N., Villalon-Reina, J. E., Toga, A. W., Jack, C. R., Weiner, M. W., et al. (2013). Effectiveness of regional DTI measures in distinguishing Alzheimer's disease, MCI, and normal aging. *Neuroimage Clin.* 3, 180–195 doi: 10.1016/j.nicl.2013.07.006

Nowrangi, M. A., Lyketsos, C. G., Leoutsakos, J. M. S., Oishi, K., Albert, M., Mori, S., et al. (2013). Longitudinal, region-specific course of diffusion tensor imaging measures in mild cognitive impairment and Alzheimer's disease. *Alzheimers Dement.* 9, 519–528 doi: 10.1016/j.jalz.2012.05.2186

Nowrangi, M. A., and Rosenberg, P. B. (2015). The fornix in mild cognitive impairment and Alzheimer's disease. *Front. Aging Neurosci.* 7:1. doi: 10.3389/fnagi.2015.00001

Oakley, H., Cole, S. L., Logan, S., Maus, E., Shao, P., Craft, J., et al. (2006). Intraneuronal beta-amyloid aggregates, neurodegeneration, and neuron loss in transgenic mice with five familial Alzheimer's disease mutations: Potential factors in amyloid plaque formation. *J. Neurosci.* 26, 10129–10140 doi: 10.1523/JNEUROSCI.1202-06.2006

Oblak, A. L., Lin, P. B., Kotredes, K. P., Pandey, R. S., Garceau, D., Williams, H. M., et al. (2021). Comprehensive evaluation of the 5xFAD mouse model for preclinical testing applications: A MODEL-AD study. *Front. Aging Neurosci.* 13:713726. doi: 10.3389/fnagi.2021.713726

Praet, J., Manyakov, N. V., Muchene, L., Mai, Z. H., Terzopoulos, V., De Backer, S., et al. (2018). Diffusion kurtosis imaging allows the early detection and longitudinal follow-up of amyloid-beta-induced pathology. *Alzheimers Res. Therapy* 10:1 doi: 10.1186/s13195-017-0329-8

Qin, Y. Y., Li, M. W., Zhang, S., Zhang, Y., Zhao, L. Y., Lei, H., et al. (2013). In vivo quantitative whole-brain diffusion tensor imaging analysis of APP/PS1 transgenic mice using voxel-based and atlas-based methods. *Neuroradiology* 55, 1027–1038 doi: 10.1007/s00234-013-1195-0

Reger, M. A., Watson, G. S., Green, P. S., Wilkinson, C. W., Baker, L. D., Cholerton, B., et al. (2008). Intranasal insulin improves cognition and modulates beta-amyloid in early AD. *Neurology* 70, 440–448 doi: 10.1212/01.WNL.0000265401.62434.36

Rose, S. E., Chen, F., Chalk, J. B., Zelaya, F. O., Strugnell, W. E., Benson, M., et al. (2000). Loss of connectivity in Alzheimer's disease: An evaluation of white matter tract integrity with colour coded MR diffusion tensor imaging. *J. Neurol. Neurosurg. Psychiatry* 69, 528–530 doi: 10.1136/jnnp.69.4.528

Sachdev, P. S., Zhuang, L., Braidy, N., and Wen, W. (2013). Is Alzheimer's a disease of the white matter? *Curr. Opin. Psychiatry* 26, 244–251 doi: 10.1097/YCO.0b013e32835ed6e8

Santin, M. D., Vandenberghe, M. E., Herardi, A. S., Pradier, L., Cohen, C., Debeir, T., et al. (2016). In vivo detection of amyloid plaques by gadolinium-stained MRI can be used to demonstrate the efficacy of an anti-amyloid immunotherapy. *Front. Aging Neurosci.* 8:55. doi: 10.3389/fnagi.2016.00055

Sasaguri, H., Nilsson, P., Hashimoto, S., Nagata, K., Saito, T., De Strooper, B., et al. (2017). APP mouse models for Alzheimer's disease preclinical studies. *Embo J.* 36, 2473–2487 doi: 10.15252/embj.201797397

Shu, X. G., Qin, Y. Y., Zhang, S., Jiang, J. J., Zhang, Y., Zhao, L. Y., et al. (2013). Voxel-based diffusion tensor imaging of an APP/PS1 mouse model of Alzheimer's disease. *Mol. Neurobiol.* 48, 78–83 doi: 10.1007/s12035-013-8418-6

Snow, W. M., Dale, R., O'brien-Moran, Z., Buist, R., Peirson, D., Martin, M., et al. (2017). In vivo detection of gray matter neuropathology in the 3xTg mouse model of alzheimer's disease with diffusion tensor imaging. *J. Alzheimers Dis.* 58, 841–853 doi: 10.3233/JAD-170136

Stebbins, G. T., and Murphy, C. M. (2009). Diffusion tensor imaging in Alzheimer's disease and mild cognitive impairment. *Behav. Neurol.* 21, 39–49 doi: 10.1155/2009/915041

Stone, D. B., Ryman, S. G., Hartman, A. P., Wertz, C. J., Vakhtin, A. A., and Initi, A. S. D. N. (2021). Specific white matter tracts and diffusion properties predict conversion from mild cognitive impairment to Alzheimer's disease. *Front. Aging Neurosci.* 13:711579. doi: 10.3389/fnagi.2021.711579

Takahashi, R. H., Capetillo-Zarate, E., Lin, M. T., Milner, T. A., and Gouras, G. K. (2010). Co-occurrence of Alzheimer's disease beta-amyloid and tau pathologies at synapses. *Neurobiol. Aging* 31, 1145–1152 doi: 10.1016/j.neurobiolaging.2008.07.021

Teipel, S. J., Meindl, T., Grinberg, L., Grothe, M., Cantero, J. L., Reiser, M. F., et al. (2011). The cholinergic system in mild cognitive impairment and Alzheimer's disease: An in vivo MRI and DTI study. *Hum. Brain Mapp.* 32, 1349–1362 doi: 10.1002/hbm.21111

Teipel, S. J., Wegrzyn, M., Meindl, T., Frisoni, G., Bokde, A. L. W., Fellgiebel, A., et al. (2012). Anatomical MRI and DTI in the diagnosis of Alzheimer's disease: A european multicenter study. *J. Alzheimers Dis.* 31, S33–S47 doi: 10.3233/JAD-2012-112118

Thal, D. R., Attems, J., and Ewers, M. (2014). Spreading of amyloid, tau, and microvascular pathology in Alzheimer's disease: Findings from neuropathological and neuroimaging studies. *J. Alzheimers Dis.* 42, S421–S429. doi: 10.3233/JAD-141461

Torso, M., Bozzali, M., Zamboni, G., Jenkinson, M., Chance, S. A., and Neuroimage, A. D. (2021). Detection of Alzheimer's disease using cortical diffusion tensor imaging. *Hum. Brain Mapp.* 42, 967–977 doi: 10.1002/hbm.25271

Tsai, A. P., Lin, P. B.-C., Dong, C., Moutinho, M., Casali, B. T., Liu, Y., et al. (2021). INPP5D expression is associated with risk for Alzheimer's disease and induced by plaque-associated microglia. *Neurobiol. Dis.* 153:105303 doi: 10.1016/j.nbd.2021.105303

Veale, T., Malone, I. B., Poole, T., Parker, T. D., Slattery, C. F., Paterson, R. W., et al. (2021). Loss and dispersion of superficial white matter in Alzheimer's disease: A diffusion MRI study. *Brain Commun.* 3:fcab272 doi: 10.1093/braincomms/fcab272

Vyas, Y., Montgomery, J. M., and Cheyne, J. E. (2020). Hippocampal deficits in amyloid-beta-related rodent models of Alzheimer's disease. *Front. Neurosci.* 14:266. doi: 10.3389/fnins.2020.00266

Wang, L., Benzinger, T. L., Su, Y., Christensen, J., Friedrichsen, K., Aldea, P., et al. (2016). Evaluation of tau imaging in staging Alzheimer disease and revealing interactions between beta-amyloid and tauopathy. *JAMA Neurol.* 73, 1070–1077. doi: 10.1001/jamaneurol.2016.2078

Wang, N., Anderson, R. J., Ashbrook, D. G., Gopalakrishnan, V., Park, Y., Priebe, C. E., et al. (2020a). Variability and heritability of mouse brain structure: Microscopic MRI atlases and connectomes for diverse strains. *Neuroimage* 222:117274 doi: 10.1016/j.neuroimage.2020.117274

Wang, N., White, L. E., Qi, Y., Cofer, G., and Johnson, G. A. (2020b). Cytoarchitecture of the mouse brain by high resolution diffusion magnetic resonance imaging. *Neuroimage* 216:116876 doi: 10.1016/j.neuroimage.2020.116876

Wang, N., Anderson, R. J., Badea, A., Cofer, G., Dibb, R., Qi, Y., et al. (2018a). Whole mouse brain structural connectomics using magnetic resonance histology. *Brain Struct. Funct.* 223, 4323–4335 doi: 10.1007/s00429-018-1750-x

Wang, N., Cofer, G., Anderson, R. J., Qi, Y., Liu, C. L., and Johnson, G. A. (2018b). Accelerating quantitative susceptibility imaging acquisition using compressed sensing. *Phys. Med. Biol.* 63:245002. doi: 10.1088/1361-6560/aaf15d

Wang, N., Zhuang, J., Wei, H. J., Dibb, R., Qi, Y., and Liu, C. L. (2019b). Probing demyelination and remyelination of the cuprizone mouse model using multimodality MRI. *J. Magnetic Resonance Imaging* 50, 1852–1865 doi: 10.1002/jmri.26758

Wang, N., Zhang, J. Y., Cofer, G., Qi, Y., Anderson, R. J., White, L. E., et al. (2019a). Neurite orientation dispersion and density imaging of mouse brain microstructure. *Brain Struct. Funct.* 224, 1797–1813 doi: 10.1007/s00429-019-01877-x

Wu, D., Lei, J., Xie, H., Dong, J., and Burd, I. (2020). Diffusion MRI revealed altered inter-hippocampal projections in the mouse brain after intrauterine inflammation. *Brain Imaging Behav.* 14, 383–395 doi: 10.1007/s11682-019-{\break}00246-w doi: 10.1007/s11682-019-00246-w

Yeh, F. C., Wedeen, V. J., and Tseng, W. Y. I. (2010). Generalized q-Sampling imaging. *Ieee Trans. Med. Imaging* 29, 1626–1635 doi: 10.1109/TMI.2010.2045126

Zhang, J. Y., Aggarwal, M., and Mori, S. (2012). Structural insights into the rodent CNS via diffusion tensor imaging. *Trends Neurosci.* 35, 412–421 doi: 10.1016/j.tins.2012.04.010

frontiers | Frontiers in Neuroscience

TYPE Correction
PUBLISHED 13 October 2022
DOI 10.3389/fnins.2022.1025457

OPEN ACCESS

EDITED AND REVIEWED BY
Jie Wang,
Wuhan Institute of Physics and Mathematics (CAS), China

*CORRESPONDENCE
Nian Wang
nianwang@iu.edu

SPECIALTY SECTION
This article was submitted to Brain Imaging Methods, a section of the journal Frontiers in Neuroscience

RECEIVED 22 August 2021
ACCEPTED 21 September 2021
PUBLISHED 13 October 2022

CITATION
Maharjan S, Tsai AP, Lin PB, Ingraham C, Jewett MR, Landreth GE, Oblak AL and Wang N (2022) Corrigendum: Age-dependent microstructure alterations in 5xFAD mice by high-resolution diffusion tensor imaging.
Front. Neurosci. 16:1025457.
doi: 10.3389/fnins.2022.1025457

Corrigendum: Age-dependent microstructure alterations in 5xFAD mice by high-resolution diffusion tensor imaging

Surendra Maharjan[1], Andy P. Tsai[2], Peter B. Lin[2], Cynthia Ingraham[2], Megan R. Jewett[1], Gary E. Landreth[2,3], Adrian L. Oblak[1,2] and Nian Wang[1,2]*

[1]Department of Radiology and Imaging Sciences, Indiana University, Indianapolis, IN, United States, [2]Stark Neurosciences Research Institute, Indiana University, Indianapolis, IN, United States, [3]Department of Anatomy, Cell Biology and Physiology, Indiana University, Indianapolis, IN, United States

KEYWORDS

Alzheimer's disease, 5xFAD, MRI, DTI, diffusion MRI (dMRI)

A corrigendum on
Age-dependent microstructure alterations in 5xFAD mice by high-resolution diffusion tensor imaging

by Maharjan, S., Tsai, A. P., Lin, P. B., Ingraham, C., Jewett, M. R., Landreth, G. E., Oblak, A. L., and Wang, N. (2022). *Front. Neurosci.* 16:964654. doi: 10.3389/fnins.2022.964654

In the published article, there was an error in **Materials and methods**, "*Histology*," paragraph 1. The incorrect histology protocol was used and the description of the histology (slice thickness, antibody of NeuN, microscope) was therefore incorrect. The paragraph previously stated:

"Histological examinations were performed on the mice brains as previous described (Oblak et al., 2021; Tsai et al., 2021). Coronal 8-μm thick slices were stained immunocytochemically stained for the neuronal nuclear antigen (NeuN) (MAB377, lot 2967854, Millipore, Burlington, MA, United States) and 6E10 staining (BioLegend #803001 in mouse, 1:1000; AB_2564653) for beta-amyloid plaques. The slides were imaged using Axioscop2 FSmot optical microscope with EC PlanNeofluar Zeiss lens at 20× magnification, 0.3 aperture under the same settings and light conditions."

The corrected paragraph appears below:

"Histological examinations were performed on the mice brains as previous described (Oblak et al., 2021; Tsai et al., 2021). Thirty micron-thick sections were stained to visualize neuronal cell bodies and beta-amyloid plaques using antibodies directed against NeuN (Abcam #ab104225, 1:1000, Boston, MA) and 6E10 (BioLegend #803001, 1:1000). The slides were imaged using Leica DVM6 digital microscope."

The authors apologize for this error and state that this does not change the scientific conclusions of the article in any way. The original article has been updated.

Publisher's note

References

Oblak, A. L., Lin, P. B., Kotredes, K. P., Pandey, R. S., Garceau, D., Williams, H. M., et al. (2021). Comprehensive evaluation of the 5xFAD mouse model for preclinical testing applications: A MODEL-AD study. *Front. Aging Neurosci.* 13:713726. doi: 10.3389/fnagi.2021.713726

Tsai, A. P., Lin, P. B.-C., Dong, C., Moutinho, M., Casali, B. T., et al. (2021). INPP5D expression is associated with risk for Alzheimer's disease and induced by plaque-associated microglia. *Neurobiol. Dis.* 153:105303 doi: 10.1016/j.nbd.2021.105303

frontiers | Frontiers in Neuroscience

TYPE Original Research
PUBLISHED 23 September 2022
DOI 10.3389/fnins.2022.963175

OPEN ACCESS

EDITED BY
Abbas Babajani-Feremi,
University of Florida, United States

REVIEWED BY
Basavaraju G. Sanganahalli,
Yale University, United States
Arun Sasidharan,
National Institute of Mental Health and Neurosciences, India
Zhiliang Wei,
Johns Hopkins University, United States

*CORRESPONDENCE
Shengxiang Liang
sxliang@fjtcm.edu.cn

†These authors have contributed equally to this work

SPECIALTY SECTION
This article was submitted to Brain Imaging Methods, a section of the journal Frontiers in Neuroscience

RECEIVED 07 June 2022
ACCEPTED 05 August 2022
PUBLISHED 23 September 2022

CITATION
Huang J, Zhang Y, Zhang Q, Wei L, Zhang X, Jin C, Yang J, Li Z and Liang S (2022) The current status and trend of the functional magnetic resonance combined with stimulation in animals. *Front. Neurosci.* 16:963175. doi: 10.3389/fnins.2022.963175

The current status and trend of the functional magnetic resonance combined with stimulation in animals

Jiayang Huang[1,2,3†], Yusi Zhang[1,2,3†], Qi Zhang[3†], Linxuan Wei[3], Xiwen Zhang[3], Caiping Jin[4], Junchao Yang[1,2,3], Zuanfang Li[1,5] and Shengxiang Liang[1,2,6*]

[1]National-Local Joint Engineering Research Center of Rehabilitation Medicine Technology, Fujian University of Traditional Chinese Medicine, Fuzhou, China, [2]Rehabilitation Industry Institute, Fujian University of Traditional Chinese Medicine, Fuzhou, China, [3]College of Rehabilitation Medicine, Fujian University of Traditional Chinese Medicine, Fuzhou, China, [4]Basic Medicine College, Hebei University of Chinese Medicine, Shijiazhuang, China, [5]Innovation and Transformation Center, Fujian University of Traditional Chinese Medicine, Fuzhou, China, [6]Traditional Chinese Medicine Rehabilitation Research Center of State Administration of Traditional Chinese Medicine, Fujian University of Traditional Chinese Medicine, Fuzhou, China

As a non-radiative, non-invasive imaging technique, functional magnetic resonance imaging (fMRI) has excellent effects on studying the activation of blood oxygen levels and functional connectivity of the brain in human and animal models. Compared with resting-state fMRI, fMRI combined with stimulation could be used to assess the activation of specific brain regions and the connectivity of specific pathways and achieve better signal capture with a clear purpose and more significant results. Various fMRI methods and specific stimulation paradigms have been proposed to investigate brain activation in a specific state, such as electrical, mechanical, visual, olfactory, and direct brain stimulation. In this review, the studies on animal brain activation using fMRI combined with different stimulation methods were retrieved. The instruments, experimental parameters, anesthesia, and animal models in different stimulation conditions were summarized. The findings would provide a reference for studies on estimating specific brain activation using fMRI combined with stimulation.

KEYWORDS

functional magnetic resonance imaging, stimulation, animal, brain, activation

Introduction

Since the 1930s, magnetic resonance imaging (MRI) has been used as an effective tool for neuroscience research *in vivo*. Seiji Ogawa discovered the MR contrast mechanism of functional magnetic resonance imaging (fMRI) in 1990 (Ogawa et al., 1990). It relies on blood oxygen level-dependent (BOLD) changes in brain tissue. With the development of magnetic resonance technology, this oxygenation contrast becomes more obvious in high spatial resolution magnetic resonance imaging, which makes fMRI a non-radiative and non-invasive technique for studying neural activity changes (Liang S. et al., 2017; Zhang et al., 2021). In the initial human sensory stimulation studies, scientists realized that this was a reasonable way to map brain function (Ogawa et al., 1992).

fMRI can reflect the fluctuation of blood flow in the brain, which could map the patterns of brain activity in the resting state, the directional activation of specific brain regions, or the pathways caused by external stimulation (Sanganahalli et al., 2009). Humans and animals are connected to their environment (Arora, 2021). They receive information from the outside world all the time and send it to the brain for analysis (Ferezou and Deneux, 2017), which is the basis for human beings to perceive the world. Resting-state fMRI studies are meaningful, but evoked-state fMRI is preferred in dynamic interactions because it can reflect BOLD changes in the brain from multiple dimensions (Han et al., 2019). As early as 1995, Yang et al. (1996) performed vibration stimulation on the rats' whiskers to reflect the changes of external stimulation in the brain. A series of studies focusing on different stimulation modes has gradually emerged with the development of science and technology. Early studies have used electrical (Scanley et al., 1997), visual, olfactory, and auditory stimulation (Jezzard et al., 1997). Later, optogenetic, deep brain stimulation, electrical microstimulation, and multiple stimulations emerged (Kamada et al., 1999; Ferris et al., 2001). A variety of stimulation paradigms have been devised to accurately reflect the different brain regions and pathways through which animals communicate with the outside world, and the application of the stimulation provides a dependent variable for fMRI studies (Sanganahalli et al., 2009). Since stimulation intensity, location, electrode selection, and stimulation method may all affect imaging quality and stability (Spenger et al., 2000; Luo et al., 2009; Zhao et al., 2020), it is particularly important to design a suitable, reliable, and repeatable paradigm to meet the specific experiment objective (Chen et al., 2020).

In this review, we aimed to describe the current status and trends of animal fMRI combined with stimulation. Both the stimulation paradigms and the corresponding changes in fMRI activation during stimulation were explored *via* collecting and analyzing the activation states, the facility information, and the relevant information of stimulations in the previous animal fMRI studies. The findings would provide a basis for the choice of the stimulation paradigm and the parameter settings of fMRI to explore brain activation in animal studies.

Methods

We searched for the relevant articles in the PubMed database on September 25, 2021, using the following searching strategy. "Search (functional magnetic resonance imaging [Title/Abstract]) or (fMRI [Title/Abstract]) or (functional MRI [Title/Abstract]) and (stimu* [Title/Abstract]) Sort by: Best Match Filters: Abstract; Filters: Other Animals, from 1992–2021; Other Animals." We retrieved a total of 1,556 research articles. After screening the titles and abstracts, we excluded studies that did not use stimulation in the fMRI scanning process and received a total of 667 articles in the end. We extracted all kinds of parameters related to the stimulation methods, species, and anesthesia methods.

Results and discussion

Year distribution

The imaging quality of fMRI is related to the strength of the magnetic field and the scan sequence. As early as 1995, relevant research studies had already been performed, and they were reproducible in and among animals within the experimental error range (Yang et al., 1996). The specific time distribution of the studies is shown by the broken line graph (Figure 1A). "Most studies were" means that most of the early experiments were centered around electrical, visual, and mechanical stimulation. And as you can see from the year distribution (Figure 1A) these three types of stimuli have been studied earlier. With the development of optogenetics, deep brain stimulation (DBS), and electrical microstimulation (EM), there has been an increasing number of related fMRI studies because of their compatibility. Besides, the number of multistimulation experimental studies was increasing. At the same time, two of the most frequently used methods of experimental stimulation in the past—electrical and visual stimulation—showed a downward trend. Among other stimulations, the number of studies using direct brain stimulation and combined multistimulation has increased, while the number of studies using olfactory, auditory, mechanical, and other types of stimulation showed no obvious change. It indicated that multistimulation and direct brain stimulation are likely to be used more often in future studies.

Methods of animal anesthetization for scanning

During MRI scanning, the state of the animal can be classified as awake or anesthetized (Figure 2A). Awake imaging does not need an anesthetic during the scan, which usually achieves stable imaging through early adaptive training and restriction devices in different animals (Ferris, 2022). Under certain circumstances, a faster scan sequence (fast low-angle shot, FLASH) may be used to obtain a sharper image (Tsurugizawa et al., 2009b, 2010). While anesthesia imaging needs to maintain stable imaging of animals with an anesthetic, inhalation of isoflurane is the most commonly used anesthetic method in anesthesia experiments. Alpha-chloralose is also a more common choice. The choice of anesthetics is not limited to a single type, but mixed anesthesia (multiple mixed uses) is also often used. Ketamine is often used in a mixed way, and there are fewer ways to use ketamine alone (Figure 2B).

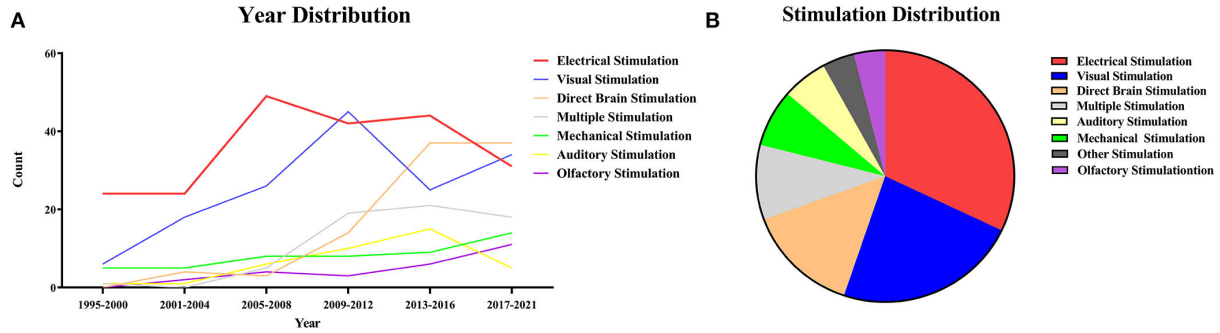

FIGURE 1
(A) Year distribution of stimuli. The years of the collected articles were sorted out according to the types of stimuli and then plotted into a line graph of year distribution. The line graph can intuitively reflect the hot spots and trends of the research on stimulation combined with functional magnetic resonance. **(B)** Stimulation distribution. All stimulation is divided according to the method of the stimulus, including electrical stimulation, visual stimulation, direct brain stimulation, multiple stimulation, mechanical stimulation, olfactory stimulation, auditory stimulation, and others. Among them, electrical stimulation (n = 214, 32.08%), visual stimulation (n = 154, 23.09%) and direct brain stimulation (n = 95, 14.24%) are the main methods.

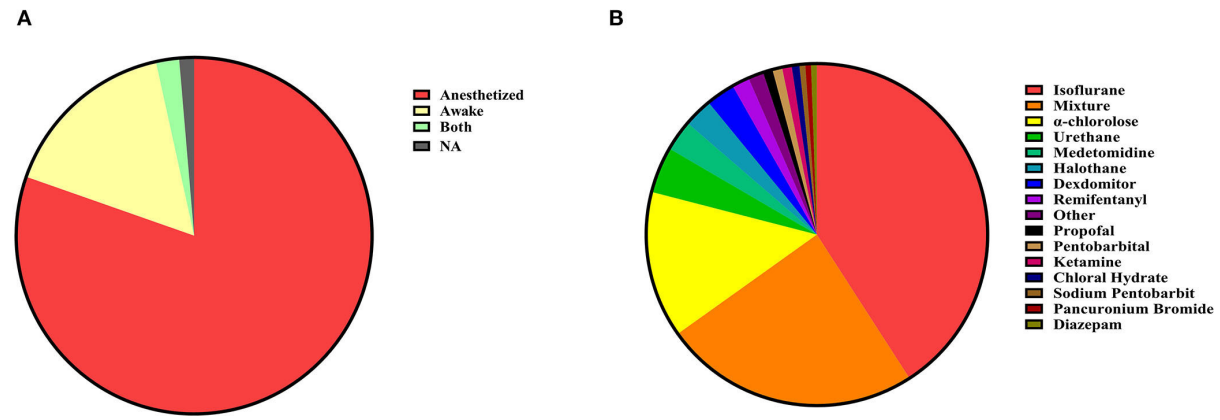

FIGURE 2
(A) Animal preparation. Animal fMRI relies mainly on anesthesia to help restrain animals; most studies are still conducted under anesthesia (n = 536, 80.36%). Compared with numerous articles under anesthesia, the awake experiment is more valuable (n = 108, 16.19%). A very few contained both animal states (n = 9, 1.35%) and unstated articles (NA, n = 14, 2.10%). **(B)** Anesthetics distribution. Isoflurane is the most commonly used anesthetic in experiments related to anesthesia, and the combination of anesthetics is also a popular choice.

Anesthetizing the experimental animals is more time-saving, labor-saving, and convenient for intervention than dealing with them in an awake state. Therefore, anesthetized animal models are preferred in research studies. For example, the neurovascular coupling has been studied extensively in anesthetized animal models. However, it showed severe disruption of brain metabolism, neural activity, and cardiovascular function. When the rodent models are anesthetized, fMRI scanning is a common method, but the physiological parameters of animals might change in the anesthetized state, which would affect fMRI results. With the emergence of different scanning schemes, designs, and modifications of scanning beds, it is now possible to study neurovascular coupling and brain circuit function in animals when they are awake and behaving normally. As long as these factors are not objectively quantified, the scientific validity of fMRI application in rodents will be compromised (Steiner et al., 2021). The imaging process of fMRI in the awake state is also worth further study, as it is closer to a normal physiological state. Some studies on the wakefulness state have been carried out in different animals, which showed repeatable stability (Hirano et al., 2018).

Sensory stimulation

The distribution maps of different stimulation types were plotted through data statistics (Figure 1B). fMRI studies with stimulation can be divided into electrical, mechanical, multiple,

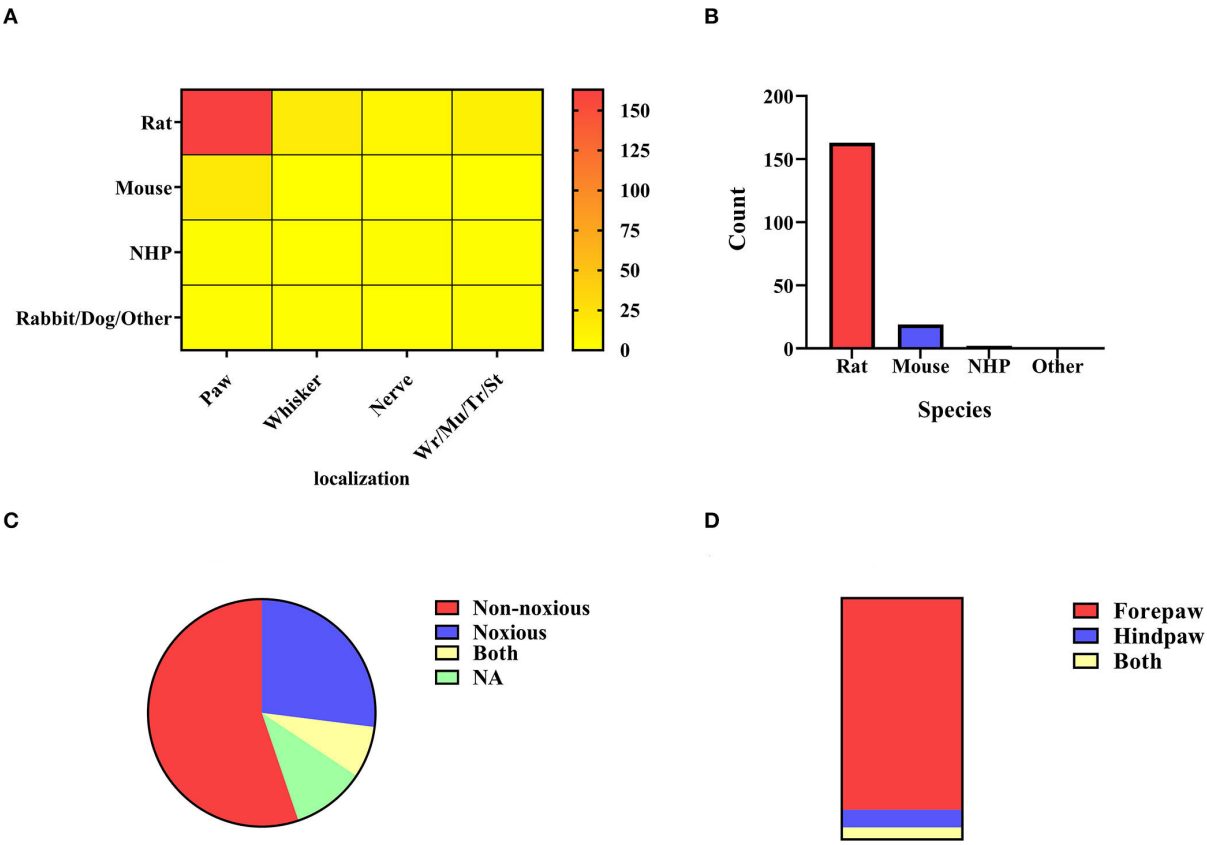

FIGURE 3
(A) Electrical stimulation localization. All electrical stimulation is classified according to the localization of stimulation, including paw stimulation (n = 183, 82.43%), whisker stimulation (N = 15, 6.76%), nerve stimulation (n = 9, 4.05%), and others (n = 15, 6.76%) including muscle, stomach, trunk, wrist. The color bar means the number of studies. **(B)** Paw stimulation. The species distribution of paw stimulation is rat (n = 161, 87.98%), mouse (n = 19, 10.38%), non-human primate (n = 2, 1.09%), and NA (n = 1, 0.55%). **(C)** Rats' paw stimulation. Noxious stimulation <2 mA (n = 42, 26.09%) and non-noxious stimulation ≤2 m (n = 90, 55.90%). Some experiments covered both stimulus intensities (n = 12, 7.45%), and different stimulus intensities were adopted in the remaining chapters, or no specific description was given (n = 17, 10.56%). **(D)** Rats' paw localization. A bar graph was obtained by distinguishing the sites of stimulation by the forepaw (n = 141, 87.58%), the hind paw (n = 12, 7.45%), and both (n = 8, 4.97%).

visual, olfactory, direct brain, and other kinds of stimulation based on the type and location of stimulation. The different stimulation methods will be elaborated on separately in the following sections.

The studies were categorized according to the method of the stimulation, including electrical (n = 214, 32.08%), visual (n = 154, 23.09%), direct brain (n = 95, 14.24%), multiple (n = 64, 9.60%), mechanical (n = 49, 7.35%), auditory (n = 38, 5.70%), olfactory stimulation (n = 24, 3.60%), and others (n = 29, 4.35%) (Figure 1B). Among them, the main methods were electrical, visual, and direct brain stimulation.

Electrical stimulation

The distribution of electrical stimulation sites and animal selection is illustrated in Figure 3A. It can be seen that rats (n = 194, 87.39%) were mostly used in the studies involving the electrical stimulation paradigm. As a simple and mature technology, electrical stimulation is widely used in the forepaw, hindpaw, and whiskers (Yu et al., 2016; Todd et al., 2019; Cywiak et al., 2020), in which the activated area is stable. The activated brain region for forepaw stimulation is the sensory cortex (somatosensory fore-limb region, S1FL) (Kim et al., 2005; Crofts et al., 2020), and the corresponding activated brain region for hind paw stimulation is the somatosensory hind-limb regions (S1HL) (Todd et al., 2019). Several studies have reported that whisker stimulation mainly activates the barrel cortex (S1BC) (Yu et al., 2012; Martin et al., 2013). It should be noted that there are various whisker stimulation methods, including mechanical stimulation and electrical stimulation. Whisker stimulation in this part refers to electrical stimulation of the whisker to achieve the activation effect. There were other stimulation methods, such as wrist electrode implantation to the median nerve, masticatory muscle implanted electrode to the trigeminal nerve (Just et al.,

2010), stomach direct electrical stimulation (Yu et al., 2014; Cao et al., 2019), and trunk stimulation (Endo et al., 2008; Meuwissen et al., 2020). In short, electrical stimulation was set up in various ways with different blood oxygen fluctuations in the cortex. The cortex is the core region that responds to electrical stimulation (Sanganahalli et al., 2009).

Forepaw/hindpaw stimulation

In existing studies, electrical paw stimulation is a relatively mature stimulation paradigm, which has been applied to different animals (Figure 2A). Electrodes compatible with the MRI scanning system were implanted between the digits of the animals to apply stimulation, and the BOLD signals were observed in the brain regions or networks by setting different current parameters. The paw stimulation in rats was most widely studied (n = 161, 87.98%) (Figure 3B). The location of the rats' paw stimulation (Figure 3D) in most studies was the forepaw of rats (n = 141, 87.58%), and a small amount was in the hindpaw (n = 12, 7.45%). We further classified the paw electrical stimulation into noxious (n = 42, 26.09%) and non-noxious stimulation (n = 90, 55.90%) (Figure 3C). In the previous study, the threshold of the stimulating current was set at 2 mA. When the current was below the threshold value, only the contralateral corresponding sensory cortex was activated. Noxious forepaw stimulation greater than the threshold triggered activation of other brain regions associated with pain perception, including the secondary somatosensory cortex (S2), thalamus, insula, and limbic regions (Luo et al., 2009). Because of the species difference, the stimulating current threshold of mice (Luo et al., 2009; Adamczak et al., 2010; Jung et al., 2019) and non-human primates (NHP) (Luo et al., 2009; Qi et al., 2016; Yen et al., 2018) may not be the same. More detailed and targeted research studies are needed to determine the current threshold for different species.

Non-noxious and noxious electrical paw stimulation

As mentioned above, noxious electrical paw stimulation refers to a current intensity >2 mA. Due to its pain-causing characteristic, noxious electrical stimulation exceeding the stimulation threshold has been used in the study of a variety of inhibitors, like lidocaine. It has shown a decrease in global brain activation after lidocaine injection compared with the control group, suggesting that lidocaine may be a reasonable sedative and analgesic substance (Haile et al., 2019). A series of studies have investigated the CBF and BOLD signal changes in the bilateral striatum after the combined use of noxious electrical stimulation. The results show CBF reductions and reduced BOLD activation (Shih et al., 2011). Further studies are needed to explain the relationship between CBF and BOLD signal changes in the striatum and the current traumatic stimulation. For both noxious and non-noxious stimulation, the regions activated were the corresponding regions of the contralateral cortex areas, such as the contralateral primary somatosensory cortex. In a study on the cortex, S1 was divided into six layers, with the increase of current intensity (1–10 mA), cortical CBF in six layers also appeared in the change and was particularly pronounced in the II-V layer (non-noxious) and V-VI layer (noxious) of contralateral primary somatosensory cortex (Shih et al., 2013). The significance of noxious electrical stimulation is to create a visualized fMRI activation of pain-related regions (Pawela et al., 2017) and to study changes in cerebral blood flow (CBF) in the brain caused by pain inhibition or changes in pain intensity. Intuitive vascular and neural coupling observations are more convincing. Among paw stimulations, a class of studies investigated the effects of inhaled anesthetics on the intracerebral imaging of frequency-dependent paw stimulation, just like the effects of anesthesia on neural coupling mentioned above. Comparative experimental studies have also showed different BOLD signals under different anesthetics at the same frequency (Schroeter et al., 2014). Some studies have shown that anesthesia can also affect the adaptability of neural activity (Masamoto et al., 2007). This may indicate that anesthesia may modulate frequency-dependent sensory activation. The electrical stimulation at 3 Hz in chloralose anesthetized rats induced the greatest effect (Gyngell et al., 1996), while the maximum frequency of effect in isoflurane-induced rats was 8–12 Hz for a short period (10 s) and 6–8 Hz for an extended period (30 s) (Kim et al., 2010), which might provide a valuable reference for parameter setting of non-noxious paw stimulation.

Non-noxious electrical paw stimulation refers to a current intensity of <2 mA, which generates stable activation in the brain regions. Compared with the wide-range activation of noxious stimulation, the activation range of non-noxious stimulation is limited, which was commonly used in the study of different disease models such as Alzheimer's disease model (Sanganahalli et al., 2013), stroke model (Sicard et al., 2006; Kim et al., 2007; Suzuki J. et al., 2013), and spinal cord injury model (Ramu et al., 2006, 2007). Neurovascular changes of model animals were reflected and compared through changes in blood flow in cortical areas by mapping brain activation after stimulation interventions. The non-noxious electrical stimulation had a stable paradigm. Therefore, it enabled comparisons of different anesthesia states (Verley et al., 2018), scan sequences (Seehafer et al., 2010), and contrast agents (Kim et al., 2005). Non-noxious electrical stimulation can be used as a more stable model to reflect changes in CBF and activation state induced by changes in external conditions. Interesting research about stimulating the bilateral ventricle and forepaw simultaneously showed differences in brain activation. This phenomenon may be related to the different afferent innervation of the heart, which overlaps with the clinical results of different ischemic lesions in the left and right ventricles (left or right ventricular myocardial ischemia) (Suzuki H. et al., 2013). By coupling nerve blood vessels, the research findings could provide evidence for the clinic.

Nerve electrical stimulation

Nerve stimulation was applied by inserting electrodes or placing electrical pads precisely into the target peripheral nerve regions (Figure 3A). The electrodes can be placed directly on the skin or surgically implanted. The main difference is that skin stimulation is pure sensory stimulation, while surgically implanted electrodes stimulate not only the sensory system but also motor activity and the deep brain structures (Cho et al., 2008). A few studies of direct nerve stimulation mainly involve stimulation of the trigeminal nerve (Cho et al., 2008; Just et al., 2010; Sonnay et al., 2017), the median nerve (Kennan et al., 1998, 2000; Hettinger et al., 2011; Liu et al., 2013). However, stimulation of multi nerves, such as the median, ulnar, radial, and musculocutaneous nerves, was occasionally reported. In this way, a distinct pattern of cortical activation was found with each nerve correlated with known sensorimotor afferent and efferent pathways to the rat forepaw (Cho et al., 2008). There were many related studies on median nerve electrical stimulation, some of which used the C7 nerve root transplanted rat model to evaluate the treatment effect through nerve stimulation to verify its clinical effectiveness (Stephenson et al., 2013). One study used implanted devices to study survival models in rats (Hettinger et al., 2011). The trigeminal nerve was stimulated by inserting the cathode into the suborbital hiatus and the anode into the masticatory muscle or neck muscle to observe the activation of S1BC in rats (Sonnay et al., 2017). Electrical stimulation was also performed on NHP, and greater activation of brain regions was observed in awake monkeys than in macaques under propofol anesthesia (Liu et al., 2013). The pathway of direct neural stimulation differs from sensory stimulation through the body surface to neural stimulation. Nerve stimulation is indeed a superior method to activate the brain regions of interest, which could avoid interference activation generated by other cortical sensory stimulation (Kida and Yamamoto, 2010).

Whisker pad electrical stimulation

As not all animal whiskers were susceptible to irritation, rodents were the primary subjects in the study on whisker electrical stimulation (Figure 3A). There were many ways of observing the changes in blood flow in the barrel cortex by stimulating the rats' whiskers, including pneumatic, mechanical, and electrical stimulation of the whisker pad. The whiskers were electrically stimulated on one side to alter the effect of the contralateral barrel cortex (Wehrl et al., 2014; Shih et al., 2021). In drug-related studies, Cheng et al. explored the effects of caffeine injection on the activation of the barrel cortex of whiskers in α-chloralose anesthetized rats (Shih et al., 2021). H2(15)O-PET and fMRI brain activation contrast experiments revealed that two kinds of brain activation maps can generate complementary physiological information, which is important for experimental research and clinical practice (Wehrl et al., 2014). These studies usually analyzed the neurovascular coupling (Hewson-Stoate et al., 2005; Devonshire et al., 2012), in which personal errors, such as the pressing of experimental animals' whiskers, should be avoided during scanning (Kida and Yamamoto, 2010).

Other electrical stimulation

The other types of electrical stimulation included wrist (Schwindt et al., 2004; Gsell et al., 2006; Hirano et al., 2018), trunk (Meuwissen et al., 2020), and stomach (Yu et al., 2014) (Figure 3A). For the wrist (Duricki et al., 2019) and trunk (Endo et al., 2008) electrical stimulation, electrodes were placed directly on the skin. For gastric stimulation, the abdomen is opened from the xiphoid process to expose the organs fully, and the electrode patch is implanted into the anterior stomach and then sutured. Gastric stimulation can drive somatosensory and cingulate cortices to generate extensive fMRI responses (Cao et al., 2019).

Although implanting electrodes in the stomach is difficult and risky, it is an effective way to stimulate nerves directly. Future studies could focus on the innervation effect of the stomach with electrical stimulation. The study on wrist electrical stimulation is not as valuable as that of median nerve stimulation implanted in the muscle, as the latter is more advanced in exploring the neurovascular coupling through fMRI f (see 3.3.1.3 Nerve Electrical Stimulation for more information) (Kida and Yamamoto, 2010).

Trunk stimulation has been carried out in studies on low back pain and spinal cord injury. The activation of brain regions associated with pain, such as the raphe nucleus, nucleus accumbens, and caudate putamen, can be observed by referring to the animal spinal cord stimulation model (T13) (Meuwissen et al., 2020). We can explore the mechanism of pain through different experimental designs and animal models, which may enhance our knowledge of pain and provide new insight into clinical treatment (Endo et al., 2008).

Visual and auditory stimulation

Visual stimulation

The visual stimulation paradigms use specific images, videos, light, or designed visual tasks to stimulate brain activities, which are observed during the fMRI scan. The stimulation methods can be classified according to different types of stimuli (Figure 4A). In 154 studies on visual stimulation paradigms, the types of stimuli included image (n = 43, 27.92%), light (n = 35, 22.72%), gratings (n = 34, 22.08%), checkboard (n = 12, 7.79%), color (n = 5, 3.25%), optical fiber (n = 5,3.25%), video (n = 5, 3.25%), and free view (n = 4, 2.60%). Some experiments combined several different visual stimuli (n = 11, 7.14%). Figure 4A shows images, light, and checkboards were the most commonly used visual stimuli. The stimulation's distribution in species highlights that the image is mainly used for NHP among the collected paradigms (Figure 4B). The BOLD signal changes induced by visual stimulation were mainly through gaze

training of the awake or anesthetized NHP (Figure 4B), which combined the use of an anesthetic to relax the eye muscles and keep the eyes open (Dubowitz et al., 2001). The presentation of visual stimulation determined the different visual areas studied (Tsao et al., 2006; Lau et al., 2011a). Most studies used NHP as research animals, but there were also studies on rodent and cat models (Figure 4C). Meanwhile, we summarized the sample size distribution of visual stimulation experiments (Figure 4D). As with most animal experiments, the sample sizes for NHP experiments were generally <10, while the sample sizes for other animal models varied. This sample size usually depended on the funding of the experiment and the difficulty of implementation. Since 1999, a repeatable and stable imaging method for visual stimulation based on BOLD signals has been explored (Logothetis et al., 1999). The implementation of visual stimulation requires pre-fixation training (Caspari et al., 2018; Premereur and Janssen, 2020) or keeping the animals' attention during the scanning process (Liang Z. et al., 2017; Xu et al., 2019) to achieve the desired stimulation effect. It is feasible to make the animals cooperate actively through training (Alizadeh et al., 2018). Another approach to forcing monkeys to stare at the target object was to keep the eyes passively open using a muscle relaxant (Jin and Kim, 2013). We also need to consider that different external visual signals present different stimuli that specifically activate different brain regions (Kaskan et al., 2017; Karl et al., 2020).

As an important signal of sensory input, vision is involved in many processes, such as facial recognition preferences in the brain (Russ and Leopold, 2015), the formation of reward mechanisms (Tsurugizawa et al., 2012), the processing of looming stimulation (Cléry et al., 2020), and 3D shapes. There are some classical brain regions activated (Tsurugizawa et al., 2010), but some other brain regions have been activated and reported in humans (Bunford et al., 2020), suggesting the value of studying the functional organization of the brain with visual stimulation.

Auditory stimulation

Auditory stimulation has been studied mainly in NHP and birds. Birds use calls to maintain social relationships, just as humans do with language (Van Ruijssevelt et al., 2018). Therefore, the audio types selected for auditory stimulation of birds were normally copulatory vocalization and songs of other birds (Voss et al., 2007; Maul et al., 2010). The auditory stimulation parameters in NHP were much more complex and varied. The stimulation paradigms may use human speech (Joly et al., 2012), infraspecific calls (Perrodin et al., 2011), extracted music (Wang et al., 2017), the "local-global" auditory paradigm (Uhrig et al., 2014), and broadband noise (Wong et al., 2017). These studies provide a critical basis for future studies of various functional properties of the animal auditory cortex.

As we discussed above, visual and auditory studies have used similar experimental paradigms to reveal the brain regions with specific functions. In the reported studies, many have compared the brain activations between humans and NHP to explore homology. The corresponding functional regions studied included the scene selection region (Nasr et al., 2011), the facial selection regions (Tsao et al., 2006), and the auditory cortex in a binocular blind rhesus monkey model (Wang et al., 2017). Visual or auditory stimulation can be applied as a single stimulation, but they are often combined in complex daily situations that involve the integration of higher-level complex information processing. Moreover, Guipponi et al. found that visual and auditory stimulation were closely combined and activated the superior colliculus (SC), which was of higher application value and more innovative in the study of higher-dimensional brain function (Guipponi et al., 2013; Lau et al., 2018). Research on single stimulation is also indispensable in scientific research. There were research studies on the auditory midbrain (Van der Kant et al., 2013), auditory forebrain (Maul et al., 2010), visual cortex (Boch et al., 2021), auditory cortex (Van Ruijssevelt et al., 2017), visual pathway (Leopold et al., 2002), new nerve nodes (Van Ruijssevelt et al., 2018), and nucleus functions (Lau et al., 2011b), which were the basis for further complex stimulation research.

Olfactory stimulation

Olfactory stimulation refers to the delivery of a liquid or gas containing a specific odor to the area near an animal's nose through a certain transport route or carrier, thus activating the corresponding olfactory bulb region. The olfactory stimulation can be divided into single-odorant and multiple-odorant stimulation (Figures 5A,B). In both types of olfactory stimulation studies, isoamyl-acetate was the most commonly used stimulus. The rat was the most commonly used animal in olfactory stimulation experiments (n = 14, 58.33%), but the use of other animals has been increasing in recent years (Figure 5C). The olfactory bulb (n = 6, 25.00%) was the most popular ROI in olfactory stimulation experiments. Figure 5D shows a trend of multiple ROIs in recent years.

Olfactory stimulation cannot be implemented without an MRI-compatible taste transmitter. Animals are fixed on the scanning bed, and a transmitter sends specific odors within the animals' smell range. Specific odors include alcohol, almond flavor, amyl acetate (Poplawsky et al., 2015), ethyl butyrate, methyl valerate (Sanganahalli et al., 2016), various types of odoriferous chemicals (Zhao et al., 2018), and social smells of different species or the same species (Xu et al., 2005; Tikhonova et al., 2015) were sent through an MRI-compatible device. In olfactory stimulation experiments, it is also essential to design the parameters of odor transport location and transport time.

The current research has already shown evidence of the odor transport time and location. Some studies have observed the effects of olfactory stimulation of different time lengths (Martin et al., 2007). The analysis results showed the same

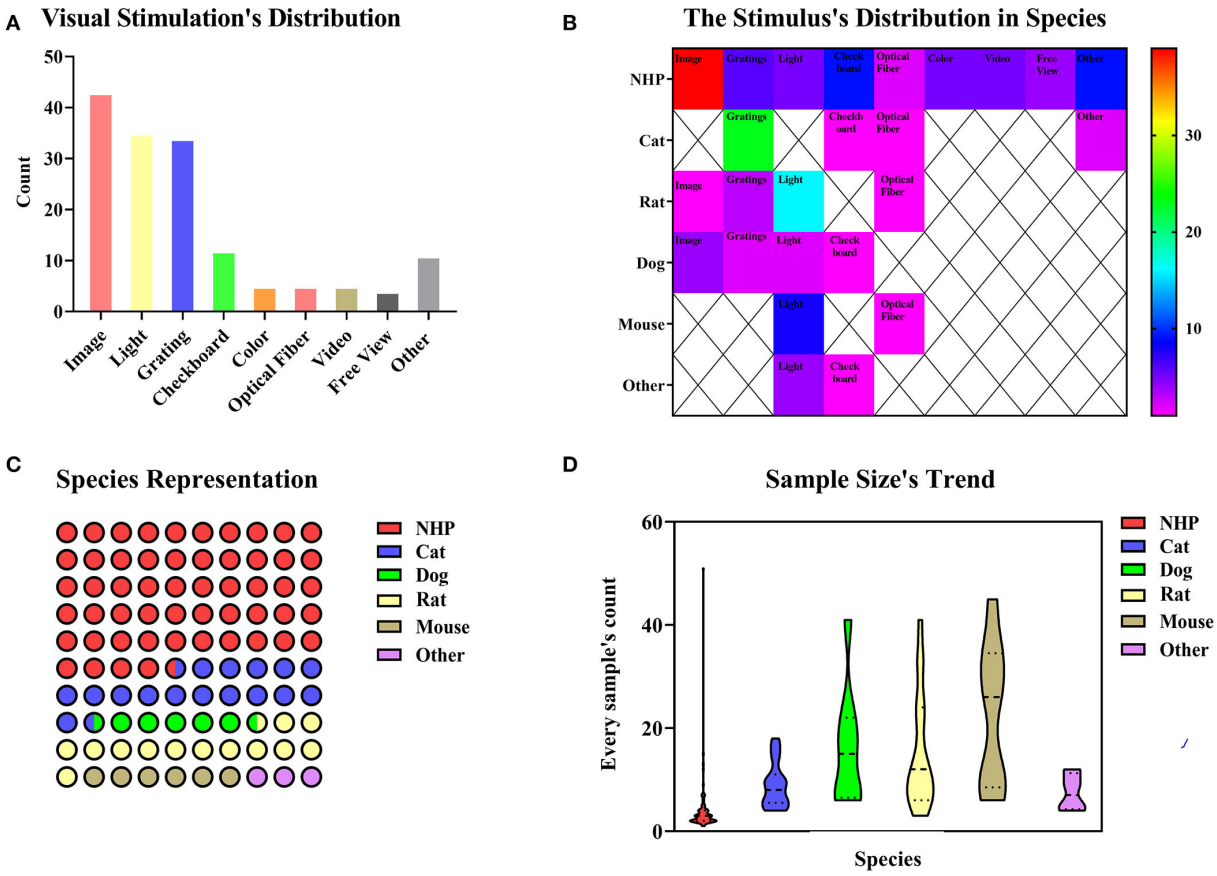

FIGURE 4
(A) In total of 154 paradigms of visual stimulation collected, we divided the methods of the stimulus into image (n = 43, 27.92%), light (n = 35, 22.72%), gratings (n = 34, 22.08%), checkboard (n = 12, 7.79%), color (n = 5, 3.25%), optical fiber (n = 5, 3.25%), video (n = 5, n = 5, 3.25%) and freeview (n = 4, 2.60%). Some experiments covered several different methods of the stimulus (n = 11, 7.14%). **(B)** Image is mainly used for NHP among the collected paradigms. Species distribution and sample size's trend. The color bar means the number of studies. **(C)** Animal representation in the collected paradigms. NHP, cats, and rats are the principal animals used for visual stimulation. **(D)** A number of animals used per fMRI study. NHP studies are carried out with fewer animals, whereas studies involving mice involve larger animals.

effects of long-term and short-term stimulation. Similar research on NHP using 1/2/8 mins of stimulation revealed the same results. On the other hand, the research applied stimulation in different locations. Orthonasal and retronasal stimulation have shown overlapping response patterns and some route-specific dominance. Orthonasal maps were dominant in dorsal-medial regions, whereas retronasal maps were dominant in caudal and lateral regions (Sanganahalli et al., 2020). In summary, when applying olfactory stimulation, one should consider the odor type and the length of time. These results indicate that fMRI is the right choice for detecting the time and locations of olfactory bulb activation.

Direct brain stimulation

Direct brain stimulation means that the electrodes or fibers used for stimulation are implanted directly into specific areas of the brain regions to regulate the target pathways and brain regions directly. The main modes of action reported in relevant literature include DBS, EM, and optogenetics functional magnetic resonance (O-fMRI).

Previous studies have not clearly distinguished between brain EM and DBS (Jiang et al., 2015). During fMRI scans, implanted objects may interfere with data collection (Shyu et al., 2004). The different locations of electrode implantation are summarized in Figure 6A, and its year-to-year distribution is described in Figure 6B. Meanwhile, researchers need to consider selecting MRI-compatible electrodes before applying stimulation. In the DBS and EM animal studies, the electrode materials selected are shown in Figure 6C. Teflon-coated tungsten (n = 10, 17.86%) was the most commonly used electrode material. Other materials included graphene fiber, non-magnetic gold electrodes, iridium, and more. In recent years, more and more new materials have been used to reduce

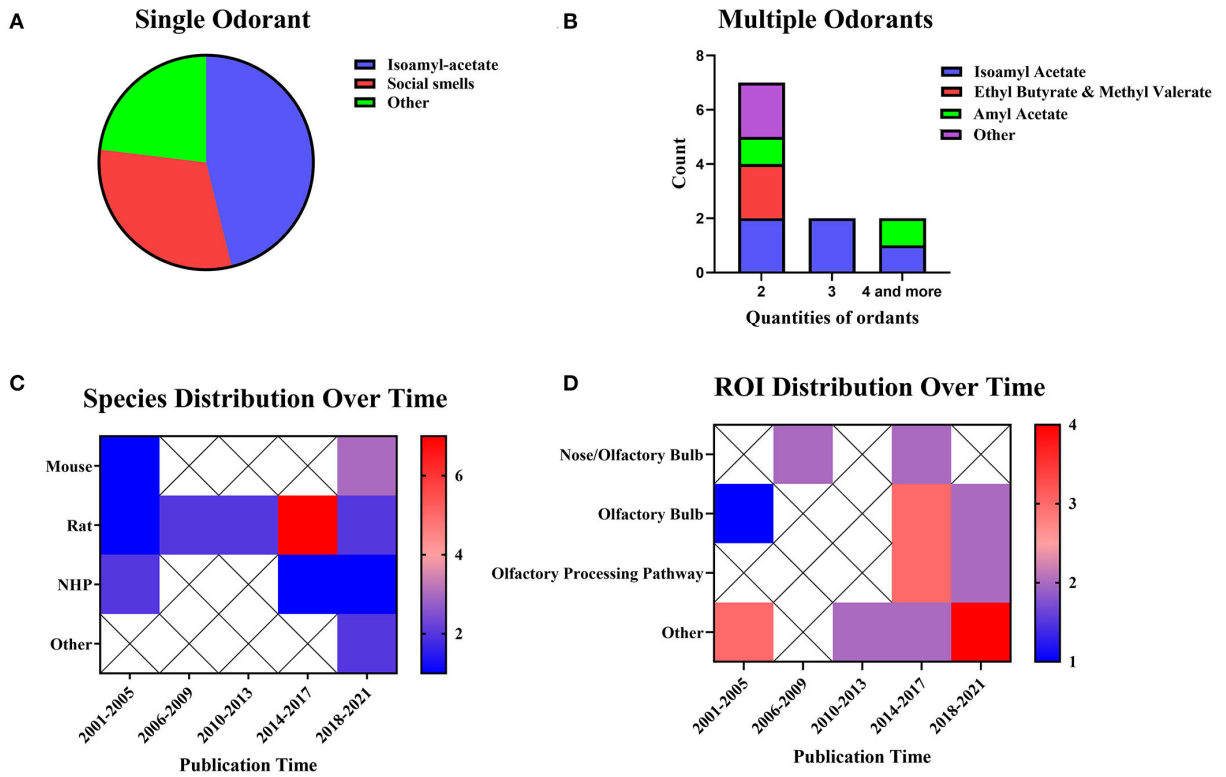

FIGURE 5
Odorants, species distribution, and ROI distributions. **(A)** Studies using single stimuli (n = 13, 54.17%). **(B)** Studies using multiple stimuli (n = 11, 45.83%). The color bar means the number of studies. **(C)** Temporal distribution of experimental animals. **(D)** Distribution of ROI over time. The color bar means the number of studies.

artifacts (Figure 6D). The thalamus (n = 20, 35.71%) was a popular site for deep brain stimulation and micro-current stimulation experiments. Other stimulating areas included the deep cerebellar nuclei, lateral olfactory tract, and more. Besides, some studies may involve two stimulating areas. Hippocampus (n = 8, 14.29%) has been a popular stimulating region in the last decade in this research field.

O-fMRI refers to the use of functional magnetic resonance to reflect certain activated or suppressed pathways or circuits in optogenetics-regulated animals. Usually, the experimental procedures for optogenetics include stereotactic injection, fiber implantation, and post-implantation stimulation, with specific photosensitive viruses implanted at corresponding intracerebral coordinates (Just and Faber, 2019). Optogenetic techniques can be a possible way to stimulate the brain regions through light-sensitive channels (Kahn et al., 2011). Different laser emitters activated the light-sensitive channels, mainly a blue laser at 473 nm and some blue and yellow (593 nm) pulsed lasers as well (Takata et al., 2015). Channel protein distribution and laser activation are described in Figures 7A,B. Rats (n = 16, 69.57%) were the most commonly used animals in O-fMRI. The opsin injection site was also collected (Figure 7C). The cerebral cortex (n = 7, 30.43%) and hippocampus (n = 7, 30.43%) have been hot spots for research. Studies mainly explore various brain regions in the cortex, such as the medial prefrontal cortex, neocortex, and S1FL.

EM and DBS are highly similar. EM uses fMRI to observe the neurovascular changes in specific brain areas through electrical stimulation alone or in combination with other stimulations. When combined with certain behavioristics, it can be verified in reality and in the brain (Murris et al., 2021). In the studies on EM and DBS in animals, the selection of different electrodes and stimulation sites deserves our attention. The current intensities of EM and DBS were low and directly affected the brain regions. Weak current (microampere) stimulation was generated for the brain regions and pathway, and changes in blood oxygen levels in brain regions corresponding to this pathway can be observed. Yang compared the functional connectivity of the lateral and medial thalamic cortical pain pathways in normal rats by using a BOLD activation pattern induced by direct electrical stimulation of the posterior ventral (VP) and middle temporal region (MT) regions of the forebrain. Such stimulation experiments directly analyzed whether there were fundamental differences in signal processing between the medial and lateral thalamic pathways (Yang et al., 2013).

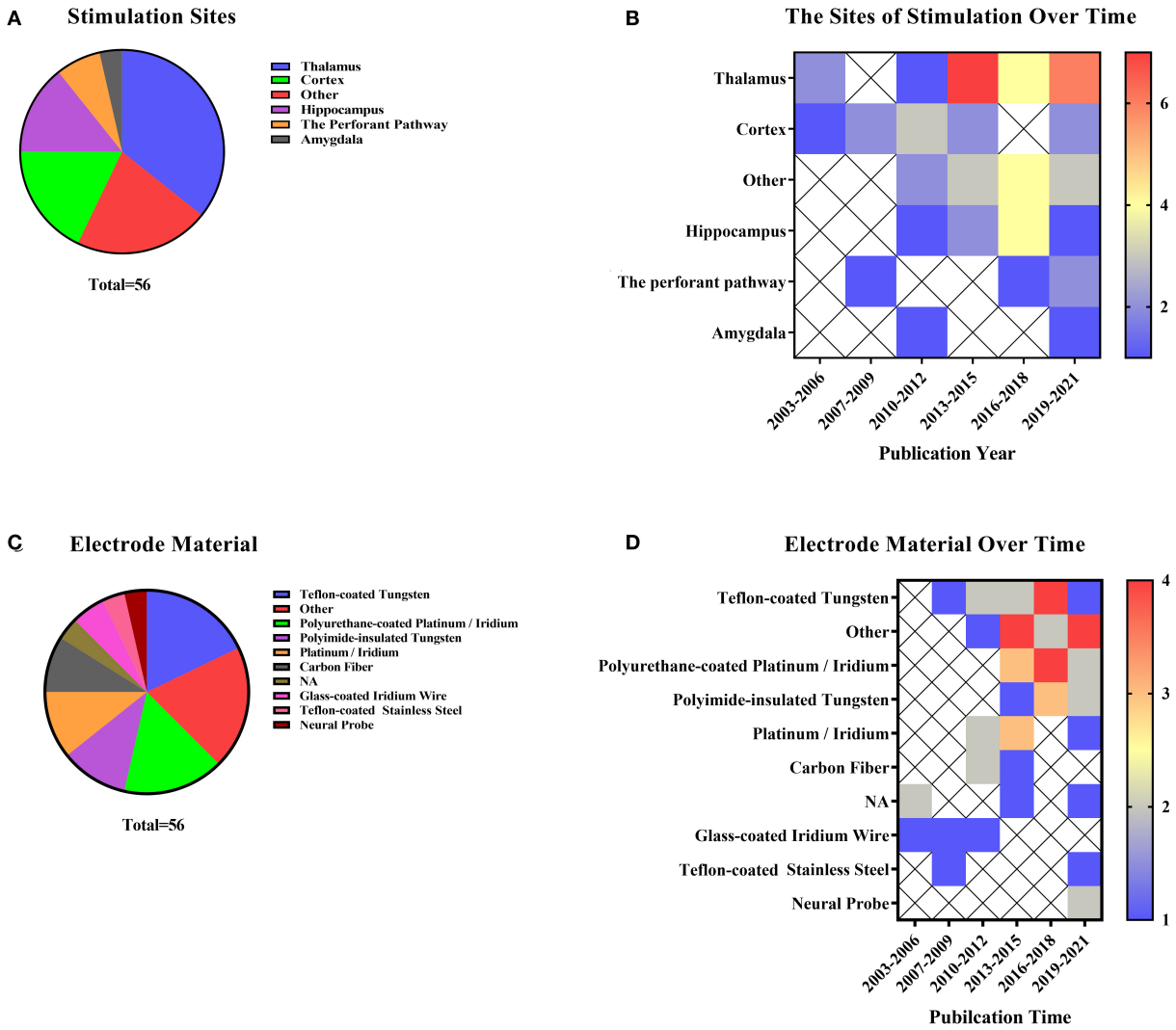

FIGURE 6
Direct brain stimulation includes deep brain stimulation, EM, and optogenetics **(A)** Stimulation site representation distribution and electrode material distribution in deep brain stimulation and micro-current stimulation. **(B)** Distribution of stimulation sites over the last two decades. The color bar means the number of studies. **(C)** Distribution of stimulating electrode materials used in articles related to direct brain stimulation. **(D)** Electrode materials occur in the literature over time. The color bar means the number of studies.

Due to the selectivity of regulating channel proteins and the numerous circuits and regions of interest in the brain, the BOLD changes in the brain can be visually observed in combination with optogenetics, thus achieving the goal of observing neurovascular coupling. Regarding the selection of channel proteins, different researchers used the same opsin to activate the ROI, such as using CHR2 to activate dHP and vHP (Wang et al., 2019); S1FL (Schmid et al., 2016, 2017; Uhlirova et al., 2016); M1 AND CPU (Ryali et al., 2016). Other studies selected inhibitory channel proteins such as eNpHR and ARCHT to inhibit frontal eye field neurons (Ohayon et al., 2013). eNpHR can be verified in both activation and inhibition (Liu et al., 2015). In conclusion, the diversity of photogenetic techniques combined with functional magnetic resonance can effectively reflect the accuracy of brain pathways or connections from the neurovascular coupling.

Mechanical stimulation

Mechanical stimulation refers to the compression of the skin of an animal by air, a drive device, comb, pin, rod, or clamp to produce a relatively simple effect of pure mechanical stimulation, including the classic monofilament skin stimulation, pneumatic skin stimulation, whisker stimulation, and vibrator sticking to the skin. The conduction pathways of skin stimulation are relatively simple, as are their stimulation

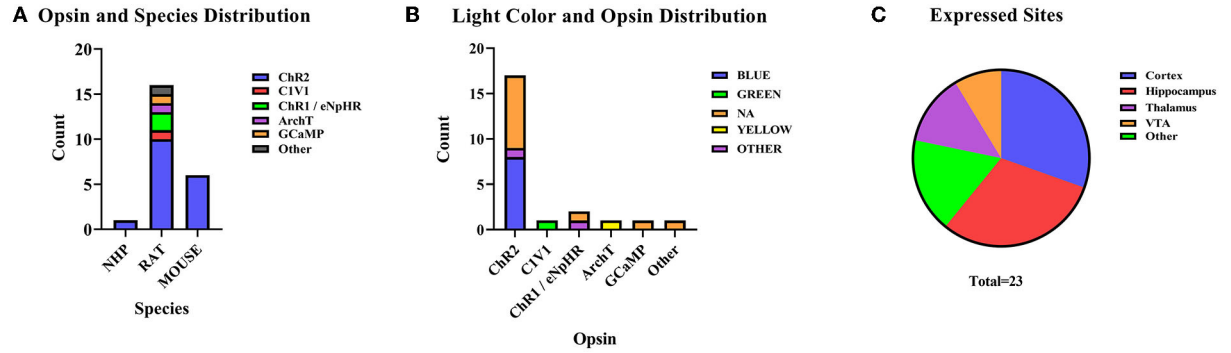

FIGURE 7
As for optogenetics fMRI (O-fMRI). **(A)** Distribution of animal species in O-fMRI, ChR2 is the most commonly used optogenetics protein. **(B)** The distribution of color of stimulating light and opsin in documented studies. **(C)** The distribution of sites of opsin expression.

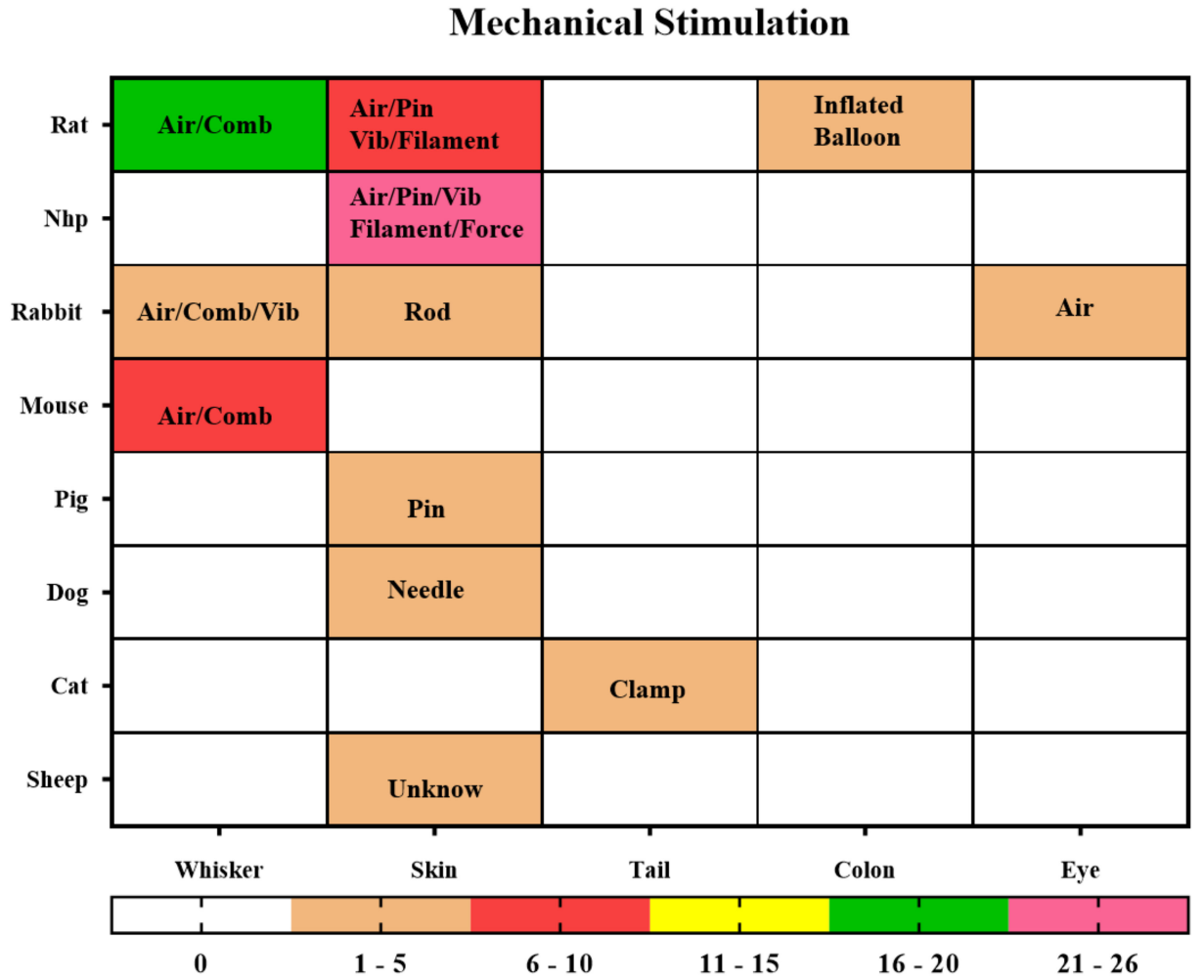

FIGURE 8
Mechanical Stimulation. The locations of stimuli and species distribution are displayed through a hotspot map, and the content in the hotspot grid is the medium used to apply the stimuli, including air, pin, vibrator (Vib), filament, force, clamp, comb, balloon. The color bar means the number of studies.

methods and species distribution (Figure 8). The most common stimulation methods are applying pneumatic equipment, plastic spin, filament, vibrator, and force on the skin of NHP, rodents, and other animals (n = 39, 54.17%). Studies on whisker stimulation were also common (n = 27, 37.5%), and the species were limited. Further studies included intestinal pressure stimulation, eye gas stimulation (Miller et al., 2003), and tail clamping stimulation (Nagakubo et al., 2017), which can be performed in a variety of easy and repeatable ways.

The intelligence of mechanical stimulation is in the application and design of the stimulation, such as the use of a balloon implanted in the colon to inflate the intestine of the rat to achieve the stimulation effect of intestinal obstruction with gas (Lazovic et al., 2005; Tsurugizawa et al., 2009a). This is an effective way to mimic colorectal distention.

Abdominal pressure stimulation was used to simulate menstrual pain in NHP (Yano et al., 2019); a vibrator was used on the NHP forearm to create tactile stimulation for the fingers (Zhang et al., 2007, 2010); blowing into the eyes of rabbits was to induce blinking (Miller et al., 2008); clamping the tail of cats with nylon wire was to produce painful mechanical stimulation (Nagakubo et al., 2017); squeezing the right hind leg muscle was used to trigger BOLD change. All these stimulation methods can be used as reasonable and repeatable paradigms in experiments.

In addition to the electrical whisker stimulation mentioned in the part on electrical stimulation, there were other ways to stimulate the whisker barrel cortex in rodents through mechanical stimulation, such as using a mechanically driven comb or pneumatic connector (Lu et al., 2003, 2004, 2016). Mechanical stimulation could be achieved in a variety of ways, but the conduction pathway is relatively fixed. Different stimulation methods are suitable for different ROIs, so we should consider study aims and nuclear magnetic compatibility to select the appropriate stimulation methods in the study design.

Multiple stimulations

Single stimulation research started early. After a certain research foundation was established, the scholars turned to another blank area to explore the fMRI brain activation mode under the combination of various stimulation paradigms. Various combined stimulation studies have been carried out in the past decades, which can be seen from the distribution of time points (Figure 1A). The combination of stimulation is sometimes not merely a superimposed benefit but rather a multichannel study (Lambers et al., 2020) of peripheral stimulation delivery equipment required to produce the same stimulation inside and outside the magnet to simulate a more realistic environment. Studies of multisensory convergence of dynamic cortical activation with information integration processing and complex sensory processing regions depend on input from various stimulation modes (Sanganahalli et al., 2009). Similarly, the repeatability of studies also depends on constant stimulation and specific activation of brain regions, which is true in single-stimulation studies and should be true in multistimulation studies. In addition, the study on the multistimulation mode is more consistent with the process of information processing and environmental interaction in daily life (Cook et al., 2016; Cléry et al., 2017; Arsenault and Vanduffel, 2019), resulting in a coherent perception of the environment (Kayser et al., 2005). With optogenetics techniques and EM, some stimulation tasks that are difficult to complete in MRI scans can be modulated by these brain stimulation techniques to achieve the same benefits (Poplawsky et al., 2015; Leong et al., 2019). As mentioned above, the bidirectional regulation of optogenetics techniques has been combined with other stimulations. The comparison of the regulatory results of optogenetics combined interventions and EM intervention alone (Schmid et al., 2017) is more convincing (Ekstrom et al., 2008, 2009). With the combination of technologies and innovations, the research technology of magnetic resonance has become more extensive, which may also be a direction for future research.

Other stimulation

In the study on the stimulation paradigm, in addition to the above studies that can be clustered, some sporadic niche stimulation is classified as other stimulation, which includes chemical, thermal, and food stimulation. The chemical stimulation should consider the selection of chemical substances and the injection site. For example, some experiments injected cocaine during the scan (Mandeville et al., 2001, 2004), or the pain-causing substances into the forepaw or directly created a hyper-carbonated environment to cause hypoxia in the brain (Kannurpatti et al., 2003). In addition to the internal chemical stimulation, stimulation can also be applied to external sites. Pepper spray applied directly to the paws can have the same effect as electrical or mechanical stimulation (Kannurpatti et al., 2002).

Intragastric administration can direct food stimulation to observe BOLD changes in the brain regions associated with intestinal stimulation, such as the amygdala, hippocampus, and the ventral tegmental area (Tsurugizawa et al., 2009a,b, 2010). There are differences among various stimulation paradigms, but there are many overlaps in BOLD changes caused by stimulation and the selection of ROI (Mazzanti et al., 2011). Researchers can apply appropriate stimulation methods to the animal models to achieve their research goals.

Conclusion

The collection and analysis of animal functional magnetic resonance combined with stimulation show that anesthesia imaging still occupies the mainstream, and awake imaging

studies have gradually appeared in recent years. Besides, the stimulation methods have gradually broadened with the progress of science and technology. Various devices and scanning technologies with high resolution and high specificity are constantly emerging, which makes the research more detailed. It is critical to choose a suitable paradigm combined with the research objectives, including the selection of stimulus mode and the setting of various parameters. Besides, a more innovative paradigm needs to be created and explored for animal functional magnetic resonance combined with stimulation needs to meet the demands of investigating the brain in future studies.

Data availability statement

The raw data supporting the conclusions of this study are available on request to the corresponding authors.

Author contributions

SL, JH, YZ, and QZ contributed to conception and design of the study. JH, YZ, QZ, LW, XZ, CJ, JY, and ZL collected the data. JH, YZ, and QZ wrote the first draft of the manuscript. SL revised the manuscript. All authors contributed to manuscript revision, read, and approved the submitted version.

Funding

This study was supported by the grants from the National Natural Science Foundation of China (82004440 and 81803883), the Natural Science Foundation of Fujian Province (2021J01961), the Youth Science Foundation of Fujian Provincial Health Commission (2019-1-65), and the Scientific Research Foundation for the High-level Talents funded by Fujian University of Traditional Chinese Medicine (X2019002-talents).

Conflict of interest

The authors declare that the research was conducted in the absence of any commercial or financial relationships that could be construed as a potential conflict of interest.

Publisher's note

References

Adamczak, J. M., Farr, T. D., Seehafer, J. U., Kalthoff, D., and Hoehn, M. (2010). High field BOLD response to forepaw stimulation in the mouse. *Neuroimage* 51, 704–712. doi: 10.1016/j.neuroimage.2010.02.083

Alizadeh, A. M., Van Dromme, I. C., and Janssen, P. (2018). Single-cell responses to three-dimensional structure in a functionally defined patch in macaque area TEO. *J. Neurophysiol.* 120, 2806–2818. doi: 10.1152/jn.00198.2018

Arora, M. (2021). Environment and human health as complex interacting systems. *Bioessays* 43, e2100177. doi: 10.1002/bies.202100177

Arsenault, J. T., and Vanduffel, W. (2019). Ventral midbrain stimulation induces perceptual learning and cortical plasticity in primates. *Nat. Commun.* 10, 3591. doi: 10.1038/s41467-019-11527-9

Boch, M., Karl, S., Sladky, R., Huber, L., Lamm, C., Wagner, I. C., et al. (2021). Tailored haemodynamic response function increases detection power of fMRI in awake dogs (Canis familiaris). *Neuroimage* 224, 117414. doi: 10.1016/j.neuroimage.2020.117414

Bunford, N., Hernández-Pérez, R., Farkas, E. B., Cuaya, L. V., Szabó, D., Szabó Á., et al. (2020). Comparative brain imaging reveals analogous and divergent patterns of species and face sensitivity in humans and dogs. *J. Neurosci.* 40, 8396–8408. doi: 10.1523/JNEUROSCI.2800-19.2020

Cao, J., Lu, K. H., Oleson, S. T., Phillips, R. J., Jaffey, D., Hendren, C. L., et al. (2019). Gastric stimulation drives fast BOLD responses of neural origin. *Neuroimage* 197, 200–211. doi: 10.1016/j.neuroimage.2019.04.064

Caspari, N., Arsenault, J. T., Vandenberghe, R., and Vanduffel, W. (2018). Functional similarity of medial superior parietal areas for shift-selective attention signals in humans and monkeys. *Cereb. Cortex* 28, 2085–2099. doi: 10.1093/cercor/bhx114

Chen, X., Tong, C., Han, Z., Zhang, K., Bo, B., Feng, Y., et al. (2020). Sensory evoked fMRI paradigms in awake mice. *Neuroimage* 204, 116242. doi: 10.1016/j.neuroimage.2019.116242

Cho, Y. R., Jones, S. R., Pawela, C. P., Li, R., Kao, D. S., Schulte, M. L., et al. (2008). Cortical brain mapping of peripheral nerves using functional magnetic resonance imaging in a rodent model. *J. Reconstr. Microsurg.* 24, 551–557. doi: 10.1055/s-0028-1088231

Cléry, J., Guipponi, O., Odouard, S., Pinède, S., Wardak, C., Ben Hamed, S., et al. (2017). The prediction of impact of a looming stimulus onto the body is subserved by multisensory integration mechanisms. *J. Neurosci.* 37, 10656–10670. doi: 10.1523/JNEUROSCI.0610-17.2017

Cléry, J. C., Schaeffer, D. J., Hori, Y., Gilbert, K. M., Hayrynen, L. K., Gati, J. S., et al. (2020). Looming and receding visual networks in awake marmosets investigated with fMRI. *Neuroimage* 215, 116815. doi: 10.16/j.neuroimage.2020.116815

Cook, P. F., Prichard, A., Spivak, M., and Berns, G. S. (2016). Awake canine fMRI predicts dogs' preference for praise vs food. *Soc. Cogn. Affect. Neurosci.* 11, 1853–1862. doi: 10.1101/062703

Crofts, A., Trotman-Lucas, M., Janus, J., Kelly, M., and Gibson, C. L. (2020). A longitudinal, multi-parametric functional MRI study to determine age-related changes in the rodent brain. *Neuroimage* 218, 116976. doi: 10.1016/j.neuroimage.2020.116976

Cywiak, C., Ashbaugh, R. C., Metto, A. C., Udpa, L., Qian, C., Gilad, A. A., et al. (2020). Non-invasive neuromodulation using rTMS and the electromagnetic-perceptive gene (EPG) facilitates plasticity after nerve injury. *Brain Stimul.* 13, 1774–1783. doi: 10.1016/j.brs.2020.10.006

Devonshire, I. M., Papadakis, N. G., Port, M., Berwick, J., Kennerley, A. J., Mayhew, J. E., et al. (2012). Neurovascular coupling is brain region-dependent. *Neuroimage* 59, 1997–2006. doi: 10.1016/j.neuroimage.2011.09.050

Dubowitz, D. J., Chen, D. Y., Atkinson, D. J., Scadeng, M., Martinez, A., Andersen, M. B., et al. (2001). Direct comparison of visual cortex activation in human and non-human primates using functional magnetic resonance imaging. *J. Neurosci. Methods* 107, 71–80. doi: 10.1016/S0165-0270(01)00353-3

Duricki, D. A., Drndarski, S., Bernanos, M., Wood, T., Bosch, K., Chen, Q., et al. (2019). Stroke recovery in rats after 24-hour-delayed intramuscular neurotrophin-3 infusion. *Ann. Neurol.* 85, 32–46. doi: 10.1002/ana.25386

Ekstrom, L. B., Roelfsema, P. R., Arsenault, J. T., Bonmassar, G., and Vanduffel, W. (2008). Bottom-up dependent gating of frontal signals in early visual cortex. *Science* 321, 414–417. doi: 10.1126/science.1153276

Ekstrom, L. B., Roelfsema, P. R., Arsenault, J. T., Kolster, H., and Vanduffel, W. (2009). Modulation of the contrast response function by electrical microstimulation of the macaque frontal eye field. *J. Neurosci.* 29, 10683–10694. doi: 10.1523/JNEUROSCI.0673-09.2009

Endo, T., Spenger, C., Hao, J., Tominaga, T., Wiesenfeld-Hallin, Z., Olson, L., et al. (2008). Functional MRI of the brain detects neuropathic pain in experimental spinal cord injury. *Pain* 138, 292–300. doi: 10.1016/j.pain.2007.12.017

Ferezou, I., and Deneux, T. (2017). Review: how do spontaneous and sensory-evoked activities interact? *Neurophotonics* 4, 031221. doi: 10.1117/1.NPh.4.3.031221

Ferris, C. F. (2022). Applications in awake animal magnetic resonance imaging. *Front. Neurosci.* 16, 854377. doi: 10.3389/fnins.2022.854377

Ferris, C. F., Snowdon, C. T., King, J. A., Duong, T. Q., Ziegler, T. E., Ugurbil, K., et al. (2001). Functional imaging of brain activity in conscious monkeys responding to sexually arousing cues. *Neuroreport* 12, 2231–2236. doi: 10.1097/00001756-200107200-00037

Gsell, W., Burke, M., Wiedermann, D., Bonvento, G., Silva, A. C., Dauphin, F., et al. (2006). Differential effects of NMDA and AMPA glutamate receptors on functional magnetic resonance imaging signals and evoked neuronal activity during forepaw stimulation of the rat. *J. Neurosci.* 26, 8409–8416. doi: 10.1523/JNEUROSCI.4615-05.2006

Guipponi, O., Wardak, C., Ibarrola, D., Comte, J. C., Sappey-Marinier, D., Pinède, S., et al. (2013). Multimodal convergence within the intraparietal sulcus of the macaque monkey. *J. Neurosci.* 33, 4128–4139. doi: 10.1523/JNEUROSCI.1421-12.2013

Gyngell, M. L., Bock, C., Schmitz, B., Hoehn-Berlage, M., and Hossmann, K. A. (1996). Variation of functional MRI signal in response to frequency of somatosensory stimulation in alpha-chloralose anesthetized rats. *Magn. Reson. Med.* 36, 13–15. doi: 10.1002/mrm.1910360104

Haile, T. M., Bohon, K. S., Romero, M. C., and Conway, B. R. (2019). Visual stimulus-driven functional organization of macaque prefrontal cortex. *Neuroimage* 188, 427–444. doi: 10.1016/j.neuroimage.2018.11.060

Han, Z., Chen, W., Chen, X., Zhang, K., Tong, C., Zhang, X., et al. (2019). Awake and behaving mouse fMRI during Go/No-Go task. *Neuroimage* 188, 733–742. doi: 10.1016/j.neuroimage.2019.01.002

Hettinger, P. C., Li, R., Yan, J. G., Matloub, H. S., Cho, Y. R., Pawela, C. P., et al. (2011). Long-term vascular access ports as a means of sedative administration in a rodent fMRI survival model. *J. Neurosci. Methods* 200, 106–112. doi: 10.1016/j.jneumeth.2011.06.018

Hewson-Stoate, N., Jones, M., Martindale, J., Berwick, J., and Mayhew, J. (2005). Further nonlinearities in neurovascular coupling in rodent barrel cortex. *Neuroimage* 24, 565–574. doi: 10.1016/j.neuroimage.2004.08.040

Hirano, Y., Yen, C. C., Liu, J. V., Mackel, J. B., Merkle, H., Nascimento, G. C., et al. (2018). Investigation of the BOLD and CBV fMRI responses to somatosensory stimulation in awake marmosets (Callithrix jacchus). *NMR Biomed.* 31, e3864. doi: 10.1002/nbm.3864

Jezzard, P., Rauschecker, J. P., and Malonek, D. (1997). An in vivo model for functional MRI in cat visual cortex. *Magn. Reson. Med.* 38, 699–705. doi: 10.1002/mrm.1910380504

Jiang, H. J., Chen, K. H., and Jaw, F. S. (2015). Deep-brain electrical microstimulation is an effective tool to explore functional characteristics of somatosensory neurons in the rat brain. *PLoS ONE* 10, e0117289. doi: 10.1371/journal.pone.0117289

Jin, T., and Kim, S. G. (2013). Characterization of non-hemodynamic functional signal measured by spin-lock fMRI. *Neuroimage* 78, 385–395. doi: 10.1016/j.neuroimage.2013.04.045

Joly, O., Ramus, F., Pressnitzer, D., Vanduffel, W., and Orban, G. A. (2012). Interhemispheric differences in auditory processing revealed by fMRI in awake rhesus monkeys. *Cereb. Cortex* 22, 838–853. doi: 10.1093/cercor/bhr150

Jung, W. B., Shim, H. J., and Kim, S. G. (2019). Mouse BOLD fMRI at ultrahigh field detects somatosensory networks including thalamic nuclei. *Neuroimage* 195, 203–214. doi: 10.1016/j.neuroimage.2019.03.063

Just, N., and Faber, C. (2019). Probing activation-induced neurochemical changes using optogenetics combined with functional magnetic resonance spectroscopy: a feasibility study in the rat primary somatosensory cortex. *J. Neurochem.* 150, 402–419. doi: 10.1111/jnc.14799

Just, N., Petersen, C., and Gruetter, R. (2010). BOLD responses to trigeminal nerve stimulation. *Magn. Reson. Imaging* 28, 1143–1151. doi: 10.1016/j.mri.2010.02.002

Kahn, I., Desai, M., Knoblich, U., Bernstein, J., Henninger, M., Graybiel, A. M., et al. (2011). Characterization of the functional MRI response temporal linearity via optical control of neocortical pyramidal neurons. *J. Neurosci.* 31, 15086–15091. doi: 10.1523/JNEUROSCI.0007-11.2011

Kamada, K., Pekar, J. J., and Kanwal, J. S. (1999). Anatomical and functional imaging of the auditory cortex in awake mustached bats using magnetic resonance technology. *Brain Res. Brain Res. Protoc.* 4, 351–359. doi: 10.1016/S1385-299X(99)00040-9

Kannurpatti, S. S., Biswal, B. B., and Hudetz, A. G. (2002). Differential fMRI-BOLD signal response to apnea in humans and anesthetized rats. *Magn. Reson. Med.* 47, 864–870. doi: 10.1002/mrm.10131

Kannurpatti, S. S., Biswal, B. B., and Hudetz, A. G. (2003). Regional dynamics of the fMRI-BOLD signal response to hypoxia-hypercapnia in the rat brain. *J. Magn. Reson. Imaging* 17, 641–647. doi: 10.1002/jmri.10311

Karl, S., Boch, M., Zamansky, A., van der Linden, D., Wagner, I. C., Völter, C. J., et al. (2020). Exploring the dog-human relationship by combining fMRI, eye-tracking and behavioural measures. *Sci. Rep.* 10, 22273. doi: 10.1038/s41598-020-79247-5

Kaskan, P. M., Costa, V. D., Eaton, H. P., Zemskova, J. A., Mitz, A. R., Leopold, D. A., et al. (2017). Learned value shapes responses to objects in frontal and ventral stream networks in macaque monkeys. *Cereb. Cortex* 27, 2739–2757. doi: 10.1093/cercor/bhw113

Kayser, C., Petkov, C. I., Augath, M., and Logothetis, N. K. (2005). Integration of touch and sound in auditory cortex. *Neuron* 48, 373–384. doi: 10.1016/j.neuron.2005.09.018

Kennan, R. P., Jacob, R. J., Sherwin, R. S., and Gore, J. C. (2000). Effects of hypoglycemia on functional magnetic resonance imaging response to median nerve stimulation in the rat brain. *J. Cereb. Blood Flow Metab.* 20, 1352–1359. doi: 10.1097/00004647-200009000-00010

Kennan, R. P., Scanley, B. E., Innis, R. B., and Gore, J. C. (1998). Physiological basis for BOLD MR signal changes due to neuronal stimulation: separation of blood volume and magnetic susceptibility effects. *Magn. Reson. Med.* 40, 840–846. doi: 10.1002/mrm.1910400609

Kida, I., and Yamamoto, T. (2010). Comprehensive correlation between neuronal activity and spin-echo blood oxygenation level-dependent signals in the rat somatosensory cortex evoked by short electrical stimulations at various frequencies and currents. *Brain Res.* 1317, 116–123. doi: 10.1016/j.brainres.2009.12.084

Kim, T., Masamoto, K., Fukuda, M., Vazquez, A., and Kim, S. G. (2010). Frequency-dependent neural activity, CBF, and BOLD fMRI to somatosensory stimuli in isoflurane-anesthetized rats. *Neuroimage* 52, 224–233. doi: 10.1016/j.neuroimage.2010.03.064

Kim, Y. R., Huang, I. J., Lee, S. R., Tejima, E., Mandeville, J. B., van Meer, M. P., et al. (2005). Measurements of BOLD/CBV ratio show altered fMRI hemodynamics during stroke recovery in rats. *J. Cereb. Blood Flow Metab.* 25, 820–829. doi: 10.1038/sj.jcbfm.9600084

Kim, Y. R., van Meer, M. P., Mandeville, J. B., Tejima, E., Dai, G., Topalkara, K., et al. (2007). fMRI of delayed albumin treatment during stroke recovery in rats: implication for fast neuronal habituation in recovering brains. *J. Cereb. Blood Flow Metab.* 27, 142–153. doi: 10.1038/sj.jcbfm.9600317

Lambers, H., Segeroth, M., Albers, F., Wachsmuth, L., van Alst, T. M., Faber, C., et al. (2020). A cortical rat hemodynamic response function for improved detection of BOLD activation under common experimental conditions. *Neuroimage* 208, 116446. doi: 10.1016/j.neuroimage.2019.116446

Lau, C., Manno, F. A. M., Dong, C. M., Chan, K. C., and Wu, E. X. (2018). Auditory-visual convergence at the superior colliculus in rat using functional MRI. *Annu. Int. Conf. IEEE Eng. Med. Biol. Soc.* 2018, 5531–5536. doi: 10.1109/EMBC.2018.8513633

Lau, C., Zhang, J. W., Xing, K. K., Zhou, I. Y., Cheung, M. M., Chan, K. C., et al. (2011a). BOLD responses in the superior colliculus and lateral geniculate nucleus of the rat viewing an apparent motion stimulus. *Neuroimage* 58, 878–884. doi: 10.1016/j.neuroimage.2011.06.055

Lau, C., Zhou, I. Y., Cheung, M. M., Chan, K. C., and Wu, E. X. (2011b). BOLD temporal dynamics of rat superior colliculus and lateral geniculate nucleus following short duration visual stimulation. *PLoS ONE* 6, e18914. doi: 10.1371/journal.pone.0018914

Lazovic, J., Wrzos, H. F., Yang, Q. X., Collins, C. M., Smith, M. B., Norgren, R., et al. (2005). Regional activation in the rat brain during visceral stimulation detected by c-fos expression and fMRI. *Neurogastroenterol. Motil.* 17, 548–556. doi: 10.1111/j.1365-2982.2005.00655.x

Leong, A. T. L., Gu, Y., Chan, Y. S., Zheng, H., Dong, C. M., Chan, R. W., et al. (2019). Optogenetic fMRI interrogation of brain-wide central vestibular pathways. *Proc. Natl. Acad. Sci. USA* 116, 10122–10129. doi: 10.1073/pnas.1812453116

Leopold, D. A., Plettenberg, H. K., and Logothetis, N. K. (2002). Visual processing in the ketamine-anesthetized monkey. Optokinetic and blood oxygenation level-dependent responses. *Exp. Brain. Res.* 143, 359–372. doi: 10.1007/s00221-001-0998-0

Liang, S., Lin, Y., Lin, B., Li, J., Liu, W., Chen, L., et al. (2017). Resting-state functional magnetic resonance imaging analysis of brain functional activity in rats with ischemic stroke treated by electro-acupuncture. *J. Stroke Cerebrovasc. Dis.* 26, 1953–1959. doi: 10.1016/j.jstrokecerebrovasdis.2017.06.018

Liang, Z., Ma, Y., Watson, G. D. R., and Zhang, N. (2017). Simultaneous GCaMP6-based fiber photometry and fMRI in rats. *J. Neurosci. Methods* 289, 31–38. doi: 10.1016/j.jneumeth.2017.07.002

Liu, J., Lee, H. J., Weitz, A. J., Fang, Z., Lin, P., Choy, M., et al. (2015). Frequency-selective control of cortical and subcortical networks by central thalamus. *Elife* 4, e09215. doi: 10.7554/eLife.09215.030

Liu, J. V., Hirano, Y., Nascimento, G. C., Stefanovic, B., Leopold, D. A., Silva, A. C., et al. (2013). fMRI in the awake marmoset: somatosensory-evoked responses, functional connectivity, and comparison with propofol anesthesia. *Neuroimage* 78, 186–195. doi: 10.1016/j.neuroimage.2013.03.038

Logothetis, N. K., Guggenberger, H., Peled, S., and Pauls, J. (1999). Functional imaging of the monkey brain. *Nat. Neurosci.* 2, 555–562. doi: 10.1038/9210

Lu, H., Mazaheri, Y., Zhang, R., Jesmanowicz, A., and Hyde, J. S. (2003). Multishot partial-k-space EPI for high-resolution fMRI demonstrated in a rat whisker barrel stimulation model at 3T. *Magn. Reson. Med.* 50, 1215–1222. doi: 10.1002/mrm.10655

Lu, H., Patel, S., Luo, F., Li, S. J., Hillard, C. J., Ward, B. D., et al. (2004). Spatial correlations of laminar BOLD and CBV responses to rat whisker stimulation with neuronal activity localized by Fos expression. *Magn. Reson. Med.* 52, 1060–1068. doi: 10.1002/mrm.20265

Lu, H., Wang, L., Rea, W. W., Brynildsen, J. K., Jaime, S., Zuo, Y., et al. (2016). Low- but not high-frequency LFP correlates with spontaneous BOLD fluctuations in rat whisker barrel cortex. *Cereb. Cortex* 26, 683–694. doi: 10.1093/cercor/bhu248

Luo, Z., Yu, M., Smith, S. D., Kritzer, M., Du, C., Ma, Y., et al. (2009). The effect of intravenous lidocaine on brain activation during non-noxious and acute noxious stimulation of the forepaw: a functional magnetic resonance imaging study in the rat. *Anesth. Analg.* 108, 334–344. doi: 10.1213/ane.0b013e31818e0d34

Mandeville, J. B., Jenkins, B. G., Chen, Y. C., Choi, J. K., Kim, Y. R., Belen, D., et al. (2004). Exogenous contrast agent improves sensitivity of gradient-echo functional magnetic resonance imaging at 9.4 T. *Magn. Reson. Med.* 52, 1272–1281. doi: 10.1002/mrm.20278

Mandeville, J. B., Jenkins, B. G., Kosofsky, B. E., Moskowitz, M. A., Rosen, B. R., Marota, J. J., et al. (2001). Regional sensitivity and coupling of BOLD and CBV changes during stimulation of rat brain. *Magn. Reson Med* 45, 443–447. doi: 10.1002/1522-2594(200103)45:3<443::aid-mrm1058>3.0.co;2-3

Martin, C., Grenier, D., Thévenet, M., Vigouroux, M., Bertrand, B., Janier, M., et al. (2007). fMRI visualization of transient activations in the rat olfactory bulb using short odor stimulations. *Neuroimage* 36, 1288–1293. doi: 10.1016/j.neuroimage.2007.04.029

Martin, C. J., Kennerley, A. J., Berwick, J., Port, M., and Mayhew, J. E. (2013). Functional MRI in conscious rats using a chronically implanted surface coil. *J. Magn. Reson. Imaging* 38, 739–744. doi: 10.1002/jmri.23914

Masamoto, K., Kim, T., Fukuda, M., Wang, P., and Kim, S. G. (2007). peRelationship between neural, vascular, and BOLD signals in isoflurane-anesthetized rat somatosensory cortex. *Cereb. Cortex* 17, 942–950. doi: 10.1093/cercor/bhl005

Maul, K. K., Voss, H. U., Parra, L. C., Salgado-Commissariat, D., Ballon, D., Tchernichovski, O., et al. (2010). The development of stimulus-specific auditory responses requires song exposure in male but not female zebra finches. *Dev. Neurobiol.* 70, 28–40. doi: 10.1002/dneu.20751

Mazzanti, M. L., Walvick, R. P., Zhou, X., Sun, Y., Shah, N., Mansour, J., et al. (2011). Distribution of hyperpolarized xenon in the brain following sensory stimulation: preliminary MRI findings. *PLoS ONE* 6, e21607. doi: 10.1371/journal.pone.0021607

Meuwissen, K. P. V., van der Toorn, A., Gu, J. W., Zhang, T. C., Dijkhuizen, R. M., Joosten, E. A. J., et al. (2020). Active recharge burst and tonic spinal cord stimulation engage different supraspinal mechanisms: a functional Magnetic Resonance Imaging study in peripherally injured chronic neuropathic rats. *Pain Pract.* 20, 510–521. doi: 10.1111/papr.12879

Miller, M. J., Chen, N. K., Li, L., Tom, B., Weiss, C., Disterhoft, J. F., et al. (2003). fMRI of the conscious rabbit during unilateral classical eyeblink conditioning reveals bilateral cerebellar activation. *J. Neurosci.* 23, 11753–11758. doi: 10.1523/JNEUROSCI.23-37-11753.2003

Miller, M. J., Weiss, C., Song, X. M., Iordanescu, G., Disterhoft, J. F., Wyrwicz, A. M., et al. (2008). Functional magnetic resonance imaging of delay and trace eyeblink conditioning in the primary visual cortex of the rabbit. *J. Neurosci.* 28, 4974–4981. doi: 10.1523/JNEUROSCI.5622-07.2008

Murris, S. R., Arsenault, J. T., Raman, R., Vogels, R., and Vanduffel, W. (2021). Electrical stimulation of the macaque ventral tegmental area drives category-selective learning without attention. *Neuron* 109, 1381–1395.e7. doi: 10.1016/j.neuron.2021.02.013

Nagakubo, D., Hamamoto, Y., Hasegawa, D., Kamata, M., Iizuka, T., Muta, K., et al. (2017). Functional MRI-based identification of brain regions activated by mechanical noxious stimulation and modulatory effect of remifentanil in cats. *Res. Vet. Sci.* 114, 444–449. doi: 10.1016/j.rvsc.2017.07.024

Nasr, S., Liu, N., Devaney, K. J., Yue, X., Rajimehr, R., Ungerleider, L. G., et al. (2011). Scene-selective cortical regions in human and nonhuman primates. *J. Neurosci.* 31, 13771–13785. doi: 10.1523/JNEUROSCI.2792-11.2011

Ogawa, S., Lee, T. M., Nayak, A. S., and Glynn, P. (1990). Oxygenation-sensitive contrast in magnetic resonance image of rodent brain at high magnetic fields. *Magn. Reson. Med.* 14, 68–78. doi: 10.1002/mrm.1910140108

Ogawa, S., Tank, D. W., Menon, R., Ellermann, J. M., Kim, S. G., Merkle, H., et al. (1992). Intrinsic signal changes accompanying sensory stimulation: functional brain mapping with magnetic resonance imaging. *Proc. Natl. Acad. Sci. USA.* 89, 5951–5955. doi: 10.1073/pnas.89.13.5951

Ohayon, S., Grimaldi, P., Schweers, N., and Tsao, D. Y. (2013). Saccade modulation by optical and electrical stimulation in the macaque frontal eye field. *J. Neurosci.* 33, 16684–16697. doi: 10.1523/JNEUROSCI.2675-13.2013

Pawela, C. P., Kramer, J. M., and Hogan, Q. H. (2017). Dorsal root ganglion stimulation attenuates the BOLD signal response to noxious sensory input in specific brain regions: insights into a possible mechanism for analgesia. *Neuroimage* 147, 10–18. doi: 10.1016/j.neuroimage.2016.11.046

Perrodin, C., Kayser, C., Logothetis, N. K., and Petkov, C. I. (2011). Voice cells in the primate temporal lobe. *Curr. Biol.* 21, 1408–1415. doi: 10.1016/j.cub.2011.07.028

Poplawsky, A. J., Fukuda, M., Murphy, M., and Kim, S. G. (2015). Layer-specific fMRI responses to excitatory and inhibitory neuronal activities in the olfactory bulb. *J. Neurosci.* 35, 15263–15275. doi: 10.1523/JNEUROSCI.1015-15.2015

Premereur, E., and Janssen, P. (2020). Effective connectivity reveals an interconnected inferotemporal network for three-dimensional structure processing. *J. Neurosci.* 40, 8501–8512. doi: 10.1523/JNEUROSCI.3024-19.2020

Qi, H. X., Wang, F., Liao, C. C., Friedman, R. M., Tang, C., Kaas, J. H., et al. (2016). Spatiotemporal trajectories of reactivation of somatosensory cortex by direct and secondary pathways after dorsal column lesions in squirrel monkeys. *Neuroimage* 142, 431–453. doi: 10.1016/j.neuroimage.2016.08.015

Ramu, J., Bockhorst, K. H., Grill, R. J., Mogatadakala, K. V., and Narayana, P. A. (2007). Cortical reorganization in NT3-treated experimental spinal cord injury: functional magnetic resonance imaging. *Exp. Neurol.* 204, 58–65. doi: 10.1016/j.expneurol.2006.09.015

Ramu, J., Bockhorst, K. H., Mogatadakala, K. V., and Narayana, P. A. (2006). Functional magnetic resonance imaging in rodents: mthodology and application to spinal cord injury. *J. Neurosci. Res.* 84, 1235–1244. doi: 10.1002/jnr.21030

Russ, B. E., and Leopold, D. A. (2015). Functional MRI mapping of dynamic visual features during natural viewing in the macaque. *Neuroimage* 109, 84–89. doi: 10.1016/j.neuroimage.2015.01.012

Ryali, S., Shih, Y. Y., Chen, T., Kochalka, J., Albaugh, D., Fang, Z., et al. (2016). Combining optogenetic stimulation and fMRI to validate a multivariate dynamical systems model for estimating causal brain interactions. *Neuroimage* 132, 398–405. doi: 10.1016/j.neuroimage.2016.02.067

Sanganahalli, B. G., Bailey, C. J., Herman, P., and Hyder, F. (2009). Tactile and non-tactile sensory paradigms for fMRI and neurophysiologic studies in rodents. *Methods Mol. Biol.* 489, 213–242. doi: 10.1007/978-1-59745-543-5_10

Sanganahalli, B. G., Baker, K. L., Thompson, G. J., Herman, P., Shepherd, G. M., Verhagen, J. V., et al. (2020). Orthonasal versus retronasal

glomerular activity in rat olfactory bulb by fMRI. *Neuroimage* 212, 116664. doi: 10.1016/j.neuroimage.2020.116664

Sanganahalli, B. G., Herman, P., Behar, K. L., Blumenfeld, H., Rothman, D. L., Hyder, F., et al. (2013). Functional MRI and neural responses in a rat model of Alzheimer's disease. *Neuroimage* 79, 404–411. doi: 10.1016/j.neuroimage.2013.04.099

Sanganahalli, B. G., Rebello, M. R., Herman, P., Papademetris, X., Shepherd, G. M., Verhagen, J. V., et al. (2016). Comparison of glomerular activity patterns by fMRI and wide-field calcium imaging: implications for principles underlying odor mapping. *Neuroimage* 126, 208–218. doi: 10.1016/j.neuroimage.2015.11.048

Scanley, B. E., Kennan, R. P., Cannan, S., Skudlarski, P., Innis, R. B., Gore, J. C., et al. (1997). Functional magnetic resonance imaging of median nerve stimulation in rats at 2.0 T. *Magn. Reson. Med.* 37, 969–972. doi: 10.1002/mrm.1910370625

Schmid, F., Wachsmuth, L., Albers, F., Schwalm, M., Stroh, A., Faber, C., et al. (2017). True and apparent optogenetic BOLD fMRI signals. *Magn. Reson. Med.* 77, 126–136. doi: 10.1002/mrm.26095

Schmid, F., Wachsmuth, L., Schwalm, M., Prouvot, P. H., Jubal, E. R., Fois, C., et al. (2016). Assessing sensory versus optogenetic network activation by combining (o)fMRI with optical Ca2+ recordings. *J. Cereb. Blood Flow Metab.* 36, 1885–1900. doi: 10.1177/0271678X15619428

Schroeter, A., Schlegel, F., Seuwen, A., Grandjean, J., and Rudin, M. (2014). Specificity of stimulus-evoked fMRI responses in the mouse: the influence of systemic physiological changes associated with innocuous stimulation under four different anesthetics. *Neuroimage* 94, 372–384. doi: 10.1016/j.neuroimage.2014.01.046

Schwindt, W., Burke, M., Pillekamp, F., Luhmann, H. J., and Hoehn, M. (2004). Functional magnetic resonance imaging and somatosensory evoked potentials in rats with a neonatally induced freeze lesion of the somatosensory cortex. *J. Cereb. Blood Flow Metab.* 24, 1409–1418. doi: 10.1097/01.WCB.0000143535.84012.CA

Seehafer, J. U., Kalthoff, D., Farr, T. D., Wiedermann, D., and Hoehn, M. (2010). No increase of the blood oxygenation level-dependent functional magnetic resonance imaging signal with higher field strength: implications for brain activation studies. *J. Neurosci.* 30, 5234–5241. doi: 10.1523/JNEUROSCI.0844-10.2010

Shih, C. T., Chiu, S. C., and Peng, S. L. (2021). Caffeine enhances BOLD responses to electrical whisker pad stimulation in rats during alpha-chloralose anaesthesia. *Eur. J. Neurosci.* 53, 601–610. doi: 10.1111/ejn.14968

Shih, Y. Y., Chen, Y. Y., Lai, H. Y., Kao, Y. C., Shyu, B. C., Duong, T. Q., et al. (2013). Ultra high-resolution fMRI and electrophysiology of the rat primary somatosensory cortex. *Neuroimage* 73, 113–120. doi: 10.1016/j.neuroimage.2013.01.062

Shih, Y. Y., Wey, H. Y., La Garza, B. H. D., e., and Duong, T. Q. (2011). Striatal and cortical BOLD, blood flow, blood volume, oxygen consumption, and glucose consumption changes in noxious forepaw electrical stimulation. *J. Cereb. Blood Flow Metab.* 31, 832–841. doi: 10.1038/jcbfm.2010.173

Shyu, B. C., Lin, C. Y., Sun, J. J., Chen, S. L., and Chang, C. (2004). BOLD response to direct thalamic stimulation reveals a functional connection between the medial thalamus and the anterior cingulate cortex in the rat. *Magn. Reson. Med.* 52, 47–55. doi: 10.1002/mrm.20111

Sicard, K. M., Henninger, N., Fisher, M., Duong, T. Q., and Ferris, C. F. (2006). Differential recovery of multimodal MRI and behavior after transient focal cerebral ischemia in rats. *J. Cereb. Blood Flow Metab.* 26, 1451–1462. doi: 10.1038/sj.jcbfm.9600299

Sonnay, S., Duarte, J. M. N., and Just, N. (2017). Lactate and glutamate dynamics during prolonged stimulation of the rat barrel cortex suggest adaptation of cerebral glucose and oxygen metabolism. *Neuroscience* 346, 337–348. doi: 10.1016/j.neuroscience.2017.01.034

Spenger, C., Josephson, A., Klason, T., Hoehn, M., Schwindt, W., Ingvar, M., et al. (2000). Functional MRI at 4.7 tesla of the rat brain during electric stimulation of forepaw, hindpaw, or tail in single- and multislice experiments. *Exp. Neurol.* 166, 246–253. doi: 10.1006/exnr.2000.7524

Steiner, A. R., Rousseau-Blass, F., Schroeter, A., Hartnack, S., and Bettschart-Wolfensberger, R. (2021). Systematic review: anesthetic protocols and management as confounders in rodent blood oxygen level dependent functional Magnetic Resonance Imaging (BOLD fMRI)-part B: effects of anesthetic agents, doses and timing. *Animals* 11:199. doi: 10.3390/ani11010199

Stephenson, J. B., Li, R., Yan, J. G., Hyde, J., and Matloub, H. (2013). Transhemispheric cortical plasticity following contralateral C7 nerve transfer: a rat functional magnetic resonance imaging survival study. *J. Hand Surg. Am.* 38, 478–487. doi: 10.1016/j.jhsa.2012.12.018

Suzuki, H., Sumiyoshi, A., Kawashima, R., and Shimokawa, H. (2013). Different brain activation under left and right ventricular stimulation: an fMRI study in anesthetized rats. *PLoS ONE* 8, e56990. doi: 10.1371/journal.pone.0056990

Suzuki, J., Sasaki, M., Harada, K., Bando, M., Kataoka, Y., Onodera, R., et al. (2013). Bilateral cortical hyperactivity detected by fMRI associates with improved motor function following intravenous infusion of mesenchymal stem cells in a rat stroke model. *Brain Res.* 1497, 15–22. doi: 10.1016/j.brainres.2012.12.028

Takata, N., Yoshida, K., Komaki, Y., Xu, M., Sakai, Y., Hikishima, K., et al. (2015). Optogenetic activation of CA1 pyramidal neurons at the dorsal and ventral hippocampus evokes distinct brain-wide responses revealed by mouse fMRI. *PLoS ONE* 10, e0121417. doi: 10.1371/journal.pone.0121417

Tikhonova, M. A., Romaschenko, A. V., Akulov, A. E., Ho, Y. J., Kolosova, N. G., Moshkin, M. P., et al. (2015). Comparative study of perception and processing of socially or sexually significant odor information in male rats with normal or accelerated senescence using fMRI. *Behav. Brain Res.* 294, 89–94. doi: 10.1016/j.bbr.2015.08.001

Todd, N., Zhang, Y., Livingstone, M., Borsook, D., and McDannold, N. (2019). The neurovascular response is attenuated by focused ultrasound-mediated disruption of the blood-brain barrier. *Neuroimage* 201, 116010. doi: 10.1016/j.neuroimage.2019.116010

Tsao, D. Y., Freiwald, W. A., Tootell, R. B., and Livingstone, M. S. (2006). A cortical region consisting entirely of face-selective cells. *Science* 311, 670–674. doi: 10.1126/science.1119983

Tsurugizawa, T., Uematsu, A., Nakamura, E., Hasumura, M., Hirota, M., Kondoh, T., et al. (2009a). Mechanisms of neural response to gastrointestinal nutritive stimuli: the gut-brain axis. *Gastroenterology* 137, 262–273. doi: 10.1053/j.gastro.2009.02.057

Tsurugizawa, T., Uematsu, A., Uneyama, H., and Torii, K. (2009b). Blood oxygenation level-dependent response to intragastric load of corn oil emulsion in conscious rats. *Neuroreport* 20, 1625–1629. doi: 10.1097/WNR.0b013e32833312e5

Tsurugizawa, T., Uematsu, A., Uneyama, H., and Torii, K. (2010). Effects of isoflurane and alpha-chloralose anesthesia on BOLD fMRI responses to ingested L-glutamate in rats. *Neuroscience* 165, 244–251. doi: 10.1016/j.neuroscience.2009.10.006

Tsurugizawa, T., Uematsu, A., Uneyama, H., and Torii, K. (2012). Functional brain mapping of conscious rats during reward anticipation. *J. Neurosci. Methods* 206, 132–137. doi: 10.1016/j.jneumeth.2012.02.014

Uhlirova, H. K., Kiliç, P., Tian, M., Thunemann, M., and Desjardins, P. A., Saisan, et al. (2016). Cell type specificity of neurovascular coupling in cerebral cortex. *Elife* 5, e14315. doi: 10.7554/eLife.14315.018

Uhrig, L., Dehaene, S., and Jarraya, B. (2014). A hierarchy of responses to auditory regularities in the macaque brain. *J. Neurosci.* 34, 1127–1132. doi: 10.1523/JNEUROSCI.3165-13.2014

Van der Kant, A., Derégnaucourt, S., Gahr, M., Van der Linden, A., and Poirier, C. (2013). Representation of early sensory experience in the adult auditory midbrain: implications for vocal learning. *PLoS ONE* 8, e61764. doi: 10.1371/journal.pone.0061764

Van Ruijssevelt, L., Chen, Y., von Eugen, K., Hamaide, J., Groof, G. D., et al. (2018). fMRI reveals a novel region for evaluating acoustic information for mate choice in a female songbird. *Curr. Biol.* 28, 711–721.e6. doi: 10.1016/j.cub.2018.01.048

Van Ruijssevelt, L., Hamaide, J., Van Gurp, M. T., Verhoye, M., and Van der Linden, A. (2017). Auditory evoked BOLD responses in awake compared to lightly anaesthetized zebra finches. *Sci. Rep.* 7, 13563. doi: 10.1038/s41598-017-13014-x

Verley, D. R., Torolira, D., Pulido, B., Gutman, B., Bragin, A., Mayer, A., et al. (2018). Remote changes in cortical excitability after experimental traumatic brain injury and functional reorganization. *J. Neurotrauma* 35, 2448–2461. doi: 10.1089/neu.2017.5536

Voss, H. U., Tabelow, K., Polzehl, J., Tchernichovski, O., Maul, K. K., Salgado-Commissariat, D., et al. (2007). Functional MRI of the zebra finch brain during song stimulation suggests a lateralized response topography. *Proc. Natl. Acad. Sci. USA* 104, 10667–10672. doi: 10.1073/pnas.0611515104

Wang, R., Wu, L., Tang, Z., Sun, X., Feng, X., Tang, W., et al. (2017). Visual cortex and auditory cortex activation in early binocularly blind macaques: a BOLD-fMRI study using auditory stimuli. *Biochem. Biophys. Res. Commun.* 485, 796–801. doi: 10.1016/j.bbrc.2017.02.133

Wang, X., Leong, A. T. L., Chan, R. W., Liu, Y., and Wu, E. X. (2019). Thalamic low frequency activity facilitates resting-state cortical interhemispheric MRI functional connectivity. *Neuroimage* 201, 115985. doi: 10.1016/j.neuroimage.2019.06.063

Wehrl, H. F., Martirosian, P., Schick, F., Reischl, G., and Pichler, B. J. (2014). Assessment of rodent brain activity using combined [(15)O]H2O-PET and BOLD-fMRI. *Neuroimage* 89, 271–279. doi: 10.1016/j.neuroimage.2013.11.044

Wong, E., Yang, B., Du, L., Ho, W. H., Lau, C., Ke, Y., et al. (2017). The multi-level impact of chronic intermittent hypoxia on central auditory processing. *Neuroimage* 156, 232–239. doi: 10.1016/j.neuroimage.2017.05.036

Xu, A. G., Qian, M., Tian, F., Xu, B., Friedman, R. M., Wang, J., et al. (2019). Focal infrared neural stimulation with high-field functional MRI: a rapid way to map mesoscale brain connectomes. *Sci Adv* 5, eaau7046. doi: 10.1126/sciadv.aau7046

Xu, F., Schaefer, M., Kida, I., Schafer, J., Liu, N., Rothman, D. L., et al. (2005). Simultaneous activation of mouse main and accessory olfactory bulbs by odors or pheromones. *J. Comp. Neurol.* 489, 491–500. doi: 10.1002/cne.20652

Yang, P. F., Chen, Y. Y., Chen, D. Y., Hu, J. W., Chen, J. H., Yen, C. T., et al. (2013). Comparison of fMRI BOLD response patterns by electrical stimulation of the ventroposterior complex and medial thalamus of the rat. *PLoS ONE* 8, e66821. doi: 10.1371/journal.pone.0066821

Yang, X., Hyder, F., and Shulman, R. G. (1996). Activation of single whisker barrel in rat brain localized by functional magnetic resonance imaging. *Proc. Natl. Acad. Sci. USA* 93, 475–478. doi: 10.1073/pnas.93.1.475

Yano, M., Matsuda, A., Natsume, T., Ogawa, S., Awaga, Y., Hayashi, I., et al. (2019). Pain-related behavior and brain activation in cynomolgus macaques with naturally occurring endometriosis. *Hum. Reprod.* 34, 469–478. doi: 10.1093/humrep/dey383

Yen, C. C., Papoti, D., and Silva, A. C. (2018). Investigating the spatiotemporal characteristics of the deoxyhemoglobin-related and deoxyhemoglobin-unrelated functional hemodynamic response across cortical layers in awake marmosets. *Neuroimage* 164, 121–130. doi: 10.1016/j.neuroimage.2017.03.005

Yu, X., Glen, D., Wang, S., Dodd, S., Hirano, Y., Saad, Z., et al. (2012). Direct imaging of macrovascular and microvascular contributions to BOLD fMRI in layers IV-V of the rat whisker-barrel cortex. *Neuroimage* 59, 1451–1460. doi: 10.1016/j.neuroimage.2011.08.001

Yu, X., He, Y., Wang, M., Merkle, H., Dodd, S. J., Silva, A. C., et al. (2016). Sensory and optogenetically driven single-vessel fMRI. *Nat. Methods* 13, 337–340. doi: 10.1038/nmeth.3765

Yu, X., Tu, L., Lei, P., Song, J., Xu, H., Hou, X., et al. (2014). Antiemesis effect and brain fMRI response of gastric electrical stimulation with different parameters in dogs. *Neurogastroenterol. Motil.* 26, 1049–1056. doi: 10.1111/nmo.12362

Zhang, N., Gore, J. C., Chen, L. M., and Avison, M. J. (2007). Dependence of BOLD signal change on tactile stimulus intensity in SI of primates. *Magn. Reson. Imaging* 25, 784–794. doi: 10.1016/j.mri.2007.05.002

Zhang, N., Wang, F., Turner, G. H., Gore, J. C., Avison, M. J., Chen, L. M., et al. (2010). Intra- and inter-subject variability of high field fMRI digit maps in somatosensory area 3b of new world monkeys. *Neuroscience* 165, 252–264. doi: 10.1016/j.neuroscience.2009.09.066

Zhang, Q. L., i., Huang, J., Yang, S., Liang, M., Liu, S., et al. (2021). Functional connectivity of the retrosplenial cortex in rats with ischemic stroke is improved by electroacupuncture. *Acupunct. Med.* 39, 200–207. doi: 10.1177/0964528420921190

Zhao, F., Holahan, M. A., Wang, X., Uslaner, J. M., Houghton, A. K., Evelhoch, J. L., et al. (2018). fMRI study of the role of glutamate NMDA receptor in the olfactory processing in monkeys. *PLoS ONE* 13, e0198395. doi: 10.1371/journal.pone.0198395

Zhao, S., Li, G., Tong, C., Chen, W., Wang, P., Dai, J., et al. (2020). Full activation pattern mapping by simultaneous deep brain stimulation and fMRI with graphene fiber electrodes. *Nat. Commun.* 11, 1788. doi: 10.1038/s41467-020-15570-9

frontiers | Frontiers in Neuroscience

TYPE Methods
PUBLISHED 29 September 2022
DOI 10.3389/fnins.2022.945594

OPEN ACCESS

EDITED BY
Shengxiang Liang,
Fujian University of Traditional Chinese Medicine, China

REVIEWED BY
Arun Sasidharan,
National Institute of Mental Health and Neurosciences, India
Nikoloz Sirmpilatze,
German Primate Center, Germany
Anagha S. Deshmukh,
Manipal Academy of Higher Education, India

*CORRESPONDENCE
Alejandra Lopez-Castro
alejandraloc@comunidad.unam.mx
Eduardo A. Garza-Villarreal
egarza@comunidad.unam.mx

SPECIALTY SECTION
This article was submitted to Brain Imaging Methods, a section of the journal Frontiers in Neuroscience

RECEIVED 16 May 2022
ACCEPTED 05 September 2022
PUBLISHED 29 September 2022

CITATION
Lopez-Castro A, Angeles-Valdez D, Rojas-Piloni G and Garza-Villarreal EA (2022) Focal electrical stimulation on an alcohol disorder model using magnetic resonance imaging-compatible chronic neural monopolar carbon fiber electrodes. *Front. Neurosci.* 16:945594. doi: 10.3389/fnins.2022.945594

Focal electrical stimulation on an alcohol disorder model using magnetic resonance imaging-compatible chronic neural monopolar carbon fiber electrodes

Alejandra Lopez-Castro[1]*, Diego Angeles-Valdez[1,2], Gerardo Rojas-Piloni[1] and Eduardo A. Garza-Villarreal[1]*

[1]Instituto de Neurobiología, Universidad Nacional Autónoma de México, Querétaro, Mexico, [2]Department of Biomedical Sciences of Cells and Systems, Cognitive Neuroscience Center, University Medical Center Groningen, University of Groningen, Groningen, Netherlands

Neuromodulation interventions, such as Deep Brain Stimulation (DBS) and repeated transcranial magnetic stimulation (rTMS), are proposed as possible new complementary therapies to treat substance use disorders (SUD) such as alcohol use disorder (AUD). It is hypothesized that neuromodulation may induce neural plasticity in the reward and frontostriatal systems *via* electrical field induction, possibly reducing symptoms. Preclinical self-administration rodent models of AUD may help us gain insight into the effects of neuromodulation therapies on different pathology, as well as the neural mechanisms behind the positive effects. DBS, or any type of brain stimulation using intracranial electrodes in rodents, would benefit from the use of magnetic resonance imaging (MRI) to study the longitudinal effects and mechanisms of stimulation as well as novel targets, as it is a non-invasive technique that allows the analysis of structural and functional changes in the brain. To do this, there is a need for MRI-compatible electrodes that allow for MRI acquisition with minimal distortion of the magnetic field. In this protocol, we present a method for the construction and surgery of chronically implantable monopolar carbon electrodes for use in rats. Unlike conventional electrodes, carbon electrodes are resistant to high temperatures, flexible, and generate fewer artifacts in MRI compared to conventional ones. We validated its use by using a focal electrical stimulation high-frequency (20 Hz) protocol that lasted ∼10 sessions. We propose that this technique can also be used for the research of the neurophysiological bases of the neuromodulatory treatment in other preclinical substance use disorders (SUD) models.

KEYWORDS

MRI, electrodes, carbon fiber, DBS, SUD, AUD, alcohol

Introduction

Neuromodulation encompasses technologies that apply electrical currents with a variety of parameters, through implanted or non-implanted electrodes, to achieve a functional activation or inhibition of a group of neurons, pathways, or circuits (Krames et al., 2009). The main neuromodulation techniques used in humans are repetitive transcranial magnetic stimulation (rTMS) and deep brain stimulation (DBS) (Klooster et al., 2016). Currently approved by the Food and Drug Administration (FDA), is rTMS therapy for adjunctive treatment for nicotine use disorder, and DBS for essential tremors, dystonia, obsessive-compulsive disorder, and Parkinson's disease (Edwards et al., 2017). Alas, no consensus exists regarding the mechanisms of action involved in rTMS or DBS (Diana et al., 2017). The effects and mechanisms of neuromodulation in SUDs can be further tested through the use of animal models (Ankeny et al., 2014) which can provide valuable information. For instance, using magnetic resonance imaging (MRI) in longitudinal animal models for SUDs treated with neuromodulation, researchers may be able to find neuroimaging biomarkers (Aydin et al., 2019), effects, and mechanisms related to clinical outcomes, which could be later translated to human studies (Silva and Bock, 2008; Spanagel, 2017). To study focal repeated stimulation in rats, intracranial electrodes are currently a practical solution. However, there are a few major methodological challenges to use intracranial electrodes in longitudinal studies with MRI. Metal electrodes are most commonly used for stimulation in rats, yet are highly susceptible to create susceptibility artifacts (Dunn et al., 2009), which leads to the loss of signal around the region where the electrode is placed, as well as distortion and lower signal-to-noise ratio (SNR) (Redpath, 1998). For DBS studies in rodents, 140 μm diameter braided platinum/iridium wire electrodes (Van De Berg, 2015), 200 μm diameter braided stainless steel wires (Morimoto et al., 2011) and 250 μm braided silver wires have been used for DBS protocols in conjunction with simultaneous MRI and EEG acquisitions. Platinum/iridium and stainless steel electrodes induce a susceptibility artifact of twice the original electrode diameter and silver electrodes do not increase the artifact compared to the electrode diameter, but there is more signal around the longitudinal diameter of the electrode (Dunn et al., 2009; Young et al., 2011; Derksen et al., 2021). Carbon fiber electrodes have been used in neuroscience as an option for recording (Chuapoco et al., 2019; Joshi-Imre et al., 2019) and stimulating brain regions (Gallino et al., 2019). These electrodes have proven to be a better choice for the improvement of SNR with little to none MRI susceptibility artifacts, due to their physical properties like high resistance, light-weight, and low density, composed of a tensile of 900 GPa, with thermal conductivity of 1,000 W/mK and electric conductivity of 106 S/m (Zhao et al., 2019). However, the viability of its use in the treatment of SUDs and in longitudinal MRI studies has not been tested.

Therefore, this work aims to provide a simple and low-cost approach for assembling chronically implantable monopolar carbon electrodes and their use for repetitive focal stimulation in alcohol use disorder (AUD). Also, we proposed it can be used in other models of SUDs.

Materials and equipment

Methods

Tables 1, **2** list the materials and doses required to perform the electrode implantation surgery. The study was approved by the Animal Research Committee of the Instituto de Neurobiología at Universidad Nacional Autónoma de México No. 119-A. All surgical, experimental, and maintenance procedures were carried out in accordance with the Reglamento de la Ley General de Salud en Materia de Investigación para la Salud (Health General Law on Health Research Regulation) of the Mexican Health Ministry that follows the "Guide for the care and use of laboratory animals" (Mexicana Norma Oficial, 1999; National Research Council et al., 2011). Also in accordance with the recommendations of the Institute of Laboratory Animal Resources Commission on Life Sciences (Guide for the Care and Use of Laboratory Animals, 1996) and the Directive 2010/63/EU of the European Parliament and of the Council.

TABLE 1 Materials.

1. Lab standard stereotaxic instrument
2. Heat pad (Beurer® HK55)
3. Gas anesthesia mask compatible with the stereotaxic setup.
4. Anesthetic gas vaporizer
5. Isoflurane (SOFLORAN VET PiSA®)
6. Anesthesia induction chamber
7. Oxygen supply
8. Surgical instruments (Guttek)
9. Instrument sterilizer
10. Constructed carbon fiber electrodes
11. Nylon screws 2.4 mm length
12. Adhesive luting cement (C&B-Metabond®)
13. Orthodontic resin (ortho-jet crystal)
14. N-butyl 2 cyanoacrylate glue
15. Synthetic surgical suture (Nylon 3-0)
16. Dental drill
17. Saline solution (0.9%)
18. Hydrogen peroxide
19. Ophthalmic drops (artificial tears)
20. Antibiotic ointment (nitrofurazone 0.2 g)
21. Painkiller solution for injection (meloxicam 15 mg/ml)
22. Local injectable anesthetic (lidocaine 2%)
23. Syringes of 1 and 3 ml
24. Cotton swabs
25. Gauze
26. IceW3510

TABLE 2 Medication and dosage.

- Meloxicam
  - Intramuscular injection 0.3 ml/kg
- Lidocaine
  - Dilute to 0.5% for subcutaneous or intraincisional injection
  - Inject less than 7 mg/kg
- Isoflurane
  - 5% for induction
  - 1–3% for maintenance during surgeryW8918

Animals

Twelve adults (male $n = 6$) and (female $n = 6$) Wistar rats (*Rattus norvegicus albinus*) were obtained on postnatal day 21 (P21) from the vivarium of the Institute of Neurobiology in Queretaro, Mexico. Animals were individually housed in standard cages in a room with a 12:12 dark cycle/light, controlled temperature (23°C), and had free access to food. No rats had to be excluded due to complications with the model, treatment, or surgery.

Experimental outline

The objective of this work was to validate the use of carbon fiber monopolar electrodes for chronic implantation in an ethanol self-administration model with longitudinal structural and functional MRI acquisition (**Figure 1**). Electrode implantation was performed once the *ethanol self-administration model* was established. For this model, we used the *Intermittent access two-bottle choice (IA2BC)* (Wise, 1973; Simms et al., 2008; Carnicella et al., 2014). Rats were individually housed at P35 and received at least 1 week of acclimatization with two bottles of water, the same to be used for the IA2BC model and handling. At P45, rats received 24-h sessions of free access to two bottle choices of water and 20% ethanol solution on Monday, Wednesday, and Friday, with 48-h withdrawal periods during the weekends. The placement of the bottles was alternated each drinking session to control for side preferences. During the withdrawal periods, rats received two bottles of water.

As for the timeline, the IA2BC model started on P45 (Time 1 or T1) and lasted for 45 days which included 20 sessions in total, ending in P90. The electrode implantation surgery for stimulation was done at P90, with 10 days of recovery from surgery (Time 2 or T2). Later, at P110, the rats were MRI-scanned (Time 3 or T3). Between P110 and P144 the IA2BC was reestablished with 15 sessions in total to measure relapse and alcohol use. It was during this time that the repeated focal electrical stimulation intervention was applied. T3 was subdivided into 3-time points: pre-stimulation (PreStim), stimulation (Stim), and post-stimulation (PoStim). Before stimulation, we randomly divided the sample into sham (placebo) ($n = 6$) and active ($n = 6$) stimulation groups. The sham stimulation group was treated exactly the same way as the active group, except that, during the stimulation sessions, they did not receive any stimulation.

Carbon electrodes construction

The construction of the monopolar carbon electrodes was based on the Gallino et al. (2019) design. The electrodes were constructed using a cortical fiber of 0.28 mm in diameter and 1 cm in length (Easy Composites, Stroke on Trent, UK #CFROD-028) and an extracranial fiber of 2 mm in diameter and 5 mm in length (Good Winds, Mount Vernon, WA USA #CS070048) a 3D model of the electrode is shown in **Supplementary Figure 1**. The cortical fiber was isolated with 3 layers of spray rubber (Plasti Dip®) and both of the fibers were joined with a carbon epoxy (Atom Adhesives, Fort Lauderdale, FL, USA, #AA-CARB61), which conducts electricity between fibers. The final diameter of the cortical fiber was an average of 0.64 mm (**Supplementary Figure 2**). Finally, the resistance of the electrodes was measured with a voltmeter and marked with a range of 2–8 kω.

Surgical carbon electrodes implantation

From P80 to P90 rats were handled once a day for 5 min by caressing the top of their heads, where the electrodes will be placed later. This was to acclimate them to electrode manipulation and human-rat interactions. At P90 surgical procedure was performed; the technique was adapted from Matsumiya et al. (2012), Rigalli and Di Loreto (2016) and Santana-Chávez et al. (2020) (**Figure 2**).

Preparation for anesthesia (∼5–10 min)

Rats were anesthetized with vaporized isoflurane (∼5% induction) 50/50 isoflurane/oxygen mixture, administered in an induction chamber. A deep anesthesia state was verified with the absence of withdrawal reflexes to pain. The induction with isoflurane took between 5 and 10 min and was maintained during the positioning of the rat in the stereotaxic apparatus. The rat was placed in a prone position maintaining a permeable airway with the aid of the incisor immobilizer bar and the intra-aural position pencils. Artificial tears were then administered to the eyes and then covered with clean gauze. A rat gas anesthesia mask was used in the stereotaxic setup. The heart rate was maintained at ∼300 beats per minute and the respiratory thoracic movement was watched frequently and checked to be around 70 per min, and be regular and harmonic on both sides of the thorax. A heating pad placed on the stereotaxic apparatus base helped maintain the body temperature at 37°C during the surgery. Next, diluted lidocaine to 0.5% was applied

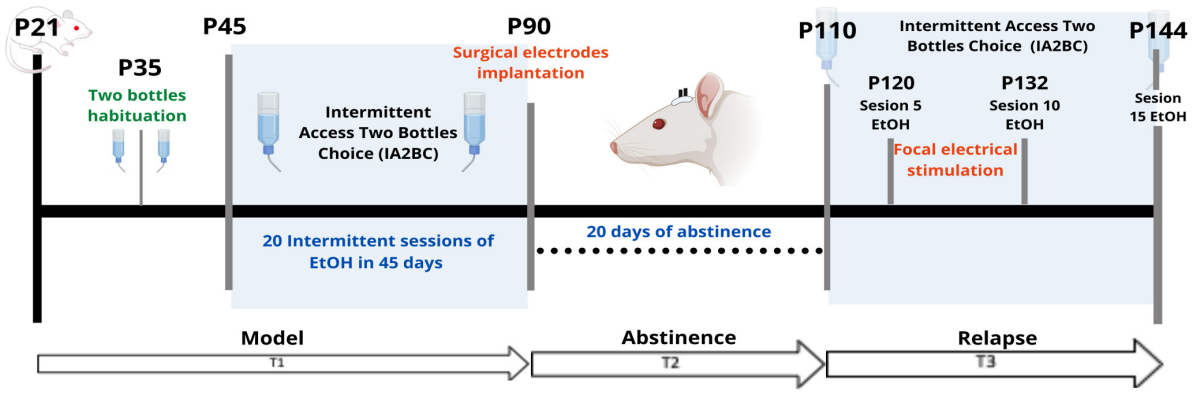

FIGURE 1
Experimental outline. T1 (Time 1) corresponds to the time encompassing the onset of IA2BC. T2 (Time 2) separates the 20-day period of abstinence. T3 (Time 3) corresponds to the phase of the model where the relapse phenomenon was observed. P, Postnatal age in days. EtOH, 20% ethanol.

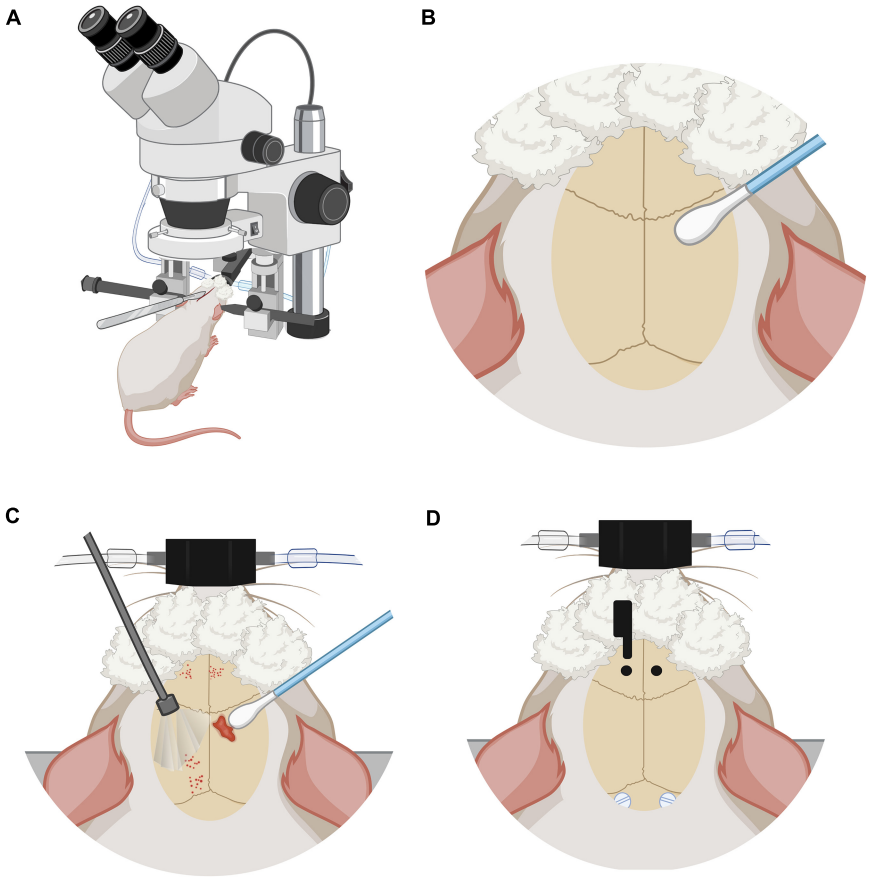

FIGURE 2
Anesthesia and stereotaxic surgery. **(A)** Rat placed in the stereotactic device. Rat under anesthesia vaporized with 3% isoflurane, on stereotaxic frame base with head fixation and a heated cushion under the body. **(B)** Preparation of the skull and control of local bleeding. Scalp incision on the midline following the direction of the mid-sagittal suture. **(C)** Curettage of skull aponeurosis and cleaning with swabs. **(D)** Coordinate marking of implantation coordinates of nylon screws and carbon electrodes under the microscope, directed by stereotaxic frame tower. Trepans on the skull are the entry site for the cortical implantation of the electrodes. Also visible are the nylon screws that are placed to keep the fibers fixed to the skull and maintain their chronicity.

subcutaneously at < 7 mg/kg, at the zone where the first incision would be made. The rats were injected with intramuscular meloxicam at 0.3 ml/kg to reduce intraoperative inflammation.

Stereotaxic procedure (∼1 h 30 min)

Once in deep anesthesia, the maintenance dose was modified from an average of 1–1.5%. A midline scalp incision of approximately 2 cm was made using a #20 scalpel blade (**Figure 2A**). The incision starts posterior to the line of the eyes. Bregma and lambda bony landmarks were exposed. Then the skin was moved to the sides with a self-retaining retractor. A peristome was used to separate the periosteum from the cranium bone. Next, hydrogen peroxide was used to achieve hemostasis with the help of cotton swabs. The importance of this step was to make sure that there was no bleeding and to dry the bone as much as possible (**Figure 2B**). With the scalpel blade, superficial cuts on the cranium bone were drawn and later washed with saline solution and hydrogen peroxide. Once the cranium was dry and there was no apparent bleeding, one drop of N-butyl 2-cyanoacrylate glue was applied to the exposed surface (**Figure 2C**).

Electrodes placement

Using the tip of the tower of the stereotaxic frame, electrodes were placed with Micropore breathable paper tape. Lambda and bregma bony landmarks were measured with the help of the tip of the electrodes and made the adjustment of ≤ 0.1 mm of a difference between both bony marks. Parallel to lambda, about half a centimeter from the midline, 2 mm diameter circles were marked to place plastic screws (P1tec, Roanoke VA, USA #0-80 × 3/32N). Subsequently, trepans were made to place the screws. Bleeding control was done with sterile 0.9% saline and cotton-tip applicators (**Figure 2D**). Finally, the position of the screws was sealed with adhesive luting cement (C&B-Metabond®).

Stereotaxic coordinates

Under the sight of a surgical microscope, a dental drill was used to make one-millimeter diameter holes bilaterally into the skull at the prelimbic cortex (PrL) (Paxinos and Watson, 2006) (Bregma 3.2 AP, 0.4 ML, 3.7 DV) or "area 32" (Paxinos and Watson, 2013). The electrodes were placed carefully and slowly, acquiring the DV coordinate 1 μm at a time. Once in place, they were sealed in position with adhesive luting cement, and a layer of resin was applied around and between all the arrays and screws to create a strong head cap fixed to the skull. Once the edges are smoothed and dried, simple stitches with nylon 3–0 closed the wound and left exposed the electrodes' extracranial fiber.

Postoperative care

Before the rat was removed from the stereotaxic apparatus, the vaporized anesthesia was stopped, but the oxygen supply was kept until spontaneous movement appeared. Meanwhile, to manage pain relief, and inflammation, meloxicam (0.3 ml/kg) was intramuscularly injected. A nitrofurazone ointment was applied along the wound, and 1 ml of saline 0.9% solution was injected between shoulder blades to maintain the electrolyte balance. The eyes were cleaned and artificial tears were applied once again. When the rat awoke, it was returned to a clean cage, and the bottom of the cage was covered with paper towels to prevent choking or ingestion of the bedding. Each rat was housed individually in cages and monitored closely for 7–10 days after the surgery. If active bleeding was detected, reddened skin, or any signs of discomfort, the nitrofurazone ointment was applied up to 3 times a day. If not, one application per day for 3 days was enough to facilitate healthy scar formation. Four rats out of 12 required wound care three times a day for 3 days, after that the healing process progressed smoothly.

Stimulation

Between P120 and P132, we began the stimulation protocol (**Figure 3**) during 10 sessions of 10 min for 10 consecutive days with 300 pulses (duration = 0.2 ms, intensity = 400 μA) at 20 Hz in 10 pulses per train of 2 s, and an inter-train interval of 20 s (**Figure 4**; Levy et al., 2007; Gersner et al., 2010). Stimulation was applied by means of GRASS S48 Square Pulse Stimulation connected to a GRASS stimulus isolation unit (SIU) and using metal alligators clips insulated exteriorly with Plasti Dip® and welded to flexible electronic cable 20 AWG. Each rat remained in its individual housing and was habituated for 10 days, prior to treatment, to the connection with the alligator clips.

Just before being implanted intraoperatively, the electrodes were checked for conduction and verified with a voltmeter. Likewise, the length of the electrode was measured to determine that it preserved its integrity. As in the work of Olds and Milner (1954), the rats were in free movement, the stimulation region was related to the reward system, and given the intensity as well as the inter-train interval and the shape of the pulses, no visible locomotor impairment was expected, such as convulsions, tremors and gait deficiencies (Tehovnik, 1995). The above was qualitatively verified by the experimenter. None of the 12 rats reported in this experiment presented such side effects. It was reported that on average in the first 2 sessions of real stimulation, the 6 rats of the group showed interruption of exploratory, grooming, and sniffing behavior, remaining immobile for an average of 3 s aligned to the stimulation train. After that, only at the beginning of the stimulation session did they show this behavior throughout the rest of the sessions.

Magnetic resonance imaging

MRI scanning was done at the Resonance Unit for Rodents and other Animals (URRA), Laboratorio Nacional de

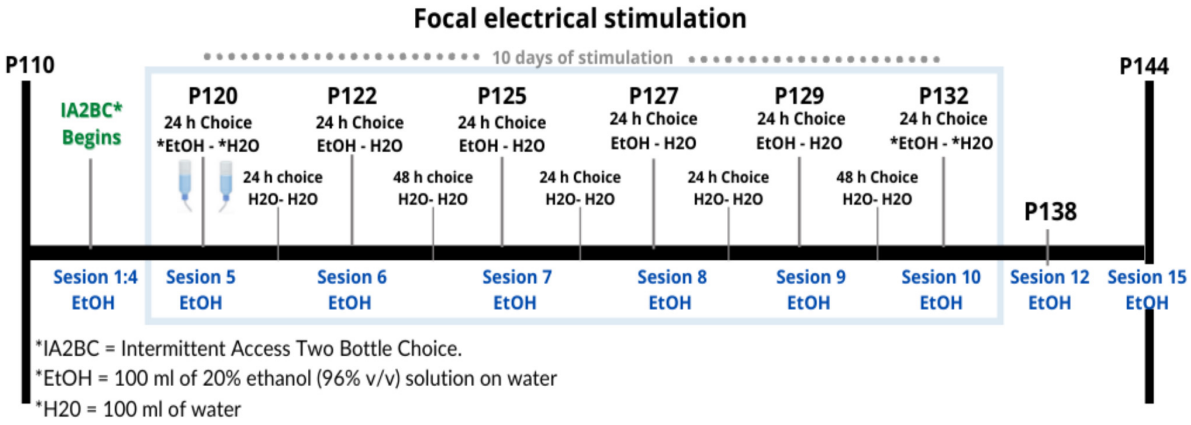

FIGURE 3
Timing of electrical stimulation and IA2BC during Time 3. Design of the schedule for repetitive focal electrical stimulation consisting of 10 days with a daily session of 10 min, this period is shown within the blue rectangle between days 120 and 132 of the age of the rat. In total there were 15 sessions where there was a bottle of water and a bottle of alcohol (EtOH-H_2O) to choose to drink, shown in blue. Between each of these sessions, they were offered two bottles of water (H_2O-H_2O).

FIGURE 4
Electrical stimulation design. With the parameters of 300 pulses (duration = 0.2 ms, intensity = 400 µA) high frequency of 20 Hz, in trains of 10 pulses every 2 s with an inter-train interval of 20 s. After the choice of the carbon electrode, the research protocol was carried out for 10 consecutive days for 10 min (Levy et al., 2007; Gersner et al., 2010; Moshe et al., 2016).

Imagenología por Resonancia Magnética (LANIREM) at the Instituto de Neurobiología, UNAM campus Juriquilla, located in Querétaro, Qro, Mexico. Before the acquisition, rats were injected subcutaneously with dexmedetomidine 0.012 mg/kg (Sirmpilatze et al., 2019). During imaging, rats were anesthetized with vaporized isoflurane 5% at induction and 0.5% in a 50/50 mixture of oxygen and vaporized anesthesia. Image acquisition was conducted using a 7T Bruker Pharmascan (Bruker Pharmasan 70/16, US) with a 2 × 2 surface coil and acquired using Paravision 6.0.1. A 3D FLASH sequence T2w with 2 repetitions TR = 30.76 ms, TE = 5 ms, flip angle = 10°, and FOV = 25.6 × 19.098 × 25.6 mm and an isometric voxel of 160 microns, and GE EPI sequences were: (1) TR = 1,000 ms, TE = 20 ms, flip angle = 60, slice thickness = 1 mm, FOV = 30 × 30, number of slices = 24, volumes = 600 and axial as primary slice orientation, (2) TR = 1,800 ms, TE = 20 ms, flip angle = 60, slice thickness = 0.75 mm FOV = 30 × 30, number of slices = 32, volumes = 334 and axial as primary slice orientation. Both sequences were performed at P110 to verify the location of the electrodes and at P144, at the end of the stimulation protocol. All images were converted from Bruker format to nifti using the brkraw tool v0.3.3 (Lee et al., 2020). Anatomical images were preprocessed using an in-house pipeline developed by Gabriel *A. Devenyi* based on MINC-toolkit-v2 and ANTs which performed the following steps: intensity normalization, center image, denoising, and registering in LSQ6 alignment.[1] The preprocessing in this manuscript was done for better visualization. Functional images were preprocessed using RABIES software.[2] A quality control (QC) of the acquisitions was performed based on considering spatial resolution and contrast, artifacts, and SNR.

1 https://github.com/psilantrolab/Documentation/wiki/Preprocessing-Rat-Structural-in~vivo

2 https://github.com/CoBrALab/RABIES

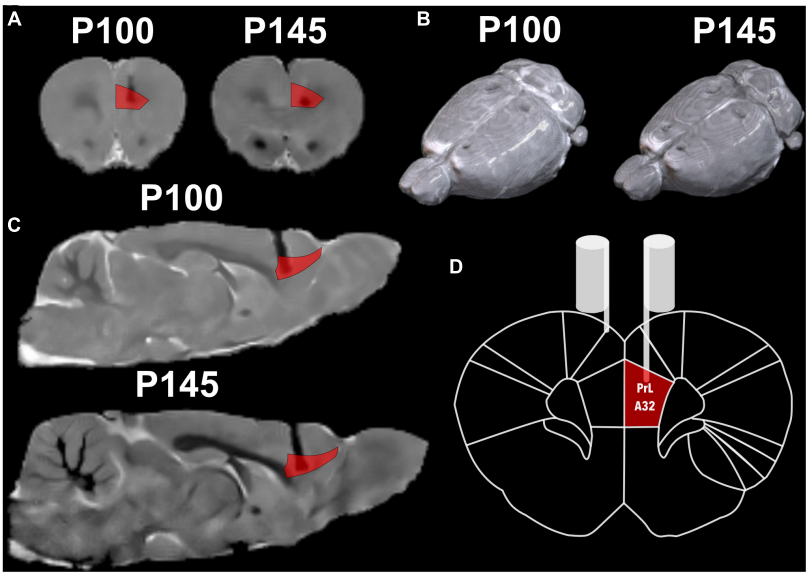

FIGURE 5
Structural MRI with a reference atlas (Paxinos and Watson, 2006) of Rat 2. **(A)** Coronal slide with atlas region PrL/A32 (prelimbic) region in red and the shadow of the electrode. **(B)** Render of rat brain dorsal view with electrodes marks and posterior to lambda two fixation screws. **(C)** Sagittal slide with atlas region PrL/A32 in red. **(D)** Schematic coronal slide from the atlas, with the left electrode on PrL/A32 and the right on the surface of the cortex.

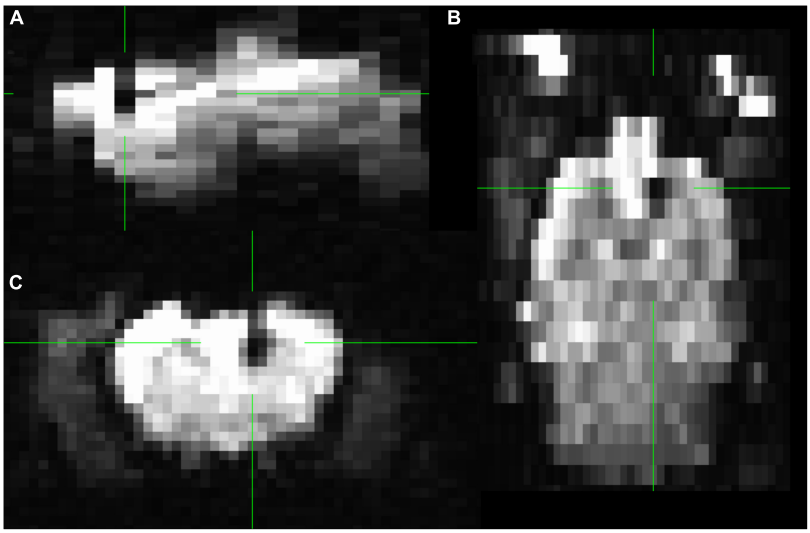

FIGURE 6
Functional MRI of rat 2. In the middle of the green markers, the black shadow of the artifact induced by the carbon fiber is seen, without affecting the areas surrounding the electrode. Slices **(A)** sagittal **(B)** axial **(C)** coronal. Group GE EPI sagittal view is shown in **Supplementary Figure 3**.

Results

Twelve rats conserved both stimulation electrodes and remained available for the stimulation protocol for the longitudinal follow-up. To ensure the feasibility of the electrode, we measured electrode resistance between sessions, and all the electrodes held their original values (2–8 kω). Additionally, MRI, as a non-invasive technique, was chosen for longitudinal monitoring, and the resulting images were anatomically compared to the Paxinos atlas (Paxinos and Watson, 2006; **Figure 5**). There were difficulties in adjusting the 2 × 2 surface coil in the male rats' heads, hence to their body size plus the

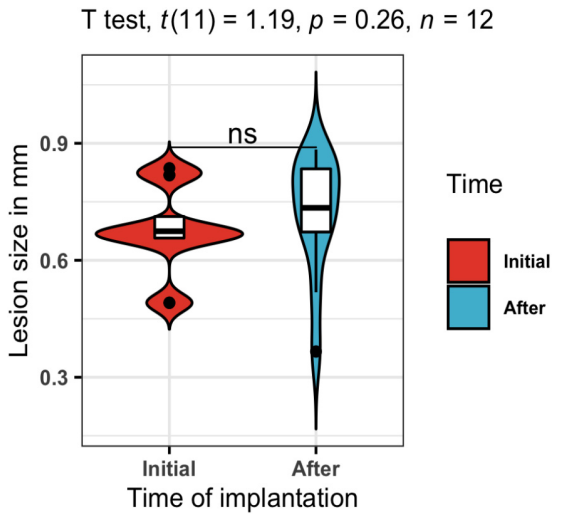

FIGURE 7
Lesion size in mm. A *t*-test was calculated to compare the lesion size at 2 points right after the surgical implantation P100 in blue (Initial) and at the end of the stimulation protocol P145 in red (After). The average lesion size of the twelve rats was not significantly increased after the treatment (stimulation) application, $t(11) = 1.19$, $p = 0.26$, $d = 0.344$.

tip of the extracranial portion of the electrode, with this the acquisition resulted in a non-orthogonal position that later required an adjustment.

No 3D FLASH and GE-EPI acquisition of any rat at P100 and P145 were discarded after QC. On the GE-EPI sequence, the electrode is shown as a black area, and there was no geometric distortion around the implantation (**Figure 6**).

Regarding the susceptibility artifact of the electrode in the T2w, the contrast of the area where the intracranial portion of the electrode was manifested as a black area. Around the electrode area, there were no displacement artifacts, geometric distortion, or signal loss (Hargreaves et al., 2011; **Supplementary Figure 4**). One of our main objectives was to prove that our electrodes would cause only a small lesion in the stimulation area, and with minimal inflammation. In the longitudinal follow-up of a rat in **Figure 5**, there were no structural changes measured with the 3D FLASH sequence, the measure of the major diameter in the landing area of the tip of the electrode was performed in all rats to calculate the mean and standard deviation of the lesions sizes. To corroborate the previous, we measured the lesion size at P100 and P145 of all twelve rats. A paired *T*-test was calculated to compare the lesion size at 2 points right after the surgical implantation P100 (Initial) (mean = 0.677 mm, *SD* = 0.111 mm) and at the end of the stimulation protocol P145 (After) (mean = 0.721 mm, *SD* = 0.152 mm). The average lesion size of the 12 rats was not significantly increased after the treatment (stimulation) application, $t(11) = 1.19$ $p = 0.26$, $d = 0.344$ (**Figure 7**).

Figure 8 shows the results on ethanol intake at all stages of the experiment (T1, T2, T3). The beginning of T3 is also the relapse phase, and all the rats increased their intake compared to the baseline. After the stimulation, there were no group differences in alcohol consumption. However, the individual plots showed high variability (**Supplementary Table 1**) in individual consumption. Two rats in the sham group, as well as 2 in the active group, reduced their ethanol consumption, while 2 rats in the active group and 1 in the sham group maintained their consumption stable. Two rats in the active group and 3 rats in the sham group increased their ethanol consumption after stimulation. Overall, our results show that 66% of the rats in the active group had a positive effect of stimulation/surgery, while 50% of the rats in the sham group also showed a reduction in consumption. A non-parametric method to compare means, Wilcoxon test, was used to assess the alcohol consumption of the sham and active stimulation groups at the times of pre-stimulation (PreStim) and post-stimulation (PoStim). For the active stimulation group, the median ethanol intake PreStim was 3.59 g/kg/24 h (IQR = 3), and PoStim 3.73 g/kg/24 h (IQR = 3.34) the differences were not significant $p = 0.97$ $r = 0.0687$ (**Supplementary Figure 5A**). The median ethanol intake PreStim for the sham stimulation group was 3.77 g/kg/24 h (IQR = 3.86), whereas the median PoStim was 3.27 g/kg/24 h (IQR = 3.40). The Wilcoxon test showed that the difference was not significant $p = 0.77$, with effect size $r = 0.0395$ (**Supplementary Figure 5B**).

Discussion

Without a doubt it was challenging to assemble electrodes that met the requirements (Geddes and Roeder, 2003), of being: (1) MRI compatible, (2) able to perform focal electrical stimulation, and (3) well accepted by the body chronically. For future studies, we intend to demonstrate that they are capable of recording electrophysiological signals as LFPs, based on the report that they maintained their integrity throughout our study. Here we describe a method for the construction of carbon monopolar electrodes (Gallino et al., 2019) and propose their use for focal electrical stimulation as an intervention in a preclinical model of AUD (McBride and Li, 1998). Because of the study design, treatment follow-up did not allow us to draw a subsample to cohort and assess electrode viability, so it was monitored by electrical resistance and MRI. From the above we obtained that the rats that received active stimulation expressed immobilization behavior on average during the first 2 sessions, interrupting their exploratory, grooming, and sniffing behavior for an average of 3 s aligned with the stimulation train, similar to what was previously reported as behavioral evidence of the effect of electrical stimulation (Olds and Milner, 1954). The importance of the intended intervention was to stimulate a brain region that is thought to be the

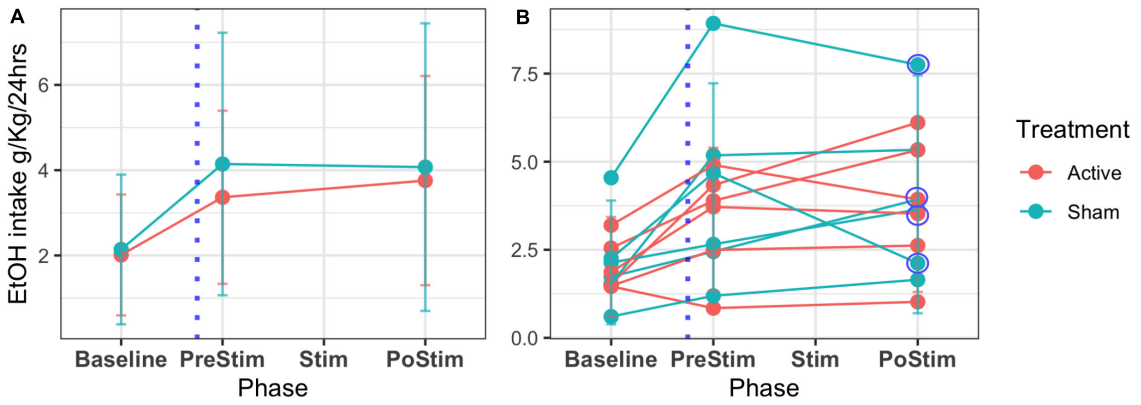

FIGURE 8
Mean EtOH intake and SD across phases of follow-up of the 12 rats. T1 or IA2BC development (baseline) is the 45 days where alcohol is offered in an elective model. The time for the surgery is marked with a blue dotted line (T2 or abstinence). T3 (relapse) comprehends a period before the stimulation treatment (PreStim) and the application of treatment under two conditions: sham/active (Stim) and a period of follow-up after the treatment (PostStim). **(A)** Mean and SD of the groups' intake. **(B)** Individual mean ethanol intake and SD. Circled are the decreasing intakes between PreStim and PostStim evaluation of four rats.

human homolog of the dorsolateral prefrontal cortex, which is the most commonly stimulated target region in rTMS. This region, the prelimbic cortex (PrL) or area 32, is an essential hub of the mesocorticolimbic network (Koob, 2013). The nucleus accumbens (NAc) and prefrontal cortex (PFC) PrL, or medial PFC in rats (Laubach et al., 2018) are brain regions that promise to be therapeutic targets for SUDs. Previously, implanted stimulation methods in PFC have decreased alcohol consumption in humans (Voges et al., 2013) and cocaine in rats (Levy et al., 2007). In this work, we stimulated rats that were previously exposed to IA2BC, and we found that four subjects with the greatest consumption of ethanol, decreased their intake in comparison to their consumption at the beginning of relapse or T3. To explain why both sham and active conditions on those four rats had an effect, we agree with Chakravarty et al. (2016) findings, who proposed that there were changes at the level of synaptic connections in both active and sham stimulation. In their study, active stimulation revealed a remodeling of the structure of the vasculature so that the diameter of the vessels increased. They also found increased volume in the subjects who received stimulation in remote regions, suggesting that neuroanatomical rearrangement also occurs in remote regions connected across multiple synapses (Stone et al., 2011). For future studies, we will analyze the functional and structural effects of stimulation in this AUD model (Bashir et al., 2011), and apply it to other SUD models.

Lastly, the model and the stimulation protocol have limitations. Firstly the sample acquisition time is 124 days, secondly the IA2BC is performed in conditions of reverse cycle (dark/light) for that a room that meets this criteria is required and thirdly, as previously described by Carnicella et al. (2014), only 30–40% of the rats in the IA2BC model become high drinkers. All of the above conditions interfere with the sample size, and it is due to this that possibly no differences were established, taking into account the tendencies to decrease the consumption of the subjects in the groups with higher alcohol. Nevertheless, we are working on further experiments to increase the sample size.

In summary, this work describes chronic, MRI-compatible, carbon electrode implantation, and the use of focal electrical stimulation on a preclinical model of AUD with a longitudinal follow-up. Our findings suggest the possibility of decreasing ethanol intake after the stimulation protocol. Further work is needed to elucidate the effects of stimulation in AUD and other SUDs.

Data availability statement

The raw data supporting the conclusions of this article will be made available by the authors, without undue reservation.

Ethics statement

The animal study was reviewed and approved by Comité de Bioética del Instituto de Neurobiología UNAM Campus Juriquilla, México.

Author contributions

AL-C, GR-P, and EG-V contributed to the conception and design of the study. AL-C performed the surgeries and creation

of the electrodes, performed data analysis, visualizations, and wrote the first draft of the manuscript. AL-C and DA-V worked on the main ethanol model and acquired MRI data. AL-C and EG-V wrote sections of the manuscript. EG-V was in charge of the funding of the research. All authors contributed to manuscript revision, read, and approved the submitted version.

Funding

This study was supported by Programa de Apoyo a Proyectos de Investigación e Innovación Tecnológica, Dirección General de Asuntos del Personal Académico (PAPIIT) (grants IA202120 and PAPIIT IA201622). AL-C received a CONACyT fellowship (1003251).

Acknowledgments

We would like to acknowledge the vivarium of Instituto de Neurobiología (Maria Antonieta Carbajo Mata, Alejandra Castilla León, and MVZ Martin García Servín), and the National Laboratory for Magnetic Resonance Imaging, particularly Juan Ortiz-Retana for technical assistance. We greatly acknowledge the technical support of Rafael Olivares. We thank M.S. Alfonso Fajardo-Valdez for his assistance in the MRI visualization. We thank BSc. Diego Ortuzar for the grammatical revision of the manuscript, and Pavel E. Rueda-Orozco for his recommendations regarding the surgery. **Figure 2** and elements from **Figure 1** were created with BioRender.com. Finally, we would like to thank Daniel Gallino for his feedback and support with the electrode construction.

Conflict of interest

The authors declare that the research was conducted in the absence of any commercial or financial relationships that could be construed as a potential conflict of interest.

Publisher's note

All claims expressed in this article are solely those of the authors and do not necessarily represent those of their affiliated organizations, or those of the publisher, the editors and the reviewers. Any product that may be evaluated in this article, or claim that may be made by its manufacturer, is not guaranteed or endorsed by the publisher.

Supplementary material

The Supplementary Material for this article can be found online at: https://www.frontiersin.org/articles/10.3389/fnins.2022.945594/full#supplementary-material

References

Ankeny, R. A., Sabina, L., Nicole, C. N., and Ramsden, E. (2014). Making Organisms Model Human Behavior: Situated Models in North-American Alcohol Research, since 1950. *Sci. Context* 27, 485–509. doi: 10.1017/s0269889714000155

Aydin, O., Pinar, U. A., and Arslan, A. (2019). Development of Neuroimaging-Based Biomarkers in Psychiatry. *Adv. Exp. Med. Biol.* 1192, 159–195.

Bashir, S., Edwards, D., and Pascual-Leone, A. (2011). Neuronavigation Increases the Physiologic and Behavioral Effects of Low-Frequency rTMS of Primary Motor Cortex in Healthy Subjects. *Brain Topogr.* 24, 54–64.

Carnicella, S., Ron, D., and Barak, S. (2014). Intermittent Ethanol Access Schedule in Rats as a Preclinical Model of Alcohol Abuse. *Alcohol* 48, 243–252. doi: 10.1016/j.alcohol.2014.01.006

Chakravarty, M. M., Hamani, C., Canabal, A. M., Ellegood, J., Laliberté, C., José, N., et al. (2016). Deep Brain Stimulation of the Ventromedial Prefrontal Cortex Causes Reorganization of Neuronal Processes and Vasculature. *NeuroImage* 125, 422–427. doi: 10.1016/j.neuroimage.2015.10.049

Chuapoco, M. R., Choy, M., Schmid, F., Ben, A. D., Lee, H. J., and Lee, J. H. (2019). Carbon Monofilament Electrodes for Unit Recording and Functional MRI in Same Subjects. *NeuroImage* 186, 806–816. doi: 10.1016/j.neuroimage.2018.10.082

Derksen, M., Rhemrev, V., van der Veer, M., Jolink, L., Zuidinga, B., Mulder, T., et al. (2021). Animal studies in clinical MRI scanners: A custom setup for combined fMRI and deep-brain stimulation in awake rats. *J. Neurosci. Methods* 360:109240. doi: 10.1016/j.jneumeth.2021.109240

Diana, M., Raij, T., Melis, M., Nummenmaa, A., Leggio, L., and Bonci, A. (2017). Rehabilitating the Addicted Brain with Transcranial Magnetic Stimulation. *Nat. Rev. Neurosci.* 18, 685–693.

Dunn, J. F., Tuor, U. I, Kmech, J., Young, N. A., Henderson, A. K., Jackson, J. C., et al. (2009). Functional brain mapping at 9.4 T using a new MRI-compatible electrode chronically implanted in rats. *Magn. Reson. Med.* 61, 222–228. doi: 10.1002/mrm.21803

Edwards, C. A., Kouzani, A., Lee, K. H., and Ross, E. K. (2017). Neurostimulation Devices for the Treatment of Neurologic Disorders. *Mayo Clin. Proc. Mayo Clin.* 92, 1427–1444.

Gallino, D., Devenyi, G. A., Germann, J., Guma, E., Anastassiadis, C., and Chakravarty, M. M. (2019). Longitudinal Assessment of the Neuroanatomical Consequences of Deep Brain Stimulation: Application of Fornical DBS in an Alzheimer's Mouse Model. *Brain Res* 1715:213. doi: 10.1016/j.brainres.2019.03.030

Geddes, L. A., and Roeder, R. (2003). Criteria for the Selection of Materials for Implanted Electrodes. *Ann. Biomed. Eng.* 31, 879–890.

Gersner, R., Kravetz, E., Levit, O., and Zangen, A. (2010). P.1.010 Repeated Brain Stimulation Affects Markers for Neuroplasticity: Differential Outcomes in Anaesthetized and Awake Animals. *Eur Neuropsychopharmacol.* 20:S10–S11. doi: 10.1016/s0924-977x(10)70013-4

Guide for the Care and Use of Laboratory Animals (1996). *Institute of laboratory animal resources, commission on life sciences, national research council.*

Hargreaves, B., Worters, P. W., Pauly, K. B., Pauly, J. M., Koch, K. M., and Gold, G. E. (2011). Metal induced artifacts in MRI. *AJR. Am. J. Roentgenol.* 197, 547.

Joshi-Imre, A., Bryan, J. B., Abbott, J., Kanneganti, A., Rihani, R., Chakraborty, B., et al. (2019). Chronic Recording and Electrochemical Performance of Amorphous Silicon Carbide-Coated Utah Electrode Arrays Implanted in Rat Motor Cortex. *J. Neural Eng.* 16:046006. doi: 10.1088/1741-2552/ab1bc8

Klooster, D. C. W., de Louw, A. J. A., Aldenkamp, A. P., Besseling, R. M. H., Mestrom, R. M. C., Carrette, S., et al. (2016). Technical Aspects of Neurostimulation: Focus on Equipment, Electric Field Modeling, and Stimulation Protocols. *Neurosci. Biobehav. Rev.* 65, 113–141. doi: 10.1016/j.neubiorev.2016.02.016

Koob, G. F. (2013). Neurobiological Mechanisms of Drug Addiction. *Biol. Res. Addict.* 304–314. doi: 10.1016/b978-0-12-398335-0.00001-7

Krames, E. S., Peckham, P. H., Rezai, A., and Aboelsaad, F. (2009). "What Is Neuromodulation?," in *Neuromodulation*, eds H. Knotkova and D. Rasche (Amsterdam, NL: Elsevier), 3–8.

Laubach, M., Amarante, L. M., Swanson, K., and White, S. R. (2018). What, If Anything, Is Rodent Prefrontal Cortex? *eNeuro* 5, ENEURO.315–ENEURO.318. doi: 10.1523/ENEURO.0315-18.2018

Lee, S. H., Ban, W., and Shih, Y. Y. (2020). *BrkRaw/bruker: BrkRaw v0.3.3*. doi: 10.5281/zenodo.3877179

Levy, D., Shabat-Simon, M., Shalev, U., Barnea-Ygael, N., Cooper, A., and Zangen, A. (2007). "Repeated Electrical Stimulation of Reward-Related Brain Regions Affects Cocaine but Not 'Natural' Reinforcement. *J. Neurosci.* 27, 14179–14189. doi: 10.1523/JNEUROSCI.4477-07.2007

Matsumiya, L. C., Robert, E. S., Susana, G. S., Tabaka, J. M., Wieskopf, J. S., Oliver, D. K., et al. (2012). Using the Mouse Grimace Scale to Reevaluate the Efficacy of Postoperative Analgesics in Laboratory Mice. *J. Am. Assoc. Lab. Anim. Sci.* 51, 42–49.

McBride, W. J., and Li, T. K. (1998). Animal Models of Alcoholism: Neurobiology of High Alcohol-Drinking Behavior in Rodents. *Crit. Rev. Neurobiol.* 12, 339–369.

Mexicana, Norma Oficial (1999). "NOM-062-ZOO-1999," in *Technical specifications for production, care and use of lab animals.*

Morimoto, T., Yasuhara, T., Kameda, M., Baba, T., Kuramoto, S., Kondo, A., et al. (2011). Striatal stimulation nurtures endogenous neurogenesis and angiogenesis in chronic-phase ischemic stroke rats. *Cell Transplant.* 20, 1049–1064. doi: 10.3727/096368910X544915

Moshe, H., Gal, R., Barnea-Ygael, N., Gulevsky, T., Alyagon, U., and Zangen, A. (2016). Prelimbic stimulation ameliorates depressive-like behaviors and increases regional BDNF expression in a novel drug-resistant animal model of depression. *Brain Stimul.* 9, 243–250.

National Research Council, Division on Earth and Life Studies, Institute for Laboratory Animal Research, and Committee for the Update of the Guide for the Care and Use of Laboratory Animals. (2011). *Guide for the Care and Use of Laboratory Animals*, Eighth Edn. Washington, DC: National Academies Press.

Olds, J., and Milner, P. (1954). Positive reinforcement produced by electrical stimulation of septal area and other regions of rat brain. *J. Comp. Physiol. Psychol.* 47, 419–427. doi: 10.1037/h0058775

Paxinos, G., and Watson, C. (2006). *The Rat Brain in Stereotaxic Coordinates: Hard Cover Edition*. Amsterdam, NY: Elsevier.

Paxinos, G., and Watson, C. (2013). *The Rat Brain in Stereotaxic Coordinates*. Amsterdam, NL: Elsevier Science.

Redpath, T. W. (1998). Signal-to-Noise Ratio in MRI. *Br. J. Radiol.* 71, 704–707.

Rigalli, A., and Di Loreto, V. (2016). *Experimental Surgical Models in the Laboratory Rat*. Boca Raton: CRC press.

Santana-Chávez, G., Rodriguez-Moreno, P., R Olivares-Moreno, M. L. H., Moreno-López, Y., and Rojas-Piloni, G. (2020). Operant Conditioning Paradigm for Juxtacellular Recordings in Functionally Identified Cortical Neurons during Motor Execution in Head-Fixed Rats. *J. Neurosci. Methods* 329:108454. doi: 10.1016/j.jneumeth.2019.108454

Silva, A. C., and Bock, N. A. (2008). Manganese-Enhanced MRI: An Exceptional Tool in Translational Neuroimaging. *Schizophrenia Bull.* 34, 595–604. doi: 10.1093/schbul/sbn056

Simms, J. A., Pia Steensland, B. M., Kenneth, E., Abernathy, L. J., Chandler, R. W., and Selena, E. B. (2008). Intermittent Access to 20% Ethanol Induces High Ethanol Consumption in Long-Evans and Wistar Rats. *Alcohol. Clin. Exp. Res.* 32, 1816–1823.

Sirmpilatze, N., Jürgen, B., and Susann, B. (2019). Temporal Stability of fMRI in Medetomidine-Anesthetized Rats. *Sci. Rep.* 9:16673. doi: 10.1038/s41598-019-53144-y

Spanagel, R. (2017). Animal Models of Addiction. *Dial. Clin. Neurosci.* 19, 247–258.

Stone, S. S. D., Cátia, M. T., Devito, L. M., Sheena, A. J., Andres, M. L., and Paul, W. F. (2011). Stimulation of Entorhinal Cortex Promotes Adult Neurogenesis and Facilitates Spatial Memory. *J. Neurosci.* 31, 13469–13484.

Tehovnik, E. J. (1995). The dorsomedial frontal cortex: eye and forelimb fields. *Behav. Brain Res.* 67.2, 147–163.

Van De Berg, R., Guinand, N., Nguyen, T. K., Ranieri, M., Cavuscens, S., Guyot, J. P., et al. (2015). The vestibular implant: frequency-dependency of the electrically evoked vestibulo-ocular reflex in humans. *Front. Syst. Neurosci.* 8, 255.

Voges, J., Ulf, M., Brnhard, B., Thomas, M., and Heinze, H. J. (2013). Deep Brain Stimulation Surgery for Alcohol Addiction. *World Neurosurg.* 80: S28.e21-31.

Wise, R. A. (1973). Voluntary Ethanol Intake in Rats Following Exposure to Ethanol on Various Schedules. *Psychopharmacologia* 29, 203–210.

Young, C. K., Brown, A. R., Robinson, J. H., Tuor, U. I., Dunn, J. F., Bland, B. H., et al. (2011). Functional MRI response and correlated electrophysiological changes during posterior hypothalamic nucleus deep brain stimulation. *Neuroimage* 56, 35–44. doi: 10.1016/j.neuroimage.2011.02.023

Zhao, Q., Zhang, K., Zhu, S., Xu, H., Cao, D., Zhao, L., et al. (2019). Review on the Electrical Resistance/Conductivity of Carbon Fiber Reinforced Polymer. *NATO Adv. Sci. Institutes Series E* 9:2390.

frontiers | Frontiers in Neuroscience

TYPE Original Research
PUBLISHED 17 November 2022
DOI 10.3389/fnins.2022.1032098

OPEN ACCESS

EDITED BY
Georgios A. Keliris,
University of Antwerp, Belgium

REVIEWED BY
Giuseppe Barisano,
Stanford University, United States
Liming Hsu,
University of North Carolina at Chapel Hill, United States

*CORRESPONDENCE
Hongguang Bao
hongguang_bao@hotmail.com

†These authors have contributed equally to this work and share first authorship

SPECIALTY SECTION
This article was submitted to Brain Imaging Methods, a section of the journal Frontiers in Neuroscience

RECEIVED 30 August 2022
ACCEPTED 31 October 2022
PUBLISHED 17 November 2022

CITATION
Li H, Liao H, Zhang C, Xu Y, Xu X, Chen Y, Song S, Li Q, Si Y and Bao H (2022) Disrupted metabolic and spontaneous neuronal activity of hippocampus in sepsis associated encephalopathy rats: A study combining magnetic resonance spectroscopy and resting-state functional magnetic resonance imaging.
Front. Neurosci. 16:1032098.
doi: 10.3389/fnins.2022.1032098

Disrupted metabolic and spontaneous neuronal activity of hippocampus in sepsis associated encephalopathy rats: A study combining magnetic resonance spectroscopy and resting-state functional magnetic resonance imaging

Haojia Li[1†], Hongsen Liao[1†], Chen Zhang[1], Yajie Xu[1], Xiaomin Xu[2], Yuchen Chen[2], Shaozheng Song[3], Qian Li[4], Yanna Si[1] and Hongguang Bao[1*]

[1]Department of Anesthesiology, Nanjing First Hospital, Nanjing Medical University, Nanjing, Jiangsu, China, [2]Department of Radiology, Nanjing First Hospital Nanjing Medical University, Nanjing, Jiangsu, China, [3]Department of Basic Medicine, School of Health and Nursing, Wuxi Taihu University, Wuxi, Jiangsu, China, [4]Department of Anesthesiology, Jiangning Hospital Affiliated to Nanjing Medical University, Nanjing, Jiangsu, China

Background: The diagnosis of sepsis associated encephalopathy (SAE) remains challenging in clinical settings because of a lack of specific biomarkers. Functional magnetic resonance imaging (fMRI) and proton magnetic resonance spectroscopy (1H-MRS) can be used to aid in the diagnosis of cognition related diseases. This study investigated changes in functional activities and brain metabolites in the hippocampus in SAE rats by fMRI and 1H-MRS.

Materials and methods: Sepsis associated encephalopathy rats underwent cecal ligation and perforation (CLP) surgery. The Morris water maze (MWM) test was then used to evaluate cognitive function. Resting state-fMRI and 1H-MRS scanning were performed 7 and 14 days after CLP surgery to reveal spontaneous neuronal activity and metabolite changes in the hippocampus. The amplitude of low-frequency fluctuation (ALFF) was used to evaluate spontaneous neuronal activity in the hippocampus. Creatine (Cr), Myo-inositol (mI), and glutamine/glutamate (Glx) levels were measured with 1H-MRS scanning. Immunofluorescence and levels of interleukin (IL)-1β, interleukin (IL)-6, and C-reactive protein (CRP) in the hippocampus were additionally detected to evaluate microglial mediated inflammatory responses. Statistical analysis was performed to evaluate correlations between hippocampal metabolism and behavioral findings.

Results: Cecal ligation and perforation treated rats exhibited impaired learning and memory function in the MWM test at days 7 and 14. Elevation of IL-1β in the hippocampus, as well as immunofluorescence results, confirmed severe neuro inflammation in the hippocampus in SAE rats. Compared with the sham group, the ALFF of the right CA-1 area of the hippocampus was higher at day 7after CLP surgery. The Glx/Cr and mI/Cr ratios were enhanced at day 7 after CLP surgery and slightly lower at day 14 after CLP surgery. The ALFF value, and Glx/Cr and mI/Cr ratios were negatively correlated with time spent in the target quadrant in the MWM test.

Conclusion: Spontaneous neuronal activity and metabolites showed significant alterations in SAE rats. The elevated ALFF value, Glx/Cr ratio, and mI/Cr ratio in the hippocampus were positively associated with cognitive deficits. Changes in ALFF and metabolites in hippocampus may serve as potential neuroimaging biomarkers of cognitive disorders in patients with SAE.

KEYWORDS

cecal ligation and puncture (CLP), hydrogen proton magnetic resonance spectroscopy (1H-MRS), neural inflammation, resting-state functional magnetic resonance imaging (rs-fMRI), sepsis-associated encephalopathy (SAE)

Introduction

Sepsis-associated encephalopathy (SAE) is one of the most serious complications of sepsis characterized by delirium and cognitive dysfunction (Tauber et al., 2021). More than 50% of surviving patients with sepsis suffer from severe and long-term cognitive deficits (Chung et al., 2020). In general, neuroinflammation, metabolic disorders, and depressed spontaneous neuronal activity have been considered to be causative factors for cognitive impairment in SAE patients (Peng et al., 2021). Studies have shown that the levels of inflammatory cytokines, such as interleukin (IL)-1β, interleukin (IL)-6, and tumor necrosis factor α, increase significantly in the hippocampus of SAE rats, accompanied by microglial activation (Tauber et al., 2021). But the research in metabolites and excitability of neurons in SAE patients by non-invasive and objective methods was limited.

Recently, neuroimaging studies investigated brain functional and metabolic changes with functional magnetic resonance imaging (fMRI) and hydrogen proton magnetic resonance spectroscopy (1H-MRS) in various neurodegenerative diseases (Piersson et al., 2021). Resting-state fMRI (rs-fMRI) detected the blood oxygenation level dependent (BOLD) signal, and provided information on regional spontaneous neuronal activity with the amplitude of low-frequency fluctuation (ALFF), which is the most commonly used analysis method for fMRI (Zou et al., 2008; Huang et al., 2021). A decreased ALFF values in the right hippocampus was shown to be directly related to the deterioration cognitive function in mild cognitive impairment patients (Tao et al., 2019). However, more researches were needed to investigate the trends of ALFF value in hippocampus of SAE rats. Besides rs-fMRI imaging analysis, 1H-MRS has been shown to be an accurate tool for gaining insights into brain metabolic function. Metabolic alterations which were detected by 1H-MRS provide valuable information on cerebral diseases (Hsu et al., 2021). Myo-inositol (mI) indicated microglial-induced neuroinflammation in the brain (El-Abtah et al., 2022 Feb), while the increased concentration of glutamate/glutamine (Glx) was found in patients with hepatic encephalopathy (Kuan et al., 2021). To date, whether these metabolic alterations present in the hippocampus of SAE rats remains unclear. Further research is needed on whether these metabolic alterations are due to sepsis and can be correlated with cognitive related behaviors.

Since sepsis is a heterogeneous and complex pathology, *in vivo* models are valuable tools to explore its underlying mechanisms. The cecal ligation and puncture (CLP) surgery yields reliable outcomes of sepsis associated encephalopathy in rats (Gao et al., 2021). Previous studies have found that serious inflammation of the hippocampus lasted 15 days post CLP surgery, and that the result of cognitive related behavior tests performed 1–2 weeks post CLP surgery indicated a significant cognitive decline in SAE rats (Li et al., 2020). The hippocampus participates in mediating cognition and emotion. Our previous studies suggest that abnormal hippocampal inflammation is an essential pathogenic trait of SAE (Cai et al., 2021). Neuro inflammation in the hippocampus caused by SAE may lay the groundwork for the cognitive dysfunction. However, it remains unknown the relationship between neuro inflammation and metabolic alterations, as well as impairs cognitive function in SAE rats.

In the present study, we examined brain ALFF and metabolites changes in the hippocampus of SAE rates during 7–14 days post CLP surgery by rs-fMRI and1H-MRS. We further investigated the relationship between Morris water maze tests and rs-fMRI results at 7 and 14 days post CLP surgery in SAE rats. The serum levels of IL-1β and IL-6, as well as immunofluorescence, were also analyzed at the same time points. The objective of this research is to investigate the features of ALFF and metabolite changes in hippocampus of SAE rats, and to further explore its relationship with impairment of cognitive functions in SAE rats. Our findings may provide potential reference for comprehension of the neural mechanisms underlying SAE.

Materials and methods

Animal model

All animal procedures were approved by the Institutional Animal Care and Use Committee of Nanjing Medical University (IACUC: 2103051; Animal Use Permit SYXK(Su)2020-0022). In total 24 adult male Sprague Dawley rats (Nanjing, Jiangsu Laboratory Animal Center, China; 8 weeks, 280–320 g) were divided into three groups, sham group, day 7 post CLP group and day 14 post CLP group. The room in which the rats were housed was maintained at 22°C with a 12-h light–dark cycle. The animals were treated humanely with free access to food and water with regard for alleviation of suffering.

For surgical procedures, rats were anesthetized by pentobarbital sodium at a dose of 35 mg/kg intraperitoneally (i.p.) according to previous research (Rittirsch et al., 2009). CLP surgery was performed on 16 rats to induce sepsis. Briefly, under aseptic conditions, a 3 cm midline laparotomy was performed to allow exposure of the cecum with adjoining intestine. The cecum was then ligated tightly with a 3.0 silk suture at its base under the ileocecal valve and punctured twice with a 22-gauge needle. The cecum was then gently squeezed to extrude a small amount of feces from the perforation site. The cecum was returned to the peritoneal cavity, and the laparotomy incision was closed with 4-0 polyglactin sutures. Following surgery, fluid losses were replenished by administration of 5 ml/100 g of warm (37°C) isotonic saline i.p., and the rats were placed in their cages. In the sham group, under aseptic conditions, only laparotomy was performed, and the cecum was neither ligated nor punctured. All animals displayed signs of encephalopathy at 24 h post CLP surgery (lethargy, mild ataxia, lack of spontaneous movement).

MRI acquisition

Following CLP surgery, all animals were subjected to MRI of their brain, 7 days and 14 days post-CLP surgery. MRI scans were performed with a 7 Tesla horizontal bore magnet (Bruker Biospec 7T/20 USR; Bruker, Karlsruhe, Germany). Accurately 2% isoflurane in oxygen and air was used to produce anesthesia. The rats were then placed in a prone posture on a small animal MRI scan bed and their heads were fixed with dental hooks and ear bars to reduce head movements. Throughout the scanning period, the degree of anesthesia was maintained by modulating the isoflurane concentration (2–2.5%) to preserve the respiration rate of 80–100 breaths per minute and oxygen saturation of 95–100%. Magnetic resonance scanning was started after the respiration, heart rate and saturation of rats were observed to be stable. Fast spin-echo T2 weighted MR images were obtained for visualizing the structure of the brains with the following parameters: slice = 25, repetition time (TR)/echo time (TE) = 3000/33 ms, FA = 90°, TA = 4 min 48 s, SI = 1.00/1.00 mm, FOV = 3.17/2.50 cm, image size = 256. Functional images were obtained using BOLD sequence, TR/TE = 2000 ms/25 ms, slices = 18, slice thickness = 1 mm, TA = 5 min, image size = 128 × 128, flip angle = 90°, repetition = 150, FOV = 28.80/18.00 mm, Image resolution = 128 × 128.

Resting-state functional magnetic resonance imaging data preprocessing and analysis

The first ten volumes of rs-fMRI data were discarded for MRI signaling to reach a steady state. Then, the images were realigned in a time series. Those on which the head moved by more than 0.2 mm and 2 degrees were excluded. We first magnify the BOLD image by 10 times (Suzuki et al., 2013), and then the BOLD images were registered to T2 structure images of each rat by non-linear transformation. Following, the images were registered to Wistar rat brain templates (resampling voxel size = 3 mm × 3 mm × 3 mm) using the Statistical Parametric Mapping package in SPM8.[1] Next, the fMRI image voxels were spatially normalized to 0.3 × 0.3 × 0.3 mm and smoothed with an isotropic Gaussian kernel (FWHM = 0.4 mm) as actual sizes of rats. The time series for each voxel was transformed to the frequency domain and the power spectrum was then obtained. The square root was calculated at each frequency of the power spectrum and the average square root was obtained across 0.01–0.08 Hz at each voxel. This averaged square root was taken as the ALFFs were normalized by the mean within-brain ALFF value for each subject with DPABI software.[2] We performed an ANOVA among the three groups (sham vs. day 7 post CLP vs. day 14 post CLP) using the toolbox in SPM8. After significant clusters were generated within a binary mask, *post-hoc* two-sample *t*-tests were performed between the two experimental

1 https://www.fil.ion.ucl.ac.uk/spm/
2 http://rfmri.org/dpabi

groups within the previously generated mask. All significance tests were conducted at an FDR threshold of $P = 0.005$. We abstracted right CA-1 area from ANOVA analysis results, and the ALFF values of the right CA-1 area of hippocampus were extracted from mean within-brain ALFF maps. These ALFF values were used as biomarker to evaluate brain function of rats.

Hydrogen proton magnetic resonance spectroscopy acquisition and analysis

Hydrogen proton magnetic resonance spectroscopy scans were performed after fMRI scan using 7 Tesla MRI scans. A Fast Spin Echo T2W image was performed to position 1-H MRS voxels of the hippocampus using an ultrashort echo time (TR/TE = 2500/16.6 ms) spectroscopy method. The target voxel of interest = 2 × 2 × 1 mm^3 with a TA = 5 min 20 s. After extracting MR spectra in these groups, we analyzed and quantified the curve using Mestrenova software.[3] The compound was located by the position of the curve crest, N-acetylaspartate (NAA) located at 2.02ppm, creatine (Cr) located at 3.05 ppm, choline-compound (Cho) located at 3.20 ppm, Myo-inositol (mI) located at 3.56 ppm, lipid (Lip) located at 1.30 ppm and glutamine/glutamate (Glx) located at 3.75 ppm. The areas under a peak of NAA, Cr, Cho, mI, and Glx were measured, and the Cho/Cr, Glx/Cr, mI/Cr, NAA/Cho, and Lip/Cr ratios were determined.

Hippocampus-dependent behavioral tasks

Cognitive functions of spatial learning and memory were evaluated in the three groups rats by MWM test according to the methods of Wang et al. (2017). The diameter of the pool and the platform were 180 and 10 cm, respectively, and the platform was placed 2 cm below the water. The temperature of water was kept range from 22 to 24°C. The tests were recorded by a camera that was hung above the pool and the results were analyzed by ANY maze Video Tracking System (Stoelting Co., Wood Dale, IL, USA). The rats in the sham group and day 7 post CLP group were subjected to the MWM during day 3–7 post CLP surgery, while the rats in the day 14 CLP group were subjected to the MWM during day 10–14 post CLP surgery. During the continuous 4 days of training, each rat was released into the pool to find a platform placed under the water. This was performed four times from every different quadrant each day. The escape latency was recorded for each training session. Space exploration training was performed at the end day of the MWM test. The platform was removed, and all rats were monitored for 60 s in order to observe the time spent in the target quadrant and frequency of crossing the platform.

3 https://resources.mestrelab.com

Enzyme-linked immunosorbent assay

The hippocampus was removed after the rats were sacrificed, lysed with radioimmunoprecipitation assay (RIPA) buffer (Abcam, ab156034, Cambridge, UK), homogenized and centrifuged at 20,000 g for 1 min at 4°C. The levels of IL-1β, IL-6, and CRP were determined by ELISA kits (Solarbio, Beijing, China) according to the manufacturer's instructions, and the absorbance was measured with a micro-plate reader at 450 nm [optical density(OD) value].

Immunofluorescence

The rats were injected i.p. with pentobarbital sodium, and the brains harvested at 7 and 14 days post-surgery. Brains were fixed in 4% paraformaldehyde for 24 h at room temperature, embedded in paraffin, and cut into 5-μm coronal sections. The sections were blocked with 1% bovine serum albumin and incubated overnight at 4°C with a primary antibody against Iba-1 (1:100; Abcam, ab178846, Cambridge, UK), and then with a goat anti-rabbit IgG H&L (Cy3) (1:100, Abcam, ab6939) for 1 h at 4°C. Sections were then counterstained with 4,6-diamidino-2-phenylindole for 10 min at room temperature. Images were taken using a servicebio fluorescence microscope (Pannoram) and the fluorescence intensity of Iba-1 was analyzed using ImageJ software (National Institutes of Health, Bethesda, MD, USA).

Statistical analysis

Data are presented as mean ± SD was analyzed and were analyzed using SPSS 22.0 (SPSS Inc., Chicago, IL, USA) and GraphPad Prism 8 (GraphPad Software, San Diego, USA). Behavior test results, ALFF values, metabolism concentrations and ELISA results were analyzed using one-way ANOVA, followed by Tukey's honest significant difference test. Statistical significance was accepted at $p < 0.05$. The relationships between ALFF values, metabolism concentrations, and total time spent in the target quadrant in MWM were explored using Spearman's correlation analysis.

Results

Cecal ligation and perforation surgery induced amplitude of low-frequency fluctuation value abnormalities in sepsis associated encephalopathy rats

After CLP surgery intervention, compared with the sham group, the ALFF values in the day 7 post CLP group were

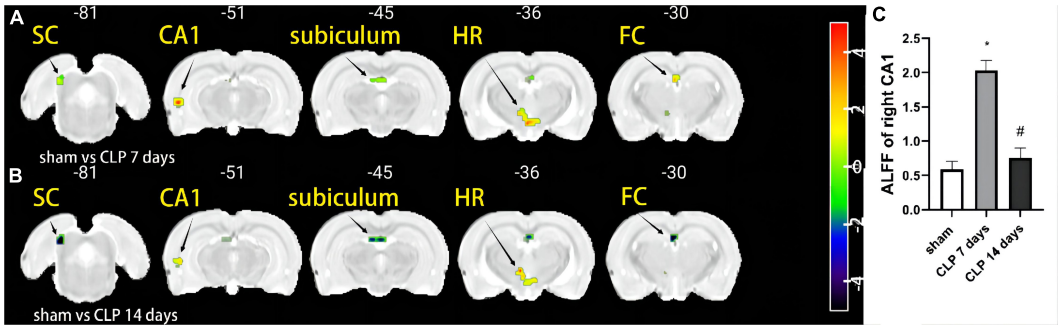

FIGURE 1
The amplitude of low-frequency fluctuation (ALFF) differences in the day 7 post cecal ligation and perforation (CLP), and day 14 post CLP groups. Warm (red-yellow) colors represent increased and cold (blue-green) colors decreased ALFF values in the day 7 post CLP, and day 14 post CLP groups. **(A)** ALFF values were higher in the right CA-1, left FC, and HR in the day 7 post CLP group. **(B)** The left FC, right deep layers of the SC, CA-1, and subiculum showed lower ALFF in the day 14 post CLP group (n = 8 in each group. FDR corrected $p < 0.005$, cluster size > 10 voxels). **(C)** The ALFF value of right CA-1 was significantly higher in the day 7 post CLP group than sham group, but lower in day 14 post group (n = 8, $^{*}p < 0.05$, compared with sham group, $^{\#}p < 0.05$, compared with day 7 post CLP group, analyzed by one-way ANOVA). CA-1: Cornu ammonis-1; SC: deep layers of the superior colliculus; FC: fasciola cinereum; HR: hypothalamic region.

higher in the right cornu ammonis-1 (CA-1) area, left fasciola cinereum (FC), and hypothalamic region (HR) compared with sham group ($p < 0.005$, FDR corrected, n = 8, Figure 1A). The ALFF values were lower in the left FC, right deep layers of the superior colliculus (SC) and subiculum in the day 14 post CLP group ($p < 0.005$, FDR corrected, n = 8, Figure 1B). The ALFF value of right CA-1 followed the rule of "enhanced-decreased" at day 7 and 14 post CLP surgery (Figure 1C). The number of voxels and Montreal Neurological Institute (MNI) coordinates of the abnormal brain regions in rats of CLP groups were listed in Table 1.

Altered brain metabolism in the hippocampus post cecal ligation and perforation surgery

Metabolites in the hippocampus were detected by 1H-MRS, and the spectrums are shown in Figure 2. There was no significant difference among the three groups in the Cho/Cr ratio ($p > 0.05$, Figure 3A). Significantly higher Glx/Cr and mI/Cr ratios were observed on day 7 and 14 post CLP surgery. Compared with the day 7 post CLP group, the Glx/Cr and mI/Cr ratios were significantly lower on day 14 post CLP group ($p < 0.05$, Figures 3B,C). The NAA/Cho metabolite ratio was significantly lower in the day 7 post CLP group than in sham group ($p < 0.05$). However, NAA/Cho ratio in the day 14 post CLP group was higher than that in day 7 post CLP group ($p < 0.05$, Figure 3D). The ratio of Lip/Cr rose continuously after CLP surgery, compared with sham group ($p < 0.05$, Figure 3E).

TABLE 1 Regions showing amplitude of low-frequency fluctuation (ALFF) differences among the sham, day 7 post cecal ligation and perforation (CLP), and day 14 post CLP groups.

Location cluster (AAL)	Number of voxels	MNI coordinates			Peak F
		x	*y*	*z*	
Hypothalamic region L	14	2.0	35.1	14.8	40.1
Cornu ammonis 1 R	10	65.0	50.1	9.2	34.2
Deeper layers of the superior colliculus R	13	29.0	80.1	36.2	80.5
Subiculum R	10	−1.0	44.1	36.2	55.5
Fasciola cinereum L	12	2.0	29.1	39.2	55.4

Cecal ligation and perforation surgery enhanced microglia related inflammation in sepsis associated encephalopathy rats

We examined the expression of IL-1β (Figure 4A), IL-6 (Figure 4B), and CRP (Figure 4C) to assess the severity of inflammation in hippocampus of SAE rats. It was observed that IL-1β, IL-6, and CRP levels in hippocampus of SAE rats were notably higher than those in the sham group ($p < 0.05$). The expression of IL-1β in the day 14 post CLP group were significantly lower than those in the day 14 post CLP group ($p < 0.05$). However, the expression of IL-6 was higher in the day 14 post CLP group than that in day 7 post CLP group ($p < 0.05$). No significant difference in CRP levels was found between the day 7 and 14 post CLP groups.

Ionized calcium binding adaptor molecule-1 (Iba-1) immunofluorescence staining was performed to detect the microglial distribution in the hippocampus (Figure 4E). In the day 7 post CLP groups, the fluorescence intensity of

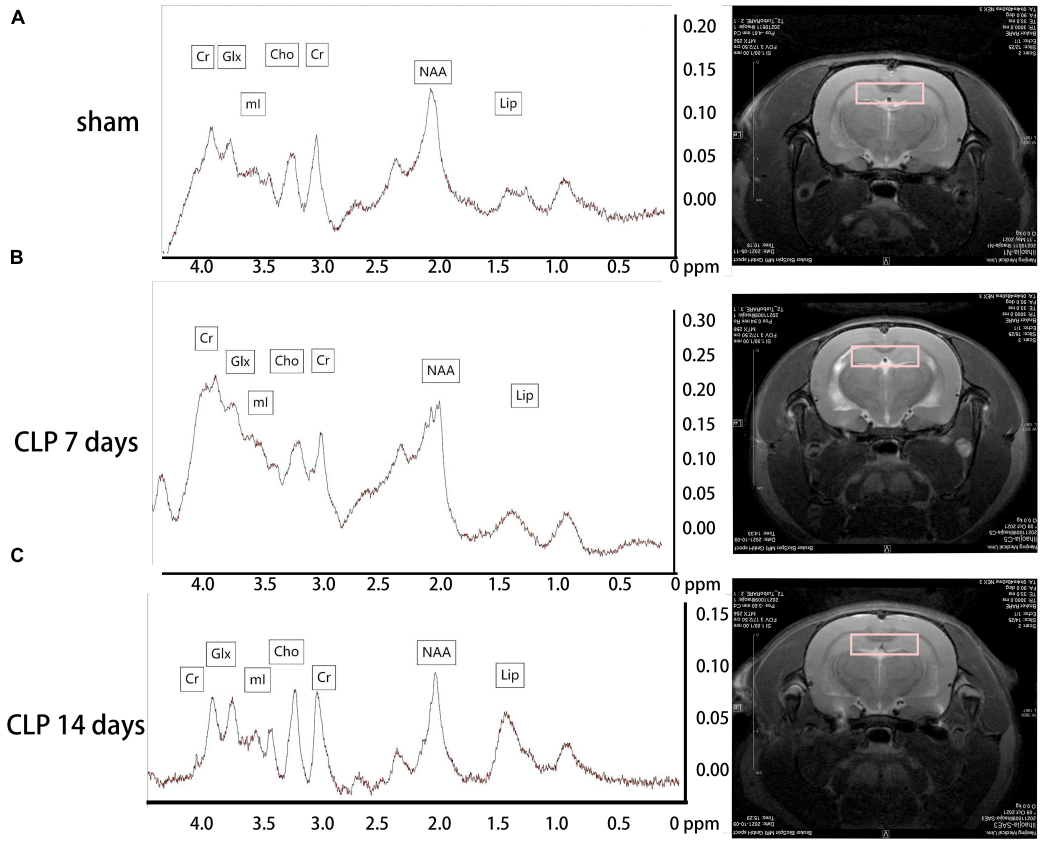

FIGURE 2
Metabolites in the hippocampus detected by 1H-MRS. Metabolites in the hippocampus were analyzed by 1H-MRS, and the spectrums determined by MestReNova. The representative metabolite spectrum in the hippocampus of rats and region position in the coronal image in the sham group **(A)**; in the day 7 post CLP group **(B)**; in the day 14 post CLP group **(C)**.

Iba-1 increased significantly than that in the sham group, but decreased in day 14 post CLP group compared with day 7 post CLP group (Figure 4D). These results indicated that Iba-1-positive cells gathered in the hippocampus after CLP surgery.

Cecal ligation and perforation surgery deteriorates cognitive performance in the Morris water maze task

To evaluate CLP-induced memory impairment over time, we studied the learning and memory performance of rats at 7 and 14 days after CLP surgery by MWM test. The tracks of rats in probe tests of MWM were shown in Figure 5A. During the training session of MWM, the rats in day 7 post CLP group exhibited decreased in learning function, as was demonstrated by increased latency to platform. However, the platform latency changed little in day 14 post CLP group compared with that in day 7 post CLP group (Figure 5B). In the space exploration experiment, memory performance of the rats was analyzed in terms of the time spent in the target quadrant of MWM test. CLP treated rats exhibited decreased duration in the target quadrant at 7 and 14 days (Figure 5C). Furthermore, CLP surgery decreased the number of crossing platform at 7 and 14 days post CLP (Figure 5D). However, the differences in the time spent in the target quadrant and the times of crossing the platform were not significantly between 7 and 14 post CLP groups. The results suggested that the learning and memory functions of CLP treated groups were impaired from 7 to 14 days after CLP surgery in the Morris water maze test.

The correlation analysis between the amplitude of low-frequency fluctuation values, metabolites, and behavioral parameters

As we found that the ALFF values and Glx/Cr and mI/Cr ratios fluctuated post CLP surgery, we evaluated the correlation between ALFF values of the CA-1 region with Glx/Cr and mI/Cr ratios and behavior test results. The ALFF value of the right

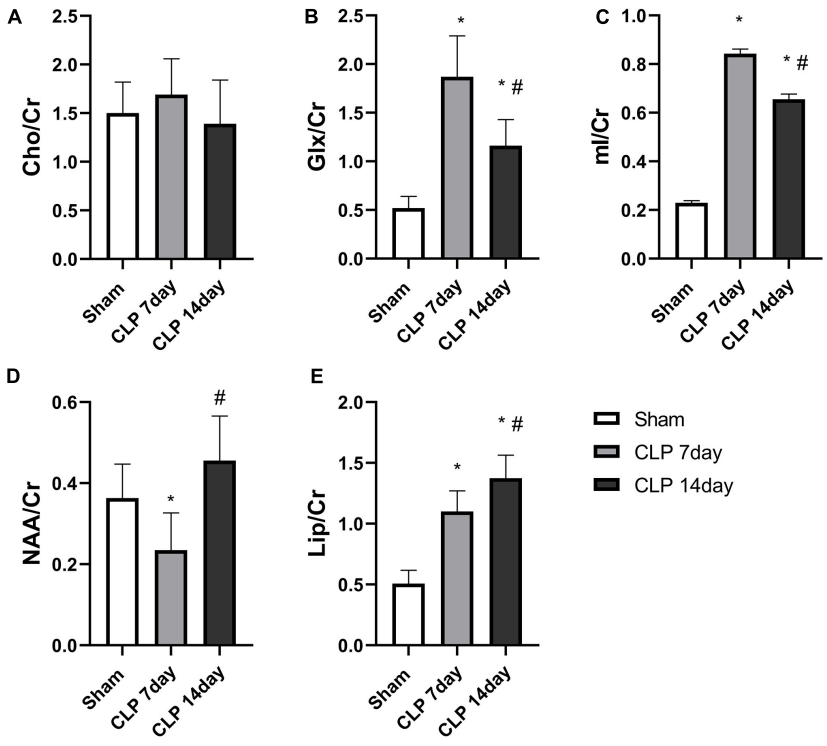

FIGURE 3
Metabolite analysis among the three groups. There was no obvious difference in the **(A)** Cho/Cr ratio among the groups ($p > 0.05$, analyzed by one-way ANOVA, $n = 8$); The Glx/Cr **(B)** and mI/Cr ratios **(C)** were significantly increased in the hippocampi of day 7 post CLP group, but were obviously lower in day 14 post group. **(D)** NAA/Cr ratios in the right hippocampus generally followed the rule of "decreased-enhancement" post CLP surgery. **(E)** Lip/Cr ratios increased gradually post CLP surgery (*$p < 0.05$, compared with sham group, $^{\#}p < 0.05$, compared with day 7 post CLP group, analyzed by one-way ANOVA) ($n = 8$. Data are expressed as the mean ± SD).

CA-1 was negatively correlated with the total time in spent in the target quadrant, which reflected the capacity of episodic memory (**Figure 6A**; $r^2 = 0.520$, $p = 0.0016$). We also analyzed the correlation between metabolites and time spent in the target quadrant. The mI/Cr ratio was negatively correlated (**Figure 6B**; $r^2 = 0.630$, $p = 0.0002$), whereas the Glx/Cr ratio was negatively correlated (**Figure 6C**; $r^2 = 0.479$, $p = 0.003$), with time spent in the target quadrant.

Discussion

In this study, we measured the ALFF value and metabolite changes in the hippocampus during the progression of sepsis associated cognitive impairments 7 and 14 days post CLP surgery. We found that the ALFF values in the right CA-1 area of the hippocampus was higher at day 7 post CLP surgery than sham group, and lower at 14 days post CLP surgery. Conversely, the Glx/Cr and mI/Cr ratios were higher at day 7 post CLP surgery and were lower at 14 days post CLP surgery; trends of which were coincident with IL-1β levels in the hippocampus. Furthermore, ALFF value of right CA-1, the Glx/Cr and mI/Cr ratios were negatively related to cognitive function, suggesting brain ALFF values and metabolite alterations can be used to evaluate cognitive deficits in SAE rats.

It is known that SAE is the most common cause of encephalopathy in medical-surgical ICUs. The neural metabolic disturbance sand functional deficits in the CNS are responsible for cognitive impairment of SAE patients (Xie et al., 2022). Previous studies have shown that the diagnosis of SAE relies on questionnaires such as the Confusion Assessment Method for the ICU, as well as delirium screening tools (Feng et al., 2019; Klawitter et al., 2020). Currently, rs-fMRI is gaining growing popularity in the clinical evaluation of cognitive impairment such as Alzheimer's disease, post-traumatic stress disorder, and post-operative cognitive dysfunction (Herringa, 2017; Zhang et al., 2019), but studies on its use in SAE patients are still limited. In our study, we found significantly higher ALFF values in the right CA-1, left FC, and HR in SAE rats at 7 days post CLP surgery by rs-fMRI. Conversely, the ALFF values were lower in the left FC, right deep layers of the SC, CA-1, and subiculum at 14 days post CLP. The regions studied, including the FC, CA-1, and subiculum are important components of the hippocampus, which play a significant role in spatial learning and memory in rats. The relationship between ALFF values and cognitive function test remains to be further elucidated.

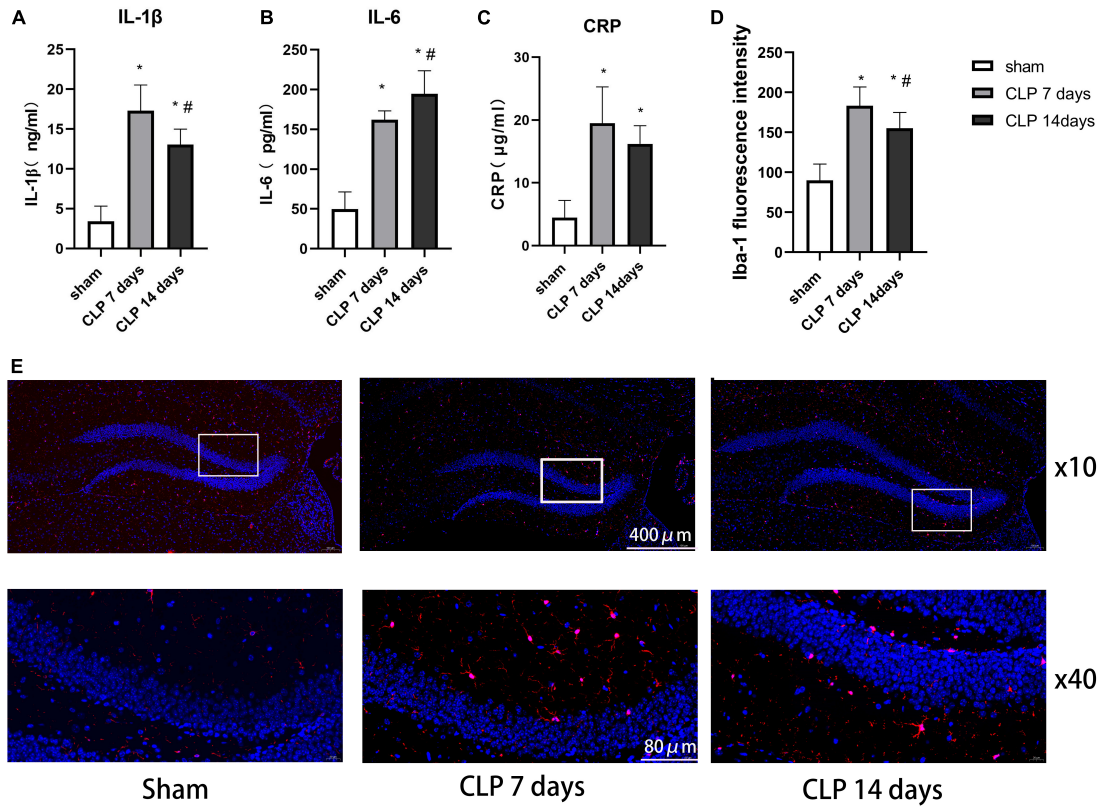

FIGURE 4
Cecal ligation and perforation surgery enhanced microglia related inflammation in hippocampus of SAE rats. The difference in panel **(A)** IL-1β, **(B)** IL-6, and **(C)** CRP levels in hippocampus among the three groups. **(D)** The intensity of Iba-1 in the hippocampus detected by immunofluorescence staining ($^{*}p < 0.05$, compared with the sham group, $^{\#}p < 0.05$, compared with day 7 CLP group, analyzed by one-way ANOVA, $n = 8$). Data are expressed as the mean ± SD. **(E)** Representative immunofluorescence staining of Iba-1 (red) in the hippocampus, $n = 8$ per group.

The hippocampus is well known for its role in long-term memory and MWM-associated spatial learning and memory in rodents has been linked to the hippocampus (Liu et al., 2021). As CLP surgery has been shown to cause sustained cognitive impairment 5–15 days post-surgery and a previous study performed the MWM test at 1–2 weeks post CLP surgery to assess cognitive function in SAE rats (Shen et al., 2020; Giridharan et al., 2022), we further analyzed the ALFF values and metabolism changes during the same time period. In our results, the increased ALFF values in the hippocampus supported the deteriorated behavioral results in the MWM test, which was consistent with a previous studies using the MWM test to evaluate hippocampal function (Barnhart et al., 2015). As shown in previous research, the brain functional connection between right hippocampus and thalamus increased in CLP induced SAE rats, and the enhanced functional values between the two regions were negatively correlated with behavioral performance in rats with SAE (Yao et al., 2022). These results suggested that CLP surgery not only increased regional spontaneous neuronal activity in hippocampus, but also enhanced the functional connection between hippocampus and other brain regions. This is in agreement with the findings of a previous study indicated that changes in hippocampal function biomarkers detected by fMRI might reflect the spatial memory ability of rats (Shah et al., 2019). Therefore, the ALFF values of the right CA-1 area are an excellent biomarker to evaluate the cognitive function in SAE rats.

In recent years, 1H-MRS has been widely used to detect neurochemical alterations in specific brain regions of patients with brain tumors, indicating that metabolic changes can be used as biomarkers to identify brain tumors (Liu et al., 2021). In the present study, we obtained 1H-MRS data from the hippocampi of rats in the sham and CLP surgery groups. The mI/Cr ratio, a marker for the glial cell proliferation, was significantly increased in the day 7 and 14 post CLP group, consistent with the trend of IL-1β levels in serum. Recent research demonstrated that mI can cause glial cells differentiation, and that the elevation of the mI/Cr ratio is often interpreted to reflect glial cell activation (Schnider et al., 2020). With a focus on changes in immunofluorescence staining results after CLP surgery, we observed that microglial cells activated in the hippocamp of SAE rats, which supported the hypothesis

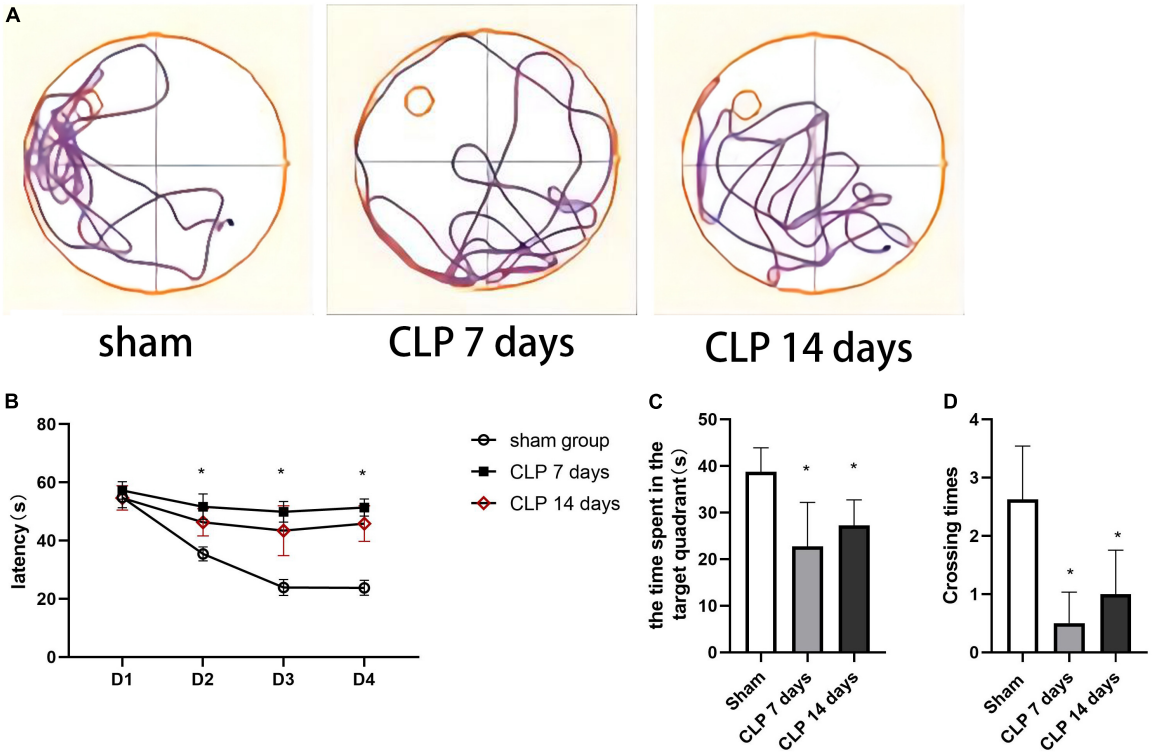

FIGURE 5
Cecal ligation and perforation surgery deteriorates cognitive performance in the MWM task. **(A)** The typical tracks of rats in the three groups in the probe test. **(B)** The latency of finding the hidden platform in on training days (*$p < 0.05$, versus sham group, $n = 8$) analyzed by repeated measures ANOVA and Tukey's *post hoc* comparison. **(C)** The time spent in the target quadrant in the probe trail and **(D)** the number of crossings the platform location (*$p < 0.05$, versus sham group, $n = 8$) analyzed by one-way ANOVA. Data are expressed as the mean ± SD.

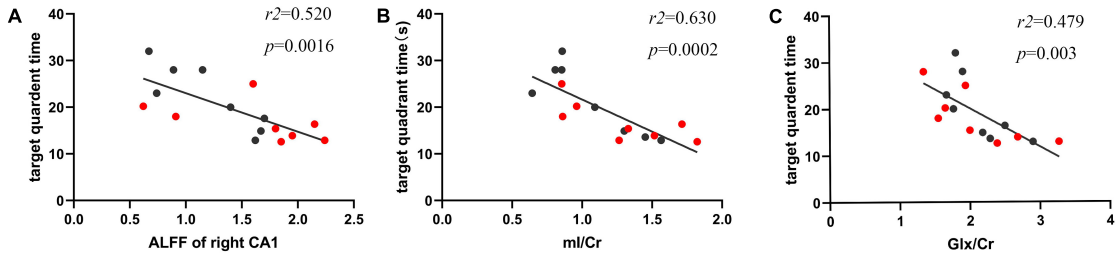

FIGURE 6
The ALFF values and metabolites in the hippocampus were negatively correlated with duration in the target quadrant. **(A)** The ALFF value of the right CA-1 was negatively correlated with total time spent in the target quadrant ($r^2 = 0.520$, $p = 0.0016$). **(B)** The mI/Cr ratio was negatively correlated with target time spent in the target quadrant ($r^2 = 0.630$, $p = 0.0002$). **(C)** The Glx/Cr ratio was negatively correlated with total time spent in the target quadrant ($r^2 = 0.479$, $p = 0.003$). The red samples represented the rats from day 7 post CLP group, and black samples from day 14 post CLP group.

that the mI/Cr can reflect central inflammation in SAE rats. We also found the Glx/Cr ratio was elevated in the day 7 and 14 post CLP groups. Recent studies have shown that higher Glx/Cr ratio was obvious in minimal hepatic encephalopathy patients (Chen et al., 2020). The increase in the levels of intracellular glutamine leads to osmotic dysregulation and astrocyte swelling in hippocampus (Karczewska-Kupczewska et al., 2018). In addition to the findings presented above, we detected the higher mI/Cr and Glx/Cr ratios were negatively correlated with time spent in the target quadrant of MWM test. Our results demonstrate that the mI/Cr and Glx/Cr ratios are significant bio-markers in the CLP induced SAE rat model. As there is mounting evidence that differences in metabolites are evident in early SAE rats, future studies to assess cognitive decline of SAE patients by 1H-MRS are needed.

There were some limitations in our study. First, we did not distinguish between lipid and lactate, since these two metabolites show overlapping resonance frequencies (chemical shifts) at 1.33–1.35 PPM. Observations of higher Lip/Cr may reflect neuronal damage in SAE rats, a finding that awaits further investigation with newer acquisition techniques. Furthermore, we only tested the rats in at day 7 and 14 post CLP surgy by rs-fMRI and pathological methods; long-term observation should be administered in future study. In regard to pre-processing methods of BOLD signal, we only registered the BOLD images by non-linear transformation. We would improve pre-processing methods to reduce the distorted regions and guarantee the BOLD signal reliability by the 3D reversed phase encoding method in our further study.

Conclusion

In conclusion, this study applied rs-fMRI and 1H-MRS to detect functional and metabolites changes in the hippocampus of SAE rats. Briefly, we conclude from the present study that alterations in ALFF values and the mI/Cr and Glx/Cr ratios in the hippocampus are negatively related to cognitive function in SAE rats. Furthermore, microglial activation and accompanied inflammation were closely related to brain function during early SAE. Further research will help to improve the understanding of earlier identification of cognitive deficits in SAE.

Data availability statement

The raw data supporting the conclusions of this article will be made available by the authors, without undue reservation.

Ethics statement

The animal study was reviewed and approved by the Institutional Animal Care and Use Committee of Nanjing Medical University (IACUC: 2103051).

Author contributions

HJL, HB, and HSL designed the research. HJL, HSL, YX, and CZ performed the research. HJL, YS, YC, SS, and XX collected and analyzed the data. YS and HB provided the administrative support. HJL, QL, and HB drafted the manuscript. All authors edited and approved the manuscript.

Funding

This work was supported by grants from the National Natural Science Foundation of China (grant numbers: 81971872 and 81873954).

Acknowledgments

We thank Dandan Liang for her help with the MRI scan and Jing Xiao for his critical comments on the manuscript.

Conflict of interest

The authors declare that the research was conducted in the absence of any commercial or financial relationships that could be construed as a potential conflict of interest.

Publisher's note

References

Barnhart, C. D., Yang, D., and Lein, P. J. (2015). Using the morris water maze to assess spatial learning and memory in weanling mice. *PLoS One* 10:e0124521. doi: 10.1371/journal.pone.0124521

Cai, M., Du, B., Si, Y., Miao, J., Ge, J., Zhang, J., et al. (2021). Knockdown of VDAC1 alleviates the cognitive dysfunction secondary to sepsis-associated encephalopathy. *Am. J. Transl. Res.* 13, 7538–7555.

Chen, L. H., Shi, J. Y., Zou, T. X., Zhang, L., Gou, Y., Lin, Y., et al. (2020). Disturbance of thalamic metabolism and its association with regional neural dysfunction and cognitive impairment in minimal hepatic encephalopathy. *Eur. J. Radiol.* 131:109252. doi: 10.1016/j.ejrad.2020.109252

Chung, H. Y., Wickel, J., Brunkhorst, F. M., and Geis, C. (2020). Sepsis-associated encephalopathy: From delirium to dementia? *J. Clin. Med.* 9:703. doi: 10.3390/jcm9030703

El-Abtah, M. E., Wenke, M. R., Talati, P., Fu, M., Kim, D., Weerasekera, A., et al. (2022). Myo-inositol levels measured with MR spectroscopy can help predict failure of antiangiogenic treatment in recurrent glioblastoma. *Radiology* 302, 410–418. doi: 10.1148/radiol.2021210826

Feng, Q., Ai, Y. H., Gong, H., Wu, L., Ai, M. L., Deng, S. Y., et al. (2019). Characterization of sepsis and sepsis-associated encephalopathy. *J. Intensive Care Med.* 34, 938–945. doi: 10.1177/0885066617719750

Gao, M., Yu, T., Liu, D., Shi, Y., Yang, P., Zhang, J., et al. (2021). Sepsis plasma-derived exosomal miR-1-3p induces endothelial cell dysfunction by targeting SERP1. *Clin. Sci.* 135, 347–365. doi: 10.1042/CS20200573

Giridharan, V. V., Generoso, J. S., Lence, L., Candiotto, G., Streck, E., Petronilho, F., et al. (2022). A crosstalk between gut and brain in sepsis-induced cognitive decline. *J. Neuroinflamm.* 19:114. doi: 10.1186/s12974-022-02472-4

Herringa, R. J. (2017). Trauma, PTSD, and the developing brain. *Curr. Psychiatry Rep.* 19:69. doi: 10.1007/s11920-017-0825-3

Hsu, C. H., Lin, S., Ho, A. C., Johnson, T. D., Wang, P. C., Scafidi, J., et al. (2021). Comparison of *in vivo* and in situ detection of hippocampal metabolites in mouse brain using (1) H-MRS. *NMR Biomed.* 34:e4451. doi: 10.1002/nbm.4451

Huang, L., Huang, G., Ding, Q., Liang, P., Hu, C., Zhang, H., et al. (2021). Amplitude of low-frequency fluctuation (ALFF) alterations in adults with subthreshold depression after physical exercise: A resting-state fMRI study. *J. Affect. Disord.* 295, 1057–1065. doi: 10.1016/j.jad.2021.08.094

Karczewska-Kupczewska, M., Nikolajuk, A., Filarski, R., Majewski, R., and Tarasow, E. (2018). Intralipid/heparin infusion alters brain metabolites assessed with 1H-MRS spectroscopy in young healthy men. *J. Clin. Endocrinol. Metab.* 103, 2563–2570. doi: 10.1210/jc.2018-00107

Klawitter, F., Jager, M., Klinkmann, G., Saller, T., Söhle, M., von Möllendorff, F., et al. (2020). Sepsis-assoziierte enzephalopathie. *Anaesthesist* 70, 112–120. doi: 10.1007/s00101-020-00853-z

Kuan, E., Chen, X., Du, F., and Ongur, D. (2021). N-acetylaspartate concentration in psychotic disorders: T2-relaxation effects. *Schizophr. Res.* 232, 42–44. doi: 10.1016/j.schres.2021.04.012

Li, C., Yu, T. Y., Zhang, Y., Wei, L. P., Dong, S. A., Shi, J., et al. (2020). Electroacupuncture improves cognition in rats with sepsis-associated encephalopathy. *J. Surg. Res.* 256, 258–266. doi: 10.1016/j.jss.2020.06.056

Liu, Y., Fu, H., Wu, Y., Nie, B., Liu, F., Wang, T., et al. (2021). Elamipretide (SS-31) improves functional connectivity in hippocampus and other related regions following prolonged neuroinflammation induced by lipopolysaccharide in aged rats. *Front. Aging Neurosci.* 13:600484. doi: 10.3389/fnagi.2021.600484

Peng, X., Luo, Z., He, S., Zhang, L., and Li, Y. (2021). Blood-brain barrier disruption by lipopolysaccharide and sepsis-associated encephalopathy. *Front. Cell. Infect. Microbiol.* 11:768108. doi: 10.3389/fcimb.2021.768108

Piersson, A. D., Ibrahim, B., Suppiah, S., Mohamad, M., Hassan, H. A., Omar, N. F., et al. (2021). Multiparametric MRI for the improved diagnostic accuracy of alzheimer's disease and mild cognitive impairment: Research protocol of a case-control study design. *PLoS One* 16:e0252883. doi: 10.1371/journal.pone.0252883

Rittirsch, D., Huber-Lang, M. S., Flierl, M. A., and Ward, P. A. (2009). Immunodesign of experimental sepsis by cecal ligation and puncture. *Nat. Protoc.* 4, 31–36. doi: 10.1038/nprot.2008.214

Schnider, B., Tuura, R., Disselhoff, V., Latal, B., Wehrle, F. M., and Hagmann, C. F. (2020). Altered brain metabolism contributes to executive function deficits in school-aged children born very preterm. *Pediatr. Res.* 88, 739–748. doi: 10.1038/s41390-020-1024-1

Shah, D., Verhoye, M., Van der Linden, A., and D'Hooge, R. (2019). Acquisition of spatial search strategies and reversal learning in the morris water maze depend on disparate brain functional connectivity in mice. *Cereb. Cortex* 29, 4519–4529. doi: 10.1093/cercor/bhy329

Shen, Y., Jing, L., Zhang, Y., Bao, H., Vohra, A., Si, Y., et al. (2020). CXCR5 knockdown attenuates hippocampal neurogenesis deficits and cognitive impairment in a mouse model of sepsis-associated encephalopathy. *Neuroscience* 433, 212–220. doi: 10.1016/j.neuroscience.2020.03.013

Suzuki, H., Sumiyoshi, A., Kawashima, R., and Shimokawa, H. (2013). Different brain activation under left and right ventricular stimulation: An fMRI study in anesthetized rats. *PLoS One* 8:e56990. doi: 10.1371/journal.pone.0056990

Tao, J., Liu, J., Chen, X., Xia, R., Li, M., Huang, M., et al. (2019). Mind-body exercise improves cognitive function and modulates the function and structure of the hippocampus and anterior cingulate cortex in patients with mild cognitive impairment. *Neuroimage Clin.* 23:101834. doi: 10.1016/j.nicl.2019.101834

Tauber, S. C., Djukic, M., Gossner, J., Eiffert, H., Bruck, W., and Nau, R. (2021). Sepsis-associated encephalopathy and septic encephalitis: An update. *Expert Rev. Anti Infect. Ther.* 19, 215–231. doi: 10.1080/14787210.2020.1812384

Wang, W., Liu, L., Jiang, P., Chen, C., and Zhang, T. (2017). Levodopa improves learning and memory ability on global cerebral ischemia-reperfusion injured rats in the Morris water maze test. *Neurosci. Lett.* 636, 233–240. doi: 10.1016/j.neulet.2016.11.026

Xie, Z., Xu, M., Xie, J., Liu, T., Xu, X., Gao, W., et al. (2022). Inhibition of ferroptosis attenuates glutamate excitotoxicity and nuclear autophagy in a CLP septic mouse model. *Shock* 57, 694–702. doi: 10.1097/SHK.0000000000001893

Yao, Y., Lu, C., Chen, J., Sun, J., Zhou, C., Tan, C., et al. (2022). Increased resting-state functional connectivity of the hippocampus in rats with sepsis-associated encephalopathy. *Front. Neurosci.* 16:894720. doi: 10.3389/fnins.2022.894720

Zhang, X., Li, H., Lv, Y., Zhu, Z., Shen, X., Lu, Q., et al. (2019). Premorbid alterations of spontaneous brain activity in elderly patients with early post-operative cognitive dysfunction: A pilot resting-state functional MRI study. *Front. Neurol.* 10:1062. doi: 10.3389/fneur.2019.01062

Zou, Q. H., Zhu, C. Z., Yang, Y., Zuo, X. N., Long, X. Y., Cao, Q. J., et al. (2008). An improved approach to detection of amplitude of low-frequency fluctuation (ALFF) for resting-state fMRI: Fractional ALFF. *J. Neurosci. Methods* 172, 137–141. doi: 10.1016/j.jneumeth.2008.04.012

Frontiers in Neuroscience

Provides a holistic understanding of brain function from genes to behavior

Part of the most cited neuroscience journal series which explores the brain - from the new eras of causation and anatomical neurosciences to neuroeconomics and neuroenergetics.

Discover the latest Research Topics

See more →

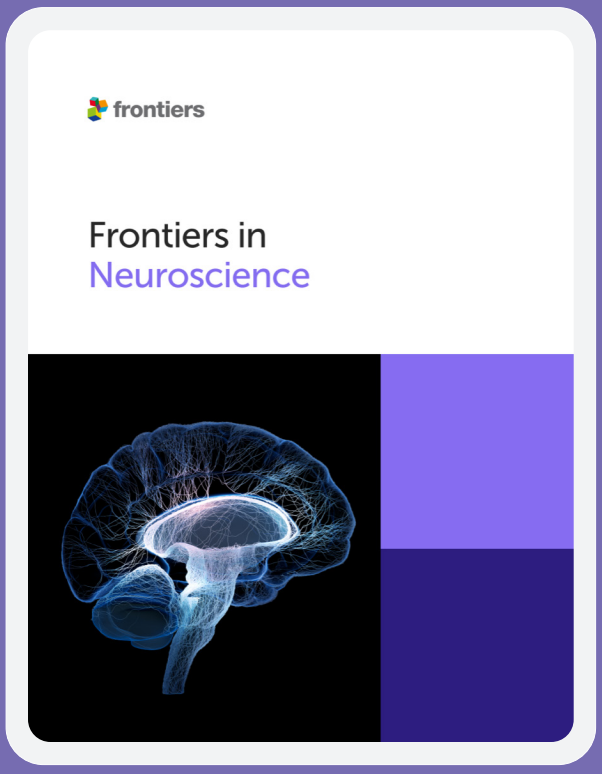

Frontiers

Avenue du Tribunal-Fédéral 34
1005 Lausanne, Switzerland
frontiersin.org

Contact us

+41 (0)21 510 17 00
frontiersin.org/about/contact